THÈSE

pour l'obtention du titre de

Docteur de l'Université de Lorraine

présenté par :

Muhammad ARIF

préparée au sein du :
Laboratoire Matériaux Optiques, Photonique et Systèmes EA 4423
Université de Lorraine et CentraleSupélec
et
Unité Mixte Internationale GT-CNRS 2958
Georgia Tech Lorraine et CNRS

Etude de deux nouvelle approches pour la réalisation de cellule solaire à base d'InGaN

Thèse soutenue publiquement à Metz
devant le jury composé de :

Mme. Eva Monroy	Chercheur CEA INAC/SP2M, Grenoble	Rapporteur
M. Farid Medjdoub	Chercheur CNRS IEMN, Lille	Rapporteur
M. Abdel Hadi Kassiba	Professeur Université du Maines, Le Mans	Examinateur
M. Ali Ahaitouf	Professeur USMBA Fès, Maroc	Examinateur
M. Philippe Gros	Professeur Université de Lorraine, Nancy	Examinateur
M. Zakaria Djebbour	Professeur Université de Paris-Saclay	Examinateur
M. Abdallah Ougazzaden	Professeur Georgia Institute of Technology	Co-directeur
M. Jean-Paul Salvestrini	Professeur Université de Lorraine, Metz	Directeur

THESIS

DOCTOR OF PHILOSOPHY

UNIVERSITÉ DE LORRAINE

Muhammad ARIF

prepared at:

Laboratoire Matériaux Optiques, Photonique et Systèmes EA 4423

Université de Lorraine and CentraleSupélec

et

Unité Mixte Internationale GT-CNRS 2958

Georgia Tech Lorraine and CNRS

Investigation of new approaches for the realization of InGaN based solar cells

---

Mme. Eva Monroy	Researcher CEA INAC/SP2M, Grenoble	Reporter
M. Farid Medjdoub	Researcher CNRS-IEMN, Lille	Reporter
M. Abdel Hadi Kassiba	Professor Univeristy of Maines, Mans	Examiner
M. Ali Ahaitouf	Professor USMBA Fès, Marocco	Examiner
M. Philippe Gros	Professor University of Lorraine, Nancy	Examiner
M. Zakaria Djebbour	Professor University of Paris-Saclay	Examiner
M. Abdallah Ougazzaden	Professor Georgia Institute of Technology	Co-director
M. Jean-Paul Salvestrini	Professor University of Lorraine, Metz	Director

To my parents,
for their prayers, support and sacrifices...

Contents

Acknowledgments

I would like to thank my advisers, Professor Jean-Paul Salvestrini and Professor Abdallah Ougazzaden, for their guidance, encouragement, and support. It has been an honor and privilege to be their PhD student. Their endless knowledge and ability to relate many ideas together has made this work possible.

I'm very grateful to Professor Paul L. Voss for his encouragement and generous support. His detailed and constructive comments in all kind of topics related to this work were an indispensable help.

I convey my thanks to the members of the jury: Dr. Eva Monroy, Dr. Farid Medjdoub, Dr. Abdel Hadi Kassiba, Dr. Ali Ahaitouf, Dr. Philippe Gros and Dr. Zakaria Djebbour for accepting to serve in the jury, despite of their busy schedule.

I would like to thank Dr. François Montaigne, Dr. Badreddine Assour and Laurent Bouvot for their support and help in accessing the clean room facilities and performing the device processing. I am grateful to Dr. Ramdane Abderrahim and Dr. Sofiane Belahsene from "Laboratoire de Photonique et de Nanostructures" for their valuable help in fabrication. I would like to thank Dr. Abdellilah Slaoui and Dr. Thomas Fix for their help in accessing the facilities of iCUBE (Université de Strasbourg).

Also, I would like to acknowledge the help from adminstration and technical staff. A big thank you to Ms. Cecile Schreiber, Ms. Évelyne steiner, Jean-Claud Petit and Hadrien Chaynes for their assistance in many ways during my studies. A very special thank you to Céline Jobard for her lots of help not only in administration but also in accessing and using the chemistry room during the studies. I am grateful to have had her as a colleague and friend.

I would like to say thank you to my colleagues and friends, Hassan, Nadia, Imen, Cherifa, Ivan, Imed, Elise, Wahab, Sarrah, Marie, Joris, Mohammdou, bachirou, Yacine, Jérémy, Youssef, Suresh, Xin, Matt, Chris, Peter, Renaud, Taha, Saiful, Mohammed for providing such a pleasant working atmosphere and whose support and encouragement always perpetually refreshed, helped and inspired me through the hard times. It was fortunate for me to have met such supportive and friendly colleagues.

I would also like to thank my brother Dr. M. Sadiq Khattak, who deserve special mention for his inseparable support and encouragement during my PhD. A special thanks to my parents and whole family. Your prayers and support made all this possible.

Finally, I would like to thank everybody who was important to the successful realization of my thesis and my apology for those whom I could not mention personally one by one.

Introduction

III-Nitride semiconductor materials are predominately used for applications including light emitting diodes (LEDs), high electron mobility transistors etc. In the early 90's, Indium Gallium Nitride (InGaN) was developed as a new material to be used in LEDs. However, after the re-evaluation of the InN bandgap (0.64 eV), making possible to tune the InGaN bandgap (with indium incorporation) across nearly the entire solar spectrum (0.64 - 3.4 eV), attracted much more attention of the scientific community for another possible application: Photovltaics. In addition to that, InGaN material possesses the desired properties, such as high radiation resistance and high absorption coefficient (10^5 cm^{-1}), for high efficiency concentrated PV technologies, in which lenses and mirrors focus the sunlight on a small area solar cell, significantly decreasing the amount of material required and, consequently, the overall cost of the photovoltaic device. The varying badgap of InGaN alloy offers unique opportunity to design multijunction solar cells, with the flexibility of choosing the number and bandgap energies of the constituent junctions. It (bandgap tunability) is also able to utilize high energy photons with more efficiency than those made from traditional III-V alloys, which are limited to bandgaps of less than 2.2 eV, making possible to overcome the required bandgap >2.4 eV to go beyond the 50% efficiency barrier [1] for III-V (GaAs) based 4-junction solar cell with current efficiency of 46% under concentrated light (508 suns) [2]. Similarly InGaN added on top of Si (InGaN/Si multijunction solar cell) has a predicted power conversion efficiency of 36% under 500 times concentrated AM 1.5G solar spectrum [3]. In theory the unique properties of InGaN should translate into high efficiency, long lifetimes, and ultra thin solar cells. However, tuning the bandgap of InGaN epitaxial layer to lower energy with high indium incorporation has proven difficulties such as phase separation (compositional instability) due to the poor miscibility of InN and GaN and relaxation of the mismatch stress accommodated in the InGaN layers due to its growth on foreign substrates (with lattice and thermal expansion coefficient mismatch) restricts the critical layer thickness of the InGaN epilayer for a given indium concentration. These factors result in intensive generation of extended defects (threading dislocations) in InGaN that (i) lead to formation of the conductive channels shunting the PV device and (ii) make shorter the carrier lifetime in the InGaN light absorption region [4]. Therefore, InGaN solar cells reported until now results in low power conversion efficiency than what is expected theoretically.

In this context, the objective of this work is to investigate new approaches that could help to obtain high efficiency InGaN solar cells by overcoming the challenges mentioned above. These new approaches are developed by our joint team at UMI GT-CNRS 2958 (Georgia Tech Lorraine) and LMOPS EA 4423 (Université de Lorraine et CentraleSupélec). The two laboratories with the state-of-the-art equipment's work on the growth of III-Nitride materials. For this project of realization of high efficiency InGaN solar cells using those newly developed approaches, all the InGaN PIN structures are grown using MOCVD by our joint team at UMI GT-CNRS 2958 and LMOPS EA 4423. The device

fabrication is partially carried out at LMOPS EA 4423 and partner laboratories, including CNRS /LPN : Laboratoire de Photonique et de Nanostructures (France), IEMN - Institut d'électronique de microélectronique et de nanotechnologie (France) and Georgia Institute of Technology, (Atlanta, USA). The device design is done by UMI GT-CNRS 2958 and Geeps - Génie Electrique et Electronique de Paris-Saclay (France). The structural, morphological and electro-optical characterization of these InGaN solar cells is carried out at UMI GT-CNRS 2958 and LMOPS EA 4423. I contributed to the device design in collaboration with Geeps. I also worked on optimization of the p-GaN metal contacting, and partially contributed to the final device processing of InGaN solar cells. I performed the morphological and electro-optical characterization of the functional InGaN solar cells. In this study, the structural and morphological investigations are carried out using X-ray diffraction (XRD), Scanning electron microscopy (SEM) and High angular annular dark field electron microscopy (HAADF-STEM), and the electro-optical characterization of the solar cells are performed using, current-voltage, external quantum efficiency (EQE) and electron beam induced current (EBIC) measurements. These results are organized in the manuscript as follows;

Chapter 1 presents a brief introduction to III-Nitride materials, followed by the context and goals of the study. The chapter provide details of the two new solar cell design concepts developed by our team, for the realization of high efficiency InGaN solar cells.

Chapter 2 introduces the main challenges in InGaN materials that limits the potential use of InGaN for high efficiency solar cells. A literature study of the current state-of-the-art is presented for InGaN PV cells, with different active region designs, *i.e.* InGaN bulk heterojunction, InGaN multiple quantum wells (MQWs) and InGaN homojunction solar cells. Finally the two new solar cell design concepts developed by our team, *i.e.* Semibulk (multi-layered InGaN/GaN) and Nano-structure are presented.

Chapter 3 presents the results for bulk InGaN heterojunction solar cells. This type of solar cell design is used as a reference, for comparison with the new approaches developed by our team. During this study, we investigated the influence of V-pits in the p-GaN layer on the overall conversion efficiency of InGaN solar cells.

Chapter 4 presents the results for the first approach "semibulk" developed by our team. The power conversion efficiency for this type of PV cells is almost three times higher than state of the art, and the short circuit current density is almost four times higher than the typical bulk InGaN heterojunction solar cells.

Chapter 5 presents the results for the second approach "nano-structure" developed by our team. A PIN heterojunction structure based on nano selective area growth consisting of thick InGaN nano-pyramid coalesced by a p-GaN layer is presented. This unique structure solves the key challenges with the crystalline quality of thick InGaN epitaxial layers with high indium concentration thus enabling the potential use of high indium composition defect-free InGaN layers for realization of high efficiency solar cells. The structure fabricated into working solar cells exhibiting photoresponse is a proof-of-concept that this new approach developed by our team is a new route to develop monolithic InGaN-based high efficiency solar cells.

Finally a conclusion and perspectives of the study are presented in **Chapter 6**. Several suggestions for exploring the further capabilities of the semibulk approach and particularly the InGaN nano-structure approach for high indium (>30%) concentration are discussed. In addition to that, InGaN based Schottky solar cells and regrowth of p-GaN epitaxial layer using MBE technique are discussed and proposed for the future study.

The manuscript also includes five appendices as described below;

Appendix A presents the properties of III-Nitride materials along with the different challenges in these materials such as polarization, threading dislocations (V-defects) etc.

Appendix B introduces the physics of solar cells and the various parameters of PV cells like short circuit current density, open circuit voltage, fill factor and power conversion efficiency.

Appendix C provides an introduction to the growth techniques used in this study. They includes the metal organic vapor phase epitaxy (MOVPE) and nano-selective area growth (NSAG).

Appendix D presents the optimization study of achieving low resistance ohmic contacts at p-GaN interface, carried out during this study. This process was necessary to optimize the quality of the epitaxial layers grown by our team. Special attention was given to the selection of surface treatment chemicals, metal selection and annealing conditions. The details of this process optimization and comparison of the results to the literature are presented. This optimized metal contacting process is used in the fabrication of InGaN nano-structure PV devices.

Appendix E provides an overview of the characterization tools used in this study.

Chapter 1

Context and Goals of the Study

1.1 Harnessing of Solar Energy

One of the most important ingredients for continued human progress is an ample supply of energy. It is sensible, then, to concern ourselves with the sources of this energy. The main sector contributing to the huge amount of energy generation is the fossil fuel with limited resources. At present, oil covers approximately 40% of the world's energy and one-quarter of the supply comes from natural gas and coal. The remaining energy is supplied by wood, nuclear fission, and hydroelectric, in that order. The difficulty and cost of safety disposing radioactive material and toxic waste, makes the use of nuclear and chemical energy a questionable solution. There is in point of fact a massive belief that the use of fossil fuel is a contributing factor to the cause of global warming, which will ultimately result in the demise of the planet altogether. The burning of fossil fuel also detracts from public health by contributing to ground-level *ozone* which has been found to significantly increase the risk of premature death, in addition each 1% loss of total *ozone* due to environmental pollution leads to a 3 - 5% increase in skin cancer cases [5]. These quality-of-life concerns, however, pale in comparison to the drastic damage greenhouse gases to our environment. The scientific community is largely in agreement that greenhouse gas emissions are the most probable cause of the global warming, that the damage to the environment is irreversible on a timescale of hundreds of years, and that reducing CO_2 emissions should be a priority [5–7]. The emission levels of carbon dioxide that we generate by the constant use of fossil fuel are literally killing our planet. So a basic question is why not to put them in storage and use something more useful. Fortunately, our earth offers numerous renewable energy sources such as solar, wind, hydro, tidal, geothermal heat and biomass. At this time, renewable sources account for an inconsequential portion of the world's energy supply [8]. Renewable sources of energy need to be considered seriously. Hence, now it is the right time to start switching our habit of using conventional energy sources and provide better life quality for next generations.

Sun is one of the most potential candidates among the renewable energy sources. In fact, the solar energy received on the top of the atmosphere in an hour (1.7×10^5 terawatts) is remarkably much greater than the annual energy consumption of the world [9]. Nathan Lewis [10] survey of energy sources reveals that only solar energy has a large enough resource base to meet the world′s energy demands without contributing greenhouse gases to the atmosphere. Sunlight reaching the earth′s surface is almost 6000 times the average power consumed by humans. These figures encourage us to look for ways to harness solar energy and convert it into other convenient forms. The direct process of

converting sunlight into electricity is called *Photovoltaic* (PV) process. This is the most environmental friendly and reliable way of harnessing energy. Sunlight is described as full-spectrum light and includes the range of wavelengths necessary to sustain life on Earth: infrared, visible and ultraviolet (UV) as shown shown in Figure 1.1. The light that we

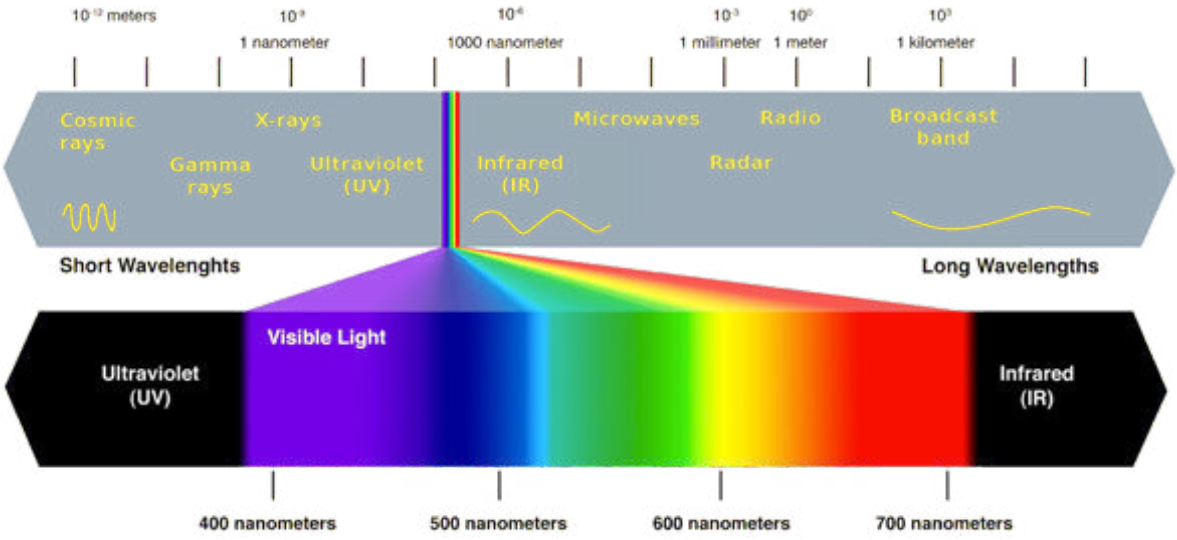

Figure 1.1: The solar spectrum (http://www.digiolighting.com/full-spectrum-lighting/).

see (visible spectrum) everyday is only a fraction of the total energy emitted by the sun incident on the earth.

The power conversion efficiency of a solar cell is sensitive to the variations in both power and spectrum of the incident light. Therefore for an accurate comparison between solar cells measured at different location i.e. at the earths surface and/or outsides the earth's atmosphere, standard solar spectrum and power density has been defined. The standard solar spectra refer to generic locations. The solar spectra are prefixed "AM", which stands for "Air Mass" and followed by a number which refers to the length of the path through the atmosphere in relation to the shortest length if the sun was in the apex. Figure 1.2 shows a comparison of the different air mass spectra at different locations. Figure 1.3 shows the spectral irradiance of sunlight as a function of photon energy for standard AM 0 and AM 1.5 G. The spectral density for a standard AM 0 and AM 1.5 G solar spectrum is 136 mW/cm^2 and 100 mW/cm^2 respectively.

The modern solar cell was first realized at Bell Laboratories in 1954 in the form of a 6% efficient crystalline-silicon (c-Si) device. Silicon solar cells has the dominant share of 80% in the PV market, because crystalline silicon based devices are well-understood and the manufacturing process is mature [11]. Due to the established crystalline silicon solar cell technology, the end product advances in efficiency are generally accomplished through incremental improvements to the production line instead of revolutionary advances [12]. The most important drawback of commercially available silicon solar cells is its low conversion efficiency. Since 2009, the solar cell industry has been rapidly growing more than 30% per year. But, in spite of the fast increase, the solar energy production makes less than 1% of the overall produced energy. Germany is able to generate 50.6% of electricity using solar energy. In 2014, the total PV- generated power of 35.2 TWh covered approximately 6.9% of Germany′s net electricity consumption [13]. The limited utilization of the solar energy is partly related to its high cost. Levelized Cost of Elec-

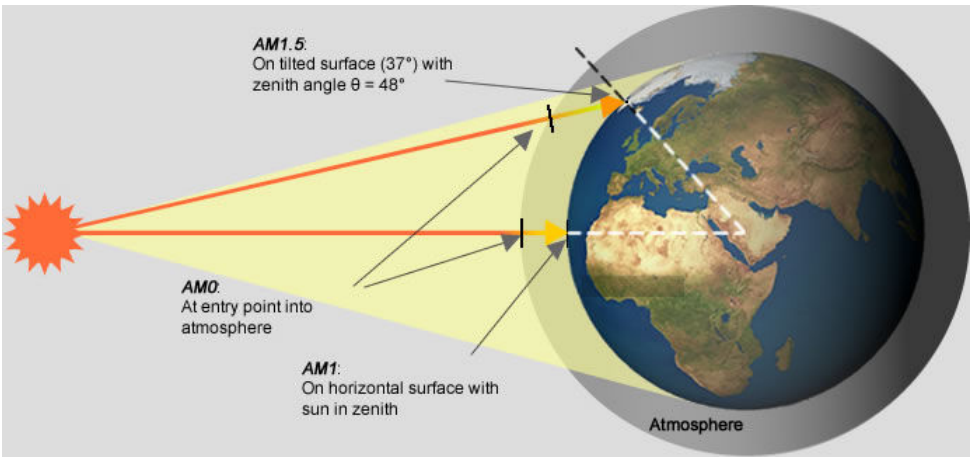

Figure 1.2: A comparison of the AM 0, AM 1 and AM 1.5G solar spectra (*http* : *//www.greenrhinoenergy.com/solar/radiation/spectra.php*)

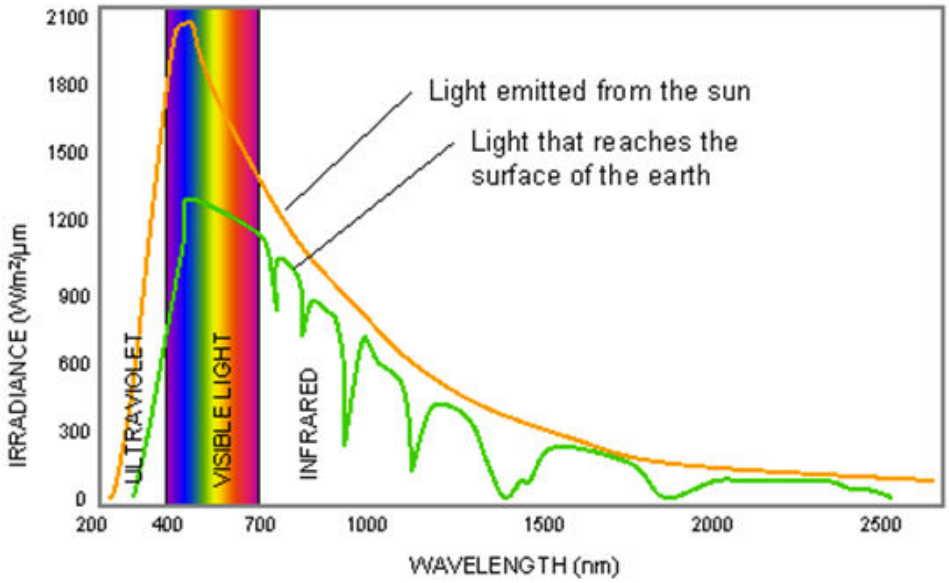

Figure 1.3: A comparison of the AM 0, AM 1 and AM 1.5G solar spectra (*http* : *//algonline.org/index.php?light*)

tricity (LCOE) is a technique of calculating and comparing the prices of electrical energy generated via different sources. It shows the ratio between the expected cost of the system during its lifetime (including construction, financing, fuel, maintenance, taxes, insurance etc) and the working lifetime of this system for a given technology. Figure 1.4 shows the comparison of levelized costs of different energy technologies to solar energy in Germany for different electricity sources. In the year 2013, the LCOE for PV panels varied from 0.078 to 0.142 €/kWh that is twice more expensive than the brow coal (0.142 €/kWh–0.053 €/kWh). The LCOE values for concentrator PV (CPV) technology that contrary to conventional PV cells uses lenses and curved mirrors to focus sunlight onto small device, are from 0.10€/kWh to 0.15€/kWh at locations with a DNI of 2000 kWh/(m^2a) and 0.08€/kWh to 0.12€/kWh with 2500 kWh/(m^2a). The analysis shows that CPV has potential for reducing the LCOE, which encourages a continued development of this technology. The cost and the performance of solar panel directly depend on the power

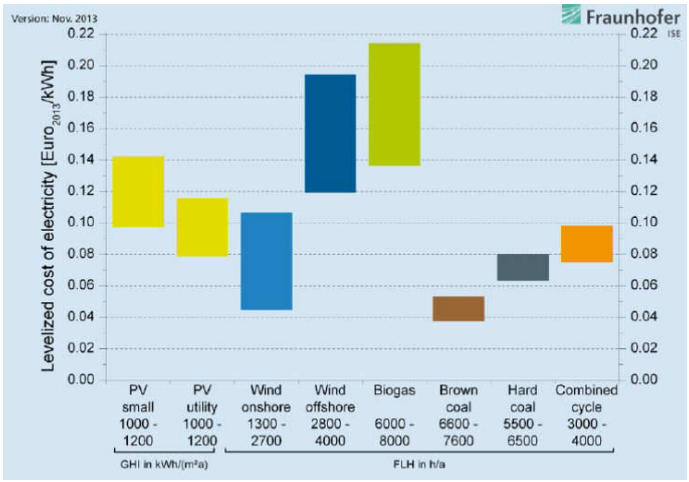

Figure 1.4: Levelized cost of electricity of conventional and renewable energy technologies, for 2013 and 2014 in Germany (http://www.ise.fraunhofer.de/en/publications/studies/cost- of-electricity).

conversion efficiency of the PV cells that consist of semiconductor material capturing and transforming the sunlight.

The reliability, durability, cost and power conversion efficiency of the photovoltaics developed using different materials led the solar community to designate them into three generations as shown in Figure 1.5. The first generation contains solar cells that are

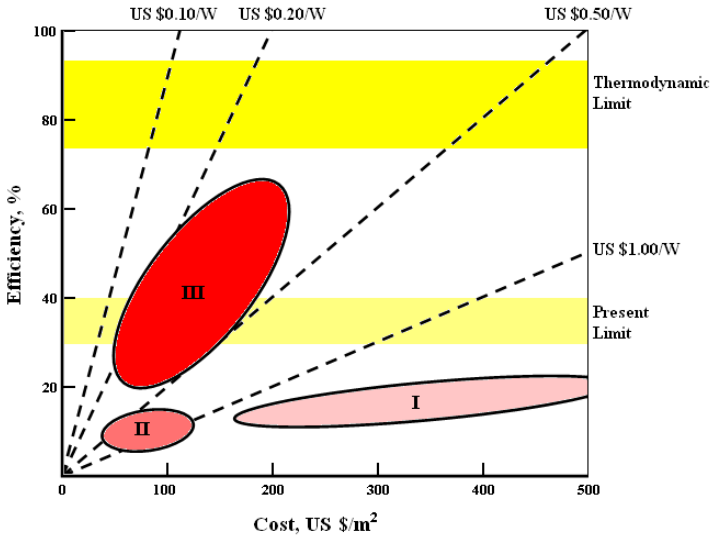

Figure 1.5: Efficiency vs. cost projections for the first, second and third generation PV cells [14].

relatively expensive to produce, and have a low efficiency. The second generation contains types of solar cells that have an even lower efficiency, but are much cheaper to produce, such that the cost per watt is lower than in first generation cells. The term third generation is used about cells that are very efficient. Most technologies in this generation are not yet commercial, but there is a lot of research going on in this area. These three generations of solar cells developed over the time are discussed below.

First generation solar cells

The first generation solar cells consist of large-area, high quality and single junction devices that are predominately made of silicon. Silicon has an indirect bandgap of 1.12 eV, that allows the absorption of the visible light. The highest power conversion efficiency achieved with crystalline silicon solar cell is 25% under non-concentrator by SunPower and 27.6% under concentrator (92x) by Amonix. This generation of the solar cells dominates the market and are mainly those seen on the rooftops. However, they are rigid and require a lot of energy in production, thus making them relatively expensive as shown in Figure 1.5. Major challenges involved in this generation of solar cells are [15]:
i). The light energy lower than the energy bandgap is not absorbed and is lost.
ii). The light energy higher than the energy bandgap is lost and excess energy appears as heat.

The demonstration of 24.5% of power conversion efficiency shows that this generation of solar cells are very close to their maximum theoretical limit of 31% [15], which leaves little room for further improvement, and because of this, different approaches to solar cells are investigated.

Second generation solar cells

The second generation of solar cells (Thin film solar cells) emerged due to their lower production costs (see Figure 1.5) and minimal material consumption, which makes these cells attractive to the end user. These solar cells also called thin film technology PV cells, are based on amorphous silicon, micro-amorphous silicon, copper indium gallium diselenide ($CuInGaSe_2$, CIGS) and cadmium telluride (CdTe), with typical power conversion efficiency of 10 - 20%. Amorphous silicon based solar cells are the most common and commercially used solar cells, in this generation of PV cells. Amorphous silicon solar cells are reported with a maximum conversion efficiency of 13.6%. These solar cells comes with several challenges, including degradation of the devices with the time and poor light absorption resulting in low conversion efficiency compared to other silicon solar cells. However, the solar cells based on CIGS and CdTe materials are more stable and results in higher power conversion efficiency. For instance, the US national renewable energy research facility (NREL) achieved an efficiency of 23.3% for the solar cells based on CIGS under concentrated light (14.7x) and 22.3% by Solar Frontier unde rnon-concentrated light, whereas the maximum power conversion efficiency reported for a PV cell based on CdTe is 22.1% by First Solar. Although the second generation PV cells have a competitive edge over the first generation PV cells, e.g. CIGS and CdTe PV cells offer high efficiency at a lower cost than silicon, the future of this technology may run into difficulty due to the use of scarce and toxic materials [16–18]. These drawbacks inspired the PV community to search for a new generation of solar cells.

Third generation solar cells

Third generation technologies aim to enhance the power conversion efficiency of second generation (thin-film technologies) while maintaining very low production costs. This

generation of solar cells has the potential to achieve the goal of \$1/W as shown in Figure 1.5, which is equivalent to the price of fossil-based electricity.

Multijunction solar cells

Multijunction solar cells consists of materials with different bandgaps that can absorb the different useful photon energies. It largely eliminates the process of thermalization and non-absorption caused by the photons with energies higher than the bandgap of the material. Multijunction solar cells with multiple cells makes possible to absorb a narrow range of photons close to its bandgap by each cell as shown in Figure 1.6. Multijunction

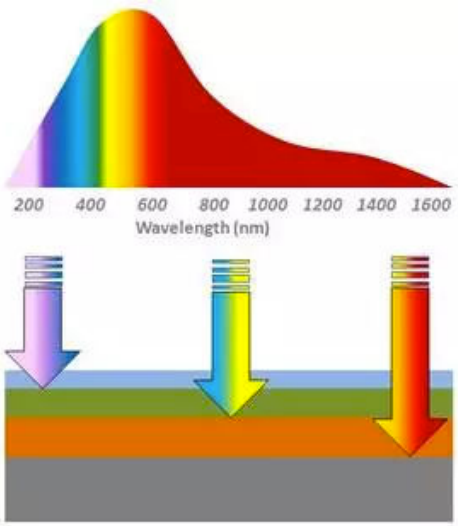

Figure 1.6: Schematic of the absorbance of the multijunction solar cell.

solar cells are one of the most promising options to obtain high efficiency, as they reduces transmission losses by splitting the spectrum and absorbing efficiently different sections of the spectrum by stacking several cells with different bandgaps. This generation of solar cells are currently successfully employed in concentrator photovoltaic (CPV) technologies, in which lenses and mirrors focus the sunlight on a small area solar cell, significantly decreasing the amount of material required and, consequently, the overall cost of the photovoltaic device. These solar cells have been extensively used in space applications because of their high power conversion efficiency, small sizes, low weights, and superior radiation resistance.

Current power conversion efficiency of 46% is held by GaAs based 4-junction (GaInP/ GaAs/ GaInAsP/ GaInAs) solar cell under concentrated light (508 suns) [2]. Boeing Spectrolab obtained an efficiency of 38.8% for a 5-junction solar cells under non-concentrator conditions. A power conversion efficiency of 44.4% under concentrated light (302x) and 37.8% under non-concentrated is achieved using a three junction by Sharp. For a two junction solar cell, a power conversion efficeincy of 31.6% is obtained by Alta Devices under non-concentrator and 34.1% under concentrator (467x) by NREL.

During the 1980s and early 1990s a sustained period of improvements to PV cell efficiencies took place in various laboratories, principally at the University of New South Wales (UNSW - Australia) and at Stanford University (USA). This is illustrated in the chart of best research cell efficiencies maintained by the National Renewable Energy Laboratories shown in Figure 1.7. The NREL data shows the power conversion efficiency for

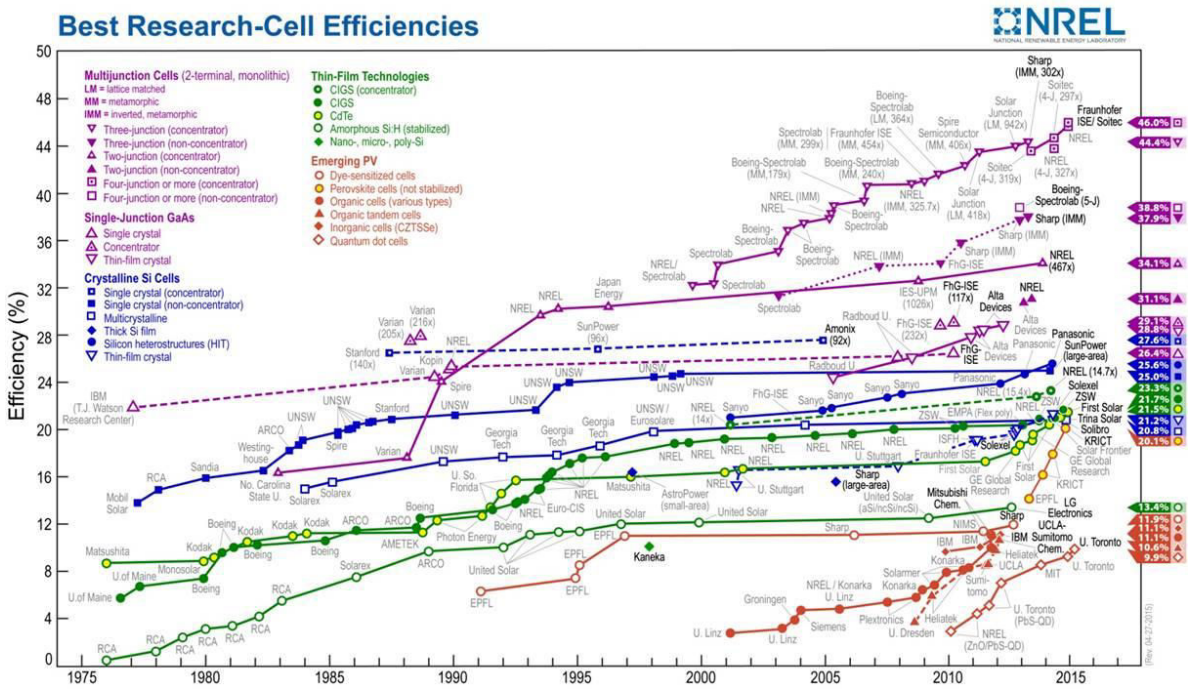

Figure 1.7: The evolution of the solar cell performance 1977 to 2015 illustrated by NREL [http://www.nrel.gov/ncpv/images/efficiency$_chart.jpg$].

the first generation solar cells improved until 1995, than saturates with no further obvious improvements. The timeline for second generation solar cell (thin film technologies) shows that the power conversion efficeincy for these PV cells improved until 2000, with a little improvement in the last decade. These solar cells are cheaper compared to the first generation solar cells but the power conversion efficiency remains lower then the silicon based solar cells. The multijunction concentrator devices have shown a dramatic increase in power conversion efficiency compared to the other technologies. They offer high power conversion efficiency compared to traditional solar cells that are made of semiconductor materials with a single layer. The emerging technologies (see Figure 1.7) received tremendous attention in the public especially after the achievements in the research of perovskite cells, as their research efficiencies recently soared above 20%. The third generation (multijunction) solar cells are typically made of compound semiconductors from III-V groups of the periodic table, because these alloys have bandgaps ranging from 0.3 eV to 2.3 eV, covering most of the solar spectrum. Nevertheless, there is an urgent search for a monolithic design that will convert sunlight into electricity with practical efficiencies higher than 50% [19]. To achieve this goal, new approaches of solar cells which consist of four or more bandgaps are required, as shown in Figure 1.8. Although, the current efficiency achieved using multijunction solar cells is very high compared to silicon based solar cells. However, practically, there is a very little range of materials that could be used to make these cells. Multijunction solar cells rely on materials with, matching bandgap with the solar spectrum, high mobility and lifetimes, thermal and lattice matching. These critical parameters makes it very challenging in finding the right fabrication materials. In order to overcome the 50% power conversion efficiency barrier [1] in a GaAs based 4-junction solar cell, material with a bandgap >2.4 eV is needed. However, there are not many materials offering a bandgap greater than 2.4 eV. The III-nitride alloys are among the few materials that can provide bandgap of greater than 2.4 eV [21].

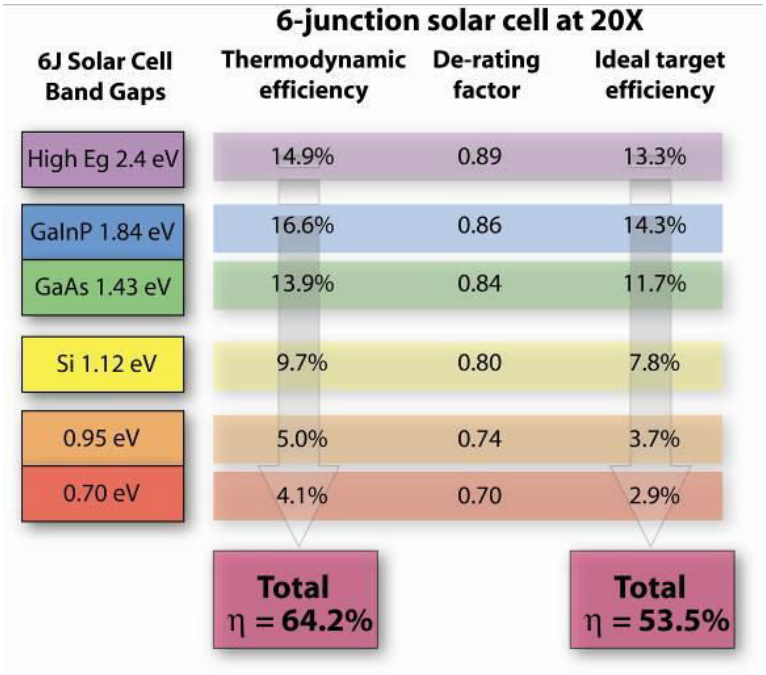

Figure 1.8: Predicted contributions of each material in a multijunction solar cell [20].

1.2 III-Nitride Materials

The key application of InGaN material is its varying badgap energy with indium incorporation, which is a critical factor in targeting the power conversion efficiency beyond 50% with a bandgap energy greater than 2.4 eV in a quadruple junction solar cell. It possesses the desired characteristics, i.e. wide and direct bandgap covering almost the entire visible solar spectrum (0.64-3.4 eV), high absorption coefficient (10^5 cm^{-1}), high thermal resistance and radiation tolerance, for achieving high efficiency PV devices. The varying badgap of InGaN alloy offers unique opportunity to design multi-junction solar cells, with the flexibility of choosing the number and band gap energies of the constituent junctions. A two-layer multi-junction cell with bandgaps of 1.1 eV and 1.7 eV can attain a theoretical 50% maximum efficiency, and by depositing multiple layers tuned to a wide range of bandgaps an efficiency up to 70% is theoretically expected [22].

In theory the unique properties of InGaN should translate into high efficiency, long lifetimes, and ultra thin solar cells. However, tuning the bandgap of InGaN epitaxial layer to lower energy with high indium incorporation has proven difficulties such as phase separation (compositional instability) due to the poor miscibility of InN and GaN and relaxation of the mismatch stress accommodated in the InGaN layers due to its growth on foreign substrates (with lattice and thermal expansion coefficient mismatch) restricts the critical layer thickness of the InGaN epilayer for a given indium concentration. These factors result in intensive generation of extended defects (threading dislocations) in InGaN that (i) lead to formation of conductive channels shunting the PV device and (ii) make shorter the carrier lifetime in the InGaN light absorption region [4]. Other issues, such as, sensitivity of InGaN absorber to the growth temperature of the subsequent top p-GaN layer for realization of PIN devices [23] and polarization [24] further reduces the efficiency of the InGaN based solar cells.

1.3 Objective of This Dissertation

The objective of this study is to investigate new approaches that may overcome as discussed previously the issues of phase separation and high dislocation density in InGaN-based PIN solar cells. Two novel approaches are proposed for the realization of high efficiency InGaN solar cells, and compared to the classical approach of bulk InGaN heterojunction solar cells (see Figure 1.9).

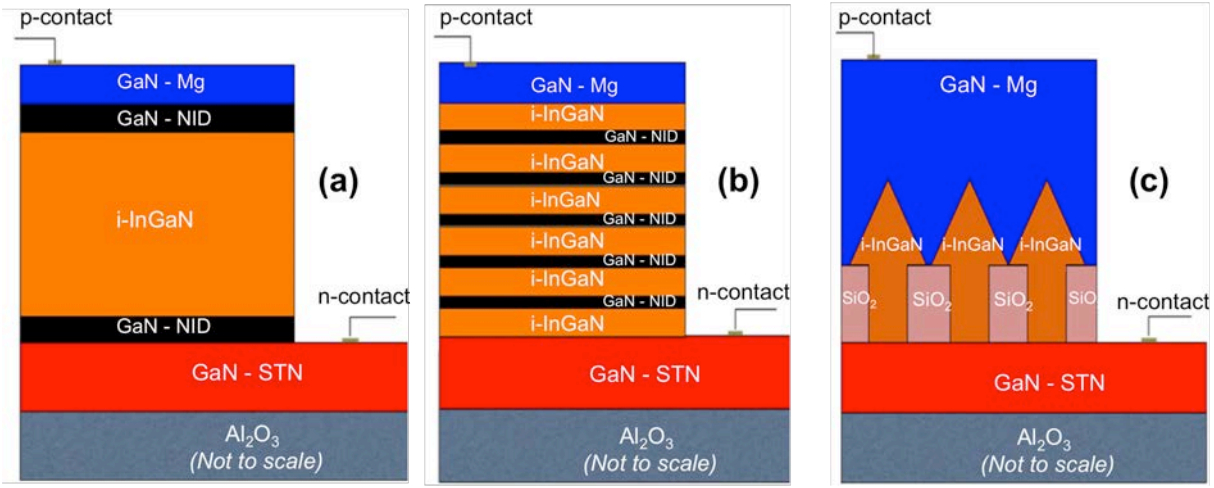

Figure 1.9: (a) Bulk InGaN, (b) Semibulk InGaN, (c) InGaN nano-structure. based PIN heterojunction solar cells.

The first approach referred as "semibulk" consists in replacing the conventional bulk absorber by a thick multilayered InGaN/GaN absorber as shown in Figure 1.9(b). The periodical insertion of the thin GaN interlayers should absorb the excess indium and relieve compressive strain. These GaN interlayers need to be thick enough to be effective and thin enough to allow carrier transport through tunneling. The InGaN layers need to be thick and numerous enough to absorb efficiently the incoming light beam, and thin enough to remain fully strained and without phase separation.

Figure 1.9(c) show the second approach that consists in the growth of InGaN nano-structures for the achievement of high indium content thick InGaN layers. It allows the elimination of the preexisting dislocations in the underlying template. It also allows strain relaxation of InGaN layers without any dislocations, leading to higher indium incorporation and reduced piezoelectric effect.

Chapter 2

InGaN Materials and Solar Cells

2.1 InGaN Materials

With the revision of bandgap for InN from 1.89 eV to 0.64 eV by Wu *et al.* [25], the InGaN material system now covers almost the entire visible solar spectrum as shown in Figure 2.1. The bandgap variation of InGaN alloy obtained with the indium concentration makes

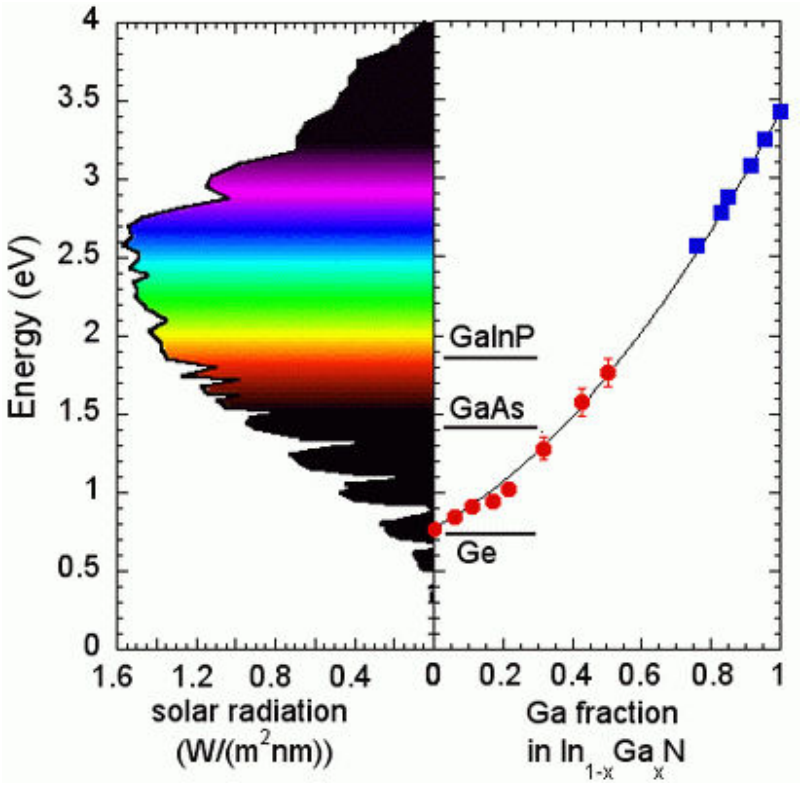

Figure 2.1: Band gap energies of the InGaN alloy system covering the entire solar spectrum [25].

it a potential candidate in multi-junction solar cells, to overcome the 50% conversion efficiency barrier [26]. Table 2.1 list the optimum values of bandgaps of multijunction solar cells calculated through detailed balance modeling. The triple junction solar cell listed in Table 2.1 has a maximum conversion efficiency of 56%, however, its thermodynamic limit can be improved to around 80% [20]. InGaN is a direct bandgap semiconductor

Table 2.1: Values of bandgap and efficiency for tandem solar cells with 3 to 8 junctions under black body radiation at 6000K for 500x (x is the number of suns). N is the number of band gaps in the device [20].

N	Values of bandgap (eV)	Efficiency (%)
3	0.70, 1.37, 2	56
4	0.60, 1.11, 1.69, 2.48	62
5	0.53, 0.95, 1.40, 1.93, 2.68	65
6	0.47, 0.84, 1.24, 1.66, 2.18, 2.93	67.3
7	0.47, 0.82, 1.19, 1.56, 2.0, 2.5, 3.21	68.9
8	0.44, 0.78, 1.09, 1.4, 1.74, 2.14, 2.65, 3.35	70.2

which means that the creation of electron-hole pairs does not require participation of crystal lattice vibrations, that results in waste of energy [27]. Following the re-revision of InGaN bandgap, several groups reported InGaN layers over whole composition range with moderate dislocations densities for re-evaluation of the absorption coefficient of InGaN alloys grown with different techniques, including metallic beam epitaxy (MBE) by Hori *et al.* [28] and Wu *et al.* [25], while MOVPE by Jani *et al.* [20]. Figure 2.2 shows the results

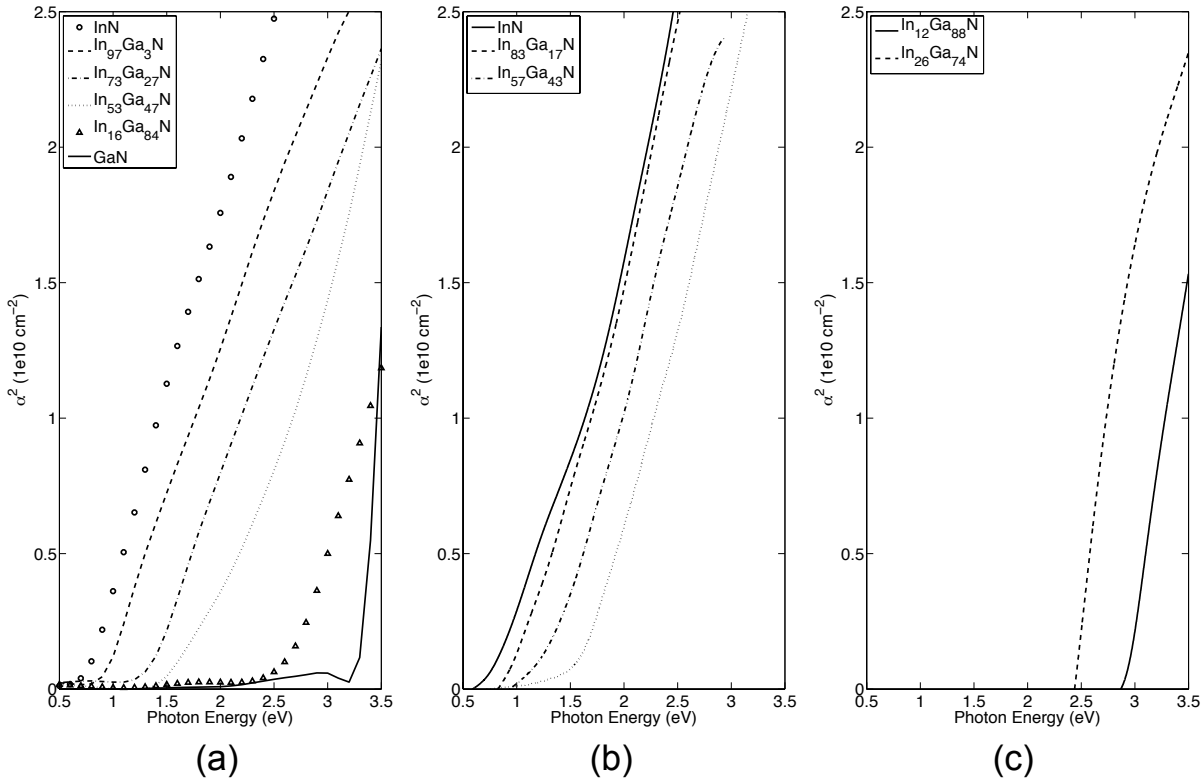

Figure 2.2: Experimental absorption curves for InGaN alloys with various indium contents (a). Hori *et al.* [28] (b). Wu *et al.* [25] (c). Jani *et al.* [20].

of the study performed by these three groups, that fits good the absorption model, given

by;

$$\alpha(E) = \alpha_0 \frac{\sqrt{(E - E_g)}}{E} \tag{2.1}$$

where $\alpha(E)$ is the absorption coefficient of the semiconductor as a function of photon energy (given in eV), E_g is the bandgap (given in eV) and α_0 is a fitting parameter that is usually given in $eV^{1/2}$ cm^{-1}. The absorption coefficient is high in all of the InGaN range, and importantly increases rapidly near the band edge. The average value of α_0 over the whole alloy composition range, computed from the data presented in Figure 2.2, is 5×10^5 $eV^{1/2}$ cm^{-1}. This high absorption coefficient makes possible to absorb 90% of incident above-bandgap light within 120 nm, making it a potential candidate for ultra thin high efficiency solar cells. A high absorption is a critical factor in achieving high collection since the absorption depth must be shorter than the diffusion length [29]. The diffusion length depends on both the minority carrier lifetime and the diffusion coefficient. The reported diffusion lengths are between 0.2 to 0.8 μm [29], but several reports [30,31] measured diffusion lengths over 1 μm .

Apart from the above mentioned properties,InGaN material do not contain toxic elements like cadmium, arsenic or phosphorous which are present in other PV technologies being currently used [32]. These properties contribute to the potential of InGaN based solar cells for use in harsh environments, especially for space applications. Despite recent significant progress in InGaN technology, several critical challenges still exist in potential use of InGaN for high efficiency solar cells. Therefore, InGaN based PV devices demonstrated so far have low experimental power conversion efficiency, compared to what is expected theoretically.

2.1.1 Challenges in InGaN Materials

2.1.1.1 Critical Layer Thickness

The epitaxial growth of InGaN III-nitride on lattice mis-matched sapphire substrates (29% between InN and sapphire, 14% between GaN and sapphire) results in the presence of in-plane strain. This in-plane strain can be compressive or tensile, depending on the lattice parameter of the top layer and the substrate. The mechanical deformations that may happen for the two possible outcomes of the lattice parameters *i.e.* in-strain plane or out-of-plane strain plane are shown in Figure 2.3. The elastic energy stored by the InGaN epilayers is proportional to its thickness. This mechanism limits the growth of InGaN epitaxial layer to a certain thickness called the "critical layer thickness", denoted by h_c. InGaN epilayers grown beyond the critical layer thickness cannot be indefinitely strained on the underlying GaN buffer, resulting in severe degradation of the InGaN crystalline quality. The excess elastic energy stored in the InGaN layer exceeding critical layer thickness contributes to the creation of misfit dislocations (threading dislocations) in the InGaN layer, eventually the InGaN epitaxial layer appears to relax on the GaN buffer layer. These threading dislocations may terminate at the layer surface as V-defects (see Appendix A) and absorb photons above and below the InGaN band gap, resulting in a shadowing of the solar cells [33].

Several theoretical models have been developed to determine the InGaN critical layer thickness depending on the type of misfit dislocation, like People and Bean [34,35], Fischer *et al.* [36] and Matthews and Blakeslee [37]. Our team recently published [38] a comparison

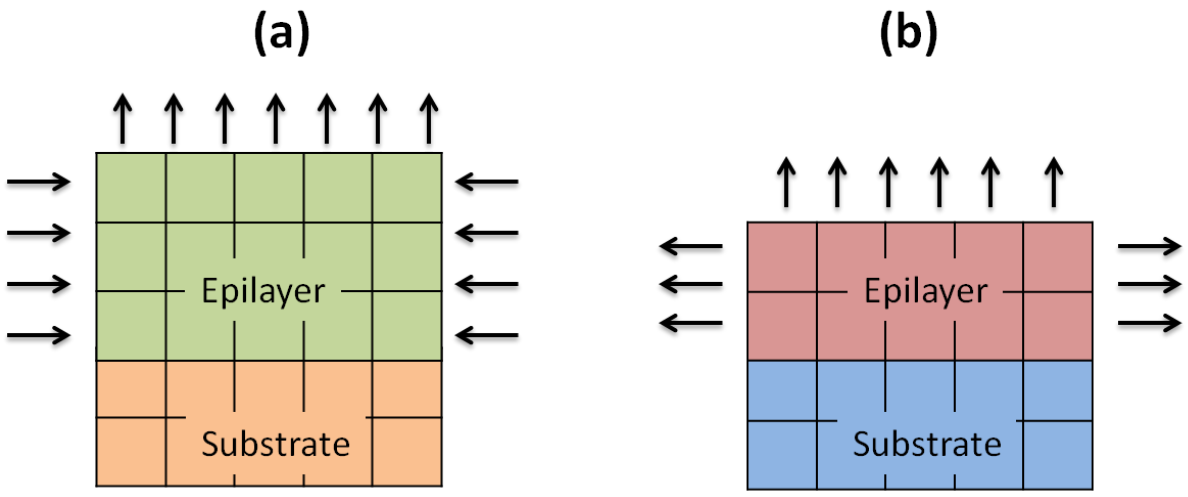

Figure 2.3: Elastic deformations in the Nitride epitaxial layers (a) Compressive strain, (b) Tensile strain.

study for the InGaN critical layer thickness based on the surface morphology of InGaN with three different sets named A, B, and C as shown in Figure 2.4. The first set (set A) that remained within the critical layer thickness exhibits 2D surface morphology and fully strained InGaN layers, while the third set (set C) exceeding the critical layer thickness show 3D surface morphology and fully relaxed InGaN layers. In between these two sets,

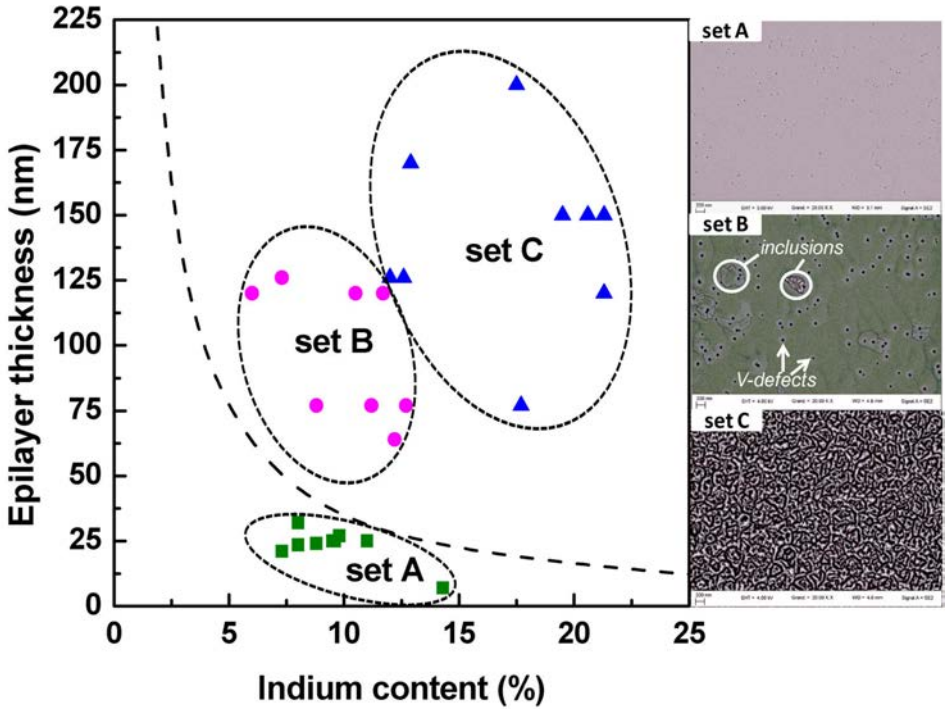

Figure 2.4: InGaN surface morphology versus indium composition and epilayer thickness. The theoretical critical layer thickness as deduced from the model of Fischer *et al.* [36] is also reported (dashed line) [38].

set B also exceeding the critical layer thickness shows 2D surface morphology, in which 3D indium rich inclusions embedded in the 2D InGaN matrix tend to appear [39], and

partially relaxed InGaN layers. These results show that the thickness of fully strained InGaN epilayer significantly depends on the indium concentration.

2.1.1.2 Phase Separation

The large difference in the inter-atomic spacing and chemical affinity between InN and GaN (11% of lattice mismatch between InN and GaN) causes a solid phase miscibility gap and phase separation in the InGaN epitaxial layers [40]. The formation of micro- and nano-scale regions within the InGaN epitaxial layer with different indium concentration is referred as phase separation [41]. Evidence of phase separation in InGaN ternary compounds has been found in material grown by a number of techniques – molecular beam epitaxy (MBE) [42], metal-organic chemical vapor phase deposition (MOCVD) [43] and hydride vapor phase epitaxy (HVPE) [44]. This results in compositional non-uniformity and defects [45]. Lai *et al.* [46] reported the trapping of carriers in the shallow quantum wells created by the indium fluctuations leads to the poor device performance. In contrary to the solar cells, the fluctuation of indium composition within the InGaN epitaxial layers is considered beneficial in the operation of high efficiency GaN based light emitting diodes. Karpov *et al.* [45] reported that the elastic strain effect considerably suppresses the phase separation in the strained InGaN layers. It can also (possibly) be controlled by optimization of the InGaN growth conditions, such as decreasing the InGaN growth rate for low indium concentration and increasing the growth rate for high indium concentration [47].

2.2 InGaN Solar Cells

Among the ternary compounds of III-nitride materials, InGaN has drawn a great deal of attention. It has been considered as the most important and indispensable material for realization of high efficiency solar cells, over the past ten years. During the early period, InGaN alloy was exclusively evaluated for single junction photovoltaic applications with Ga-rich materials owing to mature growth and doping technologies of GaN. After the revision of the InN bandgap energy, an attempt to fabricate InGaN solar cells is under way by different groups since 2003, including Dr. Anderson′s group at the University of Florida and groups at the Georgia Institute of Technology, Atlanta USA, the University of Delaware, and the National Renewable Energy Laboratories (NREL) [21, 48].

The first clear demonstrations of photovoltaic effect using InGaN material system were achieved by the design of Jani *et al.* [49] and Yang *et al.* [50] having Ga-rich PN InGaN homojunction and p-GaN/InGaN/n-GaN heterojunctions grown by metal-organic vapor phase epitaxy (MOVPE) in 2006 and 2007. Jani *et al.* [51] demonstrated the photovoltaic response with single layer solar cell with an indium content of 4–5%, in a PIN InGaN hoterojunction (i.e. an InGaN epitaxial layer sandwiched between p-type GaN and n-type GaN). Later on Yang *et al.* [50] and Jani *et al.* [52] demonstrated the photovoltaic response using InGaN homojunction (i.e. p-InGaN/n-InGaN) solar cells. With the passage of time, significant efforts were carried out to overcome the challenges of achieving high quality thick InGaN absorber with high indium content. These efforts include the growth of indium-rich InGaN layers by molecular beam epitaxy (MBE) [53], and the use of different designs including, bulk InGaN, multiple quantum wells (MQWs) and InGaN homojunction absorbers, which will be discussed in detail in the next section.

2.2.0.3 InGaN Bulk PIN Heterojunction Solar Cells

InGaN PIN heterojunction solar cells based on a single thick InGaN absorber layer also referred as bulk InGaN sandwiched between p-type GaN and n-type GaN, is the most extensively studied type of InGaN solar cells. The initiative of bulk type InGaN solar cells benefited mostly from the mature growth and fabrication of InGaN/GaN LEDs technology.

Jani *et al.* [51] demonstrated the first bulk InGaN PIN hoterojunction solar cell shown in Figure 2.5, with 5% of indium concentration, corresponding to an energy bandgap of

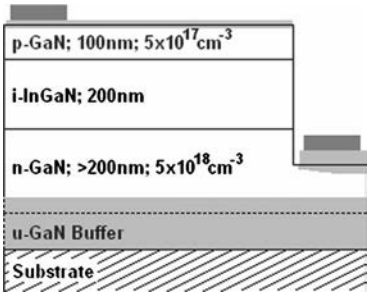

Figure 2.5: Schematic of the bulk $In_{0.05}Ga_{0.95}N$ PIN heterojunction solar cell proposed by Jani *et al.* [51].

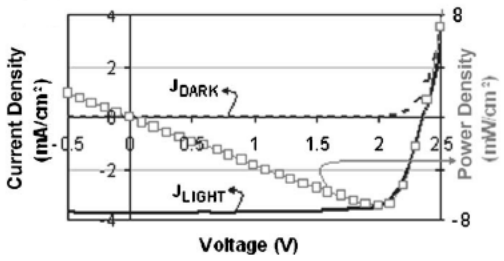

Figure 2.6: Current-voltage characteristic obtained by Jani *et al.* [51] showing V_{oc} of 2,4 V, a J_{sc} 3,7 mA/cm^2 and fill factor 78% under concentrated UV light source.

3.2 eV. They demonstrated a V_{oc}, J_{sc} and fill factor (FF) of 2,4 V, 3.7 mA/cm^2 and 78% respectively under concentrated UV light source as shown in Figure 2.6. In addition the device shows internal and external quantum efficiency around 60% and 43% respectively. Since the device was illuminated under concentrated UV light source, therefore the power conversion efficiency under one sun illumination was not reported. The primary challenge, that affected the device performance, was the phase separation in the InGaN epitaxial layer, that not only reduced the V_{oc} but also enhanced the recombination decreasing the photogenerated current. Phase separation that contributes to the charge carrier confinement is beneficial to the operation of InGaN based light emitting diodes [54]. However, the occurrence of phase separation is detrimental to InGaN solar cell performance, because it results in the trapping of the photogenerated carriers and thus reduces the carrier lifetime that ultimately reduces the J_{sc} [55]. Furthermore, due to the phase separation, the V_{oc} of the device typically collapses towards the lowest effective bandgap in the material [55]. The trap-filling due to the high dislocation density of bulk, 5.5 $\times$ 10^8 cm^{-2}, and surface traps in GaN/InGaN photovoltaic devices has been postulated as reducing the collection efficiency of the photogenerated carriers. This trapping mechanism increases the series resistance and reduce the shunt resistance (see Appendix B for details of the effect of shunt and series resistance on the performance of the PV cells), that eventually affects the power conversion efficiency of the solar cells. The issue of phase separation was addressed by Zheng *et al.* [56], demonstrating a high-quality p-GaN/i-$In_{0.10}Ga_{0.90}N$/n-GaN bulk heterojunction solar cell (Figure 2.7), with no observable phase separation and relaxation grown by MOCVD. The device results in a power conversion efficiency of 0.5% under an AM 1.5G illumination as shown in Figure 2.8. However, the measured V_{oc} of the device was substantially less than that reported by Jani *et al.* [51] 2.4 V for p-GaN/i-$In_{0.05}Ga_{0.95}N$/n-GaN. The lower V_{oc} [56] was ascribed to the relatively low built-in potential caused by

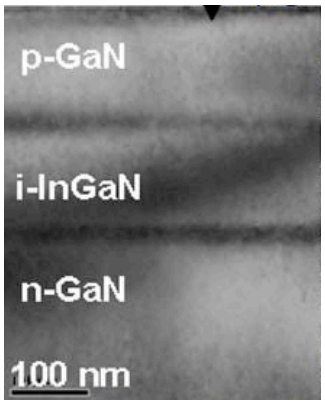

Figure 2.7: Cross-sectional TEM image obtained from GaN/InGaN/GaN epilayers. The dark background within the up and down interfaces of InGaN/GaN exhibits a strain contrast due to the stored misfit strain energy [56].

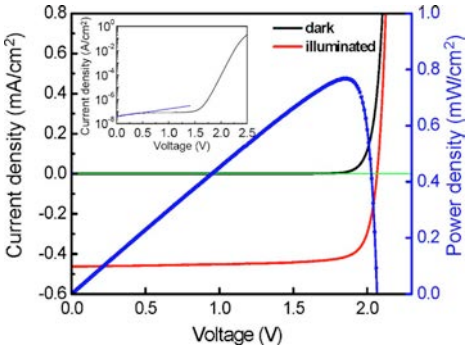

Figure 2.8: Typical $I-V$ curves of p-GaN/i-InGaN/n-GaN solar cell under the illuminated and dark conditions, along with calculated $P-V$ characteristic in the illuminated case. The inset graph shows the dark $I-V$ curve of the same photovoltaic cells using a logarithm scale [56].

the lower doping concentration in GaN and/or less incident light due to the adsorption in the metal contacts.

The effect of light absorption in metal contacts on power conversion efficiency p-GaN/i-$In_{0.12}Ga_{0.88}N$/n-GaN bulk heterojunction solar cell was studied by Neufeld *et al.* [57]. They show that the performance of the device improved by increasing the distance between the p-GaN metal grid contacting. The different measured values for both the solar cells are listed in Table 2.2. They attributed the improvement in performance to the less

Table 2.2: The different measured values for solar cell reported by Neufeld *et al.* [57].

Contact spacing	V_{oc} (V)	J_{sc} (mA/cm^2)	FF (%)	P_{max}	Peak EQE (%)
25 μm	1.75	3.5	75.1	4.6	51
166 μm	1.81	4.2	75.3	5.7	63

light absorption in the metal contact with larger spacing. Similarly Shim *et al.* [58] compared the performances of bulk $In_{0.10}Ga_{0.90}N$ solar cell with current spreading layers of Ni/Au and ITO under AM 1.5G conditions. The devices with ITO showed superior V_{oc} characteristics of 2.0 V, J_{sc} of 0.64 mA/cm^2, and 1% conversion efficiency while devices without any current spreading layer and Ni/Au current spreading layer resulted in η =0.93 and η=0.75, respectively. In a further study, Shim *et al.* reported [59] an improved η (1.2%) and J_{sc} (0.83 mA/cm^2) by utilizing a current spreading layer of graphene on the same structure .

The difficulty in the growth of high quality thick InGaN absorber layer with high indium concentration has significantly limited the power conversion efficiency of bulk InGaN heterojunction solar cells, due to the incomplete light absorption in thin InGaN absorber layers. Liang *et al.* [60] reported that when the thickness of the InGaN absorber layer was increased from 75 nm to 150 nm, the magnitude of the external quantum efficiency of the InGaN solar cell slightly increased. However, when the thickness of the InGaN ab-

sorber layer was increased to 300 nm, the external quantum efficiency sharply decreased as shown in Figure 2.9. It is well understood that thin InGaN absorber will result in

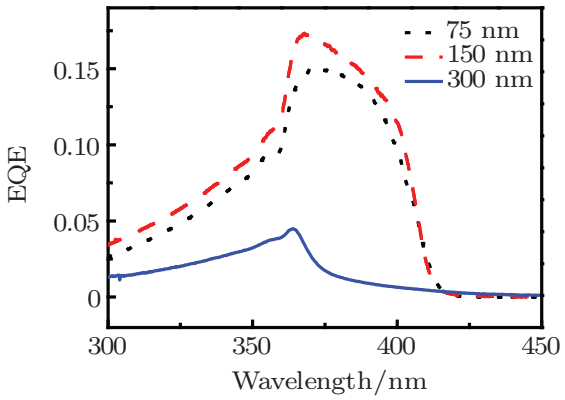

Figure 2.9: Curves of external quantum efficiency versus wavelength for InGaN/GaN PIN solar cells with different InGaN layer thickness values [60].

incomplete light absorption, on the contrary, if the InGaN absorber is grown too thick, then quality of the InGaN layer and the collection efficiency will quickly be degraded, resulting in poor photovoltaic performance. Therefore, the crystalline quality and thickness of the InGaN layer is a key parameter for improving the performance of InGaN solar cells. Zheng *et al.* [56] reported that as the thickness of an InGaN absorber layer was increased from 150 nm to 250 nm for 10% of indium concentration, the devices display the poorer photovoltaic effect, attributed to the worse crystal quality of the absorber caused by a relaxation of InGaN because the growth thickness exceeded the critical layer thickness of InGaN on GaN. An efficient conversion of lower energy photons requires high indium content InGaN, which limits the maximum thickness of this layer, reducing its light absorption. This is why many researchers, (with respect to the InGaN critical layer thickness for a given indium concentration) tried improving light absorption by surface roughening or backside reflection methods.

Several other techniques have been reported for the reduction of threading dislocations and incomplete light absorption in thin InGaN absorber layer. Liang *et al.* [61] reported that by changing the growth conditions, especially the temperature and the growth rate, the structural quality of the $In_{0.12}Ga_{0.88}N$ absorber layer was improved, resulting in an increase in peak external quantum efficiency from 17% to 57%. The use of patterned sapphire substrate for reduction of threading dislocations and improvement in the absorption of the useful light has shown very promising results [62]. In order to stop the extension of threading dislocations via the InGaN absorber into the p-GaN, Liang *et al.* [23] proposed the use of a thin low temperature GaN cap layer between p-GaN and InGaN absorber layer. This thin GaN cap layer effectively reduced the leakage current resulting in improved device performance.

The power conversion efficiency of the bulk InGaN heterojunction solar cells is not only limited by the epitaxial quality of the InGaN absorber, but also by the surface morphology and structural quality of the p-GaN epitaxial layer. The light absorption in the p-GaN layer can be significantly reduced by decreasing its thickness, that eventually results in a high J_{sc} [63]. A similar impact was also observed for the external quantum efficiency measurements. Neufeld *et al.* [63] demonstrated that optimization of the p-GaN epitaxial layer has a significant role in improving the conversion efficiency of the InGaN solar cells.

They show that the p-GaN epitaxial layers grown at low temperature results in poor crystalline quality, that contributes to the leakage current, resulting in a low V_{oc}. However, these devices results in a high J_{sc} and high external quantum efficiency, attributed to the optical path length enhancement associated with increased scattering off of the rougher, pitted p-GaN surface observed for the low temperature p-GaN growth conditions. The V-pit density was significantly reduced by growing the p-GaN layer at higher temperatures. P-GaN epitaxial layers grown at high temperature results in smoother surfaces because of longer diffusion lengths of the growth species resulting in planarization of the V-pits [64]. A similar study of the impact of p-GaN surface morphology on the overall conversion efficiency of $In_{0.12}Ga_{0.88}N$ solar cells was also studied by Matioli *et al.* [65]. It was shown that an intentional texturing of the p-GaN surface results in a high internal quantum efficiency and an improved light in-coupling, yields high external quantum efficiency (72%). The intentional texturing of p-GaN surface was achieved by growing p-GaN layer at relatively low temperature. The high measured internal quantum efficiency shows an efficient conversion of absorbed photons into electrons and holes and an efficient transport of these carriers outside the device. The textured p-GaN surface, reduced the reflection of incident light and increased the path length of the light inside the device active region, resulting in enhancement of 35% in maximum output power of the device. The different values for smooth and rough p-GaN surface measured by Matioli *et al.* [65] are listed in Table 2.3. A similar conclusion was also reported by Farell *et al.* [66], who demonstrated that the

Table 2.3: The different measured values for solar cell with p-GaN grown at different temperature as reported by Matioli *et al.* [65].

Device	V_{oc} (V)	J_{sc} (mA/cm^2)	FF (%)	P_{max}	Peak EQE (%)	Peak IQE (%)
Smooth	1.83	0.83	76.6	1.16	56	97
Rough	1.89	1.06	76.6	1.57	72	93

growth temperature of p-GaN has a significant role in the overall conversion efficiency of InGaN solar cells. They concluded that there is a correlation between an increase in the surface roughness of the p-GaN and an increase in the optical coupling between the InGaN/GaN cells and the incoming light. Although the p-GaN layer grown at low temperature results in improvement of the J_{sc}, at the same time, the V-defects results in a high leakage current, results in reduction of the V_{oc}.

The V-pits (see Appendix A) associated to threading dislocations are the major contributors to the efficiency limiting factors. They act as current leakage paths such that shunt resistance and hence V_{oc} is reduced. Zhang *et al.* [67] reported that the presence of high density of threading dislocations shown in Figure 2.10 significantly reduced the power conversion efficiency of the device. They speculated that due to the conditions adopted to grow the thick InGaN epilayers, threading dislocations opened up to form V-pits in the active region. The facets of the V-pits were probably relaxed and have a large lattice mismatch with GaN grown on the top. Consequently, the growth of the capping layer introduces in the active region more dislocations, acting as recombination centers [68] or become charged cores [69] to hinder photon-induced carriers from being collected. Hence the degradation of the InGaN epilayer with high indium concentration and the presence of threading dislocations severely damaged the performance of the solar cells. Similar

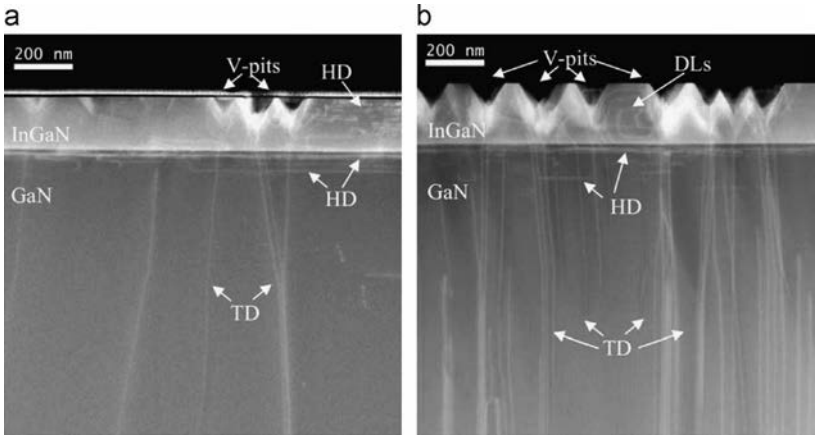

Figure 2.10: STEM images of the cross-section of (a) the low dislocation density sample and (b) the high dislocation density sample. Note that in addition to threading dislocations in the GaN template, there are V-pits and dislocations in the InGaN epilayer, as well as horizontal dislocations in the GaN template near the interface. Each V-pit is associated with a threading dislocation. Dislocation loops are visible in the InGaN [67].

observations were reported by Wu *et al.* [70], where a large difference in power conversion efficiency between experimental and theoretical values was attributed to the inferior quality of InGaN absorber and InGaN/GaN interface generated with increase of indium composition. They show using transmission electron microscopy that the solar cell with 10% of indium concentration gives an abrupt interface and there was no phase separated indium-rich quantum dots or dislocations in the InGaN active layer. However, as the indium concentration was increased to 14%, rough InGaN/GaN interface and dark spots occurred within the InGaN active layer and InGaN/GaN interface, which contributed to the degradation of the $In_{0.14}Ga_{0.86}N$ absorber layer resulting in poor device performance.

Despite all these encouraging results, the crystalline quality and high dislocation density in thick InGaN absorber layers for high indium concentration ($> 15\%$) grown on sapphire substrate remained a major challenge in achieving high efficiency bulk InGaN heterojunction solar cells. Table 2.4 summarizes the state-of-the-art for bulk InGaN heterojunction solar cells.

Table 2.4: Device performance for bulk InGaN heterojunction solar cells.

Reference	Absorber (Thickness)	V_{oc} (V)	J_{sc} mA/cm^2	FF (%)	EQE (%)	η (%)	Source
Jani *et al.* 2007 [51]	$In_{0.05}Ga_{0.95}N$ (200 nm)	2.4	3.5	79	-	-	UV concetrated light
Neufeld *et al.* 2008 [57]	$In_{0.12}Ga_{0.88}N$ (200 nm)	2.4	4.2	75.3	63	-	AM 0 concentrated
Zheng *et al.* 2008 [56]	$In_{0.10}Ga_{0.90}N$ (150 nm)	2.1	0.46	81	-	0.5	AM 1.5G

Reference	Absorber (Thickness)	V_{oc} (V)	J_{sc} mA/cm^2	FF (%)	EQE (%)	η (%)	Source
Horng *et al.* 2009 [71]	$In_{0.10}Ga_{0.90}N$ (150 nm)	2.09	0.52	73.1	-	0.8	AM 1.5G
Shim *et al.* 2010 [58]	$In_{0.108}Ga_{0.892}N$ (200 nm)	2.01	0.64	79.5	74.1	1	AM 1.5G
Tsai *et al.* 2010 *with reflector* [72]	$In_{0.09}Ga_{0.91}N$ (150 nm)	1.79	0.5	64	-	0.57	AM 1.5G
Neufeld *et al.* 2010 [63]	$In_{0.08}Ga_{0.92}N$ (150 nm)	1.65	0.11	73	-	0.10	AM 0
Lang *et al.* 2011 [73]	$In_{0.11}Ga_{0.89}N$ (90 nm)	1.75	1.11	73	54	1.04	AM 1.5G
Matioli *et al.* 2011 [65]	$In_{0.12}Ga_{0.88}N$ (60 nm)	1.89	1.06	78.6	72	1.22	AM 1.5G
Zheng *et al.* 2011 [74]	$In_{0.10}Ga_{0.90}N$ (150 nm)	2.1	0.42	77.8	55	0.68	AM 1.5G
Wu *et al.* 2011 [70]	$In_{0.12}Ga_{0.88}N$ (150 nm)	1.83	0.42	69.09	-	0.53	AM 1.5G
Liang *et al.* 2011 [60]	$In_{0.12}Ga_{0.88}N$ (150 nm)	1.60	0.45	64.6	57	0.46	AM 1.5G
Liang *et al.* 2011 [23]	$In_{0.098}Ga_{0.912}N$ (120 nm)	1.3	0.54	-	29	0.38	AM 0
Zhang *et al.* 2011 [67]	$In_{0.12}Ga_{0.88}N$ (200 nm)	0.48	1.12	30.2	29.8	0.162	AM 1.5G

2.2.0.4 InGaN MQWs PIN Heterojunction Solar Cells

The development of Multiple Quantum Wells (MQWs) absorber provided an alternative approach to improve the performance of InGaN PIN heterojunction solar cells. It enabled the growth of thick InGaN layers with high indium concentration, that could overcome the issues of incomplete light absorption. In the beginning, a key issue in using MQWs was, whether the increase in J_{sc}, due to the addition of lower bandgap well materials, can outweight the voltage drop of V_{oc} due to the recombination loss at the heterojunction interfaces. MQWs structures are extensively studied for high efficiency solar cells, by varying various parameters:

1. Dependence on indium concentration and temperature
2. Dependence on barrier thickness
3. Methods to improve light absorption

These parameters are discussed below

1. Dependence on indium concentration and temperature

Dahal *et al.* [75] fabricated $In_{0.30}Ga_{0.70}N$/GaN MQW solar cell that delivered unprecedented external quantum efficiency of 40% at long operating wavelength of 450 nm. In another study, Dahal *et al.* [76] fabricated an InGaN MWQ solar cell with 35% of indium concentration for testing under concentrated light. The structure is shown in Figure 2.11 with twelve periods of 3 nm thick InGaN (x≈0.35) QW and 17 nm GaN barrier. The $J-V$ and power density vs. Voltage ($P-V$) measured under AM 1.5G, as shown in Figure 2.12 have significantly higher values than the values reported by Lai *et al.* [46]. They attributed the improvements to the

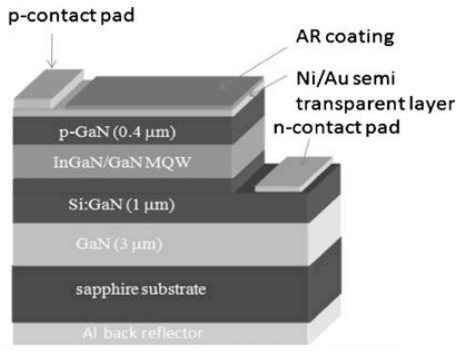

Figure 2.11: Layer structure of InGaN/GaN solar cells with twelve periods of 3 nm thick InGaN (x≈0.35) QW and 17 nm GaN barrier [76].

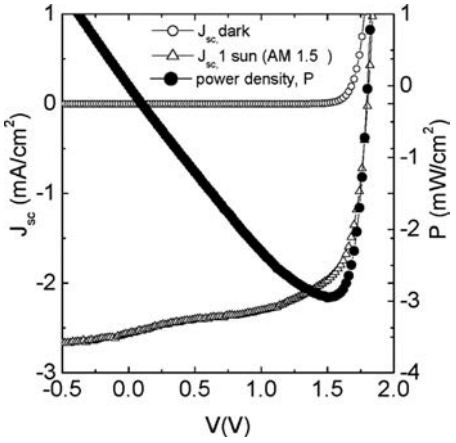

Figure 2.12: Room temperature current density versus voltage ($J_{sc}-V$) and power density versus voltage ($P-V$) characteristics of InGaN/GaN MQW (x≈0.35) solar cells under AM 1.5G irradiation. V_{oc},J_{sc}, FF and η are 1.8 V, 2.56 mA/cm^2, 64% and 2.95%, respectively [76].

high crystalline quality of InGaN material in MQWs. Though they obtained a power conversion efficiency of 2.95% under AM 1.5G and 3.03% under 30 suns but it was still much lower than the

theoretically expected value of a single junction solar cell of about 8% with that optical energy band gap. A major reason for the large difference between theoretical and experimental efficiency was attributed to the insufficient light absorption in InGaN QWs (36nm), that should, at least, be greater than 200 nm for complete light absorption. This was evidenced by the increase in photocurrent density by more than 15% when an aluminum back reflector was deposited. They also stated that it is rather challenging to obtain indium-rich InGaN/GaN MQW structures thicker than 150 nm. Additionally, they reported that the fill factor of the device decreased under concentrated sun light. This was attributed to the enhanced carrier recombination at the interface region due to high carrier densities under concentrated sun light. The reduction of the junction electric field caused by the increase of indium content was also suggested as a leading source of poor fill factor (30%) by varying the different parameters of the MQW solar cells [46]. It has been reported [46] that fill factor and efficiency of the device are substantially enhanced by increasing the temperature from 250K to 300K. The strong temperature-dependent enhancement was attributed to the additional contribution to the photocurrents by the thermally activated carriers, which were originally trapped in the shallow quantum wells resulting from the inhomogeneous indium distribution. The poor fill factor of the device has been also attributed to the high series resistance contributed induced the poor quality of metal contacts and quality of the MQW absorber [77].

2. Dependence on the barrier thickness

Wierer *et al.* [78] studied the influence of the barrier thickness on the performance of InGaN MQW solar cells. The $J-V$ characteristics given in Figure 2.13 shows that samples with barrier thickness of 3.0 nm and 10.0 nm display more leakage current compared to the 6.3 nm barrier sample, impacting the overall efficiency of these devices. They attributed the high leakage

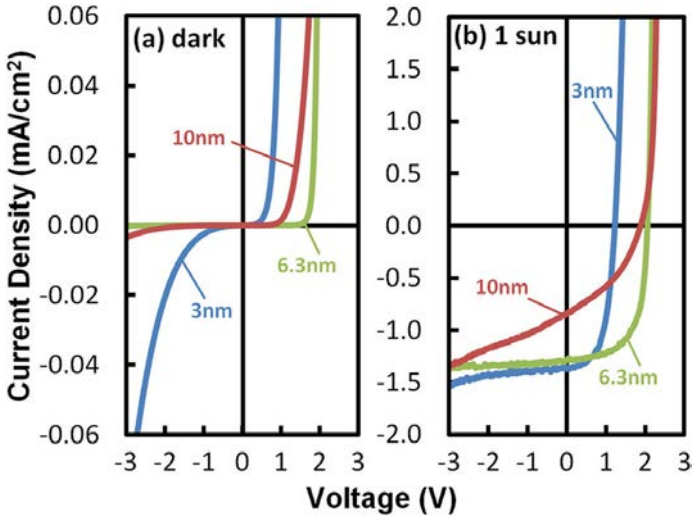

Figure 2.13: Current versus voltage characteristic of the InGaN/ GaN multiple quantum well solar cells under dark (a) and (b) 1 sun AM 1.5G conditions [78].

current to the carrier tunneling via non-radiative centers in the MQW. They reported that the sample with 6.3 nm barrier thickness exhibits the best overall performance with a V_{oc} of 2.05 V, FF of 63% and power conversion efficiency of 1.66%. The power conversion efficiency for 3.0 nm and 10.0 nm samples were 0.96% and 0.61% respectively, greatly affected by the leakage currents. Similarly, Watanab *et al.* [79] reported that under illumination, as the barrier thickness decreases, J_{sc} increases and V_{oc} decreases, shown in Figure 2.14. Under dark conditions, the

device with thinner barrier (3 nm) have high leakage current compared to the thick GaN barrier (9 nm) as shown in Figure Figure 2.15.

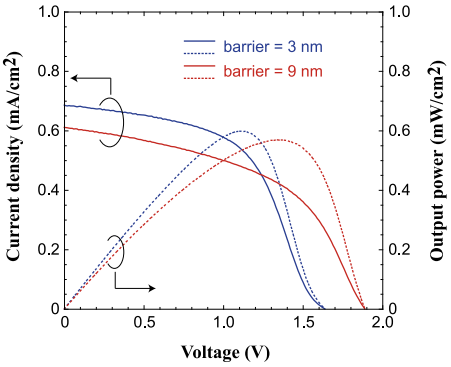

Figure 2.14: $J_{dark} - V$ curves of InGaN/GaN MQW solar cells with different barrier thicknesses without illumination [79].

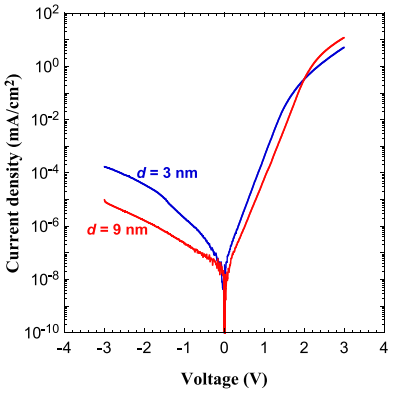

Figure 2.15: $J - V$ and $P - V$ curves of InGaN/GaN MQW solar cells with different barrier thicknesses under AM 1.5 illumination [79].

3. Methods to improve light absorption

To maximize the incident light into the solar cell, Neufeld *et al.* [80] reported $In_{0.28}Ga_{0.72}N$/GaN MQW solar cells with rough p-GaN surface. The devices exhibited an external quantum efficiency of 69% (26%) at 390 nm (460 nm), an open circuit voltage of 2.04 V, a fill factor of 63% and a short circuit current density of 2 mA/cm^2, under an AM 1.5G illumination. Tsai *et al.* [72] reported improved conversion efficiency from 0.17% to 0.27% in substrate free InGaN MQW solar cell with a bottom reflector. Ho *et al.*. [81] reported an efficient light-harvesting scheme using SiO_2 nanorods for InGaN MQW solar cells, improving the power conversion efficiency from 0.37% to 0.45%. Jeng *et al.* [82] demonstrated an increase in solar cell efficiency by using a reflective aluminum layer. Seo *et al.* [83] reported efficiency improvement by using indium tin oxide nano dots covered with ITO films. They observed that the solar cell with the ITO (50 nm) nano-dots under AM 1.5G conditions showed the best results: 2.3 V for V_{oc}, 0.69 mA/cm^2 for J_{sc}, 41.8% for peak EQE, leading to a conversion efficiency of 0.91%. They attributed the efficiency improvement to the decreased reflectance achieved by the ITO nano-dots covered with an ITO film with an optimized thickness.

Young *et al.* [84] reported InGaN/GaN MQW solar cells grown by MOCVD on a bulk (0001) substrate shown in Figure 2.16, with high-performance broadband optical coatings to improve light absorption. The device had anti-reflective coating and back-side dichroic mirror in order to minimize the reflection from the surface and maximize the rear reflection, respectively, that enhanced the power conversion efficiency of the device, as shown in Figure 2.17. The device had a power conversion efficiency of 3.33% under AM 0 illumination. These results suggested that well designed broadband optical coatings can enhance the performance of InGaN-based solar cells while also allowing for high transparency to underlying junctions. Table 2.5 summarizes the state-of the art of InGaN MQW heterojunction solar cells.

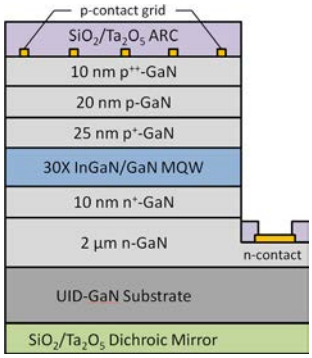

Figure 2.16: Cross sectional schematic of the device structure including contacts and optical coatings. [84].

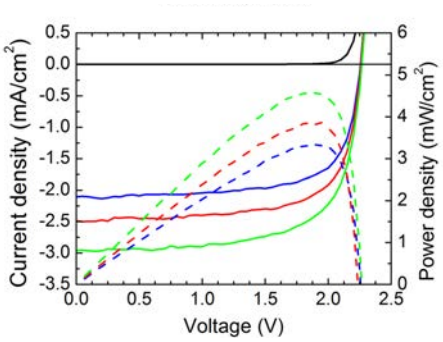

Figure 2.17: current density and power density vs. voltage characteristics of the 30 QW solar cell device before and after depositing both the ARC and DM [84].

Table 2.5: Device performance for MQWs InGaN heterojunction solar cells.

Reference	Absorber (Thickness)	V_{oc} (V)	J_{sc} mA/cm^2	FF (%)	EQE (%)	η (%)	Source
Dahal *et al.* 2009 [75]	$In_{0.30}Ga_{0.70}N$/GaN 8 pairs (3 /8 nm)	2	0.39	60	40	-	White Light
Jeng *et al.* 2009 [85]	$In_{0.20}Ga_{0.80}N$/GaN 5 pairs (3 /7 nm)	2.2	0.66	73	-	1.06	AM 1.5G
Tsai *et al.* 2009 [86]	$In_{0.23}Ga_{0.77}N$/GaN 8 pairs (3 /20 nm)	1.32	0.30	43	-	0.17	AM 1.5G
Dahal *et al.* 2010 [76]	$In_{0.35}Ga_{0.65}N$/GaN 12 pairs (3 /16 nm)	1.8	2.56	64	-	2.95	AM 1.5G
Jeng *et al.* 2010 [87]	$In_{0.13}Ga_{0.87}N$/GaN 12 pairs (5 /2 nm)	2.18	0.54	63	-	0.73	AM 1.5G
Lai *et al.* 2010 [46]	$In_{0.30}Ga_{0.70}N$/GaN 9 pairs (3 /17 nm)	1.97	0.82	30	11.3	0.48	AM 1.5G
Deng *et al.* 2010 [88]	$In_{0.15}Ga_{0.85}N$/GaN 8 pairs (3 /12 nm)	2.1	0.25	29	-	0.20	AM 1.5G

Reference	Absorber (Thickness)	V_{oc} (V)	J_{sc} mA/cm^2	FF (%)	EQE (%)	η (%)	Source
Farell *et al.* 2011 [89]	$In_{0.28}Ga_{0.72}N$/GaN 30 pairs (2.2 /8 nm)	1.93	2.53	56.4	70.9	2.75	AM 1.5G
Lee *et al.* 2011 [90]	$In_{0.23}Ga_{0.77}N$/GaN 10 pairs (2.5 /12 nm)	2.05	1.09	51	50	1.14	AM 1.5G
Liou *et al.* 2011 [91] (Si-substrate)	$In_{0.19}Ga_{0.81}N$/GaN 20 pairs (3 /13 nm)	2.92	2.72	75	50	5.95	AM 1.5G
Neufeld *et al.* 2011 [80]	$In_{0.28}Ga_{0.72}N$/GaN 30 pairs (2.2 /12 nm)	2.04	2	63	69	2.57	AM 1.5G
Neufeld *et al.* 2011 [92]	$In_{0.10}Ga_{0.90}N$/GaN 5 pairs (9 /12 nm)	1.90	1.28	71	60	1.73	AM 1.5G
Hu *et al.* 2012 [93]	$In_{0.20}Ga_{0.80}N$/GaN 10 pairs (2.2 /3 nm)	1.72	1.09	57.4	25.5	1.02	AM 1.5G
Wierer *et al.* 2012 [78]	$In_{0.21}Ga_{0.79}N$/GaN 15 pairs (2.7 /6.3 nm)	2.05	1.29	63	-	1.66	AM 1.5G
Choi *et al.* 2013 [94]	$In_{0.17}Ga_{0.83}N$/GaN 5 pairs (3 /6.3 nm)	1.6	0.36	28.5	9	1.6	AM 1.5G
Liou *et al.* 2013 [95] (n-Si substrate)	$In_{0.19}Ga_{0.81}N$/GaN 20 pairs (3 /13 nm)	2.94	2.71	75	-	5.99	AM 1.5G
Young *et al.* 2013 [96]	$In_{0.20}Ga_{0.80}N$/GaN 30 pairs (2.3 /4 nm)	2.26	2.10	70.4	43	3.33	AM 1.5G
Redaelli *et al.* 2014 [97]	$In_{0.12}Ga_{0.88}N$/GaN 30 pairs (1.3 /8 nm)	2.17	0.42	54	-	0.49	AM 1.5G
Sheu *et al.* 2014	$In_{0.28}Ga_{0.72}N$/GaN 12 pairs	1.90	2.07	55	-	2.16	AM 1.5G

Reference	Absorber (Thickness)	V_{oc} (V)	J_{sc} mA/cm^2	FF (%)	EQE (%)	η (%)	Source
[98]	(2.5 /14.5 nm)						
Mukhtarova *et al.* 2016 [99]	$In_{0.10}Ga_{0.0.90}N$/GaN 60 pairs (1.3 /8.7 nm)	2.3	0.68	56	31	0.88	AM 1.5G

2.2.0.5 InGaN Homojunctions PIN Solar Cells

The polarization in InGaN heterojunction solar cells remain a problem, especially with high indium concentration, needed for covering the entire solar spectrum. To overcome this problem InGaN homojunction solar cell is being studied. Chen *et al.* reported a V_{oc} of 0.24 V for an indium concentration of 20%. Yang *et al.* [50] reported a V_{oc} of 0.43 V for a PN homojunction InGaN solar cell, which was much lower than that expected from the bandgap. In 2008 Misra *et al.* [100] obtained a V_{oc} of 0.55V and J_{sc} of 0.24 mA/cm^2 under AM 0 equivalent illumination for a p-$In_{0.31}Ga_{0.69}N$/n-$In_{0.31}Ga_{0.69}N$ homojunction solar cell grown by MBE. However, the V_{oc} was still lower than the expected value. Yamamoto et al. [101] grew p-$In_{0.23}Ga_{0.77}N$/n^+-$In_{0.23}Ga_{0.77}N$ solar cell by MOVPE reaching the values of V_{oc} of 1.5 V and a J_{sc} of 0.5 mA/cm^2 under an AM 1.5G illumination, as shown in Figure 2.18. The low J_{sc} was attributed to the large bandgap

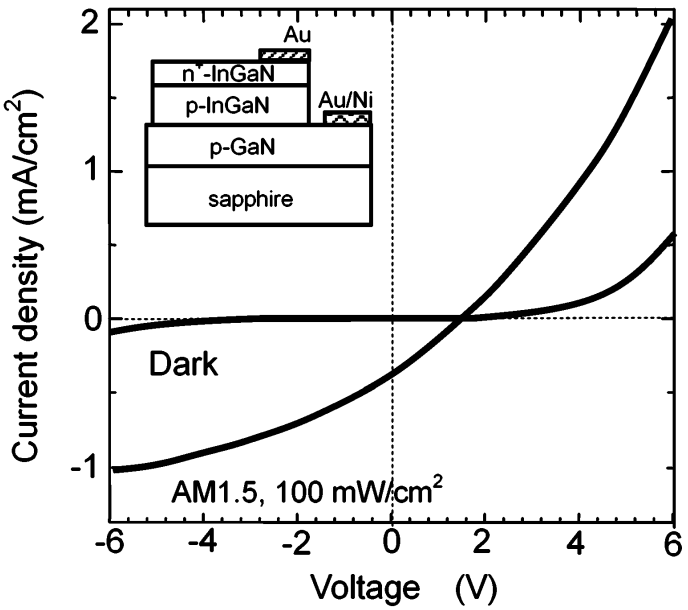

Figure 2.18: $J-V$ characteristics for an n^+-p junction of $In_{o.23}Ga_{o.77}N$ under AM 1.5G illumination. The structure of the device fabricated is shown in the inset [101].

(2.57eV) and poor quality of the thick InGaN (0.5–1 μm) films. The steep increase observed in forward current compared with that in the dark, indicated the photoconductive nature of the p-layer. The devices also suffered from the poor-doping capability of p-InGaN causing high series resistance, resulting in a poor fill factor eventually leading to a lower conversion efficiency.

In the year 2009, Cai *et al.* [102] reported values of V_{oc} as 2.24, 1.34, and 0.96 V, for 2%, 12%, and 15%, of indium concentration respectively. The $J-V$ characteristics in Figure

2.19 shows that the J_{sc} increases with the increase of indium concentration, attributed to the enhanced absorption of incident light due to the reduction of the bandgap of InGaN. The V_{oc}

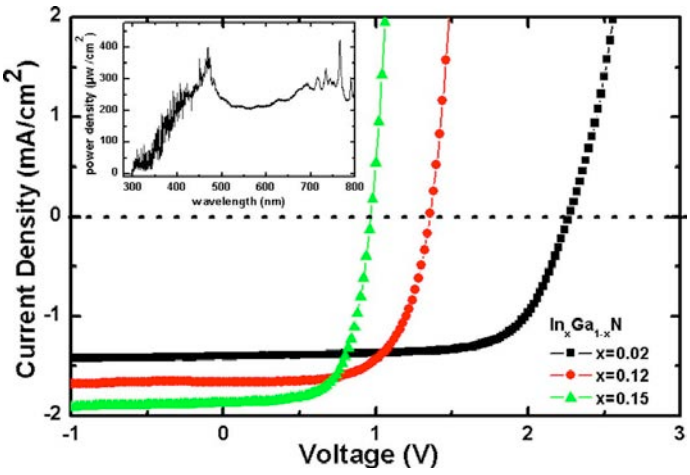

Figure 2.19: $J-V$ curves for InGaN homojunction solar cells with different indium concentration under illumination of a Xe lamp. Inset shows the emission power density of the Xe lamp as a function of wavelength [102].

decreased significantly with the increase of indium concentration, mainly due to the degradation of the InGaN crystalline quality. Jampana *et al.* [103] reported a conversion efficiency of 0.17% under AM 0 equivalent. Zeng *et al.* [104] reported a V_{oc}, J_{sc} and FF of 1.35 V, 1.68 mA/cm^2 and 64.8% respectively for 12% of indium concentration. Boney *et al.* [105] reported an InGaN homojunction solar cell with the highest indium concentration (39%). They observed an increase in the J_{sc} but the V_{oc} was extremely low.

In 2013, Cait *et al.* [106] compared the performance of a InGaN PIN homojunction and p-GaN/i- InGaN/n-GaN heterojunction solar cells. Figure 2.20 shows the structures of the devices. Figure 2.20(a) shows the design of the homojunction solar cells, HOJ-L and HOJ-H, with x = 0.12 and x = 0.15, respectively. Figure 2.20(b) shows the heterojunction solar cells, HEJ-L and HEJ-H, with x = 0.135 and x = 0.16, respectively. The photovoltaic performance of the devices is shown in Figure 2.21.

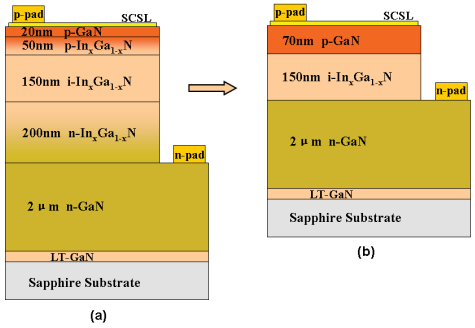

Figure 2.20: Schematic diagrams of InGaN PIN solar cells, (a). Homojunction (HOJ), (b). Heterojunction (HEJ) [106].

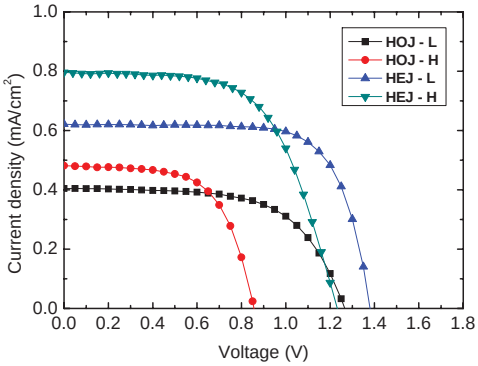

Figure 2.21: $J-V$ characteristics for InGaN PIN homjunction (HOJ) and heterojunction (HEJ) solar cells [106].

It was demonstrated that heterojunction samples show two times higher performance (η =

0.62% for HEJ-L) compared to homojunction solar cells ($\eta = 0.32\%$ for HOJ-L) under AM1.5G equivalent illumination. For a more extended review, the state-of-the-art for InGaN-based homojunction solar cells is given in Table 2.6.

Table 2.6: Device performance for homojunction InGaN solar cells.

Reference	Absorber (Thickness)	V_{oc} (V)	J_{sc} mA/cm^2	FF (%)	EQE (%)	η (%)	Source
Yang *et al.* 2007 [50]	p-$In_{0.18}Ga_{0.82}N$ (120 nm) n-$In_{0.15}Ga_{0.85}N$ (200 nm)	0.43	0.034	57	-	-	360 nm laser
Chen *et al.* 2008 [53]	i-$In_{0.20}Ga_{0.80}N$ (300 nm)	2.5	30	61	-	-	325 nm laser
Misra *et al.* 2008 [100]	i-$In_{0.31}Ga_{0.69}N$	0.55	0.24	15	-	0.02	AM 0
Yamamoto *et al.* 2008 [101]	i-$In_{0.23}Ga_{0.77}N$	1.5	0.5	-	-	0.25	AM 1.5G
Cai *et al.* 2009 [102]	i-$In_{0.02}Ga_{0.98}N$ (150 nm)	2.24	1.40	69	43	-	Xenon Lamp
Lee *et al.* 2010 [107]	i-$In_{0.13}Ga_{0.87}N$ (200 nm)	0.40	0.019	33	-	0.003	AM 1.5G
Zeng *et al.* 2010 [104]	i-$In_{0.12}Ga_{0.88}N$ (150 nm)	1.35	1.68	64.8	-	1.46	AM 1.5G
Jampana *et al.* 2010 [103]	$In_{0.16}Ga_{0.84}N$	1.73	0.91	61.04	-	0.17	AM 0
Boney *et al.* 2011 [105]	i-$In_{0.14}Ga_{0.86}N$ (300 nm)	1.79	0.99	52	-	0.71	AM 0
Sang *et al.* 2011 [108]	i-$In_{0.15}Ga_{0.85}N$ (240 nm)	1.50	1.25	56	80	1.05	AM 1.5G
Sang *et al.*	i-$In_{0.15}Ga_{0.85}N$	1.48	1.83	68	-	1.8	AM 0

Reference	Absorber (Thickness)	V_{oc} (V)	J_{sc} mA/cm^2	FF (%)	EQE (%)	η (%)	Source
2013 [109]	(240 nm)						

2.2.1 New InGaN Solar Cell Design Concepts

2.2.1.1 Semibulk InGaN PIN Heterojunction Solar Cells

Our team recently proposed a novel approach for the growth of high quality thick InGaN epitaxial layers with high indium concentrated for the realization of high efficiency solar cells. It consists in replacing the conventional bulk absorber by a thick multi-layered InGaN/GaN absorber. To distinguish the structures from Multiple-Quantum Well (MQW) and Super-lattice (SL), it is referred as "Semibulk" [110], as shown by schematic in Figure 2.22. The periodical insertion

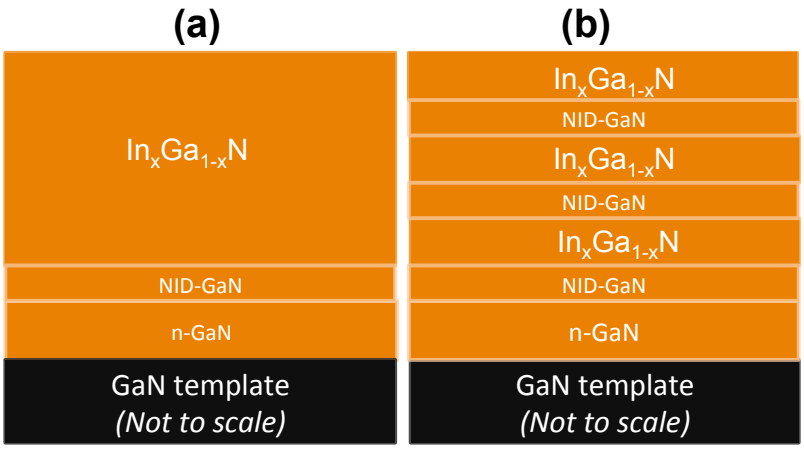

Figure 2.22: Schematic structure of the (a) Bulk InGaN, and (b) semibulk InGaN.

of the thin GaN interlayers should absorb the excess indium and relieve compressive strain, effectively resetting the growth conditions to those of the initial, two-dimensional InGaN layer. As shown in Figure 2.23 the three-dimensional sublayer in bulk InGaN has been suppressed in the semibulk, which is two-dimensional all the way to the top. These GaN interlayers need to be thick enough to be effective and thin enough to allow carrier transport through tunneling. The InGaN layers need to be thick and numerous enough to absorb efficiently the incoming light beam, and thin enough to remain fully strained and without phase separation. Gmili *et al.* [112] demonstrated that semibulk InGaN structure suppresses the indium concentration fluctuations and corresponding different states of strain relaxation with depth, both detrimental to solar cell applications. As shown by (10.5) reciprocal space maps and (00.2) $\omega - 2\theta$ scans as well ws SEM surface morphology in Figure 2.24. One can clearly observe a broad InGaN diffraction spot for the bulk InGaN. The extended profile observed along the isocompositional line indicates the presence of different strain relaxation states in the film. For the semibulk, the InGaN diffraction spot is more intense and lies on the vertical line corresponding to pseudomorphic InGaN on GaN template substrate. Figure 2.25 shows the SEM images and corresponding cathodoluminescence (CL) hyperspectra mappings at en electron beam energy of 7 KeV. The bulk InGaN exhibits rough 3-D surface growth mode with a large number of inclusions, while the semibulk InGaN shows 2-D surface growth mode with a small number of inclusions.The CL mapping in bulk

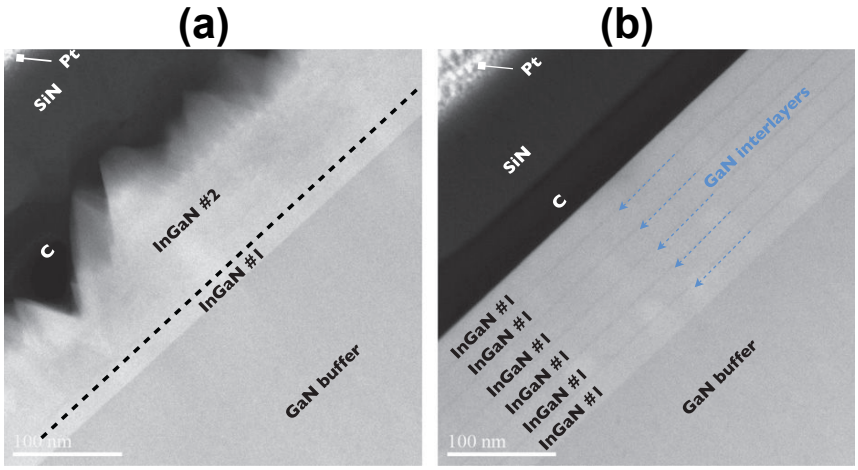

Figure 2.23: HAADF-STEM images along the $(11\bar{2}0)$ zone axis of (a) the bulk InGaN and (b) the semibulk InGaN; the interlayers in the semi-bulk sample are pointed out by blue arrows [111].

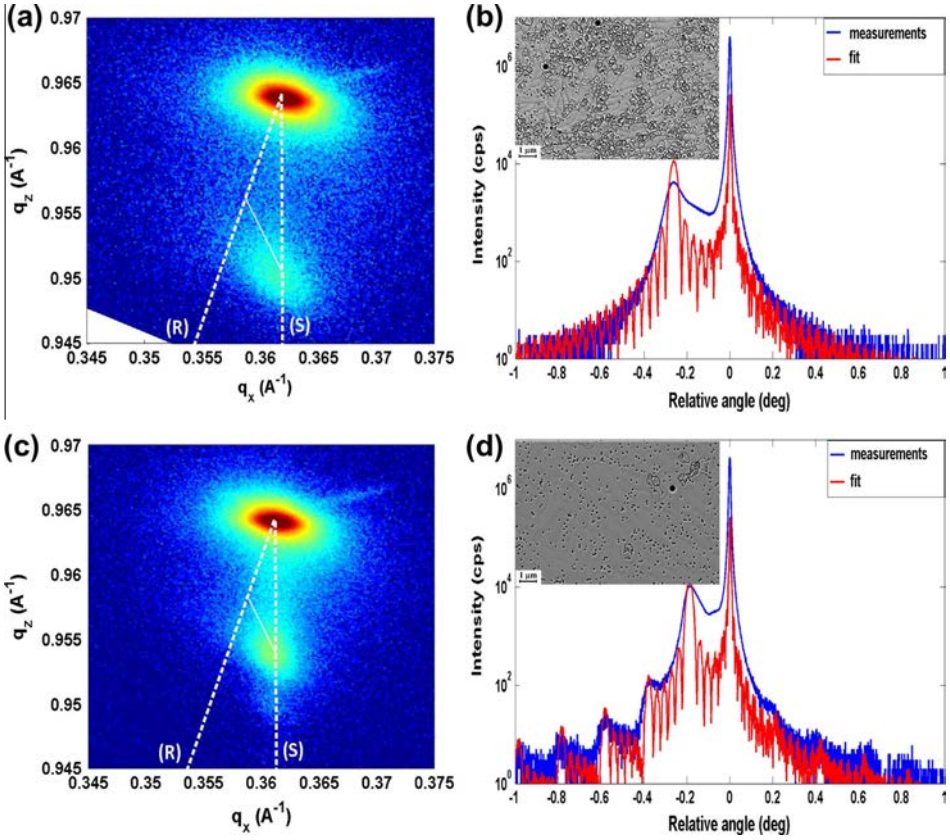

Figure 2.24: (10.5) reciprocal space maps and (00.2) $\omega - 2\theta$ scans of the (a and b)bulk structure and (c and d) semibulk structure. The isocomposition lines connect the theoretical lines of fully strained (S) and fully relaxed (R) InGaN. The inset on (b and d) shows SEM images of the bulk InGaN and semibulk InGaN surfaces, respectively [112].

InGaN (see Figure 2.25(c)(e)) exhibits two different phases with large in-homogeneity whereas the CL mapping for semibulk InGaN (see Figure 2.25(d)) reveals only one phase with a rather low in-homogeneity.

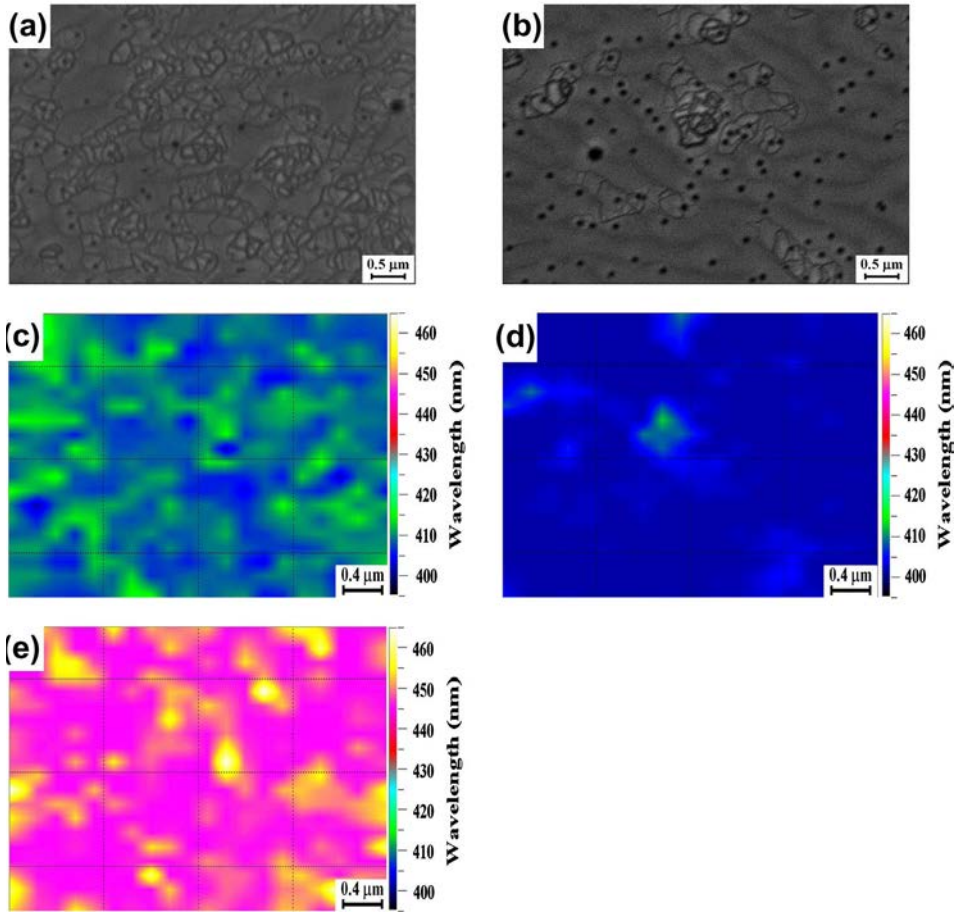

Figure 2.25: (a)–(b) SEM and (c)–(e) CL hyperspectral mapping images in the bulk and semibulk structures respectively [112].

The GaN interlayers within the semibulk InGaN should reduce the effect of both surface indium accumulation and V-pit formation, improves the crystalline quality of the epitaxial layer as demonstrated by Van *et al.* [113] during a comparison of bulk and semibulk structures shown in Figure 2.26. They show that semibulk growth approach effectively suppressed formation of surface V-pits in the InGaN layers, resulting in vastly superior crystal quality and homogeneous indium distribution compared with bulk InGaN. Improved indium consistency throughout layer growth was also observed for the semibulk InGaN layer.

All these encouraging results show that the semibulk InGaN approach is a promising solution for growth of high-quality, thick InGaN epitaxial layers with high indium concentration, required for the realization of high efficiency InGaN solar cells. To utilize this novel technique for fabrication of high efficiency solar cells is one of the objective of this dissertation.

2.2.1.2 Nano-structure InGaN PIN Heterojunction Solar Cells

Nano-structured InGaN epitaxial layers are widely used in improving the efficiency of light emitting diodes (LEDs) [114–117], however, very few studies have been reported with PV cells using nanowire arrays [118,119] and core-shell (coaxial) nanowire [120,121]. Tang *et al.* [122] reported vertically aligned Mg-doped GaN nanorod arrays on n-type Si substrates for heterojunction PV Cells. The cell has a high short-circuit photocurrent density of 7.6 mA/cm^2 and energy conversion efficiency of 2.73% under AM 1.5G illumination at 100 mW/cm^2. Goto *et al.* [118] reported the growth of core-shell InP nanowires for PV applications by selective-area metal organic vapor phase epitaxy. The device exhibited open-circuit voltage (V_{oc}), short-circuit current (I_{sc}) and fill

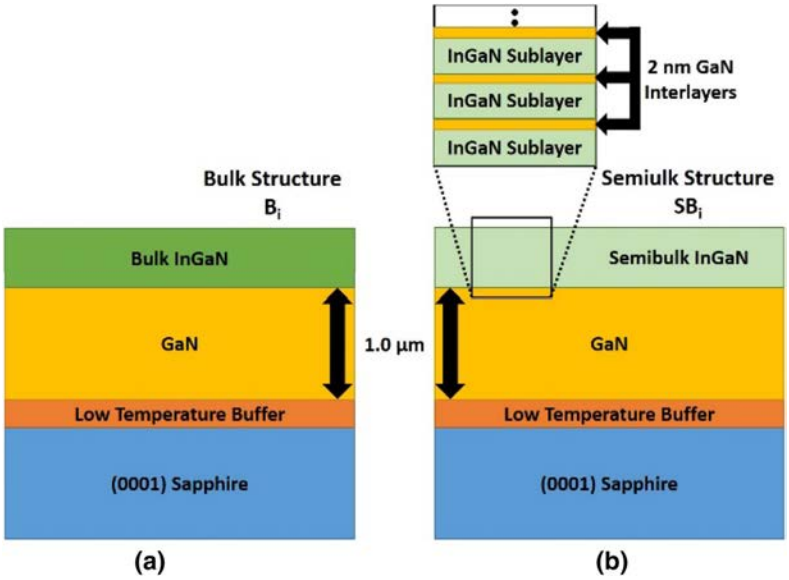

Figure 2.26: Schematic diagrams of, (a) the bulk InGaN structure and (b) the semibulk InGaN structure, inset: details of the semibulk growth process [113].

factor levels of 0.43 V, 13.72 mA/cm^2 and 0.57, respectively, which indicated a power conversion efficiency of 3.3% under AM1.5G illumination as shown in Figure 2.27. Tian *et al.* [123] reported

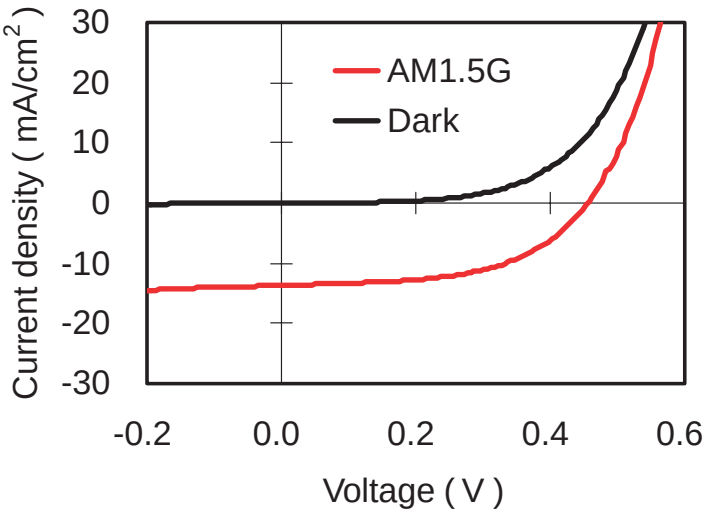

Figure 2.27: Measured $I-V$ characteristics of a solar cell fabricated with core-shell pn junction nanowires on a p-type InP (111) substrate [118].

a nanowire photovoltaic device using a Si-based core-shell structure and obtained a conversion efficiency of 3.4%. Wierer *et al.* [120] reported a J_{sc}, V_{oc} and fill factor of 1 mA/cm^2, 0.50 V and 54% respectively under 1 sun illumination, as shown in Figure 2.28. Although the resulting power conversion efficiency reported by Wierer *et al.* [120] is around 0.3%, it does represent the highest recorded efficiency in a III-nitride nanowire solar cell.

Zang *et al.* [117] demonstrated nano-structured InGaN/GaN multiple quantum wells (MQWs) grown by metalorganic chemical vapor deposition (MOCVD) on a nano-patterned SiO_2/GaN template, as shown in Figure 2.29. They observed that the intensity from the InGaN MQWs nanorods was one order of magnitude higher compared to that of the control InGaN MQWs.

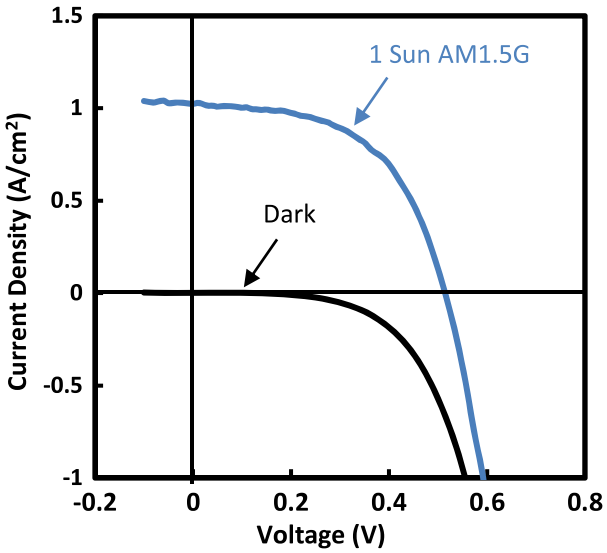

Figure 2.28: Current density versus voltage characteristics of the III-nitride nanowire solar cell under dark and 1 sun (AM 1.5G) conditions [120].

Table 2.7: Device performance reported for nano-structure PV cells.

	Absorber	V_{oc} (V)	J_{sc} (mA/cm^2)	FF %	Efficiency (%	Source
Wierer *et al.* [120] (core shell)	$In_{0.015}Ga_{0.985}N$	0.50	1	54 %	0.30	1 sun
Dong *et al.* [121] (nanowire)	$In_{0.27}Ga_{0.73}N$	1	0.39	56	0.19	1 sun
Tian *et al.* [123]	p-i-n silicon nanowire	-	-	-	3.4	-
Colombo *et al.* [119]	p-i-n GaAs nanowire	1.30	100 nA	65	4.5	AM 1.5G
Goto *et al.* [118]	InP nanowire	0.43	13.72	0.57	3.37	AM 1.5G

The improvement in light emission was attributed to the benefit of the reduction in the number of non-radiative recombination centers associated with threading dislocations. The dislocation density reduction was attributed partially due to blocking effect of the SiO_2 mask and partially due to strain relaxation in the nanometer sized nucleation and growth. However, it is difficult to grow high quality indium rich InGaN nanostructures on GaN nano-columns without interfacial defects [124]. Good quality, InGaN nanostructures with around 20% indium incorporation have been selectively grown on the GaN templates by either pulsing the precursors [125–127], or using the continuous precursors flow method [128]. Zubia *et al.* [129] reported GaN Nano-Selective Area Growth (NSAG) on silicon substrates, by MOCVD (See Appendix C for details of NSAG and MOCVD).

Our team demonstrated the growth of bulk InGaN nanopyramids. The novelty of the InGaN nano-structures grown by our team is the high quality thick InGaN nanopyramid as shown by

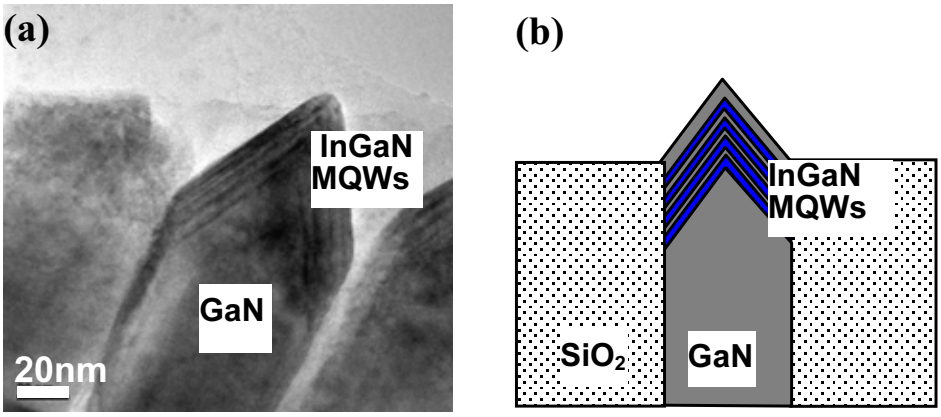

Figure 2.29: (a) Cross-sectional transmission electron microscopy (TEM) image of a single GaN nanorod with 4 periods of InGaN/GaN MQWs, showing high crystal quality with low defect density, resulting in an improvement in internal quantum efficiency [117].

schematic in Figure 2.30. The SEM images of perfectly selective InGaN nanostructures grown

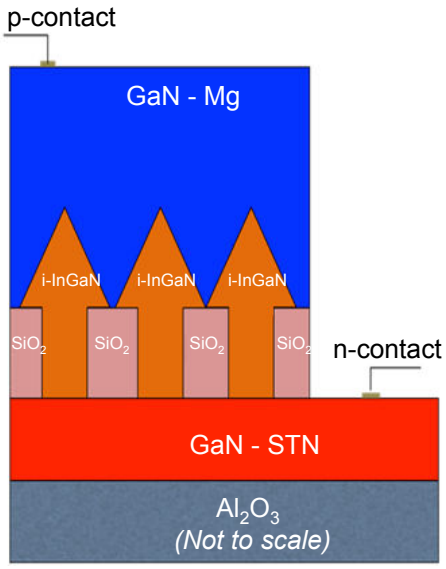

Figure 2.30: Schematic of bulk InGaN nano-structure appraoch proposed by our team.

on circular and stripe openings in the patterned substrate respectively, are shown in Figure 2.31. As a results of optimized growth conditions, more than 3000 consecutive nanorods have grown without anu defect or polycrystalline deposits. Our team also demonstrted the nano selective area growth of dislocation-free 100 nm thick hexagonal InGaN nanopyramid rrays with up to 33% of indium concentration on a patterned AlN/Si templates. The STEM study of these structures given in Figure 2.32 shows that the planar InGaN surface is completly 3D with networks of V-pits originating from threading dislocations propagating from the nanocrystalline AlN buffer layer. In contrast, the InGaN nanopyramids on patterned AlN/Si templates are monocrystalline and dislocation free with clear interfaces between InGaN/GaN and nanocrystalline AlN as shown in the HAAD-STEM image Figure 2.32(c). This shows that the nanopyramids start from a single nucleus on the AlN seed because of the small opening, and the strain relaxation is purely elastic without generation of further defects and misfit dislocations. The vertical and horizontal EDX line scan shows that the nanopyramids have uniform indium incorporation averaging around 33%, demonstrating the ability of NSAG to obtain very uniform and homogeneous

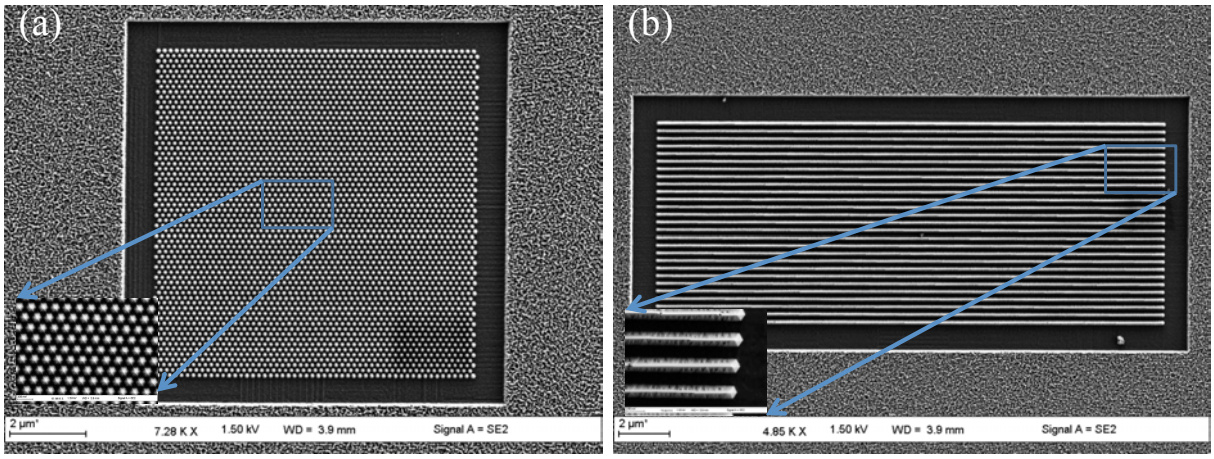

Figure 2.31: SEM images of perfectly selective InGaN nanostructure arrays grown on GaN templates in (a) circular opening and (b) stripe opening.

InGaN nanostructures without any misfit defects.

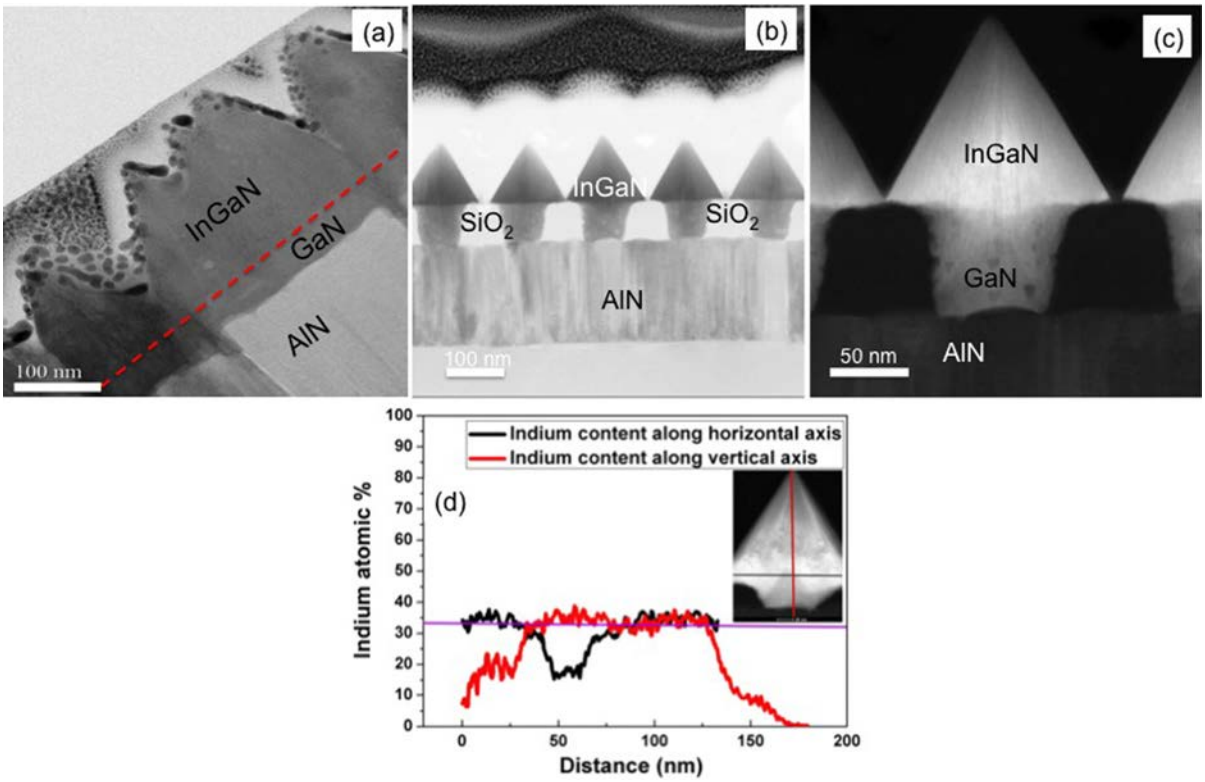

Figure 2.32: (a) SEM image of the InGaN nanopyramids grown on the patterned AlN/Si template, (b) High magnification SEM image of the InGaN nanopyramid.

The ability to incorporate more indium without deteriorating the crystalline quality of the InGaN layers using the defect-free thick InGaN nano-structures(Figure 2.30), offers a new route to develop monolithic InGaN-based high efficiency solar cells. The utilization of the potential of this new technique in realization of high efficiency InGaN based solar cells is one of the objective of this dissertation.

Chapter 3

InGaN Bulk PIN Heterojunction Solar Cells

The development of bulk InGaN heterojunction solar cells, benefited mostly from the mature growth and fabrication technology of InGaN/GaN LEDs. They have been extensively studied, but failed in accomplishing the goal of high efficiency InGaN solar cells. There are two major challenges that limit the realization of high efficiency InGaN solar cells. The first challenge is the growth of high crystalline structural quality thick InGaN absorber layer with high indium concentration [38]. Despite the high optical absorption coefficient, InGaN films with thicknesses in excess of 120 nm are required for the absorption of 90% of incident above-bandgap light. However, InGaN epitaxial layers for a given indium concentration are restricted to a certain thickness and epitaxial layer exceeding this critical layer thickness result in a poor crystalline quality [56]. The second challenge is the degradation of the optical and structural properties of the InGaN absorber during the growth of the subsequent top p-GaN layer. The latter is generally grown at a temperature (>1000°C in MOVPE) which is much higher than what the InGaN layer can withstand. InGaN is grown at temperature around 700°C– 800°C (in MOVPE). Therefore, the high growth temperature of the subsequent p-GaN layer leads to unfavorable effects such as lattice relaxation and composition redistribution in the InGaN absorber [60]. However, decreasing the growth temperature of the p-GaN layer leads to a rather low crystal quality resulting in a high leakage current, thus affects the performance of the InGaN solar cells.

This chapter present a detailed investigation of the effect of the subsequent top p-GaN growth temperature on the crystalline quality of the InGaN absorber layer. In addition, using combined electro-optical, scanning electron microscopy, high angular annular dark field scanning transmission electron microscopy (HAADF-STEM) and electron beam induced current (EBIC) characterization techniques, we study the influence of V-pits on the overall conversion efficiency of bulk $In_{0.12}Ga_{0.88}N$ absorber based heterojunction solar cells.

3.1 Design of the Structure

The design for bulk InGaN absorber PV device followed the well understood classical InGaN PIN structure, where a thick InGaN layer is sandwiched between a p-type GaN (Magnesium doped) and n-type GaN layers. For this, the structure shown in Figure 3.1, is grown on 3.5 μm thick GaN/sapphire templates. An 850 nm thick n-type GaN doped with silicon is grown, followed by a 50 nm GaN layer, used to stop the diffusion of the silicon into the InGaN absorber. The InGaN PV structure shown in Figure 3.1, afterwards will be referred as T1185-B. A 60 nm InGaN is grown to form the active region. This thickness is selected to make sure that layer remain within the critical layer thickness discussed in the previous chapter. The bulk InGaN absorber epitaxial

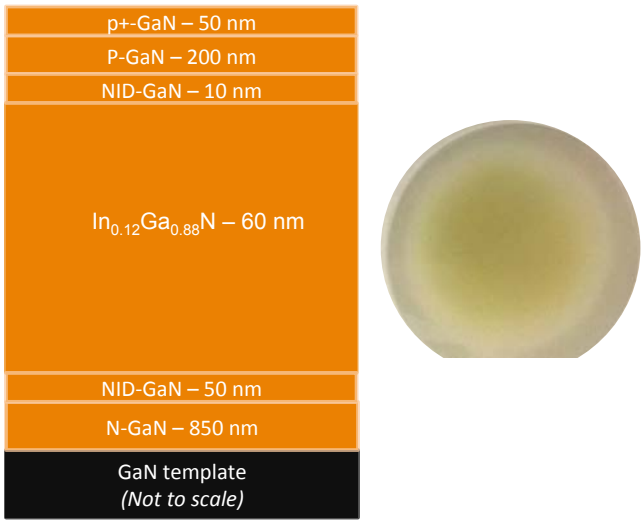

Figure 3.1: Bulk InGaN PIN PV structures grown with 12% indium concentration (T1185-B).

layer is then followed by the growth of a thin low temperature (800°C) GaN cap layer. This GaN layer is a multitask epitaxial layer, as it not only prevent indium evaporation during the growth of the top p-GaN layer but also suppresses the propagation of threading dislocations from InGaN in to p-GaN [130]. The GaN cap layer is also useful in stopping the diffusion of Mg into the InGaN absorber. Finally the p-GaN epitaxial layer is grown at different temperatures that will be discussed in next section.

3.2 Effect of the P-GaN Growth Temperature

The growth temperature of the subsequent top p-GaN layer is quite challenging, due to the fact that the crystalline quality of the InGaN absorber significantly depends on the p-GaN growth temperature. The high p-GaN growth temperature (>1000°C) leads to unfavorable effects such as lattice relaxation and composition redistribution in the InGaN absorber [23]. In contrary, when the p-GaN epitaxial layer is grown at low temperature, the crystal quality of p-GaN tends to be degraded, hindering the performance of the PV cell.

It has been reported [63, 65, 66, 89] that InGaN solar cells with p-GaN grown at low temperature results in a high leakage current, that reduces the open circuit voltage (V_{oc}). This is expected due to the high density of threading dislocations (TDs) and V-pits in the p-GaN epitaxial layer which give rise to carrier recombination that should also limit the photocurrent. Surprisingly, all of these authors reported InGaN PV cells with a high short circuit current density (J_{sc}). This is explained by a possible reduction of the light reflection at the rough p-GaN surface. Nevertheless the role of p-GaN surface morphology is not only limited to the PV cells but several reports [131–133] show that the presence of nano-sized surface V-pit results in enhancements of the performance of GaN based light emitting diodes (LEDs). However, the role of V-pit in a given device significantly depends upon the size of the V-pits, that can be controlled by the growth conditions of the p-GaN layer [133]. These results show that the growth temperature of the subsequent top p-GaN layer, may play a significant role in the overall conversion efficiency of the InGaN PV cells. To do an in-depth study of the effect of p-GaN growth temperature on the bulk InGaN absorber discussed in the previous section, several InGaN PV structures are grown, with p-type GaN grown at different temperatures *i.e.* 1000°C, 900°C, 850°C and 800°C.

3.2.1 Micro-structural Properties

Figure 3.2(a)–(d) shows the HAADF-STEM image of the InGaN PV structures, with p-GaN grown at 800°C, 850°C, 900°C and 1000°C respectively. The growth of the p-GaN layer at low temperature (800°C) allows reduction of the thermal budget effect on the active region, resulting in a well preserved InGaN absorber layer as well as an abrupt and smooth interface between the InGaN absorber and the p-GaN layer as shown in the HAADF-STEM image in Figure 3.2(a). However, as expected, a high density of threading dislocations is observed in the p-GaN layer due to the low growth temperature. These threading dislocations open up to give nanotubes or open-core defects, hence result in a high density of V-pits [134], as shown in the inset of the Figure 3.2(a). The depth of these V-pits varies from 30 nm to 100 nm. To attempt to improve the crystalline quality of the p-GaN layer, the growth temperature is increased to 850°C and 900°C but, as shown in Figure 3.2(b) and 3.2(c), the InGaN absorber degraded. Indium-rich regions that can be attributed to the inter-diffusion and re-evaporation of indium in the InGaN absorber [135] appear (area with a dark contrast in the HAADF-STEM image of (Figure 3.2(b)). The interface between the InGaN absorber and the p-GaN layer is no longer abrupt and smooth. It is to be noticed that the InGaN absorber is degraded only in the region close to the interface with the p-GaN layer. Although a higher p-GaN growth temperature is used the density of threading dislocations in the p-GaN layer is still high. A further increase of the p-GaN growth temperature to 1000°C allows to obtain a smooth p-GaN layer with a low density of threading dislocations (see Figure 3.2(d)) but the InGaN material is degraded in the full depth of the layer. Figure 3.2(d) show the HAADF-STEM image of the InGaN PV structure, with p-GaN grown at 1000°C.

3.2.2 Morphological Properties

The evolution of the p-GaN layer surface morphology with its growth temperature is confirmed by the SEM analysis of the top surface (see Figure 3.3) which reveals a decrease of the p-GaN layer roughness with increasing growth temperature. The rough surface obtained at the lowest growth temperature Figure 3.3(a) can be attributed to the fact that Ga adatoms do not have enough energy to migrate to proper lattice sites limiting the lateral growth rate because of the shorter Ga diffusion length [136]. This is evidenced in Figure 3.3(b), where an increase in the p-GaN growth temperature results in a drastic decrease of the surface roughness. However, the growth temperature (850°C) is not high enough to planarize the V-pits. This is then achieved by further increasing the p-GaN growth temperature (900°C) as shown in Figure 3.3(c). The density of V-pits is significantly reduced transitioning the rough morphology into a smooth surface. The high p-GaN growth temperature (1000°C) leads to a better planarization of the V-pits, and thus to a flat surface. Since the $In_xGa_{1-x}N$ absorber for the PV structures with p-GaN grown at 850°C, 900°C and 1000°C has been degraded, the structure with the p-GaN layer grown at 800°C is further characterized and processed to fabricate PV cells.

Figure 3.4(a) shows the RSM of the InGaN PV structure with p-GaN grown at 800°C, indicating the diffraction spots for the GaN substrate and InGaN epilayer. The InGaN diffraction spot is intense and lies vertically below the GaN spot indicating that the InGaN epilayer is mostly coherently strained to the GaN template. The extracted value for the degree of relaxation is 8% with an average indium content of 12%. EDX measurements are performed to get a direct measurement of chemical composition as shown in Figure 3.4(b), and revealed an average indium concentration of 12%.

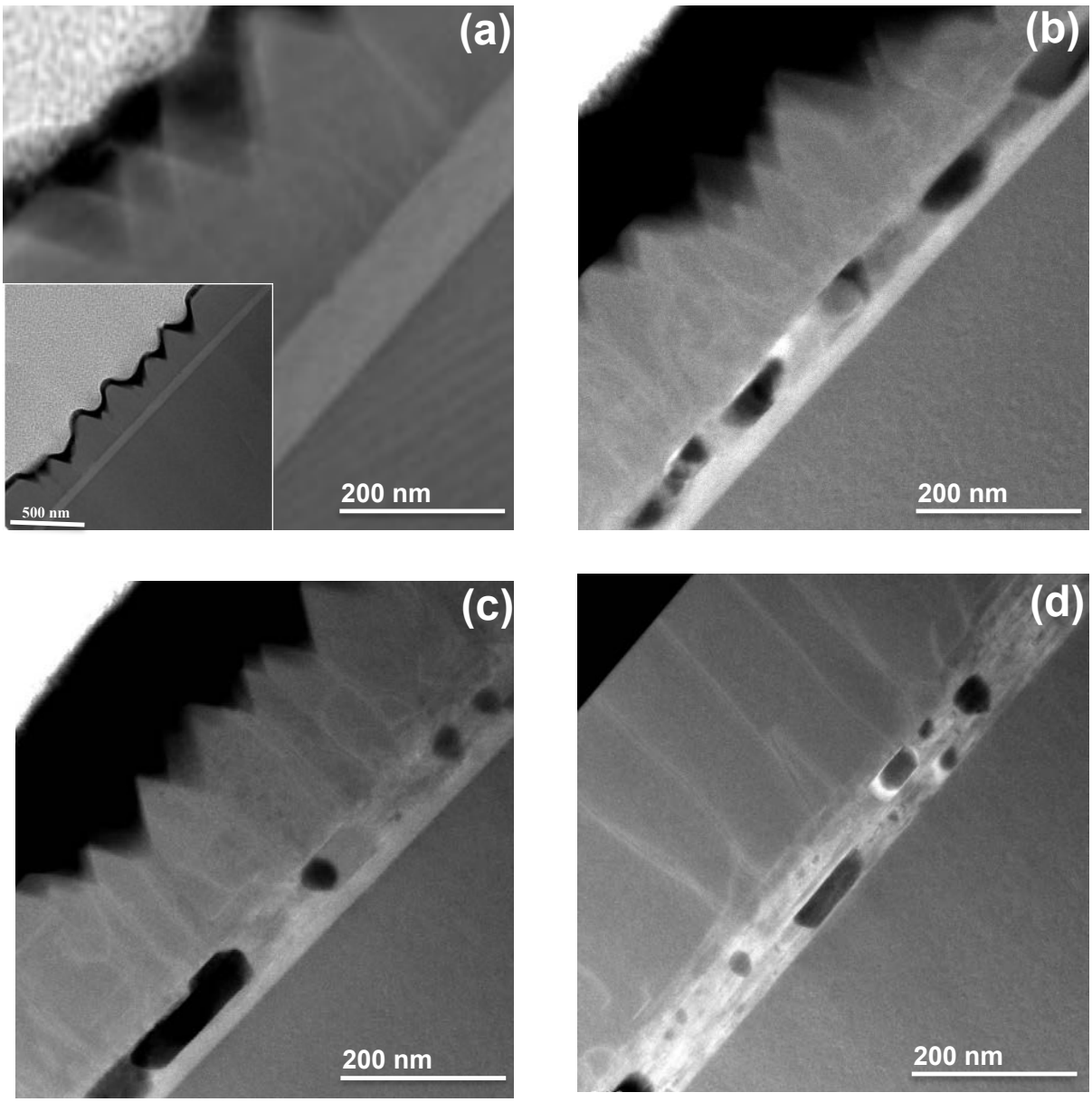

Figure 3.2: HAADF-STEM cross-sectional images of the different PV structures with p-GaN grown at, (a) 800°C, the inset show the HAADF-STEM cross-section at a large scale, (b) 850°C, (c) 900°C, (d) 1000°C.

3.3 Device Processing

The typical mask and the processed devices on T1185-B are shown in Figure 3.5. These devices are processed in collaboration with our partner laboratory, CNRS /LPN : Laboratoire de Photonique et de Nanostructures (France), The area of devices ranges from 0.35 mm^2 to 1.27 mm^2. The classical diodes were also fabricated for validation of the quality of metal contacts at each epitaxial layer.

Figure 3.6(a)–(b) show the cross section of the structure and the top view of the device respectively. This device consist of 0.8 mm × 0.8 mm mesas for accessing the n-GaN layers. The top p-GaN contacts consist of a Pd/Au grid on top of each mesa with approximately 5 μm thick fingers and a 75 μm pitch. Prior to the metallization, the sample is cleaned in organic solvents (trichloroethylene, acetone, and isopropanol) then rinsed with de-ionized water, each

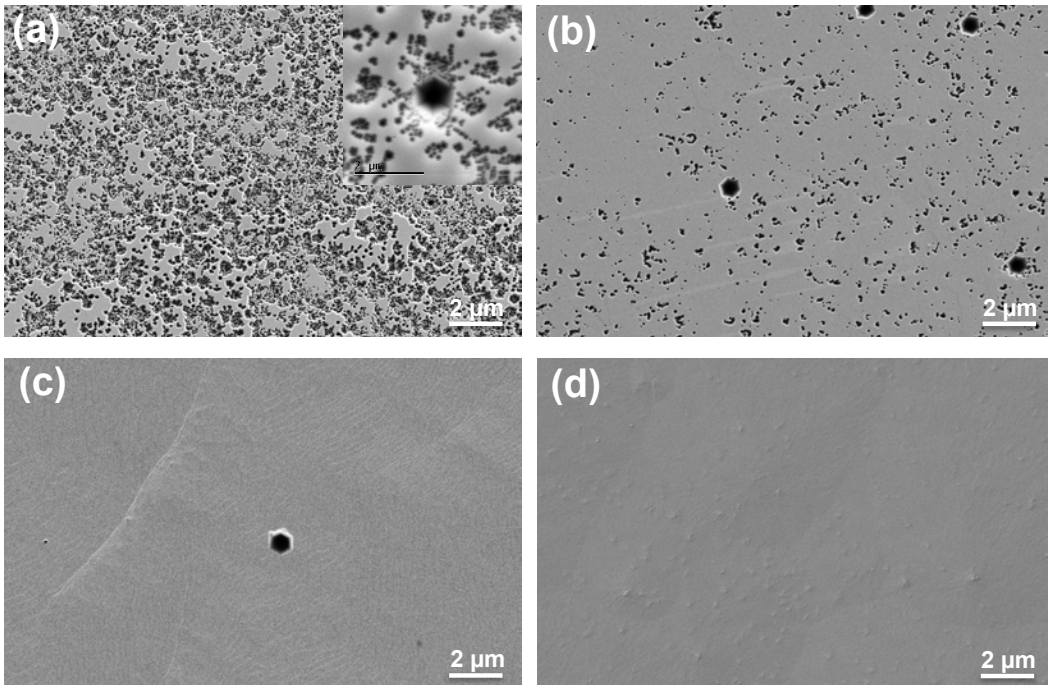

Figure 3.3: SEM image of the top surface of the different InGaN PV structures with p-GaN grown at, (a) 800°C, (b) 850°C, (c) 900°C, (d) 1000°C.

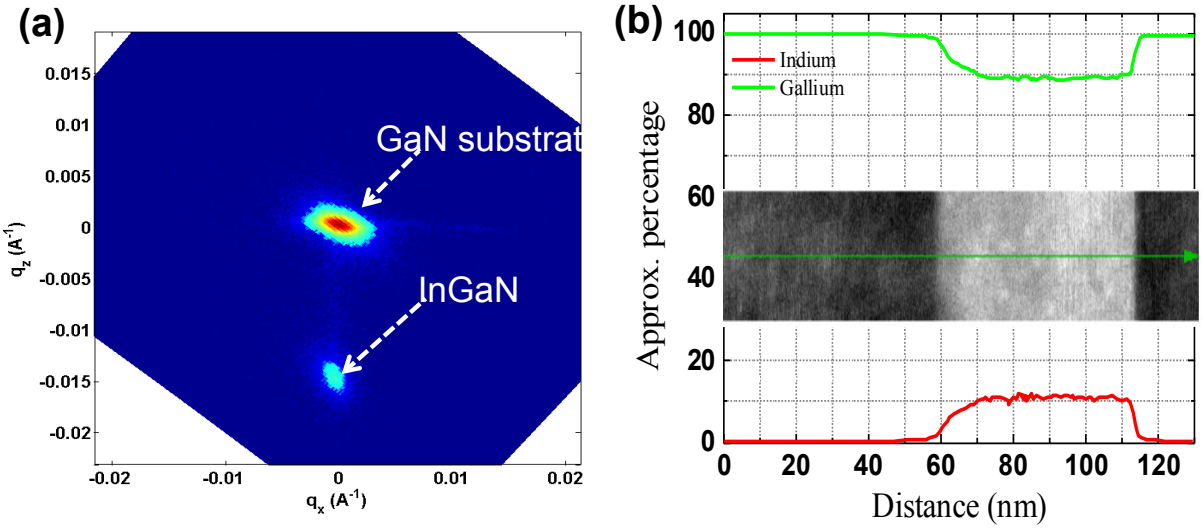

Figure 3.4: (a) (11-24) RSM, indicating GaN substrate diffraction spot and InGaN diffraction spot, (b) EDX measurements showing average In concentration of 12%.

for 5 minutes. In order to eliminate the surface oxides and to improve adhesion of metal contacts to the p-GaN layer, the sample is then cleaned in boiling aqua regia (HCl: HNO_3 = 3:1) for 10 minutes. The metal contacts are finally annealed at 800°C for 1 minute under Nitrogen to form Ohmic contacts. The bottom contacts are Ti/Al/Au. The electrical and micro-structural characteristics of the metal contacts are published in Belahsene *et al.* [137].

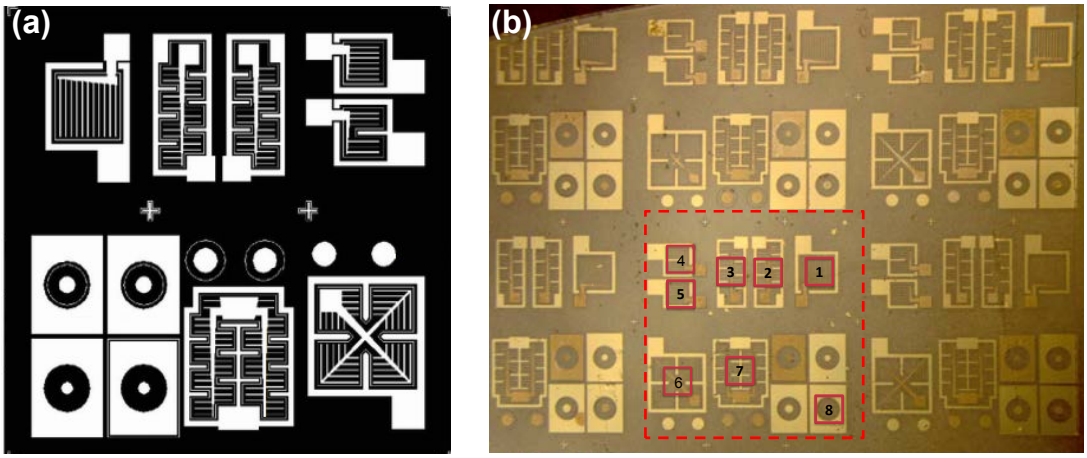

Figure 3.5: (a) The mask used for fabrication of T1185-B, (b) Typical solar cell devices processed on T1185-B.

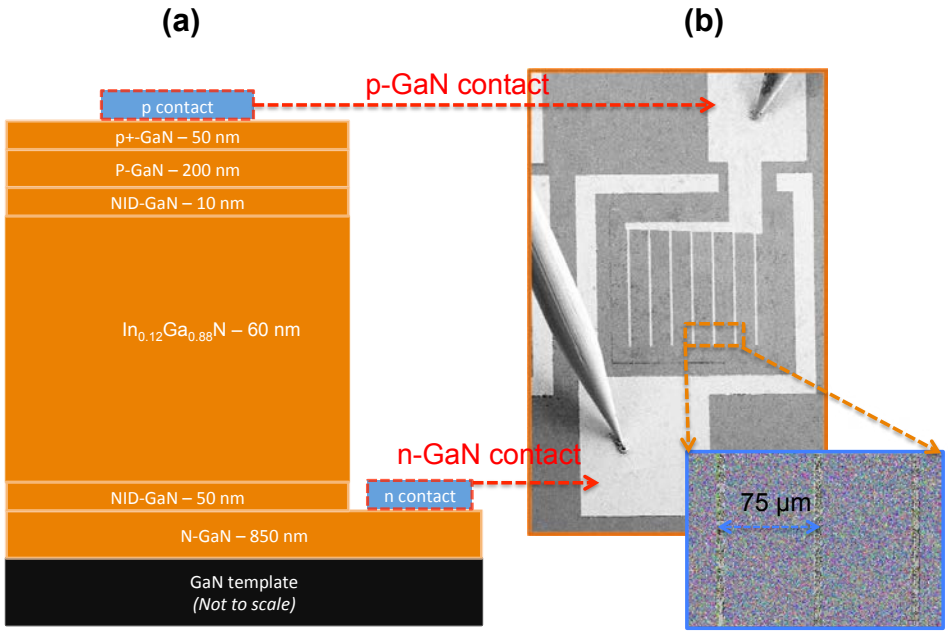

Figure 3.6: (a) Device cross-section of bulk based InGaN PV cell (T1185-B), with corresponding thickness and indium concentration for each layer, (b) SEM image of the device, showing p-GaN and n-GaN contacts, inset shows the adjacent grid spacing of 75 μm.

3.3.1 Characterization

The $J-V$ measurements are performed under both AM 1.5G solar simulator and UV concentrated light. External quantum efficiency (EQE) measurements are performed using a 100 W Xenon arc lamp calibrated with respect to a silicon photodetector. The V-pit and threading dislocation contribution to carrier generation and collection efficiency at micro- and nano-scale are characterized using electron beam induced current (EBIC) measurements in planar geometry.

3.3.2 Electro-Optical Characterization

3.3.2.1 Current-Voltage and EQE Measurements

During the electrical characterization of the devices described in Figure 3.7, we observed a rather large dispersion of their performance under dark and illuminated conditions (UV concentrated light). According to these preliminary measurements, the devices can be sorted into three sets.

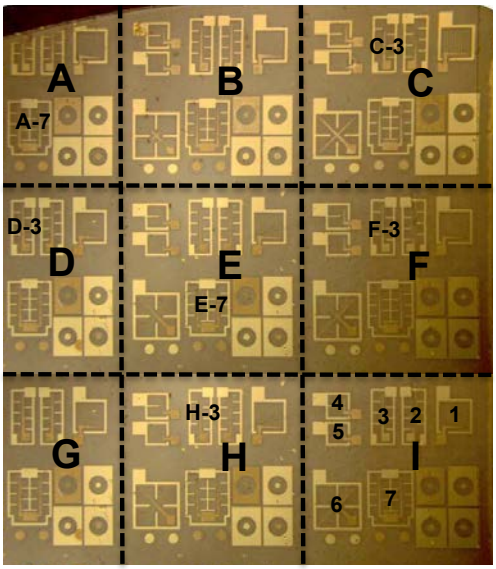

Figure 3.7: Optical image of the T1185-B $In_{0.12}Ga_{0.88}N$ PV structure, indicating the InGaN PV devices in a unit cell and labeled devices used for the $J-V$ and EBIC measurements.

The first set of devices exhibits low values of both J_{sc} (less than 8 mA/cm^2) and V_{oc} (less than 0.25 V). The second one exhibits high values of both J_{sc} (more than 12 mA/cm^2) and V_{oc} (more than 0.4 V). The last set consists of devices exhibiting high values of J_{sc} (more than 12 mA/cm^2) and low value of V_{oc} (less than 0.25 V). A detailed study on why the devices show different performance will be presented in the next section of EBIC measurements. However, the $In_{0.12}Ga_{0.88}N$ PV cell H-3 (Figure 3.7) was chosen for further characterization under AM 1.5G illumination.

Figure 3.8 shows the external quantum efficiency spectrum obtained for the device (labeled H-3 in Figure 3.7, second set) having the best performance in terms of J_{sc} and V_{oc} under UV illumination. Without any bias light, the external quantum efficiency curve has a maximum peak of 42% at a wavelength of 387 nm. This is a rather low value which is not expected since from Figure 3.9 showing the current density - voltage ($J-V$) dependence measured in device H-3 under AM 1.5G solar spectrum, a value of 2.56 mA/cm^2 for J_{sc} can be determined, which is the maximum value ever reported for a PIN heterojunction solar cell, with a 60 nm thick $In_{0.12}Ga_{0.88}N$ absorber layer under 1 sun illumination. Simple calculation shows that to get such a high value of J_{sc}, a peak EQE larger than 90% is required (see dotted curve in Figure 3.8). Since dislocations are known to behave mainly as hole traps in p-type GaN materials [138], we make the assumption that this hole trapping mechanism that takes place within the dislocations and V-pits of the p-GaN layer is responsible for the low external quantum efficiency which is observed. Indeed, this hole trapping mechanism leads to a decrease of the effective p-doping concentration and thus a decrease of the barrier height which in turn decreases the photo-carrier collection and then the photo-current and external quantum efficiency. Nevertheless, this effect could be compensated under illumination. According to a similar mechanism that has been reported for

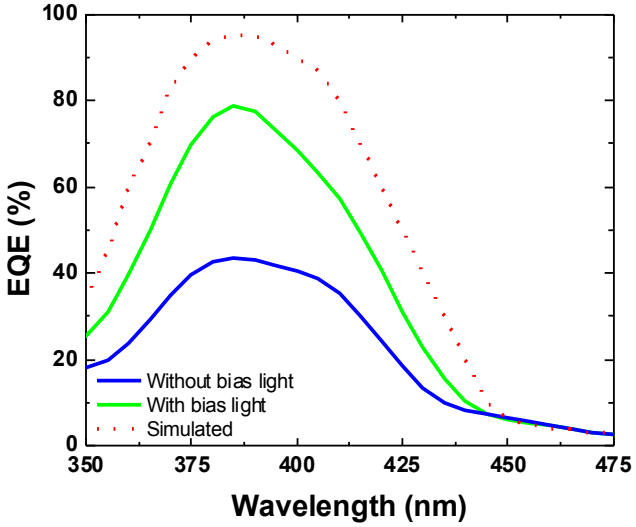

Figure 3.8: External Quantum Efficiency measured with and without bias light.

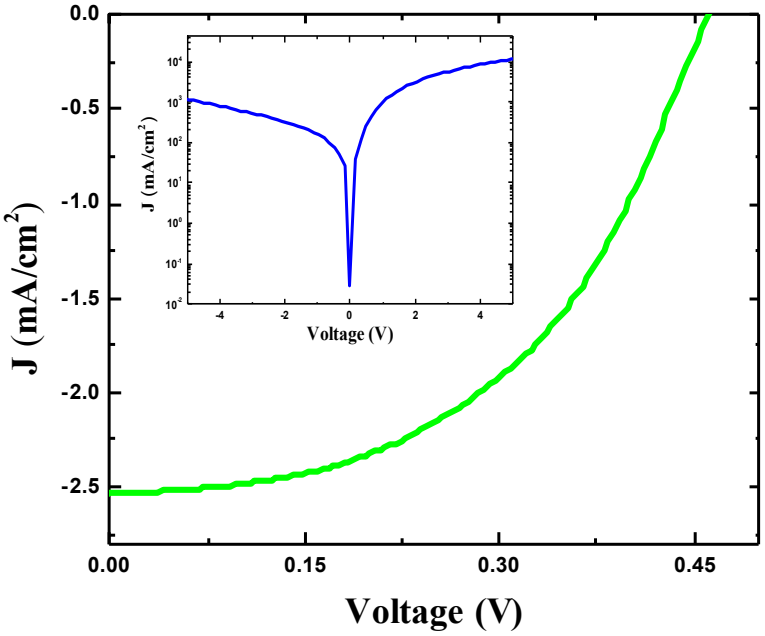

Figure 3.9: Current density - Voltage ($J-V$) measured for the bulk $In_{0.12}Ga_{0.88}N$ PV cell under AM 1.5G solar spectrum, inset shows the dark $J-V$.

CdS/CdTe [139] solar cells, under white bias light illumination, the photo generated holes in the $In_{0.12}Ga_{0.88}N$ layer are transported in the p-GaN layer where they are trapped. This leads to an increase of the positive space charge but without changing the p-doping concentration. Consequently, the depletion width in the $In_{0.12}Ga_{0.88}N$ layer must increase to maintain space charge neutrality, thus enhancing the collection of carriers in the PV cell. This is confirmed by the external quantum efficiency curve recorded under bias light (see Figure 3.8) which shows a large increase of the peak external quantum efficiency up to 79%. To our knowledge, this is one of the maximum external quantum efficiency results reported so far for an InGaN PIN heterojunction solar cell. The power of the bias light that we used is equivalent to around 12%

of the available power of the solar simulator used to measure the J_{sc}. The power distribution spectrum of the bias light used during the external quantum efficiency measurements is presented in Figure 3.10. A further increase of the peak external quantum efficiency could thus be expected

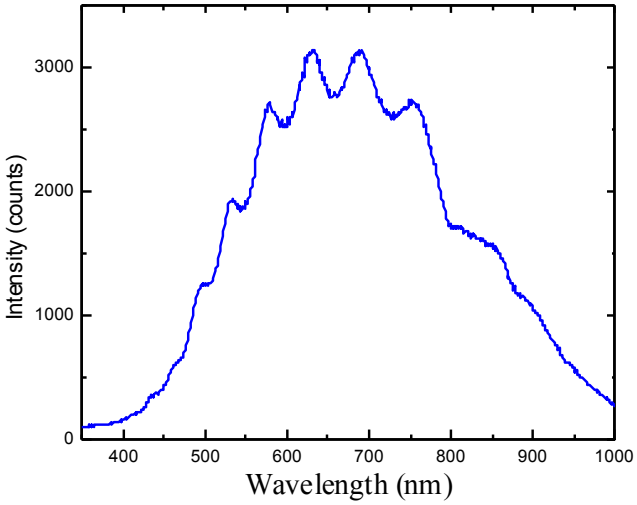

Figure 3.10: Power distribution spectrum of the bias light used during the external quantum efficiency measurements.

if the bias light power is increased. Whatever the bias light conditions, above the wavelength of 387 nm, a sharp decrease down to a wavelength of 440 nm is observed as expected and followed by a second smooth decrease down to a wavelength of 505 nm. The latter probably originates from higher In concentration regions in the partially relaxed InGaN layer. The decrease of the external quantum efficiency below 365 nm is due to photon absorption and charge generation in the p-GaN layer that cannot be collected.

The absence of p-GaN in the deep V-pits (DVP) at the $In_{0.12}Ga_{0.88}N$ interface (see Figure 3.11) should lead to an absence of the depletion region, resulting in carrier recombination without being collected, compared to the SVP. This results in low value of both V_{oc}, derived from the $J-V$ measurement shown in the Figure 3.9, and FF (see Table 3.1) which are much smaller than those reported by Matioli et al. [65] who achieved the best performance $In_{0.12}Ga_{0.88}N$ PV cells with 60 nm absorber thickness.

Table 3.1: Comparison of the performance of the 60 nm thick $In_{0.12}Ga_{0.88}N$ absorber based PV cell with literature (in the work of Matioli *et al.*, the p-GaN layer was grown at 880°C). FF is the fill factor and PCE is the power conversion efficiency.

	V_{oc} (V)	J_{sc} (mA/cm^2)	FF (%)	PCE (%)	Peak EQE (%)
This work	0.48	2.56	40	0.49	79 ; 93*
Literature [65]	1.89	1.06	78.6	1.57	72

* EQE value required to fit with the value of J_{sc} measured under 1 sun illumination.

Depending on the deep and shallow V-pits density ratio in the p-GaN layer over the full wafer surface, large variations of the performance from one device to another could be expected. For a given device, if the proportion of deep V-pits density is larger, then the values of J_{sc} and V_{oc} are expected to be low. This corresponds to devices of set #1 as discussed above. On the contrary, if the ratio is in favor of the shallow V-pits density, a high value of both J_{sc} and V_{oc} is expected. This corresponds to devices of the set #2. There remains devices of set #3 that

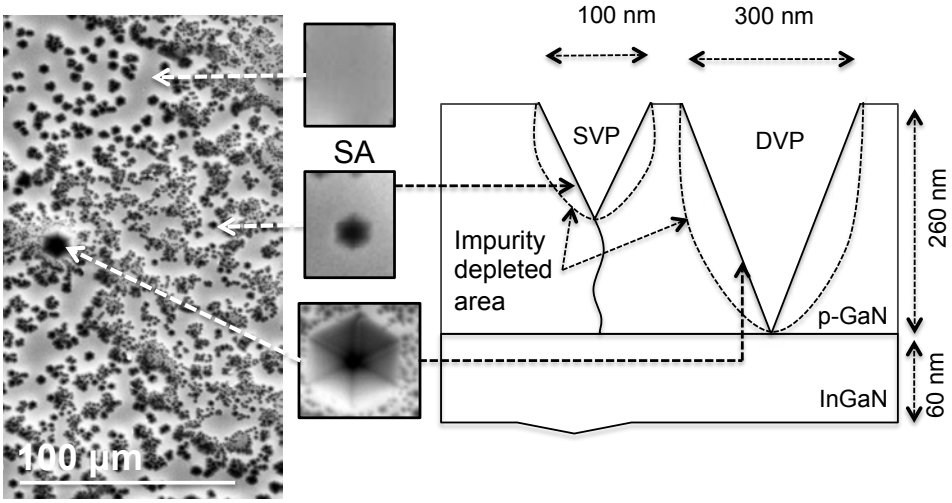

Figure 3.11: Scheme of the deep and shallow V-pits observed in the p-GaN layer of the PV devices. V-pits with opening larger than 300 nm extend down to the InGaN layer.

cannot be explained by the deep and shallow V-pit model. Indeed, a high value of J_{sc} (due to a ratio which is in favor of the shallow V-pits density) seems to not be compatible with a low value of V_{oc} (due to a ratio which is in favor of the deep V-pits density).

To further investigate this point, we carried out an in-depth EBIC analysis of 5 selected devices representative of each of the three sets of devices #1 (devices A_7 and D_3), #2 (device F_3) and #3 (devices E_7 and C_3) as discussed above. EBIC with its high spatial resolution, down to the sub-micron level, allows accurate characterization of the generated current within and around the two different types of V-pits. Correlations of EBIC results with device characteristics should allow full interpretation of the role of these defect in the performance of the devices.

3.3.2.2 Electron Beam Induced Current Measurements

The dislocation-impurity interaction, determined by the strain field around a particular defect, is very important in understanding the origin of dislocation electrical properties. Since the nature of the extended defects varies, therefore it causes a spatial non-uniform impurity distribution around the defects, leading to local inhomogeneities in the electrical properties of the material around different types of dislocations as well as in the dislocation core region [140]. The conventional characterization techniques are not enough to understand the recombination properties of the individual dislocations. However, EBIC with its high spatial resolution, down to sub-micron level with high accuracy, is a powerful tool for visualization and characterization of electrically active defects in semiconductors [141]. For physics and principle of EBIC technique, the reader is referred to Appendix E.

Figure 3.12(a)–(d) shows the SEM and the corresponding EBIC image of the InGaN PV cell in planar geometry obtained at a beam energy of 13 keV. According to the monte carlo simulations, this e-beam energy was enough to reach a depth of more then 320 nm. The large scale EBIC mapping shown in Figure 3.12(b) exhibits dark area corresponding to the metal contacts that avoid any carrier generation due the full absorption of the electron beam. Also a rather in-homogeneous bright area can be seen, indicating a rather in-homogeneous carrier collection through the full device. The tiny grey contrast regions can be attributed to a presence of non-radiative recombination and charge trapping, generally associated with extended defects as observed in Figure 3.2(a). Though there are also some dark spots observed as shown in Figure 3.12(c)–(d), which are due to some residual left over at the surface during the device processing and therefore cannot be linked to the presence of defects.

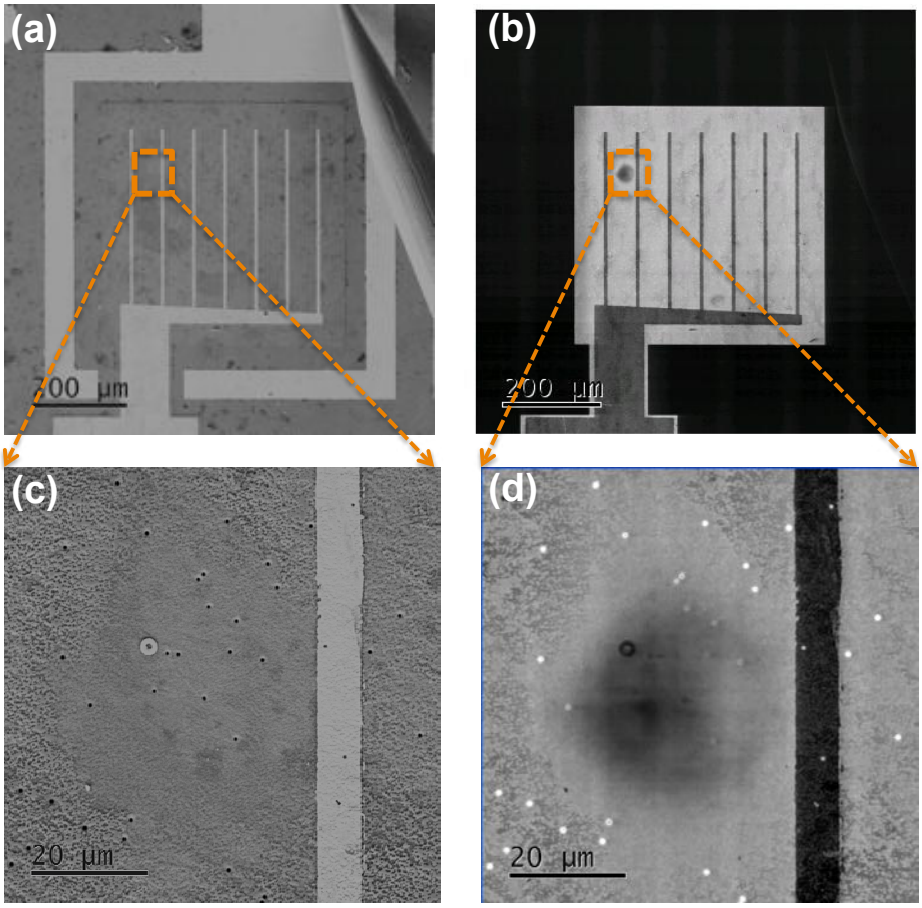

Figure 3.12: (a). SEM image of the device at 13keV (b). EBIC image of the device in the planar geometry at 13keV. (c)–(d) SEM image of some residual left over at the surface during the device processing.

Figure 3.13(a)–(d) shows the high magnification SEM and its corresponding EBIC images obtained at an e-beam of 13keV. Figures 3.13(c)–(d) show a magnification of both the SEM and EBIC image(Figure 3.13(a)–(d)), respectively. At this scale, it is clear that the non-homogeneous carrier collection matches perfectly with V-pit spatial distribution and size in the p-GaN layer. Smooth areas without any pits (SA) are less bright than areas containing small and thus shallow V-pits (SVP), which is, in turn, darker than areas containing large and thus deep V-pits (DVP). This is in opposite to what can be expected since, as discussed previously, the hole trapping process occurring in the pits should lead to a larger decrease of the carrier collection efficiency in the DVP areas than in the SVP areas and, furthermore than in SA areas.

The EBIC image in Figure 3.13(b) show that under zero bias conditions the DVP appear as bright spots. When further magnified, the SVP appear as bright spots shown in Figure 3.13(d). This apparent contradiction could be explained by the formation of impurity depleted zones in the surroundings of V-pits [140, 142, 143] (see Figure 3.11). The capturing of the impurities depends on the strain field of the dislocation. Since the different dislocations in GaN (screw, edge and mixed) have different strain field, therefore distinct behavior for the dislocation-impurity interaction can be expected. For instance, the distance at which the impurity atoms are captured by dislocations is significantly larger for screw type dislocations than for edge type dislocations [144]. The *impurity gettering effect* thus has a significant dependence on the size and density of the V-pits. The DVP at high magnification shows that the bright spots have bright halos with dark spots inside, as shown in Figure 3.14, consistent with previous findings in silicon carbide *p-n* diodes [145]. However, the SVP doesn't show any dark spots at the center,

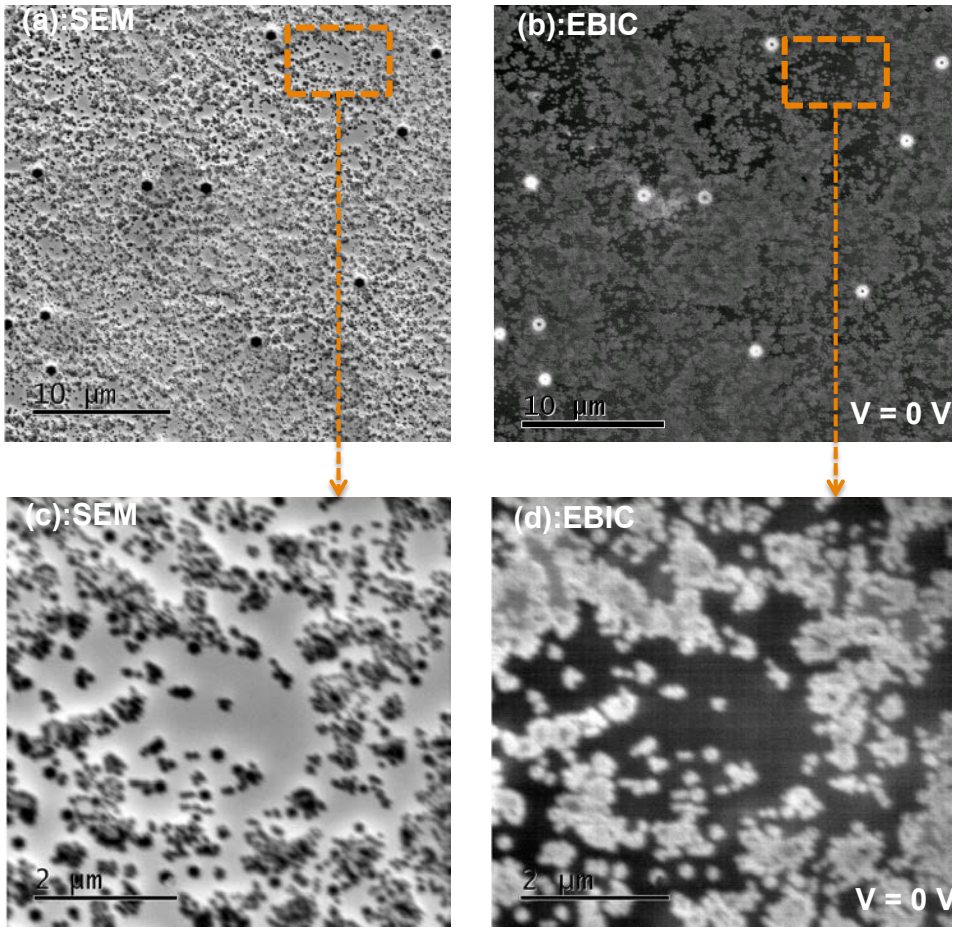

Figure 3.13: (a) SEM image of the p-GaN surface of InGaN PV cell at 13keV showing a high density of V-pits, (b) EBIC image of the InGaN PV cell in planar geometry at 13keV under zero bias (0V), (c) High resolution SEM image of the p-GaN surface of InGaN PV cell at 13keV, (d) High resolution EBIC image of the InGaN PV cell showing the V-pits as bright spots obtained at 13keV under no bias (0 V).

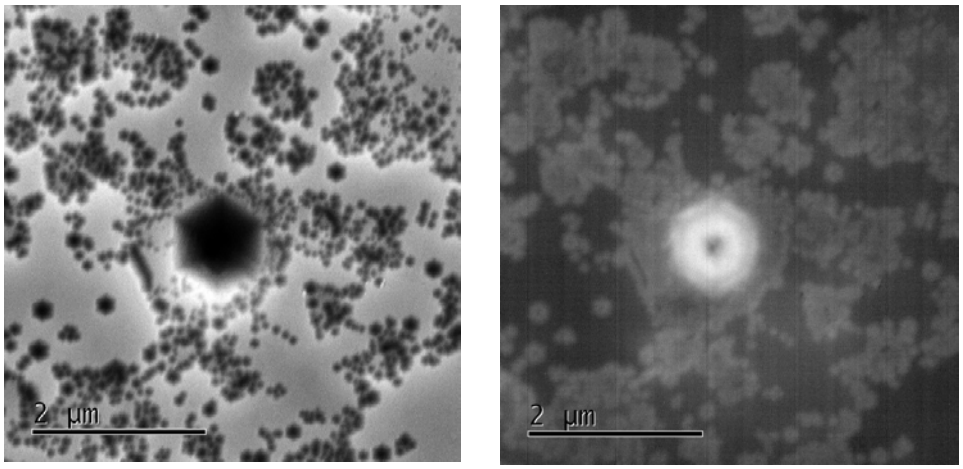

Figure 3.14: (a). High magnification SEM and EBIC image of the type A region of the InGaN PV device obtained at device at 13 keV showing two distinct contrast regions.

or its well beyond the sensitivity limit of the EBIC resolution.

Figure 3.15(a)–(b) shows the SEM and EBIC image of the InGaN PV cell obtained at 13keV under reverse bias (-1V). The EBIC current contrast of the DVP has significantly changed, while

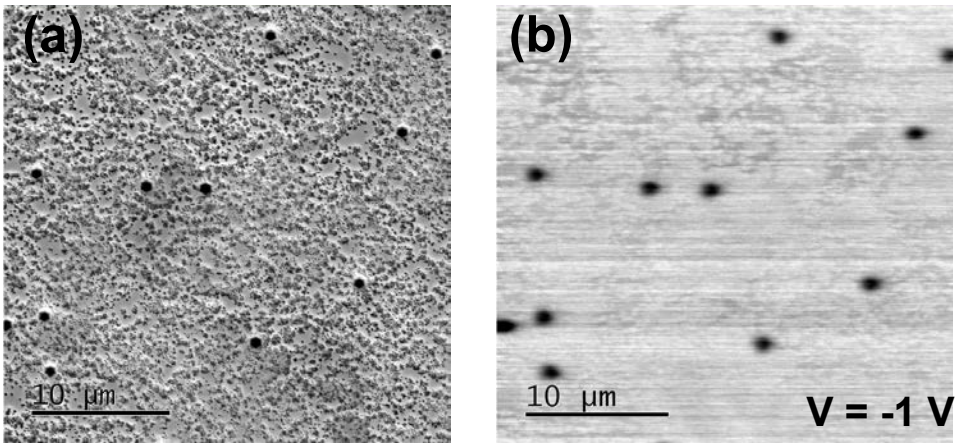

Figure 3.15: (a) SEM image of the p-GaN surface of PV cell at 13keV showing a high density of V-pits, (b) EBIC image of the PV cell in planar geometry at 13keV under reverse bias (-1V), showing the dislocations as dark spots.

the SVP remained the same. This is consistent with the observation of Maximenki *et al.* [140]. They used the change in EBIC contrast at zero bias and reverse bias (-1 V) to distinguish the type of electrically active defects in the device. They reported [140] that those V-pits that show a change in EBIC contrast under reverse bias are associated to the mixed dislocations and those (V-pits) that do not change are associated to the closed core screw dislocations.

Figure 3.16(a)–(f) show the SEM and EBIC line profile of the DVP and SVP. As expected, the center of the DVP appears fully dark (see Figures 3.16(a),(b)) since the trapping process occurs in the depletion region where the accumulation of positive charge leads to the decrease of the barrier height and more photo carrier recombinations. Under reverse bias (see Figures 3.16(c)), due to the corresponding extension of the depletion region in the p-GaN layer, the dark area increases. As expected too, this is not the case for the SVP (see Figures 3.16(d),(e),(f)) which appears and remains bright whatever the bias voltage. It is to be noticed that, due to the depletion region increase, the SA becomes brighter under reverse bias.

The EBIC images recorded at different scales in all of the six devices have been accurately analyzed. For each device, the DVP (size larger than 300 nm) and SVP (size lower than 300 nm) densities have been carefully determined using a Matlab code and correlated with the corresponding device performance (J_{sc} and V_{oc} measured under UV illumination). Depending on the deep and shallow V-pits density ratio in the p-GaN layer over the full wafer surface, large variations of the performance from one device to another are observed. An assessment of the device performances based on the DVP and SVP is summarized in Table 3.2. As soon as the total pit density is decreased from one device to the another, a lowering of J_{sc} and an increase of V_{oc} are observed. Figure 3.17 shows a strong correlation between the DVP and SVP densities and the performance of the device in terms of J_{sc} and V_{oc}. It can be seen that to increase both J_{sc} and V_{oc} an increase of the SVP density and a decrease of the DVP density are required, while to decrease both J_{sc} and V_{oc} a decrease of the SVP density and an increase of the DVP density are required. Finally, an increase of the SVP density leads to an increase of J_{sc}, while an increase of the DVP density leads to a decrease of V_{oc}. Thus, the rather low V_{oc} observed in all the six devices can be attributed to some current leakage occurring at the DVP/InGaN layer interface and through the internal DVP surface, while the large current density observed in most of the devices could originate from the total impurity depleted volume, and corresponding electric field enhancement, due to DVP and SVP. These observations are consistent with the

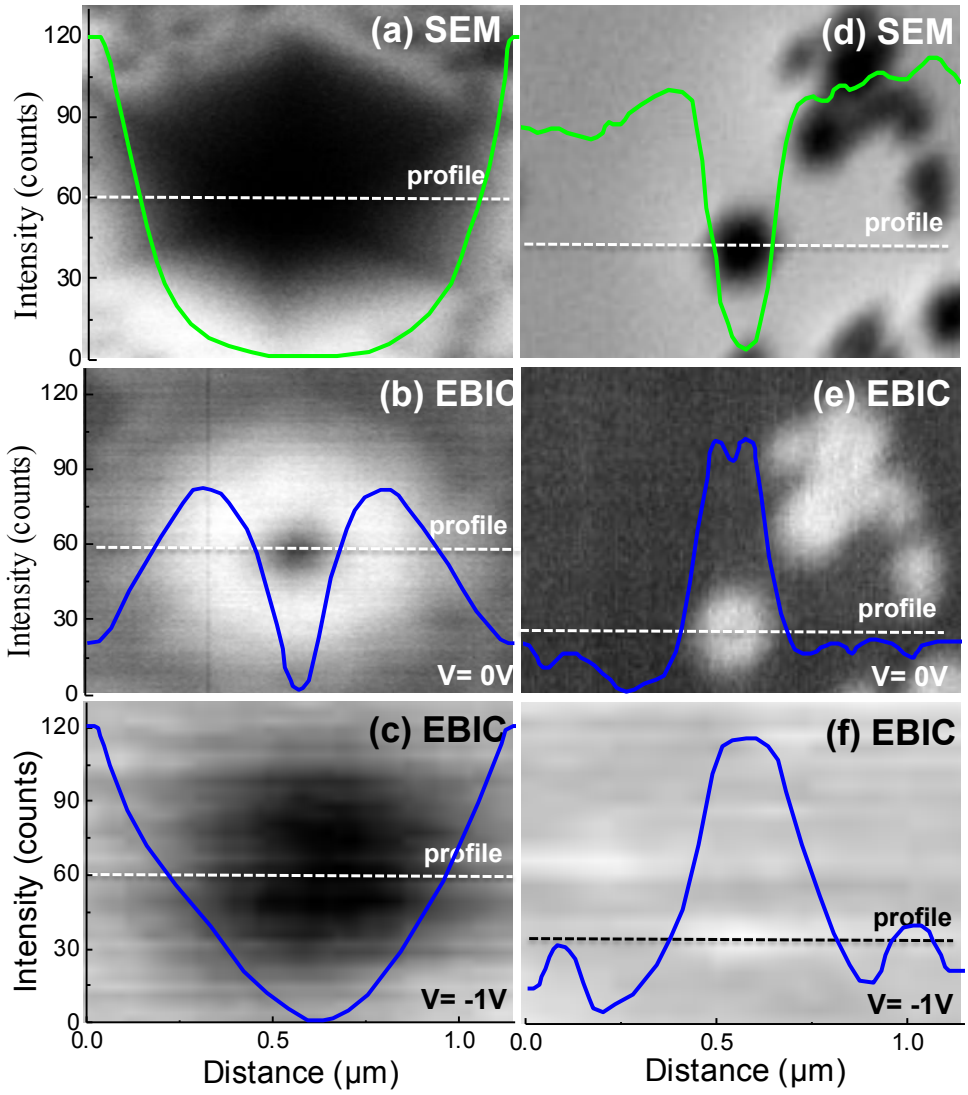

Figure 3.16: (a), (d) SEM images and profiles of both DVP and SVP of the device top surface and their corresponding EBIC images and profiles recorded at (b), (e) 0 V and (c), (f) -1 V, obtained at an e-beam energy of 13keV.

previous analyses. Accordingly, the sets of devices #1, #2, and #3 should comprise devices with p-GaN layer containing a high DVP and low SVP densities, low DVP and high SVP densities, and high DVP and SVP densities, respectively.

3.4 Summary and Perspectives

We have studied, combining results of $J-V$ curves, SEM, HAADF-STEM, and EBIC characterization, the influence of the dislocations and V-pits on the overall conversion efficiency of bulk $In_{0.12}Ga_{0.88}N$ absorber based heterojunction solar cells. Using EBIC, we have shown that the phenomenon of gettering effect, which forms an impurity depleted zone around the threading dislocations and V-pits, significantly contributes to the enhancement of the extraction of the photogenerated carriers in the InGaN absorber, resulting in a peak external quantum efficiency of 79% and a short circuit current density of 2.56 mA/cm^{-2} under an AM 1.5G solar spectrum,

Table 3.2: Performance variation between the five selected devices and their correlation with DVP and SVP densities variation. The green and blue colors indicate an increase or a decrease of the feature, respectively, (The devices are labeled in Figure 3.7).

Device	DVP density (10^5cm^{-2})	SVP density (10^8cm^{-2})	J_{sc} (mA/cm^2)	V_{oc} (V)
A-7 vs E-7	7.6→6.8	2.6 → 9.8	4.40→17.0	0.10→0.20
A-7 vs C-3	7.6→7.8	2.6 → 7.6	4.40→14.4	0.10→0.05
A-7 vs D-3	7.6→6.4	2.6 → 6.4	4.40→13.0	0.10→0.25
A-7 vs F-3	7.6→6.0	2.6 → 5.7	4.40→12.0	0.10→0.35
A-7 vs H-3	7.6→5.5	2.6 → 4.6	4.40→12.5	0.10→0.48
E-7 vs C-3	6.8→7.8	9.8 → 7.6	17.0→14.4	0.20→0.05
E-7 vs D-3	6.8→6.4	9.8 → 6.4	17.0→13.0	0.20→0.25
E-7 vs F-3	6.8→6.0	9.8 → 5.7	17.0→12.0	0.20→0.35
E-7 vs H-3	6.8→5.5	9.8 → 4.6	17.0→12.5	0.20→0.48
C-3 vs D-3	7.8→6.4	7.6 → 6.4	14.4→13.0	0.05→0.25
C-3 vs F-3	7.8→6.0	7.6 → 5.7	14.4→12.0	0.05→0.35
C-3 vs H-3	7.8→5.5	7.6 → 4.6	14.4→12.5	0.05→0.48
D-3 vs F-3	6.4→6.0	6.4 → 5.7	13.0→12.0	0.25→0.35
D-3 vs H-3	6.4→5.5	6.4 → 4.6	13.0→12.5	0.25→0.48

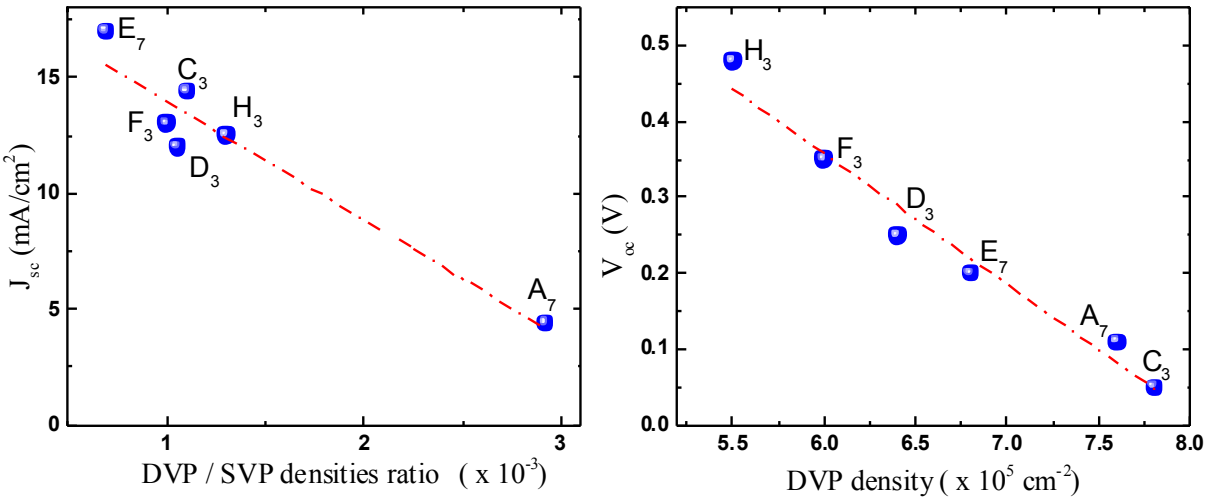

Figure 3.17: J_{sc} and V_{oc} dependence with the ratio of DVP and SVP densities and DVP density, respectively. Measurements were done under ultra-violet (UV) light and recorded in 6 different devices labeled in Figure 3.7.

i.e. a value twice the state of the art. Meanwhile, a high density of deep V-pits leads to large recombinations, resulting in high leakage current, hence reducing the open circuit voltage. Since a low growth temperature for the p-GaN layer, leading to a high dislocation and pit density, is mandatory, a way to favor the formation of shallow against deep V-pits, should help to preserve and perhaps to improve InGaN based PV device performances.

The results for the bulk $In_{0.12}Ga_{0.88}N$ PV cell presented in this chapter have been published in Applied Physics Letters Journal [146].

Chapter 4

InGaN Semibulk PIN Heterojunction Solar Cells

Most bulk InGaN heterojunction solar cells reported in the literature have very low power conversion efficiency, compared to what is expected theoretically. The growth of high quality and thick InGaN layers with high indium needed for high efficiency solar cells is not a trivial task. Issues such as strong phase separation and relaxation of the layer due to lattice mismatch with the substrate, lead to InGaN layers with large dislocation density and indium-clustering. These issues restricts the critical layer thickness of high quality InGaN with high indium concentration, thus limiting the absorption of the incident light. We propose to use semibulk approache that may overcome the issues of phase separation and high dislocation density in the absorber and thus grow InGaN-based PIN solar cells with improved properties. It consists in replacing the conventional bulk absorber by a thick multi-layered InGaN/GaN absorber. The periodical insertion of the thin GaN interlayers should absorb the excess indium and relieve compressive strain. These GaN interlayers need to be thick enough to be effective and thin enough to allow carrier transport through tunneling. The InGaN layers need to be thick and numerous enough to absorb efficiently the incoming light beam, and thin enough to remain fully strained and without phase separation.

4.1 Design of the Solar Cell

Achieving a good PV performance using a semibulk absorber layer is not a trivial task. The critical layer thickness for the InGaN layers as a function of indium composition as discussed in previous chapter, and the thickness of the NID-GaN interlayers were both factors that we had to consider in the solar cell design. The InGaN epitaxial layer needed to be within the critical layer thickness to restrict the growth transition from 2D–3D, also the GaN interlayers needed to be thick enough to absorb/desorb the excess indium that promotes InGaN relaxation. However, the GaN interlayers also provide a barrier to electronic carriers and must be made thin enough so that tunneling through them can occur [147]. For the device design of the semibulk structure, the InGaN absorber thickness is targeted to be 150 nm, while the rest of the layers including the p-type GaN and n-type GaN were kept the same, as shown by the schematic in Figure 4.1. To ensure the same amount of light absorption during the device design simulations, the thickness of bulk InGaN absorber is kept at 150 nm regardless of indium concentration. However, as we have seen in previous chapter, the growth of high quality 150 nm thick bulk InGaN absorber with indium concentration exceeding 12% is very challenging. The InGaN critical layer thickness for the semibulk InGaN PV structure on GaN templates is calculated according to the study by our team Orsal *et al.* [38] as discussed in previous chapter. The InGaN critical layer thickness results are reproduced in Table 4.1 and indicate that the critical layer thickness decreases significantly

for InGaN epilayer with a high indium concentration.

Table 4.1: InGaN epilayer critical layer thickness used in the model of the device design for semi-bulk InGaN PV structure.

InGaN (nm)	Number of periods	Indium concentration (%)
75	2	5
30	5	10
21.4	7	15
15	10	20
12.5	12	25

To assess the device design, simulations are carried out for the two InGaN PV structure shown by the schematic in Figure 4.1, using the Silvaco simulations software. These simulations are performed in collaboration with our partner laboratory Geeps (France). Each PV structure

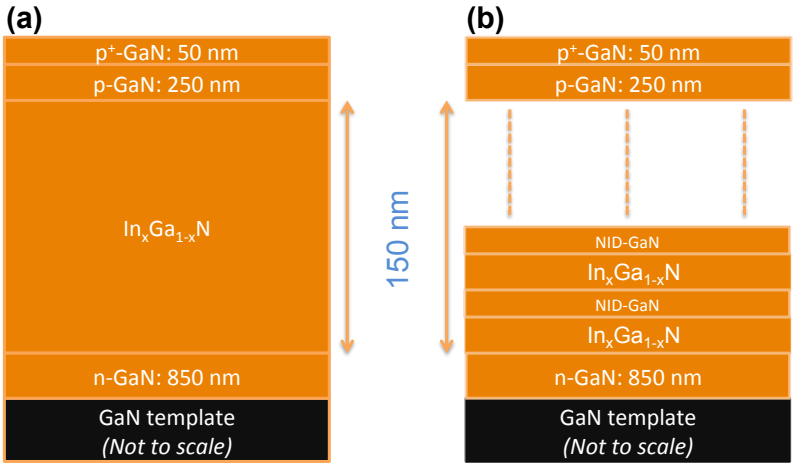

Figure 4.1: Scehmatic of the, (a) Bulk and, (b) Semibulk, InGaN PIN hetero-junction solar cell structures.

has identical doping concentrations, and thicknesses. The doping concentrations for p^+GaN, p-GaN and n-GaN used during the simulations are 3×10^{17} cm^{-3}, 1×10^{17} cm^{-3} and 5×10^{18} cm^{-3} as determined by the Hall effect measurements. The NID-GaN doping is measured to be 3×10^{16} cm^{-3}. The physical parameters required for the modeling of InGaN are widely available and were obtained from the previous studies [148, 149]. The model included doping concentration dependent mobilities based on the Caughey-Thomas model [149]. Both radiative and non-radiative recombination models are included in the model.

The effective masses for the InGaN alloy are obtained by linear interpolation between the effective masses for InN and GaN.

$$m_{e,h}^{InGaN} = x.m_{e,h}^{GaN} + (1-x)m_{e,h}^{InN} \tag{4.1}$$

where, e represents the electron, h represents the hole and where x is the indium concentration.

The bandgap for $In_xGa_{1-x}N$ is calculated by Vegard's law, given as;

$$E_g^{InGaN} = x.E_g^{InN} + (1-x)E_g^{GaN} - b.x(1-x) \tag{4.2}$$

where x is the indium composition and b is the bowing parameter [38].

The absorption coefficient (α) of InGaN is calculated as a function of the bandgap energy and indium composition, as given by [150];

$$\alpha(cm^{-1} = \sqrt[10^5]{a.(E - E_g + b.(E - E_g)^2} \tag{4.3}$$

where a and b are fitting parameters, while E and E_g are photon energy and energy bandgap of the InGaN material.

Fig. 4.2 shows the simulated dependence of the power conversion efficiency versus the concentration of indium for both bulk and semibulk structures with 150 nm total InGaN thickness and varying GaN interlayer thicknesses. The GaN interlayer thickness does not significantly

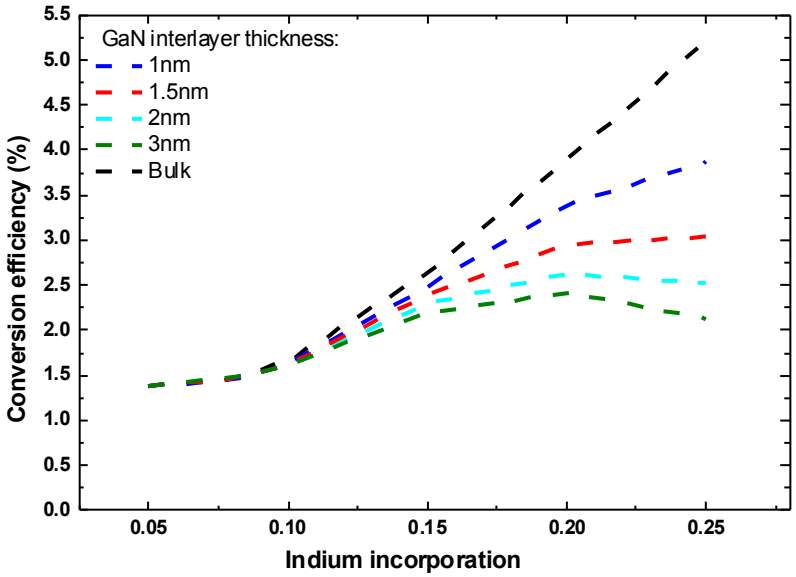

Figure 4.2: Simualted power conversion efficiency dependence on indium incorporation for bulk and semibulk structures with different NID-GaN interlayer thicknesses for semibulk InGaN PV structure.

affect the conversion efficiency for indium concentrations $< 10\%$. This is because for indium concentration $< 10\%$, the current transport is dominated by thermionic emission (Appendix D for further details).

At high indium concentrations ($> 10\%$), the barrier height increases leading to current transport via tunneling. However, the tunneling current is also affected by the barrier height, for instance at high indium concentrations, the tunneling current decreases even for the same barrier thickness (see Figure 4.2). The increase in the thickness of GaN interlayers further causes difficulty in tunneling of carriers, resulting in the reduction of the power conversion efficiency. Based on the results shown in Figure 4.2, we choose the GaN interlayer thickness 2 nm, because achieving 1 nm thick GaN interlayer using MOCVD is challenging.

The optimized InGaN PV structures designed by the simulations are shown in Figure 4.3. These structures would afterwards be referred as T1158-SB for 8% with p-GaN grown at 1000/*degree*C, T1185-SB and T1188-SB for 12% indium concentration with p-GaN grown at 850°C and 800°C respectively. The 50 nm GaN layer between InGaN and n-GaN is used to stop the diffusion of the silicon into the InGaN absorber as discussed earlier. A GaN cap layer between p-GaN and InGaN is used to stop the magnesium diffusion into absorber and to avoid any InGaN degradation during the subsequent top p-GaN layer as observed in previous chapter. Liang *et al.* [23] reported that the presence of low temperature-GaN interlayer between the p-GaN and InGaN absorber, protects the InGaN layer from unfavorable effects such as lattice relaxation and composition redistribution which occur at high p-GaN growth temperature. It

also prevents indium evaporation from the InGaN absorber during the high growth temperature of the p-GaN layer and hampers the propagation of threading dislocations from InGaN into p-GaN, leading to a reduction in the dislocation density in the p-GaN [130]. The GaN cap layer for 8% indium concentration semibulk structure (T1158-SB) is increased to 50 nm because we choose to increase the p-GaN growth temperature to 1000°C compared to the 850°C and 800°C for 12% T1185-SB and T1188-SB (see Figure 4.3). The semibulk InGaN PV structures shown in Figure 4.3 are grown on 3.5 μm thick GaN/sapphire templates using MOCVD.

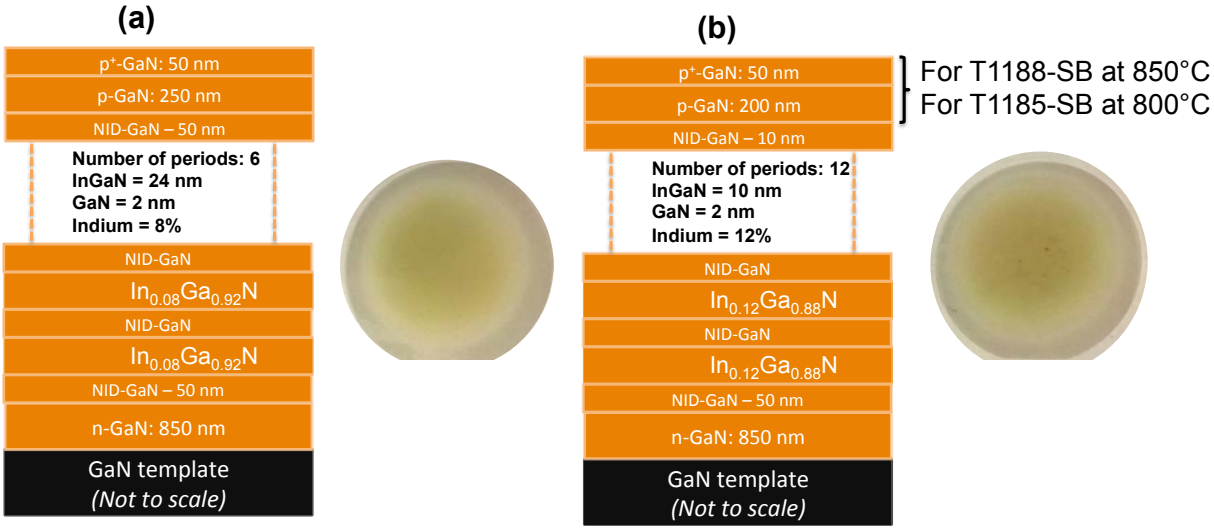

Figure 4.3: Semibulk InGaN PIN PV structures grown with indium concentrations of, (a) 8% (T1158-SB) with p-GaN grown at 1000°C, (b) 12% of indium T1185-SB and T1188-SB with p-GaN grown at 800°C and 850°C respectively.

4.2 Device Processing

The mask used for fabrication and device processing of semibulk InGaN solar cells is discussed in the previous chapter. These devices are processed in collaboration with our partner laboratory, CNRS /LPN : Laboratoire de Photonique et de Nanostructures (France). The fabricated solar cell device with area rangeing from 0.35 mm^2 to 1.27 mm^2 for T1158-SB, T1185-SB and T1188-SB are shown in Figure 4.4. Due to the issues of the p-GaN surface morphology and metal adhesion, the device processing for T1185-SB and T1188-SB remained challenging. That should affect the performance of these devices as well. Figure 4.5(a)–(b) show the cross section of the structure and the top view of the device respectively.

4.3 Characterization

The surface morphology was observed using scanning electron microscopy (SEM). The indium content, degree of relaxation and lattice parameters (a, c) are determined using symmetric (0002) $\omega - 2\theta$ scans in combination with X-ray reciprocal space maps (RSMs) of the asymmetric (11-24) planes using Panalytical X-Pert Pro diffractometer XRD. Micro-structural and micro-compositional studies were carried out through high-angle, annular dark field scanning transmissions electron microscopy (HAADF-STEM) and energy dispersive X-ray spectroscopy (EDX). The images were taken along $< 1\ 1\ \bar{2}\ 0 >$ zone axis. Homogeneity of the epitaxial layer was studied using electron beam induced current (EBIC) measurements, in planar geometry.

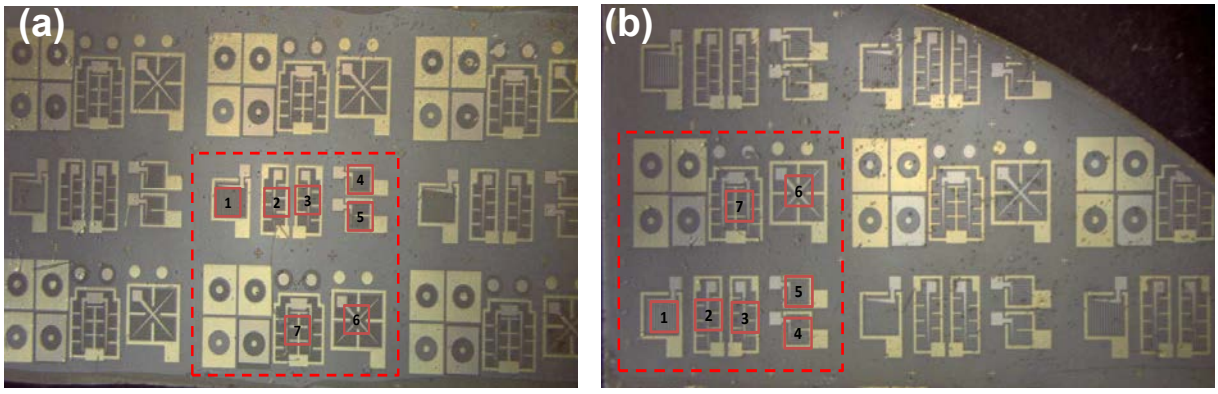

Figure 4.4: Typical solar cell devices processed on semibulk InGaN PV structures, (a) T1158-SB and (b) T1185-SB and T1188-SB.

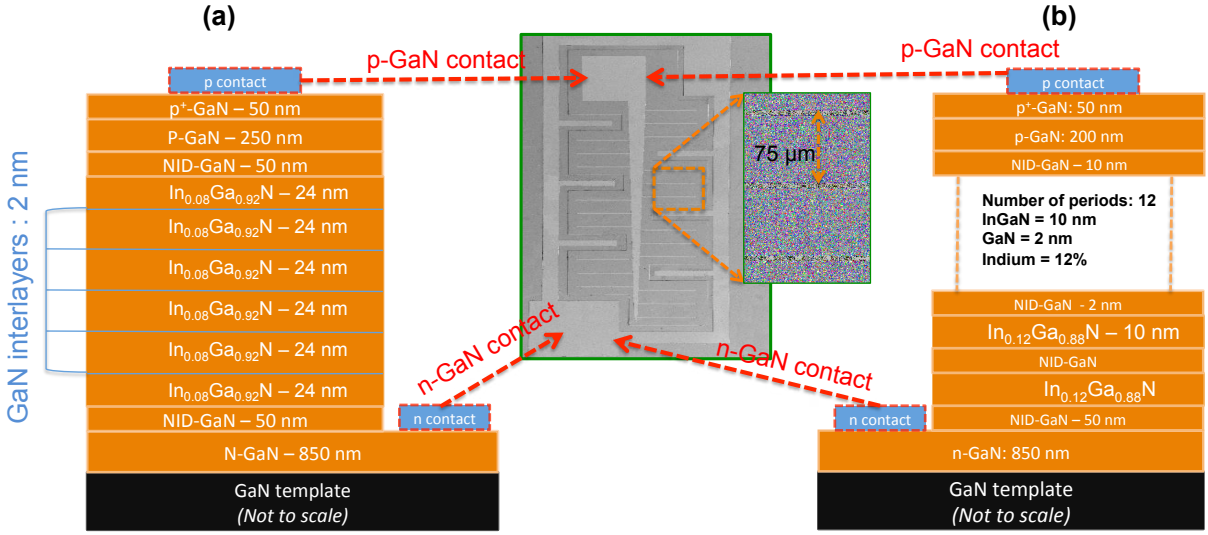

Figure 4.5: (a) Device cross-section of semibulk based InGaN PV cell, (a) T1158-SB and (b) T1185-SB and T1188-SB, inset show the scanning electron microscopy (SEM) image of the device, showing p-GaN, n-GaN contacts and the adjacent grid spacing of 75 μm.

The external quantum efficiency measurements were performed using a system equipped with 100 W Xenon arc lamp monochromator and using a calibration with a silicon photo-detector. The $J-V$ measurements were performed under standard AM 1.5G solar simulator and concentrated light.

4.4 Semibulk $In_{0.08}Ga_{0.92}N$ Solar Cell

4.4.1 Structural and Morphological Study

Figure 4.6(a) shows the (11-24) reciprocal space maps of the sample. The diffraction spot is intense and lies on the vertical line, indicating that $In_{0.08}Ga_{0.92}N$ layer is mostly coherently strained to GaN template. The extracted value for degree of relaxation is around 17% with an average indium content of around 7.8%. The ω - 2 θ rocking curve scan in Figure 4.6(b) show several orders of diffraction satellites which fit well with $\sim$ 24 nm thick $In_{0.08}Ga_{0.92}N$ layers. Energy dispersive X-ray spectroscopy measurements are also performed for direct measurement

of chemical composition, showing an average indium concentration of around 8% in the InGaN interlayers.

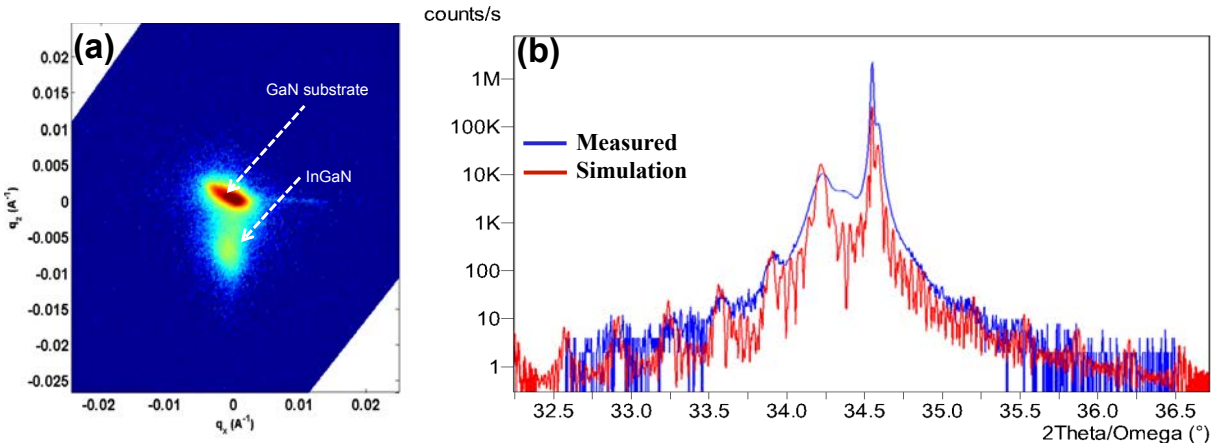

Figure 4.6: (a) (11-24) reciprocal space mapping scan for the semibulk sample, showing GaN substrate and InGaN diffraction spot, (b) ω - 2 θ rocking curve scan for the semibulk sample, showing several orders of diffraction satellites, fitted well with simulations for 24 nm of InGaN layer thickness.

Figure 4.7 shows the surface morphology of the p-GaN layer, revealing a smooth surface as expected due to the high (1000°C) growth temperature as discussed in the previous chapter.

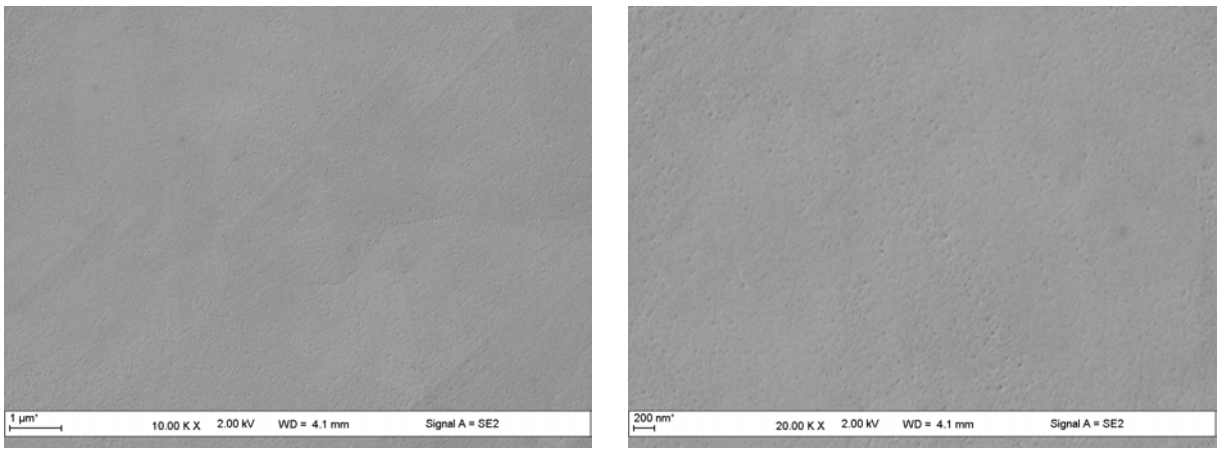

Figure 4.7: SEM image of the surface morphology of top surface (p-GaN layer).

The HAADF-STEM cross-sectional images of the $In_{0.08}Ga_{0.92}N$ PV structure are shown in Figure 4.8. The large scale STEM image (see Figure 4.8(a)) shows a flat p-GaN surface consistent to our results presented in the previous chapter. The zoom of the STEM image in Figure 4.8(b) shows a high density of threading dislocations generated at the p-GaN/InGaN interface. A possible reason for these threading dislocations is the relaxation of the top InGaN layer due to accumulation of indium. There are also threading dislocations propagating from the template as shown in Figure 4.8(c). This type of threading dislocations contributes to V-pits, in the InGaN absorber. The size of these V-pits varies between 50 nm – 1 μm. The depth of deep V-pits varies, some of them start at the first (bottom) InGaN layer and propagates until the top InGaN layer, while some of them are located only in the top InGaN layers. According to these HAADF-STEM images, the V-pits are inside the semibulk absorber filled during the p-GaN growth. These two regions (Figure 4.8(b)–(c)) should lead to degradation of the PV

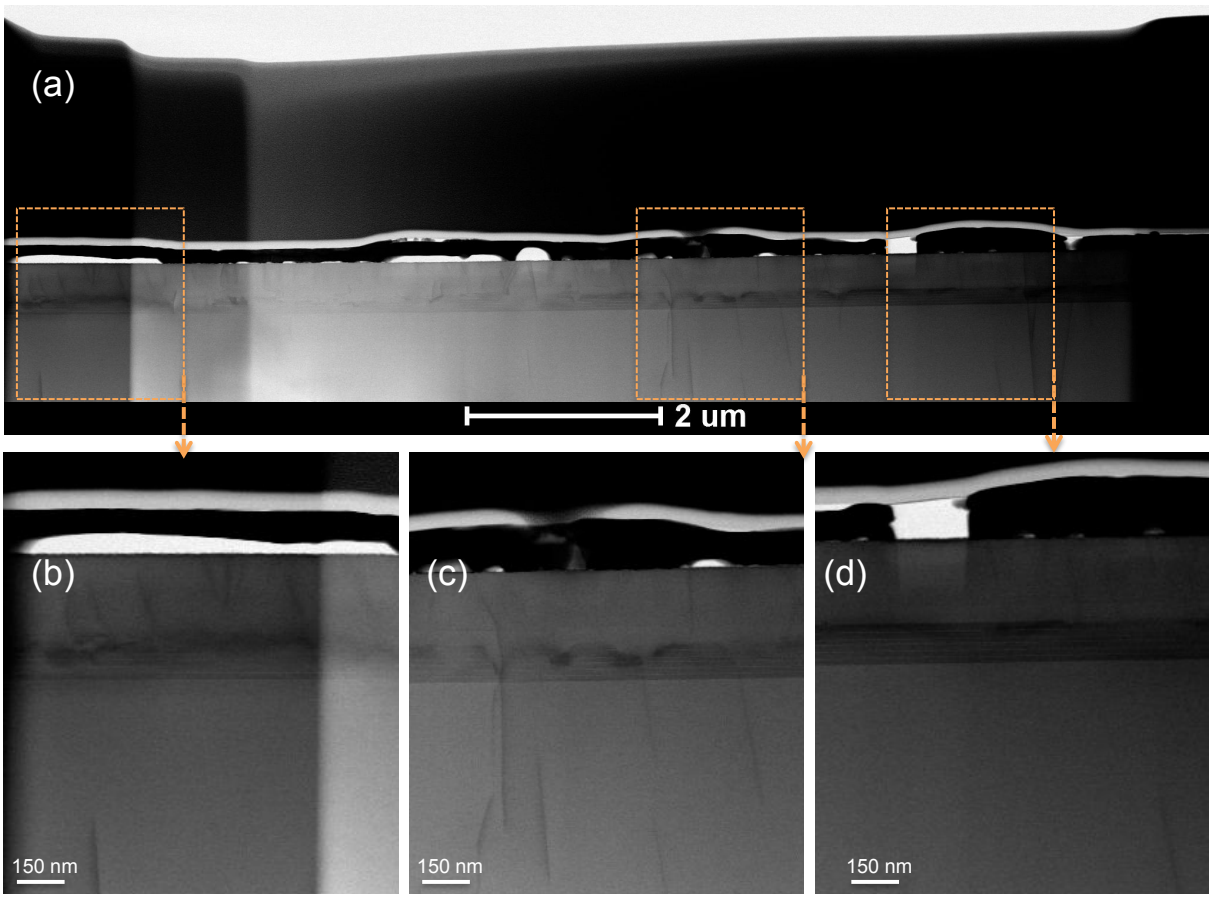

Figure 4.8: HAADF-STEM images along the $< 1\ 1\ \bar{2}\ 0 >$ zone axis; (a) semibulk sample before p-GaN growth, (b) semibulk sample after p-GaN growth, only the top $In_{0.08}Ga_{0.92}N$ layer is shown degraded during p-GaN growth.

device performance. However, the PV device on top of the region shown in Figure 4.8(b) should perform better then the region shown in Figure 4.8(c). Figure 4.8(d) shows a a high crystalline quality region with no threading dislocations and/or InGaN relaxation. PV devices on top of this region should lead to high power conversion efficiency, due to high J_{sc} and V_{oc}. In the light of these results, we expect in-homogeneity in the power conversion efficiency of the PV devices.

4.4.2 Electro-Optical Characterization

4.4.2.1 Electron Beam Induced Current Measurements

The EBIC image contrast is an e-beam function, due to the variation in the penetration depth of the e-beam, as shown in Figure 4.9. At lower beam energy, the injected carriers cannot reach the depletion region and most of the carriers are generated in the p-GaN layer that cannot be collected leading to a dark EBIC signal. The EBIC signal obtained for low beam energy is at the mesa (border) associated to the surface current. As the beam energy increases, the injected electrons reaches the depletion region where the generated electron-hole are then drifted by the built-in electric field yielding a higher value for the EBIC signal. The in-homogeneity (see Figure 4.9) is attributed to the V-pits (see Figure 4.8(c)). These results show that the EBIC signal doesn't change with any further increase of the e-beam, leading to an optimum value of 15KeV for the e-beam.

Figure 4.10(a)-(d) shows the SEM images of the device and their corresponding EBIC images,

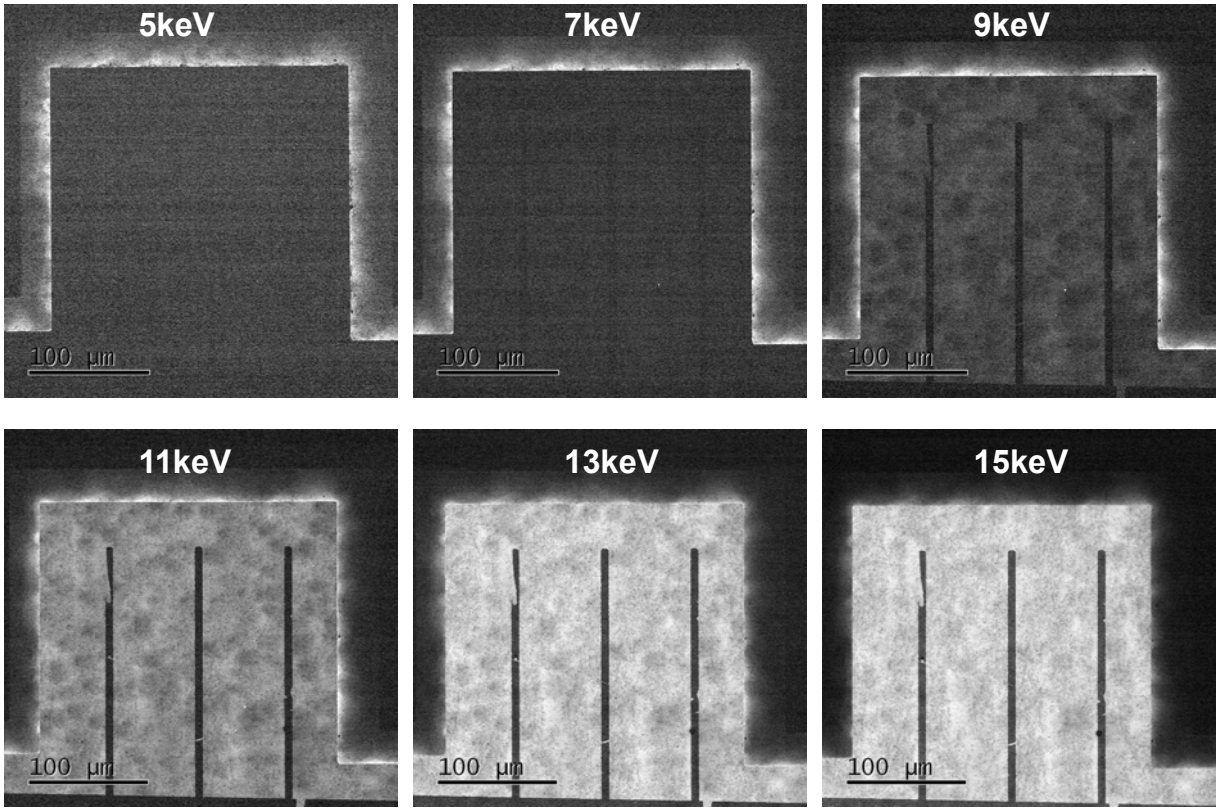

Figure 4.9: EBIC images in the planar geometry of the T1158-SB semibulk $In_{0/08}Ga_{0.92}N$ PV device with varying e-beam energy.

obtained at a beam energy of 15 keV. The large scale EBIC signal mapping shown in Figure 4.10(b) exhibits a homogeneous contrast, indicating a mostly homogeneous active region through the full device. However, a high resolution EBIC image shown in Figure 4.10(d) reveals some contrast variations which can be attributed to a slightly stronger presence of non-radiative recombination and charge trapping, generally associated with extended defects such as the nano-pits observed in Figure 4.8.

At high magnification, we observe a large in-homogeneity in the EBIC contrast as shown in Figure 4.11. Three regions can be distinguished in the EBIC signal (see Figure 4.11(c)–(d)), (i) average EBIC signal with gray region, (ii) No EBIC signal with dark region and (iii) high EBIC signal with bright region. The EBIC signal with average intensity is attributed to the region with threading dislocations in the p-GaN layer only (see Figure 4.8(b)). The dark region with no EBIC signal is attributed to the degraded semibulk InGaN with a high density of V-pits inside the absorber (see Figure 4.8(c)). The carriers generated by e-beam in this region recombines before they are collected resulting in no EBIC signal. The third region with high EBIC signal is attributed to the high crystalline quality material with no threading dislocations and/or V-pits (see Figure 4.8(d)).

4.4.2.2 External Quantum Efficiency Measurements

Figure 4.12 shows a typical external quantum efficiency (EQE)measurement. As expected, we observe a variation in the performance of the PV devices located at different regions of the wafer. It is to be noticed that more than 85% of the fabricated devices show high external quantum efficiency (85%). Some of the devices show slightly poor performance varying the external quantum efficiency between 40–85%. This means that most of the PV devices are located on the region with high crystalline quality material (see Figure 4.8(d)).

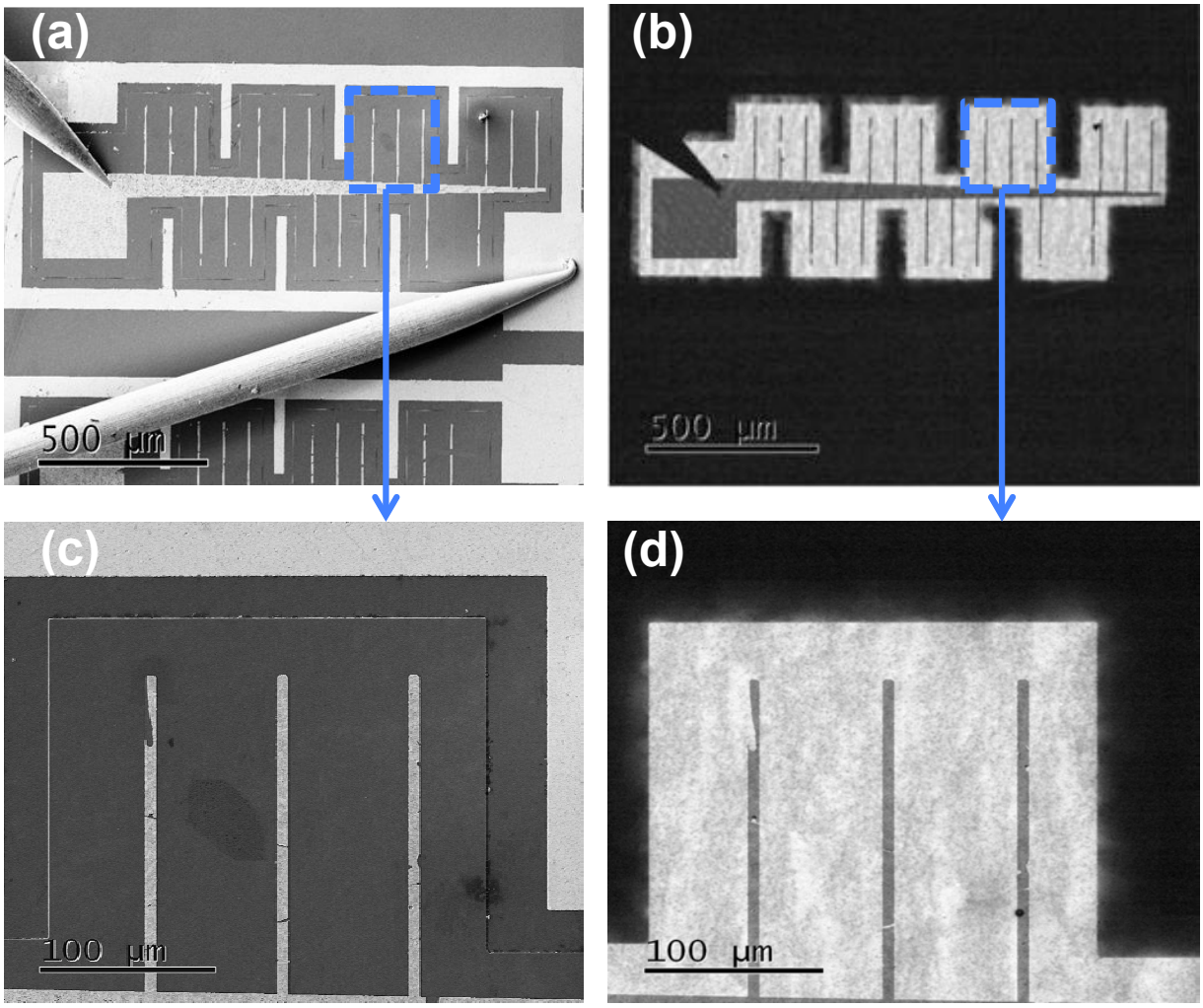

Figure 4.10: (a) SEM image of the top surface of a device (b) Corresponding EBIC mapping, (c) SEM image at high magnification of a part of the device, (d) EBIC mapping at high magnification of a part of the device. The e-beam energy used is equal to 15keV.

The external quantum efficiency for the best performing device has a maximum peak of 80% at a wavelength of 380 nm under no bias light condition. To our knowledge, this is the maximum external quantum efficiency peak reported so far for an InGaN PIN heterojunction solar cell. Above the wavelength of 380 nm, a sharp decrease down to a cut-off wavelength of 410 nm is observed. This suggests a high quality of the absorber layer. The lower spectral response for wavelengths below 365 nm is due to the photon absorption and charges generation in the p-GaN layer that cannot be collected at the metal contacts. The electron-hole pairs generated by high energy photons are located close to the interface of p-GaN and i-InGaN. The collection efficiency of these photogenerated carriers can be dramatically increased by reducing the thickness of p-GaN layer. Around 20% loss in maximum external quantum efficiency can be expected due to the absorption of light in the metal contacts and reflections from the top surface.

The external quantum efficiency is than measured under illumination of a bias light (power density around 12 mW/cm^2) as discussed in previous chapter. With increase of the bias light intensity, the spectral response in the shorter wavelength increase with an increase in the maximum external quantum efficiency peak from 80% to 85%. The maximum external quantum efficiency peak saturates with further increase in the bias light intensity (70% to 100%), while the EQE in shorter wavelength increases with light intensity without any saturation. This behavior of external quantum efficiency under bias light is in contrary to what we observed for

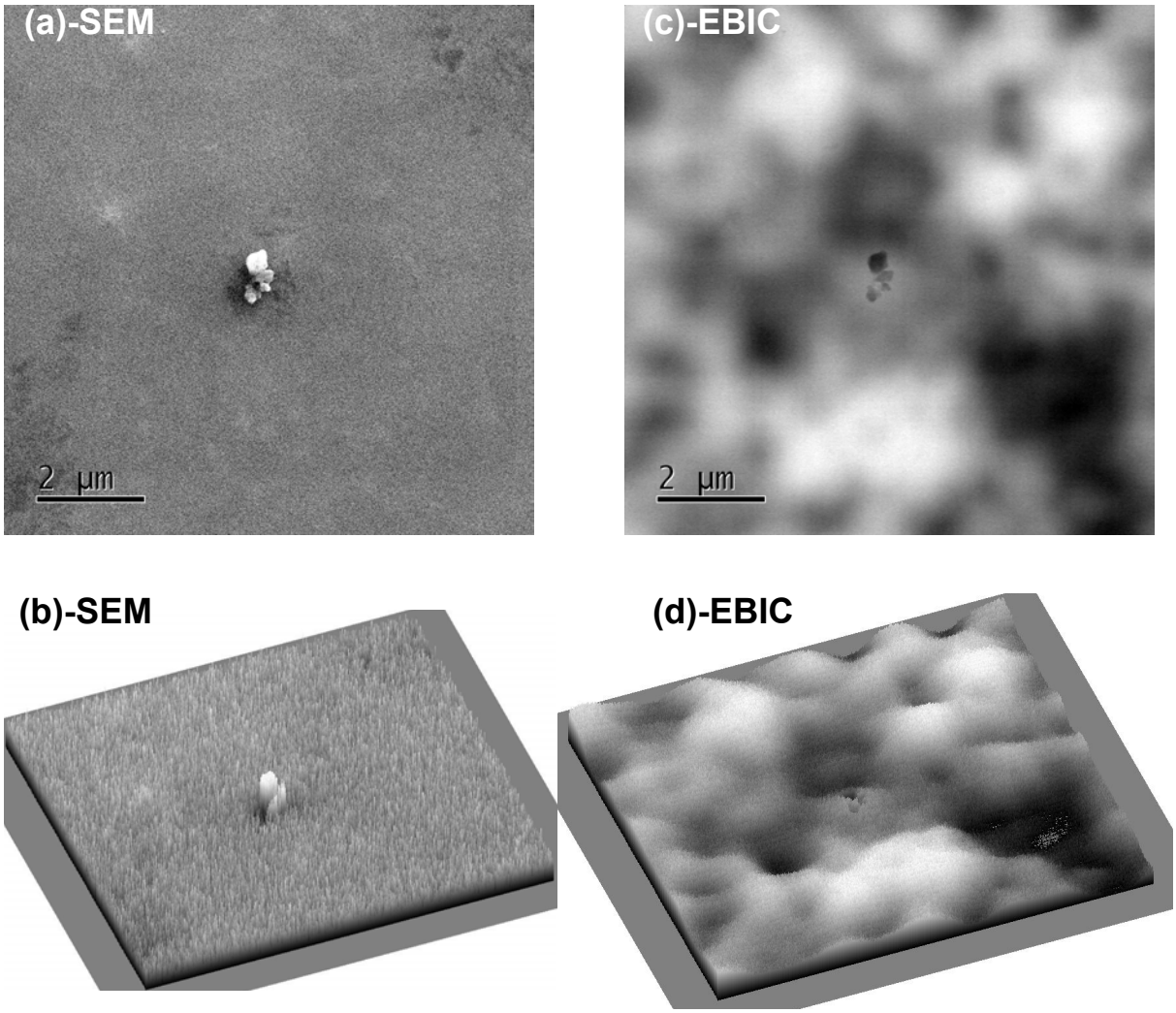

Figure 4.11: (a) High magnification images of top surface of the device obtained at 15 Kev, (a)-(b) SEM and 3D line profile and (c-d)) EBIC and 3D line profile.

bulk InGaN solar cell discussed in previous chapter. Therefore it cannot be explained by the same model presented in the previous chapter. The p-GaN layer for T1158-SB is grown at high temperature (1000°C) compared to 800°C for bulk structure in the previous chapter. This means that the density of traps in the p-GaN layer for T1158-SB is lower than the T1185-B structure. However, the HAADF-STEM study for T1158-SB (see Figure 4.8) shows the presence of V-pits in the semibulk absorber, which is not the case for T1185-B bulk structure discussed in previous chapter. This implies that in T1158-SB, its the electron trapping in semibulk absorber leading to an increase of the negative space charge. Consequently, the depletion width in the p-GaN layer must increase to maintain space charge neutrality, resulting in more absorption and collection of the shorter wavelength photons under bias light.

4.4.2.3 Current-Voltage Measurements

Figure 4.13 shows the voltage dependence of the current density, simulated and measured experimentally, under AM 1.5G solar spectrum as well as under concentrated light (see Appendix E for estimation of number of suns). The illumination intensity for AM 1.5G was calibrated at 1 sun by matching the measured short circuit current density (J_{sc}) to the value of J_{sc} extracted

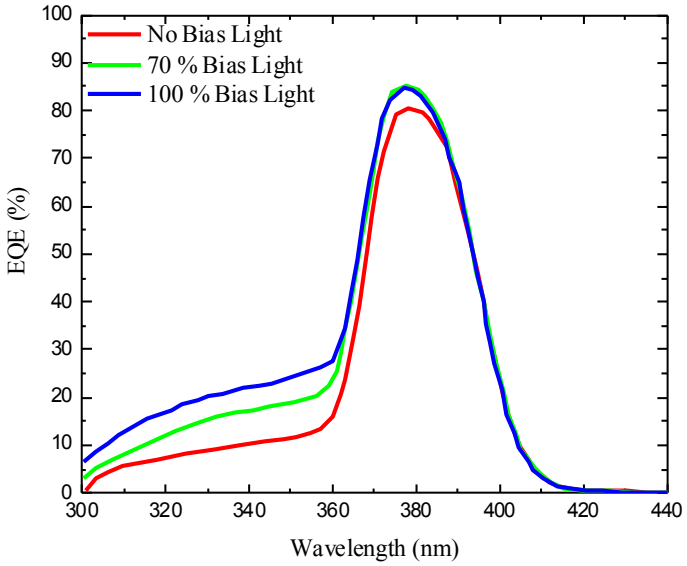

Figure 4.12: Typical External Quantum Efficiency (EQE) under different bias light conditions.

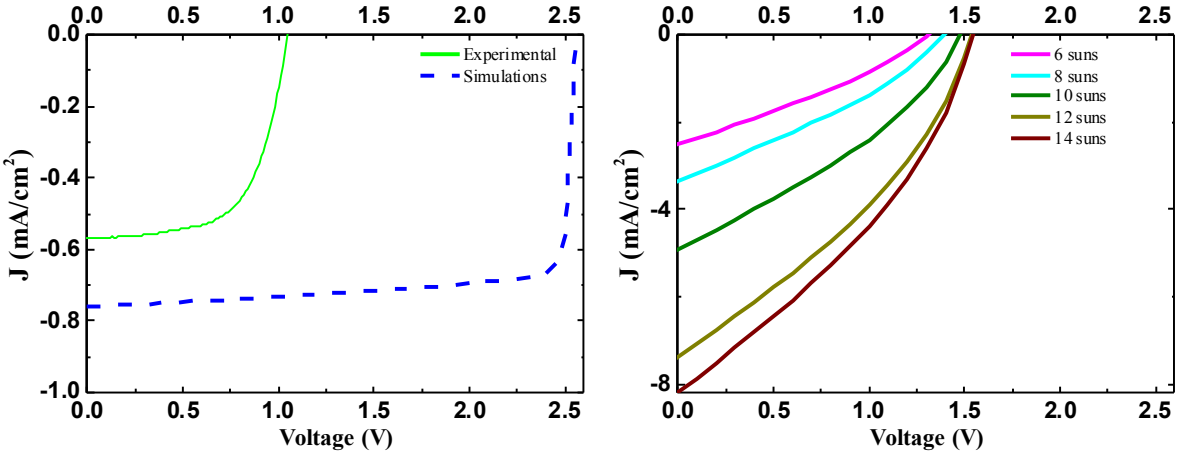

Figure 4.13: Current Density-Voltage ($J-V$) measured under AM 1.5G, experimentally and simulations (ideal) and UV concentrated light.

from the integration of external quantum efficiency measurements [65], using the equation;

$$J_{sc} = \int \frac{q}{hc} S(\lambda) E(\lambda)\, \mathrm{d}\lambda. \tag{4.4}$$

The values of J_{sc}, V_{oc}, fill factor and power conversion efficiency which can be derived from the measurement under AM 1.5G condition are listed and compared to literature in Table 4.2. While the V_{oc} and fill factor of the semibulk $In_{0.08}Ga_{0.92}N$-based PV solar cell are rather of the same order of magnitude whatever the authors works, the J_{sc} is four or five times of what has been reported for a bulk $In_{0.08}Ga_{0.92}N$ structure. This, although the literature values have been obtained under AM 0, conditions much more favorable than AM 1.5G since corresponding to much more optical power below 400 nm. These values lead to a power conversion efficiency for the semibulk $In_{0.08}Ga_{0.92}N$-based PV solar cell which is at least three times higher than power

Table 4.2: Measured and simulated values of J_{sc}, V_{oc} and fill factor, with a comparison to state of the art. (i). p-GaN grown at 890°C, (ii). p-GaN grown at 1040°C.

	In (%)	J_{sc} (mA/cm^2)	V_{oc} (v)	FF (%)	PCE (%)	illumination
Simulations (ideal)	8	0.75	2.56	80	1.4	AM 1.5G
This study	8	0.57	1.04	65	0.39	AM 1.5G
Neufeld et al. [63]$^{(i)}$	8	0.14	0.81	61	0.07	AM 0
Neufeld et al. [63]$^{(ii)}$	8	0.11	1.65	75	0.13	AM 0

conversion efficiency for the bulk $In_{0.08}Ga_{0.92}N$ structure under AM 0.

The high J_{sc} of the semibulk $In_{0.08}Ga_{0.92}N$-based PV solar cell shows that semibulk approach provides an absorber layer with efficient light absorption and carrier collection. The experimentally measured J_{sc} is slightly lower than the simulated J_{sc} for an ideal structure. This is likely due to absorption in Pd/Au p-GaN metal contacts, which could contribute to a loss of around 16% of the useful light. It is also to be noticed that J_{sc} increases significantly and linearly with the optical power as shown in Figure 4.14. As expected, this is not the case for V_{oc} (see Figure

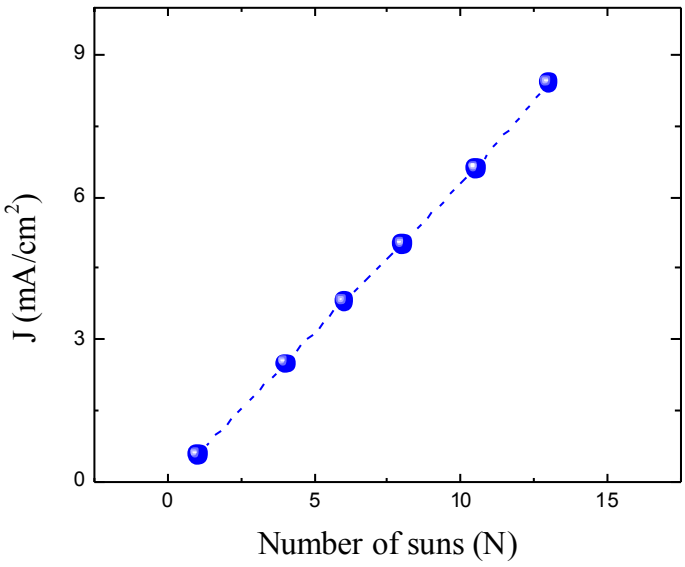

Figure 4.14: Dependence of the short circuit current density.

4.13) since its dependence with the optical power can be described by:

$$V_{oc} = \frac{nkT}{q} ln\left(\frac{J_{sc}}{J_s} + 1\right) = \frac{nkT}{q} ln\left(\frac{K \times N}{J_s} + 1\right) \tag{4.5}$$

where the thermal voltage, kT/q at 300K is 25.85 mV, N is the number of suns, and n and J_s are the ideality factor and saturation current density of the diode, respectively. $K$is the slope of the J_{sc} versus N curve (see Figure 4.14). As shown in Figure 4.15, due to large values of both J_s (equal to 2.6×10^{-3} mA/cm^{-2}) and n (equal to 7.5), a rather large difference exists between experimental and simulated values of V_{oc}.

The low unwanted residual doping concentration of NID-GaN interlayers in the semibulk absorber may contribute to the high ideality factor, as reported by Zhu *et al.* [151], who have

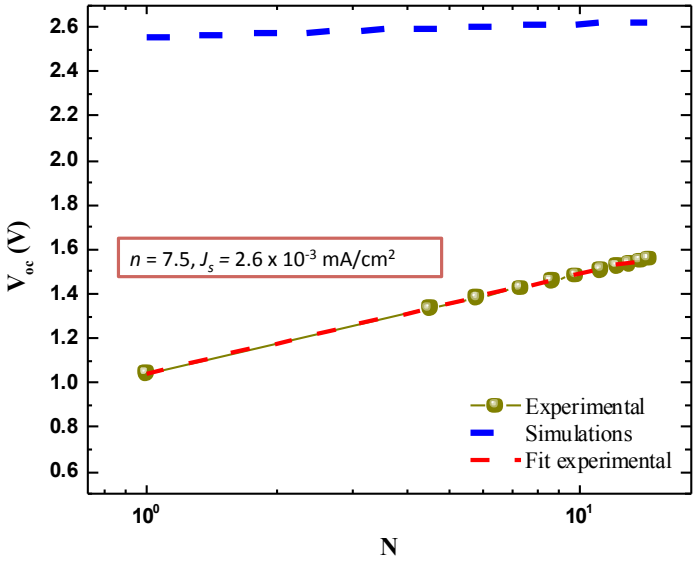

Figure 4.15: Dependence of simulated and measured open circuit voltage on optical power. The experimental data are fitted with n and J_s.

shown a strong increase of the diode-ideality factor in InGaN/GaN multiple quantum well light-emitting diodes in case of low doping of the quantum barriers. The large value of the ideality factor suggests also the presence of trap-assisted tunneling (i.e. electron tunneling to deep levels) and carrier leakage inside the active region [152]. This is revealed by the typical dark $J-V$ curve shown in Figure 4.16, in which at low bias voltage, a large carrier recombination current in the depletion region through trap levels presumably associated with threading dislocations [31, 153] is observed. This is in good agreement with threading dislocations and nano-defects (nano-

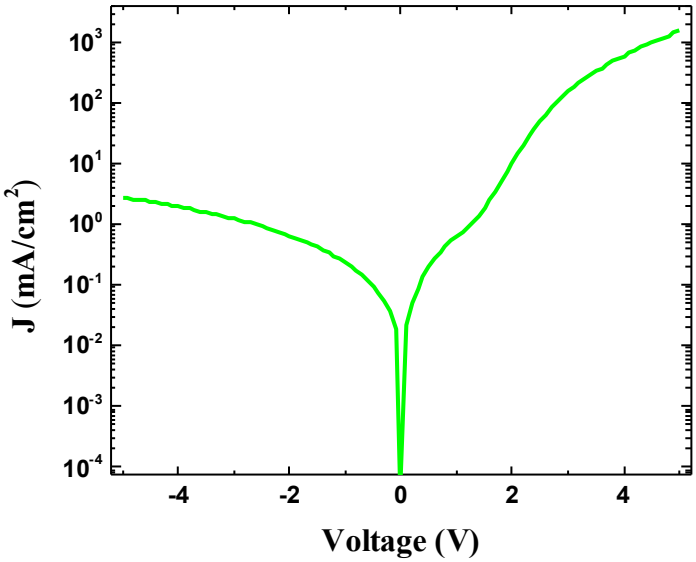

Figure 4.16: Dark current density-Voltage ($J-V$) characteristics in log scale.

precipitates and/or nano-dislocation loops) which can be seen in the p-GaN layer in Figure 4.8. These defects could contribute to the reduction of the diode barrier, resulting in increase of recombination current [153]. The reduction of threading dislocations by growing epitaxial layers particularly p-GaN with high crystalline quality at high temperature, results in high power conversion efficiency [63]. However, InGaN layers usually degrade from being exposed to high

p-GaN growth temperatures, leading to phase separation and In clustering. This reduces the maximal growth temperature for p-GaN, and thus, its quality, resulting in a low V_{oc}.

4.5 Semibulk $In_{0.12}Ga_{0.88}N$ Solar Cells

4.5.1 Structural and Morphological Study

Figure 4.17(a)–(b) show the (11-24) reciprocal space maps of T1185-SB and T1188-SB respectively. The diffraction spot for both semibulk $In_{0.12}Ga_{0.88}N$ PV structures is intense and lies on the vertical line, indicating that $In_{0.12}Ga_{0.88}N$ layer is mostly coherently strained to GaN template. The extracted value for degree of relaxation is around 18% and 8% for T1185-SB and T1188-SB respectively. The degree of relaxation for semibulk T1185-SB is greater than the bulk T1185-B with p-GaN grown at the same temperature (800°C. This can be attributed to the larger (120 nm) absorber thickness for T1185-SB compared to the 60 nm thick InGaN (within critical layer thickness) for T1185-B structure. However, the degree of relaxation for T1188-SB even with a higher p-GaN growth temterature (850°C) is lower than T1185-SB with p-GaN at 800°C.

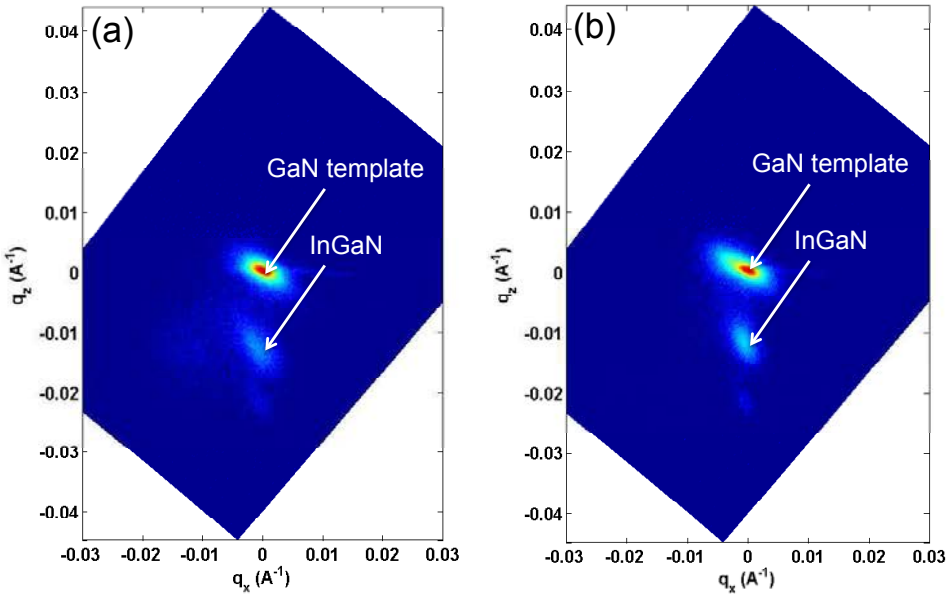

Figure 4.17: (11-24) reciprocal space mapping scan, showing GaN substrate and InGaN diffraction spot for the semibulk $In_{0.12}Ga_{0.88}N$ PV structures, (a) T1185-SB and (b) T1188-SB.

The scanning electron microscopy (SEM) images of the surface morphology of T1185-SB and T1188-SB semibulk $In_{0.12}Ga_{0.88}N$ PV structures are presented in Figure 4.18. The surface morphology of the p-GaN layer for T1185-SB shown in Figure 4.18(a)-(b) reveal a rough surface with a high density of V-pits as expected due to low growth temperature of p-GaN layer discussed in the previous chapter. In contrast for T1188-SB, the rough surface morphology of p-GaN is drastically smoothed by increasing the growth temperature of p-GaN from 800°C to 850°C as shown in Figure 4.18(c)-(d). According to our findings for the bulk InGaN (T1185-B) PIN structure, the presence of high density of shallow and deep V-pits in T1185-SB (see Figure 4.18(a)-(b)) should result in high J_{sc} compared to T1188-SB under illumination. The deep V-pits (diameter of around 1μm (see Figure 4.18(a)–(b)) should lead to a low V_{oc} for devices of both PIN structures.

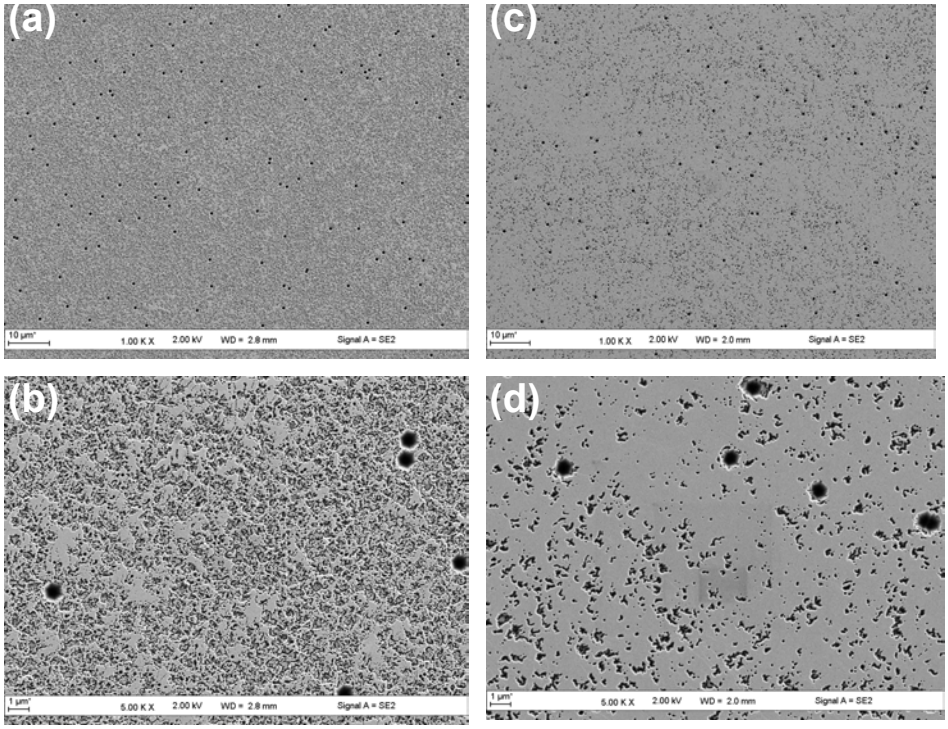

Figure 4.18: SEM images at different magnification of the surface morphology of the semibulk $In_{0.12}Ga_{0.88}N$ PV structures, (a)–(b) T1185-SB and (c)–(d) T1188-SB.

4.5.2 Electro-Optical Characterization

4.5.2.1 External Quantum Efficiency Measurements

The external quantum efficiencies (EQE) for T1185-SB and T1188-SB devices, with and without bias light are presented in Figure 4.19. Under no bias light conditions, the PV devices have

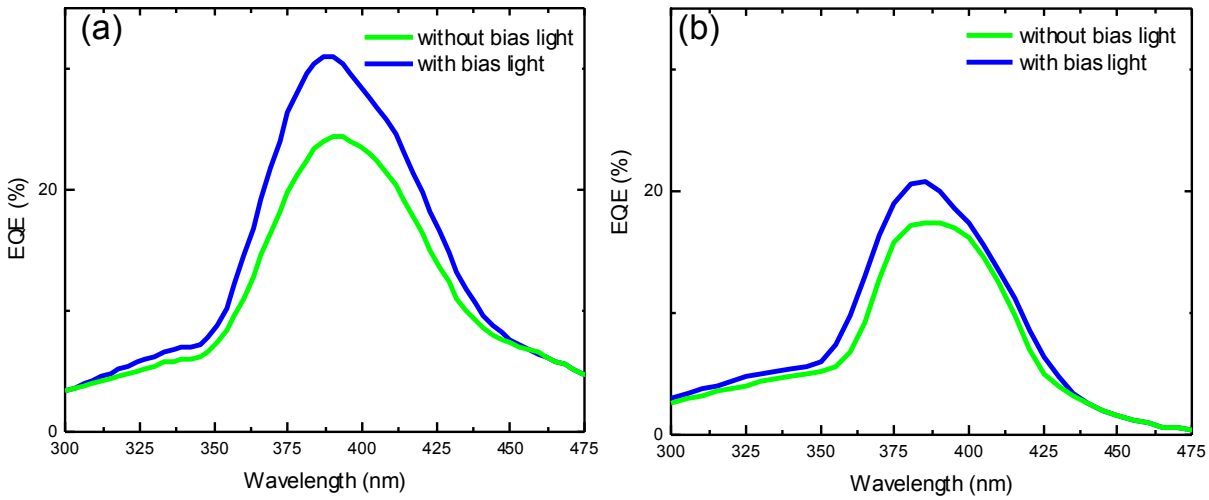

Figure 4.19: Spectral response of the semibulk $In_{0.12}Ga_{0.88}N$ PV structures,(a) T1185-SB and (b) T1188-SB.

a maximum external quantum efficiency peak of 25% and 18% at a wavelength of 387 nm for T1185-SB and T1188-SB respectively. The cut-off wavelength for a fully strained InGaN epitaxial layer with 12% of indium concentration is around 420 nm. The absorption above 420

nm is attributed to the partially relaxed InGaN layer with high indium concentration. T1185-SB have a high absorption above 420 nm consistent to the high degree of relaxation.

Under bias light conditions, the maximum external quantum efficiency peak increases from 25% to 31% for T1185-SB and 18% to 21% for T1188-SB, with a small increase of the spectral response in the shorter wavelength range as shown in Figure 4.19. This behavior of external quantum efficiency is consistent with the external quantum efficiency for bulk $In_{0.12}Ga_{0.88}N$ solar cell under bias light discussed in the previous chapter. This could be attributed to the increase of depletion width in the semibulk InGaN layer to maintain space charge neutrality, thus enhancing the collection of carriers in the PV cell. This model also explains why the increase in maximum EQE peak for T1185-SB (6%) is greater than T1188-SB (3%), this could be attributed to the high density of V-pits in T1185-SB compared to T1188-SB leading to more hole trapping and thus larger extension of the space charge region.

4.5.2.2 Current - Voltage Measurements

Figure 4.20 shows the voltage dependence of the current density for T1185-SB and T1188-SB semibulk $In_{0.12}Ga_{0.88}N$ PV structures, measured under concentrated light (see Appendix E for estimation of number of suns). The J_{sc} measured for T1185-SB is higher than T1188-SB under

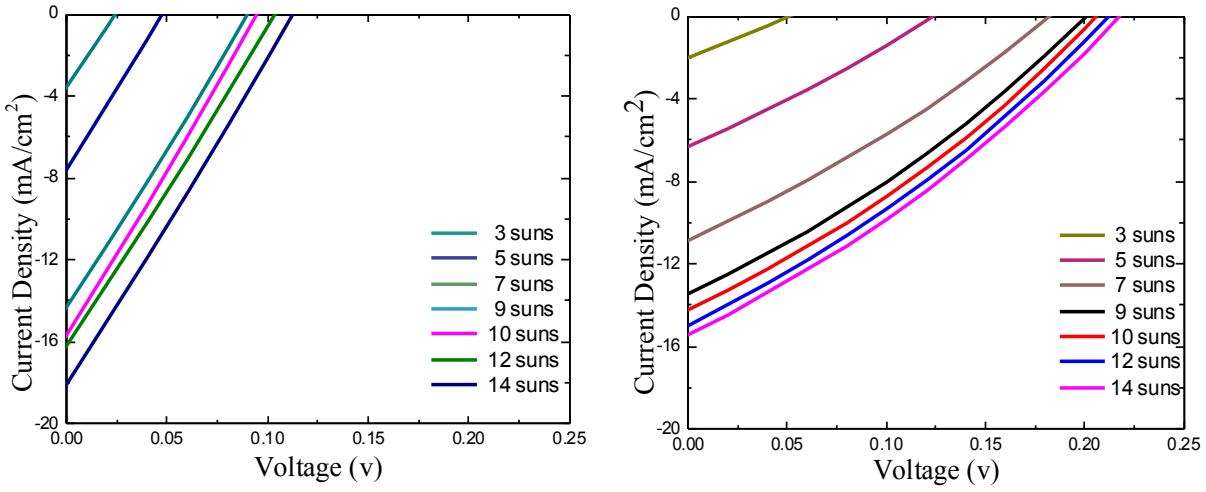

Figure 4.20: Current density - Voltage measurements for the semibulk $In_{0.12}Ga_{0.88}N$ T1188-SB PV cells.

same illumination conditions. This is consistent with the high external quantum efficiency observed in T11185-SB compared to T1188-SB. This is attributed to the presence of a higher density of shallow V-pits in T1185-SB compared to T1188-SB leading to an enhancement of the carrier collection due to the formation of the impurity depleted zone around them (see chapter 3). The V_{oc} for T1185-SB is lower than for T1188-SB. This can be attributed to the higher density of deep V-pits in T1185-SB than in T1188-SB (see Figure 4.18) as discussed in Chapter 3. A comparison of the dark $I-V$ for T1185-SB and T1188-SB is shown in Figure 4.21. This high leakage current is attributed to the deep V-pits observed in both structures. The ideality factor given in Figure 4.22 if higher for T1185-SB then T1188-SB attributed to the trap-assisted tunneling and carrier leakage inside the active region, consistent to what we observed in semibulk T1158-SB $In_{0.08}Ga_{0.92}N$ PV cells. The increase of ideality factor for semibulk T1185-SB and T1188-SB compared to T1158-SB, with an increase of indium concentration from 8% to 12% show that the tunneling of carriers increased due to the degradation of the semibulk InGaN absorber with high (12%) indium concentration. The high leakage current for T1185-SB and

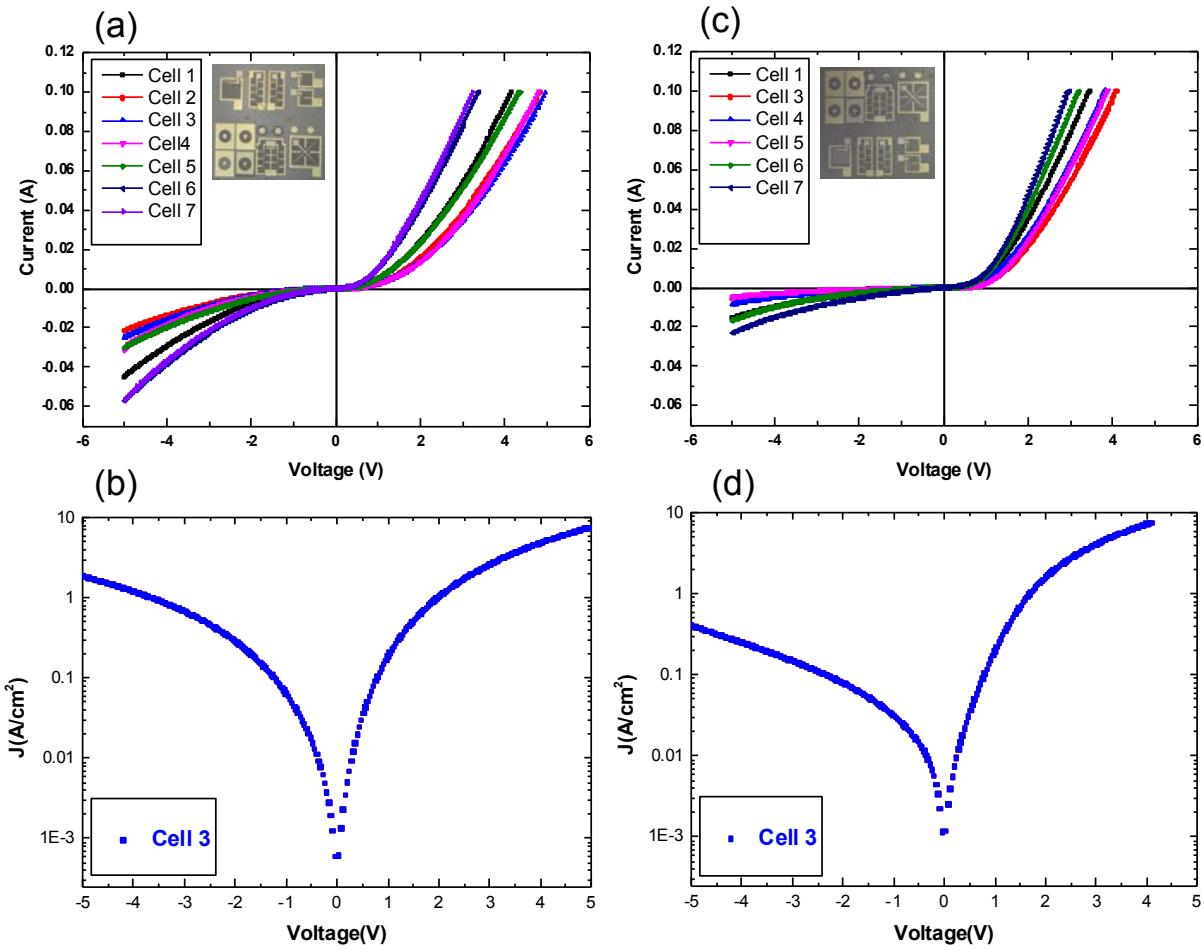

Figure 4.21: Dark $I-V$ measurements for semibulk $In_{0.12}Ga_{0.88}N$ PV structures, (a)–(b) T1185-SB and (c)–(d) T1188-SB.

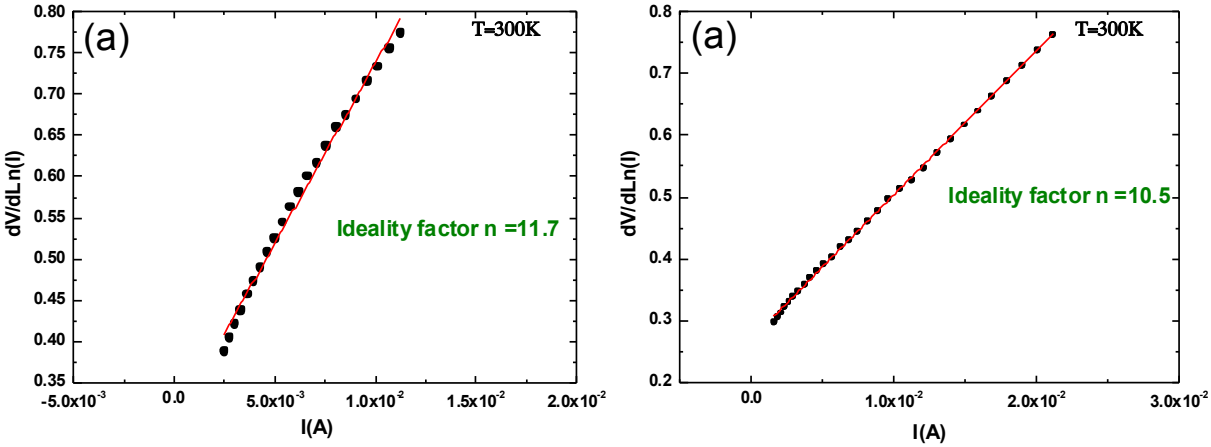

Figure 4.22: Ideality factor of the semibulk $In_{0.12}Ga_{0.88}N$ PV structures, (a) T1185-SB and (b) T1188-SB.

T1188-SB is also attributed to the issues in the device processing for these (T1185-SB and T1188-SB) wafers.

4.6 Comparison of Semibulk InGaN PV Devices

Table 4.3 presents a comparison of semibulk InGaN PIN device performances discussed so far. As shown by Fabein *et al.* [154] the J_{sc} increases linearly with indium concentration, therefore

Table 4.3: Comparison of V_{oc}, J_{sc}, fill factor and external quantum efficiency for our Bulk and Semibulk InGaN PIN devices (^{a} J_{sc} estimated to 12% of indium concentration, $*$ external quantum efficiency under bias light).

Reference	Absorber (Thickness)	V_{oc} (V)	J_{sc} (mA/cm^2)	EQE	Source	Total V-pit density
T1158-SB	144 nm (8%)	1.56	11.6^a	80% : 85%*	14 suns	Low
T1188-SB	120 nm (12%)	0.22	15.8	17% : 20%*	14 suns	Medium
T1185-SB	120 nm (12%)	0.1	18	25% : 31%*	14 suns	High

we can estimate the increase in the J_{sc} for semibulk T1158-SB from 8% to 12% of indium concentration. As expected, the results show that as the total density of V-pits increases, the J_{sc} increases, consistent with our previous findings. For T1158-SB, the p-GaN layer is grown at high temperature (1000°C) resulting in a smooth surface with no V-pits. In contrast as the p-GaN growth temperature is reduced to 850°C with medium density of V-pits in T1188-SB, the J_{sc} increases. A further decrease of the p-GaN temperature to 800°C for T1185-SB results in an increase in the J_{sc}. This is consistent to our findings that V-pits contributes to the enhancement of the carrier collection resulting in high J_{sc}. A noticeable point is that the V_{oc} decreases with decrease in the p-GaN growth temperature, consistent to our previous findings that V-pits (deep V-pits) contributes to the carrier recombination resulting in low V_{oc}.

4.7 Summary and Perspectives

The results presented for the semibulk InGaN-based PV cell in this chapter show that the InGaN semibulk absorber approach is an effective method for achieving high efficiency InGaN PIN heterojunction solar cells. This novel technique can overcome the limitations of growing thick high quality InGaN layers with high indium concentrations. The semibulk $In_{0.08}Ga_{0.92}N$ PV device has a power conversion efficiency of 0.39% under an AM 1.5G solar spectrum, almost three times higher than the current state of the art. The J_{sc} measured in semibulk $In_{0.08}Ga_{0.92}N$ PV cells under AM 1.5G is almost four times as high as previously reported values for 8% indium concentrations and thus confirms efficient light absorption and photocarriers collection in the semibulk absorber. The device has a maximum external quantum efficiency peak of 85% which is the highest external quantum efficiency peak reported so far for an InGaN PIN heterojunction solar cell. The performance of the semibulk PV devices is affected by increasing the indium concentration from 8% to 12% in semibulk absorber. The results obtained for semibulk $In_{0.12}Ga_{0.88}N$ agree well with our proposed model of enhancing the InGaN solar cells performance using V-pits. These results show that if the size and density of V-pits is controlled during the growth

conditions, the power conversion efficiency of InGaN solar cells can be significantly improved. Another possibility is to passivate the V-pits mainly the deep V-pits using SiO_2, that may allow to increase the J_{sc} without affecting the V_{oc} of the device, leading to a higher power conversion efficiency. This is currently in progress as shown Figure 4.23. For our future study, semibulk

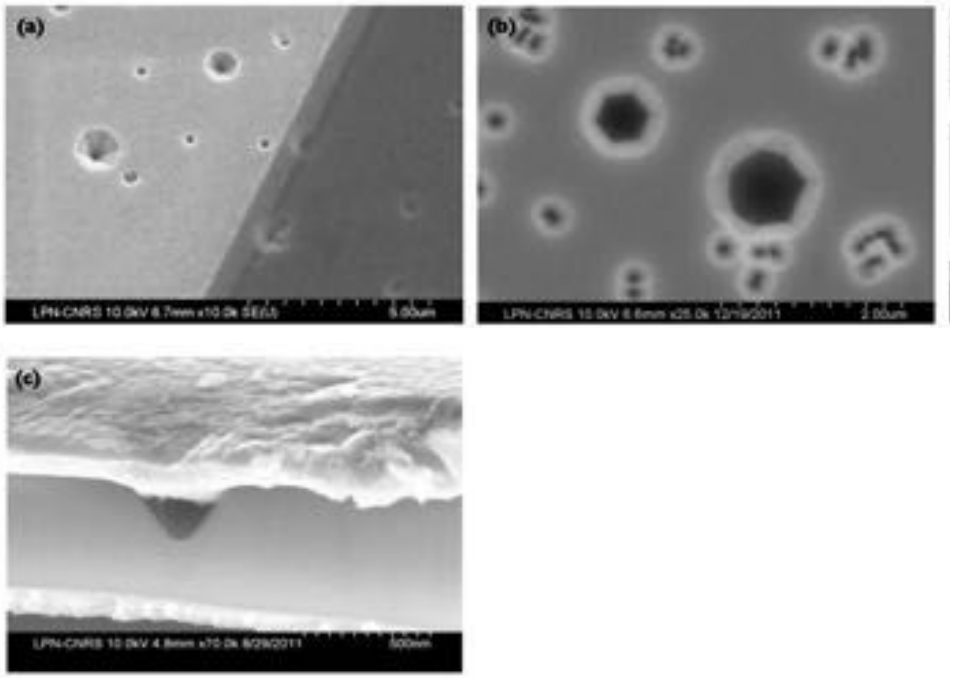

Figure 4.23: V-pit masking (a) before HSQ, (b) after HSQ, and (c) after metal deposition.

InGaN-based PV cells with high indium concentration >14% have been grown and are currently under investigations. Further optimization study in particular with the growth conditions of the subsequent top p-GaN layer is required, which until now has been the efficiency limiting factor of the semibulk InGaN solar cells. For that, several wafers for p-GaN re-growth via MBE are also under study, that will allow us to utilize the full potential of semibulk InGaN solar cells.

The results for the semibulk $In_{0.08}Ga_{0.92}N$ PV cell presented in the first part of this chapter were the subject of an oral presentation at CPV-11 International Conference on Concentrator Photovoltaic Systems, Aix-les-Bains, France [155]. They have been published in Journal of Solar Energy Materials and Solar Cells [**?**].

Chapter 5

InGaN Nano-structure PIN Heterojunction Solar Cells

As discussed in the previous chapter thick high crystalline quality InGaN absorber is readily achieved using the semibulk InGaN absorber approach, however the critical layer thickness above 20% of indium incorporation is quite challenging. In such a situation, the device design of the semibulk solar cells become similar to the multi-quantum well (MQW) structures. Such (MQWs) type of approaches are promising and are intensively investigated, however, these architectures evidence a limited indium composition and thickness due to strain, phase separation, and 2D to 3D growth mechanisms. The use of multiple quantum well absorption layers can increase the indium composition (x $\approx$ 0.25–0.30) [76, 89] and the internal quantum efficiency can be high (>70%) at high energies. These energies are far from the optimum bandgap energies required for an efficient single gap solar cell, and have kept InGaN power conversion efficiency below 3% [76]. In order for InGaN materials to gain serious consideration for photovoltaics and compete with traditional single gap solar cell materials, a new approach is required, which is presented in this chapter.

5.1 Design of the Solar Cells

The InGaN nano PV structure are grown on an n-type 2 μm thick c-oriented GaN/sapphire substrate following the procedure described by schematic in Figure 5.1. The InGaN nano mask patterning is very challenging, due to the critical parameters including, the e-beam energy, time of exposure etc. The process optimization is carried out on wafers with a 100 nm thick negative-tone resist (hydrogen silsesquioxane, HSQ) spin-coated on the template. Figure 5.2 show the typical nano-pattern hole opening exposed to e-beam for different duration. A small variation of the exposure time result in non-homogeneous HSQ hole opening and/or loss of the complete mask. The distribution is determined using a Monte Carlo simulation for a 100 keV electron beam normally incident on HSQ on GaN on Sapphire. Once the process is optimized, the resist is then patterned using an electron-beam lithography system providing a 4 nm Gaussian beam, that we used at 100 kV accelerating voltage, under a 1.9 nA current. The part of the resist exposed to electron beam cross-links into SiO_2. TMAH 25% etching treatment is used to open the nano-patterns (nano-holes). The resulting patterns are roughly 100 nm high. 60 $\times$ 60 μm^2 with 70 nm diameter holes embedded in them are fabricated using electron beam lithography. The holes are arranged in a hexagonal lattice with a pitch of 135 nm. Figure 5.3 shows the optimized nano-mask ready for the InGaN nano-structure growth. The single-step process, compared to the standard deposit-etch method, allows better preservation of the quality of the substrate, first by not exposing the underlying GaN surface to a plasma etch, and then overall by simplifying the process and hence limiting the number of chemicals used on the wafer.

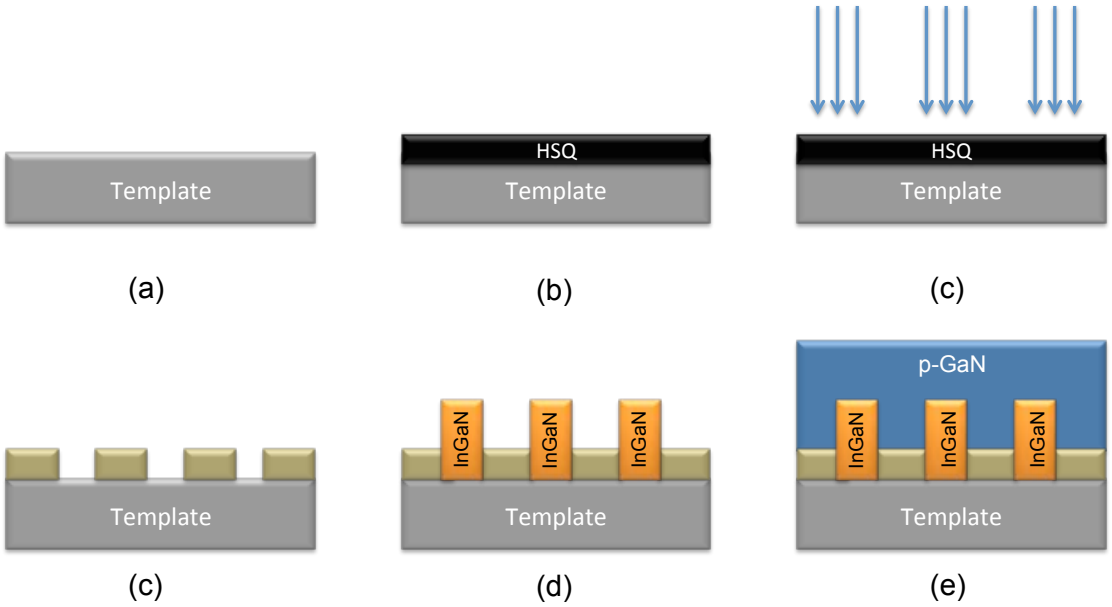

Figure 5.1: Scheme of the nano-patterning process used for the growth of InGaN nanostructures: (a) n-GaN/sapphire substrate, (b) HSQ resist spin coating, (c) electron beam lithography allowing cross-link of the resist into SiO_2 followed by etching of the unexposed resist, (d) TMAH 25% etching treatment to open the nano-patterns, (e) MOVPE InGaN nano selective area growth, and (f) p-GaN growth via MOVPE.

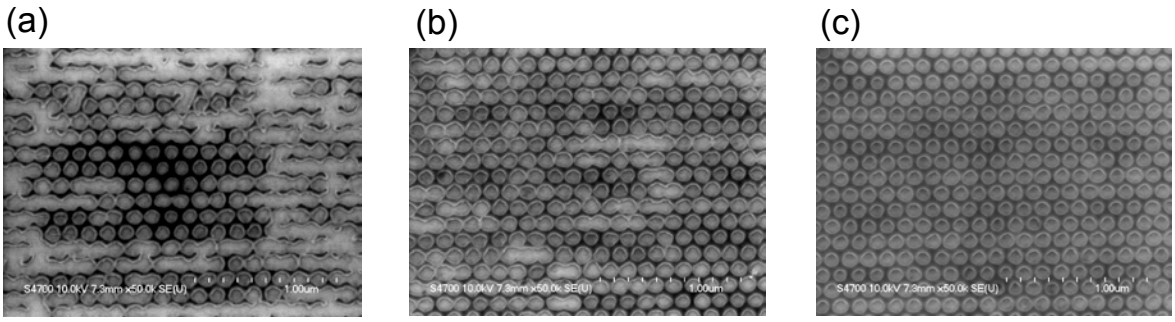

Figure 5.2: Typical nano-pattern mask hole opening with same e-beam energy but different exposure duration.

Trimethyindium (TMIn), trimethylgallium (TMG), and ammonia are used as the precursors for the growth, under nitrogen ambient at a temperature of 800°C. A 25 nm GaN layer is grown on top of a GaN-STN sapphire template, followed by 100 nm thick IngaN nano-structure growth. A 10 nm GaN cap layer is grown on top of the InGaN nano-structures, followed by a lateral growth of p-GaN for planarization. Finally a 150 nm thick p-GaN and a 50 nm p^+-GaN layer was grown at 850 °C.

The InGaN nano patterning mask and the InGaN nano PV structure is shown in Figure 5.4. The wafer contain more then 200 InGaN nano PV cells. The dose test region shown in Figure 5.4(a) is used for the optimization of the e-beam energy and exposure time for a given sample.

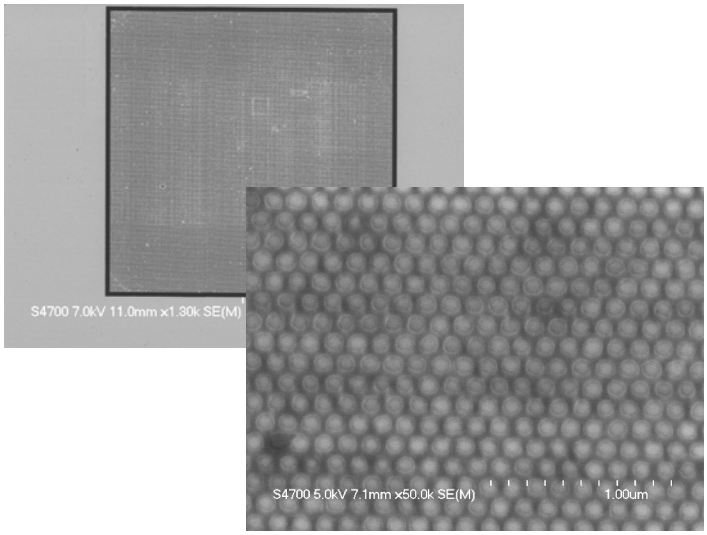

Figure 5.3: InGaN nano-mask patern, ready for the InGaN growth.

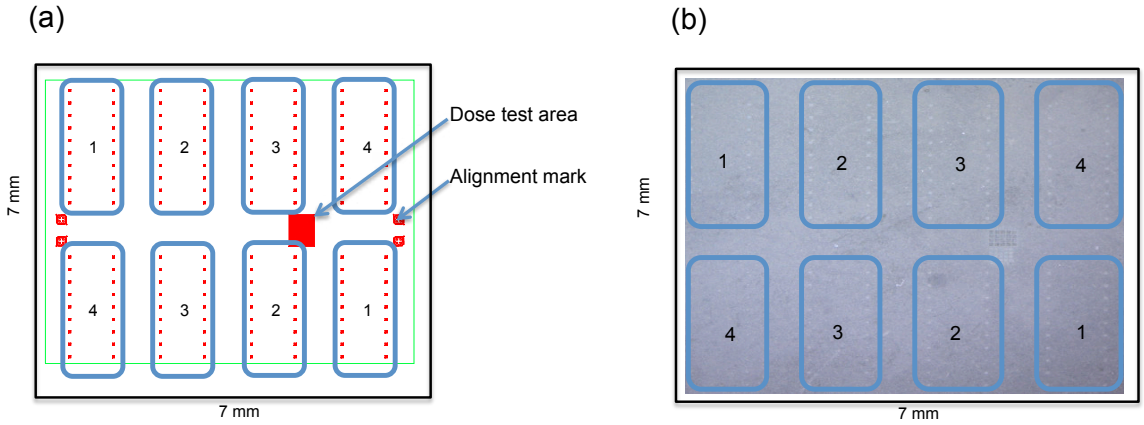

Figure 5.4: InGaN nano PV cells patterning on the GaN/sapphire template, (a) the nano mask, (b) the InGaN nano PIN PV structure.

5.2 Device Processing

The device processing of the InGaN nano PV structure is a challenging step, due to the small size of the nano regions i.e. 60×60 μm^2. These devices are processed at Georgia Institute of Technology Atlanta USA and LMOPS EA 4423. The wafer is first cleaned using organic solvents acetone and isopropanol each for 5 minutes. A 100 nm layer of SiO_2 is deposited on the wafer using PECVD with nitrogen diluted Silane and N_2O as precursors at a platen temperature of 90°C, pressure of 650 mTorr, and RF frequency of 13.56 MHz. Photo-lithography is used to define an area around the SiO_2 covered nano-structures to use for n-type contacts. The SiO_2 is removed using an inductively coupled plasma (ICP) etcher with CF_4 and H_2 as process gasses. The GaN exposed in this area, it is ICP etched again using Cl_2, BCl_3, and Ar to expose the n-type GaN around the nano-patterned 60×60 μm^2. Photo-lithography is used again to define a 50×50 μm^2 area above the nano-patterned area. The oxide is then etched using the same recipe as above to access the p-type nano-patterned area.

Contacting is made using liftoff. First the p-type contacts are defined so that the contact pad is on the SiO_2 layer with a bus bar running to the exposed p-type GaN. 10 nm of Ni and

20 nm of Au are evaporated to use as the contact. The resulting structure is lifted-off and then annealed at 500°C for 80 seconds under N_2 in a rapid thermal annealing system to promote ohmic contact. For the n-type metal contacting, the samples are cleaned using organic solvents acetone and isopropanol each for 5 minutes. Followed by a rinse in the de-ionized water and dried with nitrogen. The photo-lithography is performed to obtain the patterns for n-contacting. The metals for n-type GaN are evaporated using Ti/Al/Ti/Au with thicknesses 8/250/10/100 nm respectively. Figure 5.5 show the schematic of the cross-section and top view of the final InGaN nano-structure solar cell device. As shown by the schematic in the bottom of the Figure

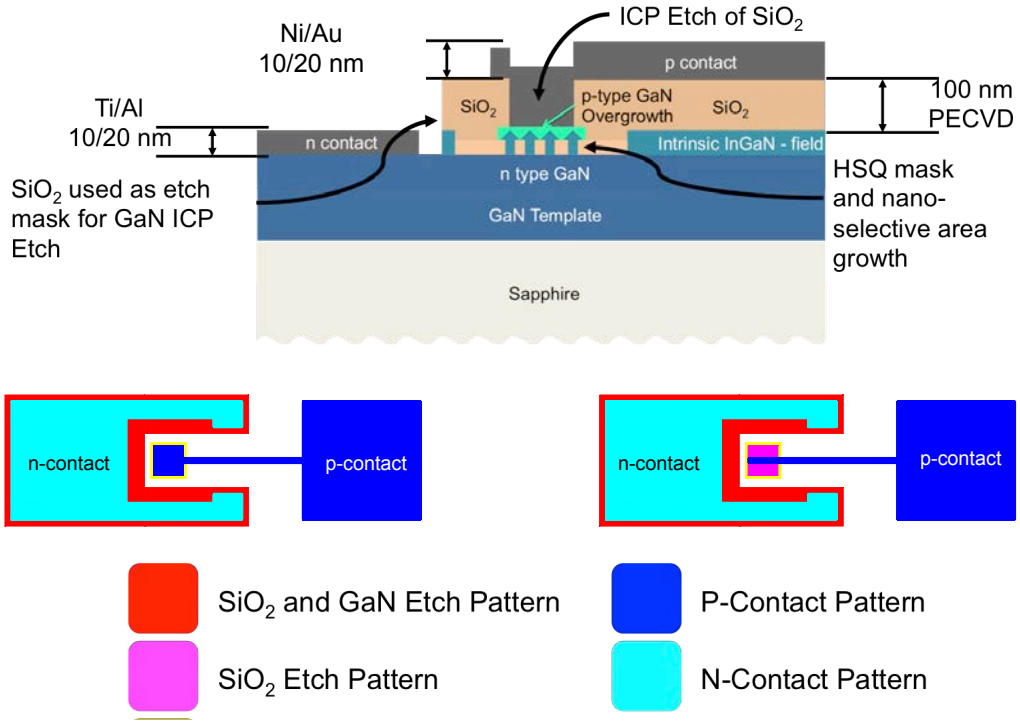

Figure 5.5: Schematic of the cross-section and top view of the InGaN nano solar cell.

5.5, two types of device designs are selected for the InGaN nano solar cells. The first one include a thin metal (Ni/Au) layer spreaded over the entire nano region. This design is expected to reduce the series resistance at the metal/p-GaN interface. However, the metal spreading layer all over the nano could also affect the light penetration into the device, as Ni/Au are known for light absorption thus reducing the efficiency of the device. The second type of device design composed of a thin Ni/Au bus bar connecting the nano and the p-contact, thus covering less then 20% of the nano region, as shown by the schematic in the bottom of Figure 5.5(right). These two metallization schemes are shown by the optical image of the InGaN nano-structure solar cell in Figure 5.6.

5.3 Characterization

The surface morphology is observed using scanning electron microscopy (SEM). The indium content, degree of relaxation and lattice parameters (a, c) are determined using symmetric (0002) $\omega - 2\theta$ scans in combination with X-ray reciprocal space maps (RSMs) of the asymmetric (11-24) planes. Micro-structural and micro-compositional studies are carried out through high-angle, annular dark field scanning transmissions electron microscopy (HAADF-STEM) and energy dispersive X-ray spectroscopy (EDX). The images are taken along $< 1\ 1\ \overline{2}\ 0 >$ zone axis.The $J - V$ measurements are performed under UV concentrated light.

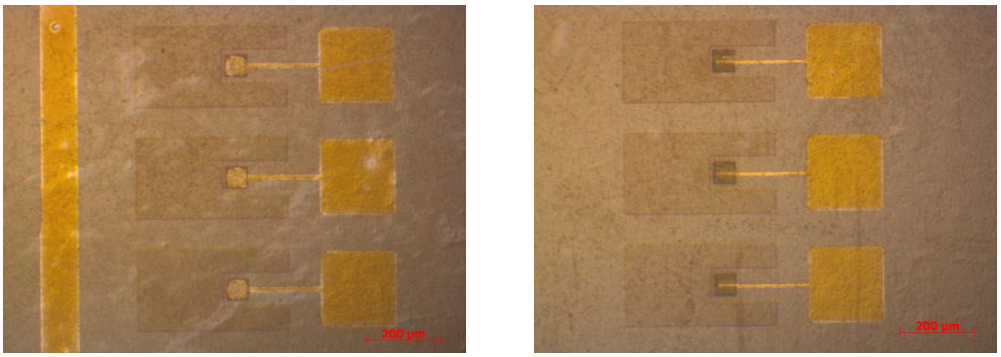

Figure 5.6: The two metallization schemes used for the InGaN nano solar cells.

5.3.1 Structural and Morphological Study

Figure 5.7(a) show the (002) symmetric $2\theta/\omega$ scans of the planar InGaN structure, with the simulation of the thick InGaN control sample grown along with the InGaN nano PV structure. From the simulation the average indium incorporation in the thick InGaN planar layer is found

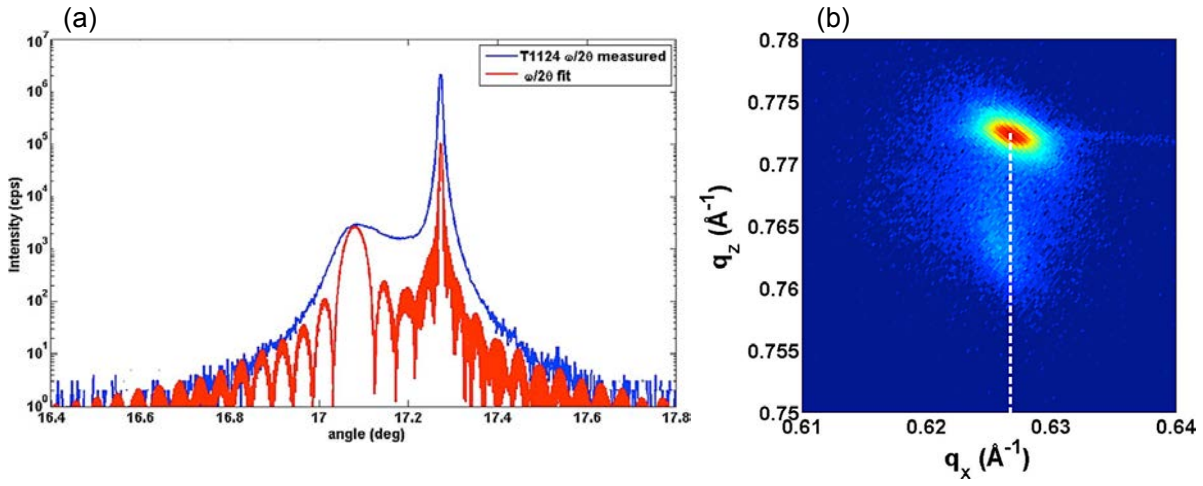

Figure 5.7: (a) Symmetric scan for 002 $2\theta/\omega$ scan for the InGaN nano PV structure on GaN template, (b) Asymmetric RSM for (114) peak of InGaN nano PV structure.

to be around 9%. Asymmetric RSM of the InGaN nano PV structure is shown in Figure 5.7(b). The intense diffraction spot in the RSM mapping correspond to the 3 μm thick GaN template. The mapping also display an additional diffraction spot, which corresponds to InGaN. The InGaN peak is intense, and located very close to the vertically aligned with the GaN peak, an indication of pseudomorphic growth of InGaN.

Figure 5.8 show the SEM images of the $In_{0.09}Ga_{0.91}N$ nano PV structure before and after the growth of InGaN and p-GaN epitaxial layers. Figure 5.8(a) shows the perfect hole opening of the mask ready for the InGaN growth. The growth of thick InGaN nano-structure (see Figure 5.8(b)) is perfectly selective grown on circular openings in the SiO_2 patterned substrate (see Figure 5.8(a)) without any polycrystalline deposits on the masks. The pattern with circular openings contains InGaN nano-rods with very good uniformity which has a hexagonal pyramid shape and has been grown without any defect. The nano-structures are smooth which means that a 3D stress relief mechanism is in place. This mechanism mitigates strain induced degradation, usually present in planar InGaN, which induces inclusions, V-pits, trench pits, indium clustering,

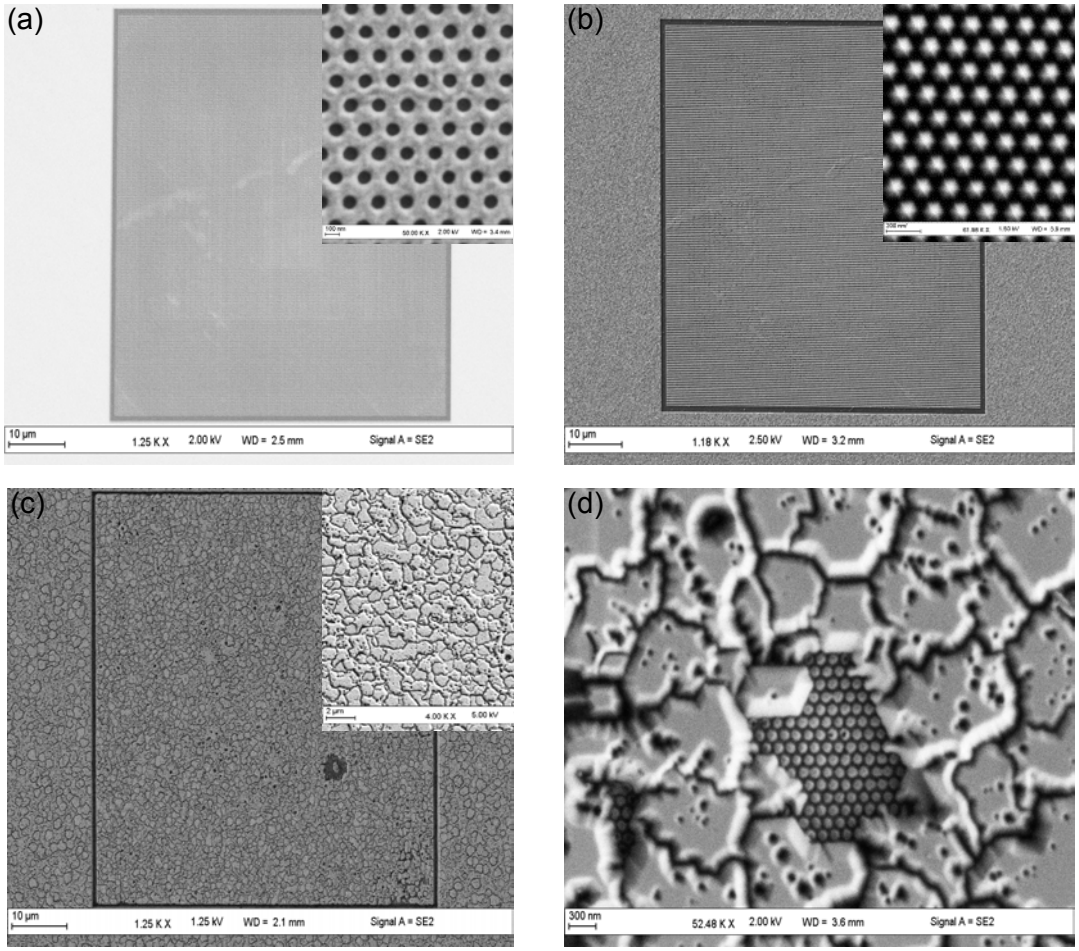

Figure 5.8: InGaN nano-structure PV cell surface morphology, (a) before InGaN growth, (b) after InGaN growth, (c) after p-GaN growth and (d) High magnification SEM image of the p-GaN.

and 3D growth. The morphology after p-GaN growth (see Figure 5.8(c)) reveals a rough surface with the presence of V-pits as expected due to the low p-GaN growth temperature (850°C), and unexpectedly with a high density of cracks. These cracks are never observed in our InGaN PIN structures. Two types of V-pits are observed, *i.e.* deep V-pits with diameter more than 100 nm and shallow V-pits with diameter less than 30 nm. According to our previous findings, these deep V-pits should reduce the V_{oc} whereas the shallow V-pits should contribute to the J_{sc} of the InGaN nano PIN devices. It is to be noticed that several InGaN nano PIN structures are not completely covered or connected to the field after p-GaN growth as shown in Figure 5.9.

5.3.2 Mirco-structural and Optical Properties

HAADF-STEM images of the InGaN nano PV structure before p-GaN growth and processing, are shown in Figure 5.10. The HAADF-STEM study after p-GaN growth is currently in progress. Figure 5.10(a)–(b) show the very good uniformity of the hexagonal pyramid shaped InGaN nano-rods, with a thickness of 150 nm. Figure 5.10(c) show a single nano-pyramid, with a clear contrast of the 20 nm GaN regrowth below the InGaN epitaxial layer. These results show clearly that the InGaN nanorod is single crystal with slightly misoriented grains, one being housed inside the SiO_2 mask and the other emerging out from the mask with hexagonal pyramid shape. Figure 5.10(d) is the high magnification of the nano-pyramid, revealing the absence of

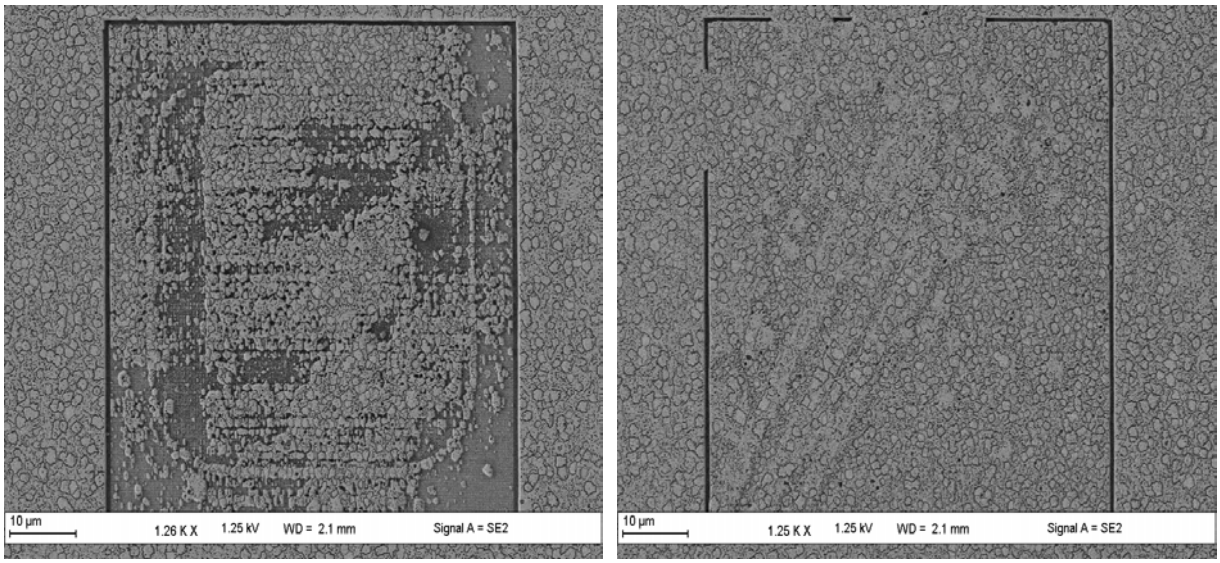

Figure 5.9: InGaN nano PIN structure surface morphology with selectiveity and with partical selectiveity after p-GaN regrowth.

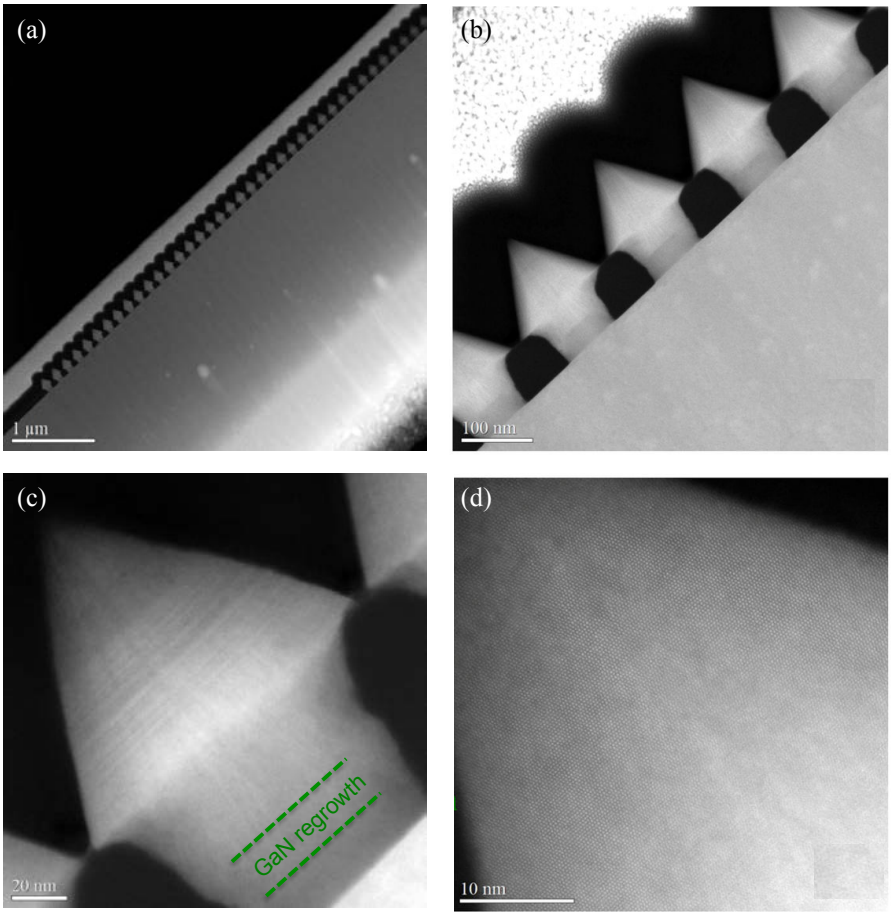

Figure 5.10: Different magnifications of HAADF cross sectional STEM images of InGaN nano-pyramids.

any defects and/or threading dislocations originating from the interfaces of the InGaN and GaN epitaxial layers.

5.3.3 Electro-Optical Characterization

5.3.3.1 Current - Voltage Measurements

The electrical characterization of the InGaN nano PIN structures are carried out before and after processing, which are presented in this section:

→ Current - Voltage Measurements - Before Processing

To perform the current density versus voltage ($J-V$) measurements, we used a scratch to reach the n-type GaN. The quality of the contact is first verified by putting both the probes on the scratch as shown in Figure 5.11. The ohmic behavior of the $I-V$ confirms that both the

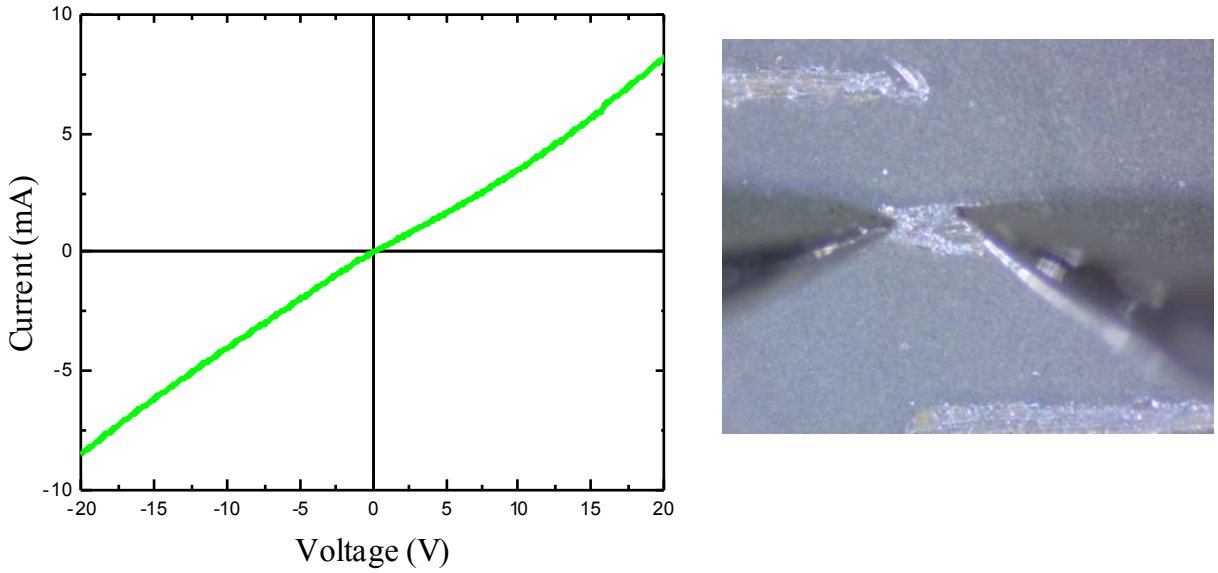

Figure 5.11: Current versus voltage characteristic and optical image of the probes on the scratch used to reach the n-type GaN.

probes are on the n-type GaN. This step is very challenging because of the scratch quality as well as the presence of the p-GaN layer and/or oxidation. Once the ohmic behavior of the $I-V$ is confirmed, we moved one probe to the nano region. This step is not an easy task. A custom designed holder is used for putting the probes on a 60×60 μm^2 area of the nano-region as shown in Figure 5.12. This holder has specially designed probes/tips able to cover the nano-region only

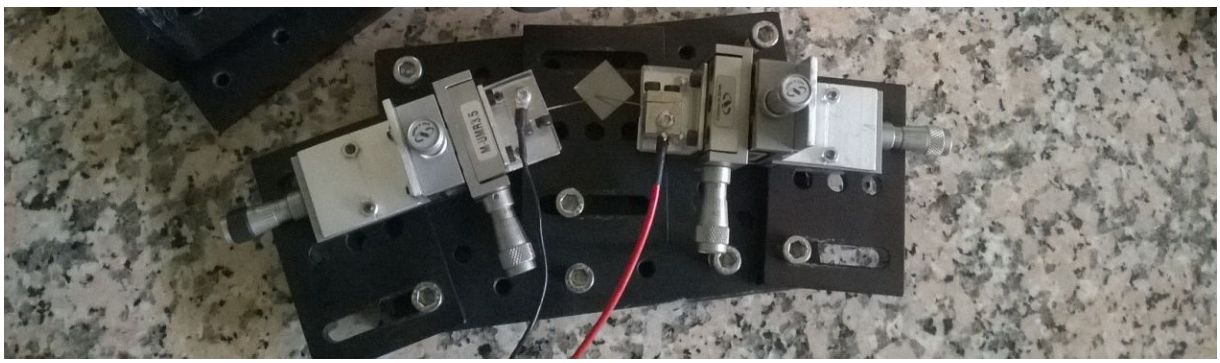

Figure 5.12: Custom designed holder used for the current versus voltage characteristic of the InGaN nano PIN structure before processing.

without touching the field, compared to the classical probes that comes with the probe station which are too thick for this type of measurements. Another interesting feature of this holder is adjusting the probes under a microscope, because it's difficult to locate the nano-region in the standard probe station with a CCD camera.

Figure 5.13 shows the dark current density versus voltage ($J-V$) characteristics of the InGaN nano PIN structure before processing. The ideality factor is deduced from the dark

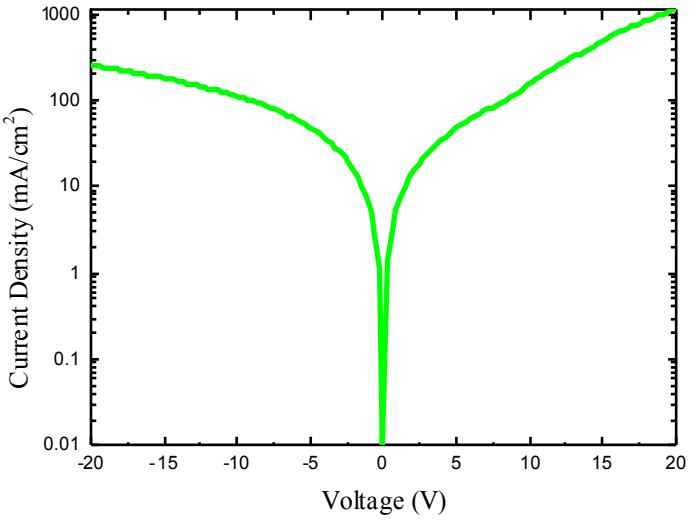

Figure 5.13: Current density versus voltage characteristic of the $In_{0.09}Ga_{0.91}N$/GaN nano-structure solar cell under dark conditions.

$J-V$, using the standard diode equation, given as,

$$V_{oc} = I_0 \left(exp(\frac{qV}{nkT}) - 1 \right) \tag{5.1}$$

where I_0 is the dark current, kT/q is the thermal voltage, at 300K is 25.85 mV, V is the voltage across the diode and n is the ideality factor. The ideality factor deduced from the dark $J-V$ (Figure 5.13(b)) is 10.2, which is rather high. This is attributed to the carrier tunneling as discussed in previous chapter.

The dark $J-V$ shows a high leakage current and large effect of the series resistance, as expected due to no metal contacts. This should contribute to the reduction of V_{oc} and fill factor (see Appendix B for effect of shunt and series resistances). The $J-V$ characteristics of the InGaN nano PIN structure under concentrated light and measurement setup are shown in Figure 5.14. The indium concentration is 9%, corresponding to an absorption below 403 nm, therefore we used a UV light source instead of AM 1.5G which has negligible power below 400 nm. The power estimation equivalence to number of suns given in Figure 5.14 is explained in Appendix E. The device shows encouraging results under illumination. The J_{sc} shows linear dependence on the light intensity and V_{oc} increases logarithmically, consistent to our discussion in previous chapters. According to the shape of the $J-V$ measurements, the fill factor is low. This could be due to the high series resistance at the n-contact. The fill factor dependence on the number of suns for InGaN nano-structure is presented in Figure 5.15 with a comparison to bulk $In_{0.12}Ga_{0.88}N$ PV. For InGaN nano PV device, the fill factor decreases with the increase of light intensity. This is due to the power loss caused by the electrical series resistance R_s which increases with the icnrease of current [156]. R_s comes from the epitaxial layers of semiconductor material, contact resistance, etc. In our case the R_s could be due to the scratch that we used for

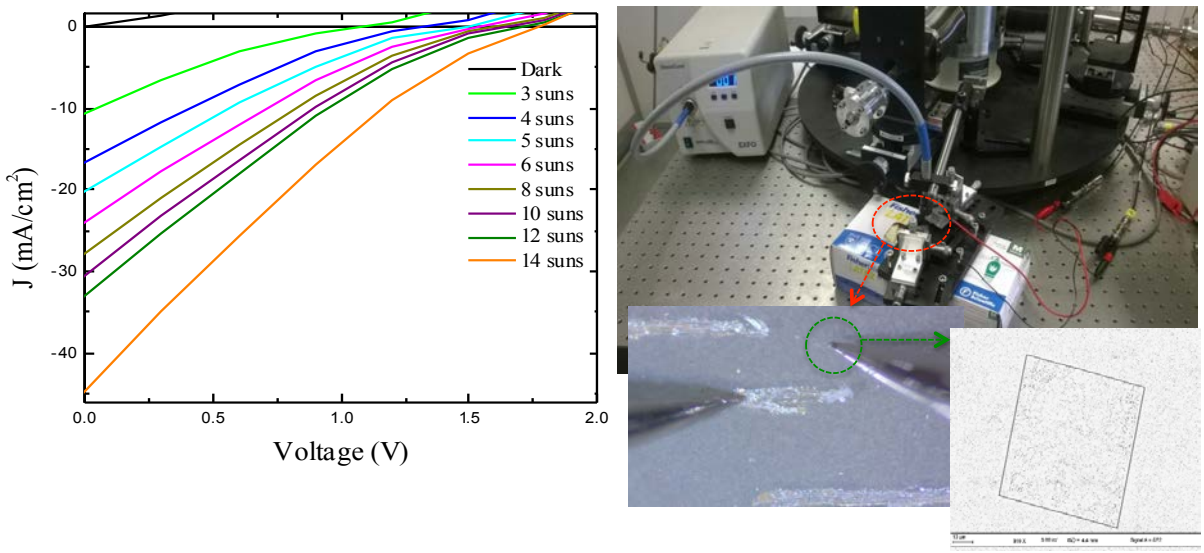

Figure 5.14: Current density versus voltage characteristic and the setup used for the $J-V$ measurements of the InGaN nano PIN structure under UV illumination before processing.

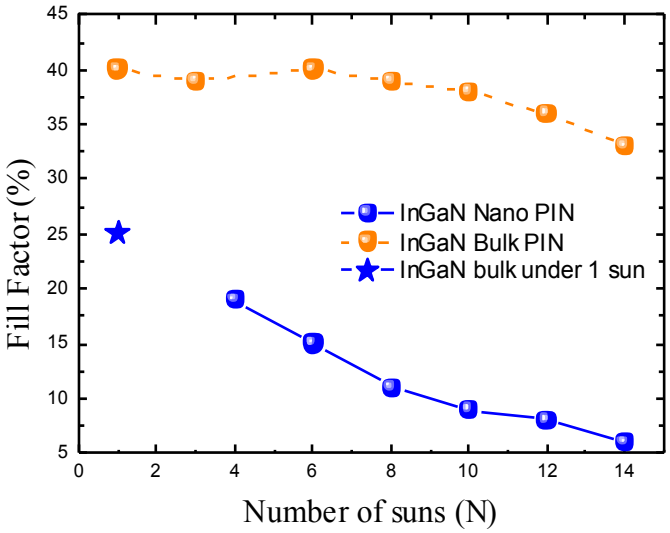

Figure 5.15: Dependence of fill factor on input light intensity for InGaN nano-structure, InGaN semibulk and InGaN bulk PV devices.

the n-contact. In contrast the fill factor for InGaN bulk PV device is constant upto 6 suns and then decreases with further increase in the light intensity. As mentioned before, this decrease is due to the power loss caused by the electrical series resistance R_s under higher current. The fill factor under 4 suns is lower in InGaN nano compared to bulk due to the use of scratch with high series resistance.

→ **Current - Voltage Measurements - After Processing**

After the device processing, we observe that the p-GaN is not etched enough to reach the n-GaN as shown in Figure 5.16. That means that both the metals contacts (p-contact and n-contact) are deposited on top of p-GaN. This problem left us with no other option but to use a scratch for the n-contacting. In addition to that several other issues such as, the non-spreading

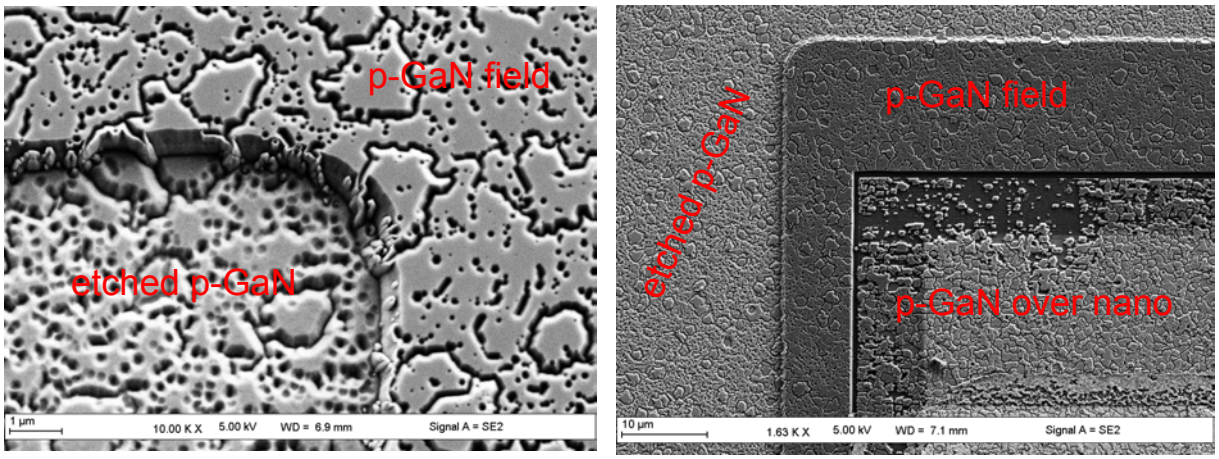

Figure 5.16: SEM images of the p-GaN surface of InGaN nano PIN structure after etching the p-GaN to reach the n-type GaN.

of the metal contact over the entire nano-region, the cracking of the p-GaN metal contact due to over annealing and a direct contact of the metal with the InGaN nano-structure (in the absence of p-GaN regrowth over the nano) as shown in Figure 5.17 degraded the performance of the devices, and only few InGaN nano PV devices out of more than 200 devices are found functioning.

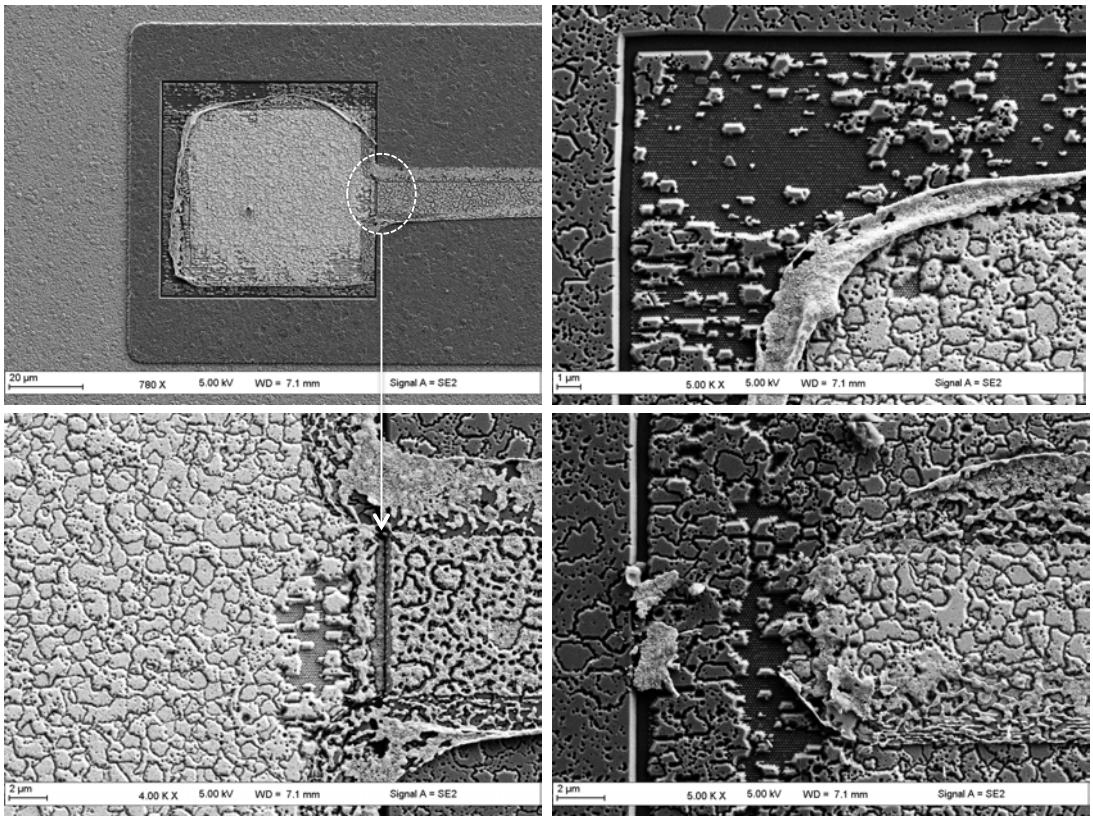

Figure 5.17: SEM images of the p-GaN surface of InGaN nano PIN structure after etching the p-GaN to reach the n-type GaN.

Figure 5.18 shows the current density versus voltage ($J-V$) characteristics of the fabricated $In_{0.09}Ga_{0.91}N$/GaN nano PV cell measured under concentrated light equivalent to 3 suns (see Appendix E for estimation of number of suns). For these measurements it is possible to use the

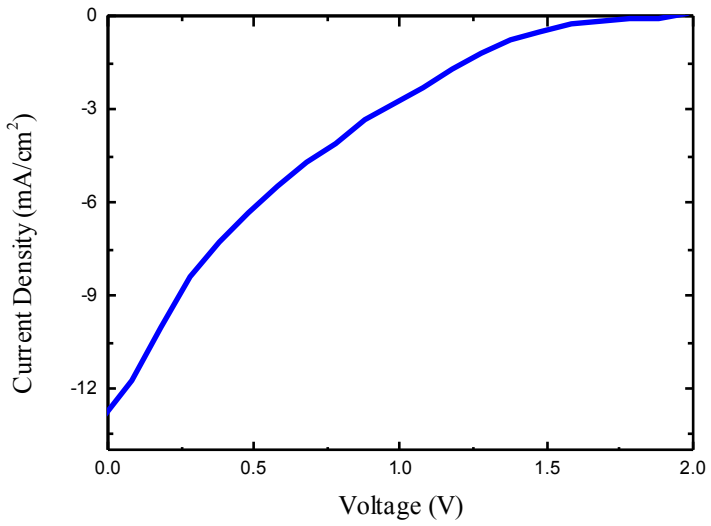

Figure 5.18: Current density versus voltage characteristic of the fabricated $In_{0.09}Ga_{0.91}N$/GaN nano-structure solar cell under UV concentrated light (equivalent to 3 suns).

classical probe station as shown in Figure 5.19 rather than the customized holder. However, as mentioned earlier, a scratch is used to reach the n-type GaN contacting. Table 5.1 lists the

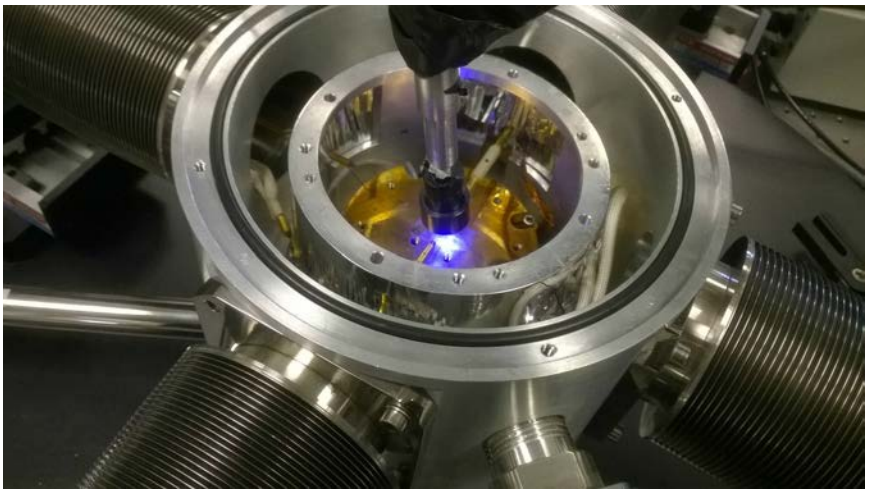

Figure 5.19: Measuring the Current density versus voltage for $In_{0.09}Ga_{0.91}N$ nano-structure solar cell under concentrated light.

values for J_{sc}, V_{oc} and fill factor (FF) deduced from the $J-V$ measurements before and after processing. It is to be noticed that, the full device area (60×60 μm^2) is taken into account for calculating the J_{sc}, however the nano-device includes InGaN nano-structures separated by SiO_2 mask that should reduce the effective area of the device as shown in Figure 5.20. The SiO_2 mask covers 25% of the total device area (60×60 μm^2), leading to an effective device area of 52×52 μm^2. This should lead to an increase of J_{sc} by 25%. The V_{oc} is slightly improved after processing but it's still lower than the expected theoretical value (2.54 V). This could be due to the presence of the cracks and deep V-pits in the p-GaN layer. The J_{sc} has improved after processing, probably because it is now fully exposed to the light. The fill factor decreased to

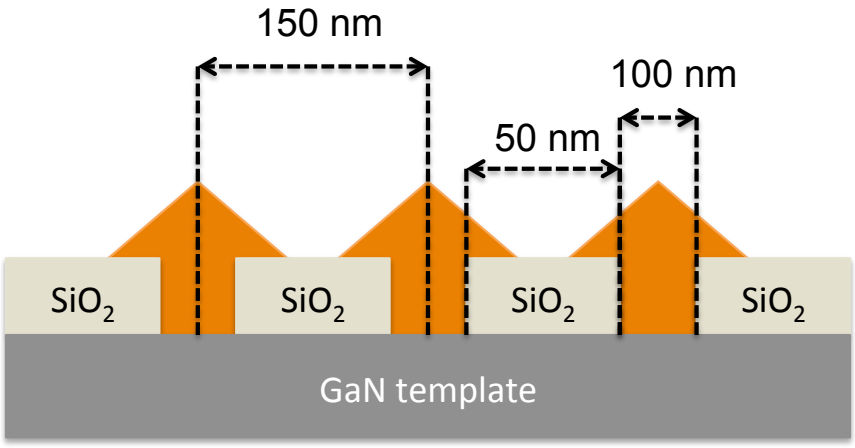

Figure 5.20: Schematic of the InGaN nano-structure for calculating the effective area of the device and SEM image of the mask indicating the distance between two consecutive InGaN nano-structures.

13% from 20% (see Table 5.1). This is due to the increase in J_{sc} after processing that increases the series resistance effect. These results show that the series resistance is mainly due to the scratch used for the n-contacting.

Table 5.1: Comparison of V_{oc}, J_{sc} and fill factor of the InGaN nano PV device before and after processing.

	V_{oc}	J_{sc}	FF	Light intensity
Before processing	1.75 V	10 mA/cm^2	20 %	UV illumination (3 suns)
After processing	1.89 V	12.8 mA/cm^2	13 %	UV illumination (3 suns)

5.4 Comparison of InGaN Nano-Structure PV Devices

Table 5.2 lists a comparison of performances of InGaN nano-structure devices to the one of the semibulk based PV device presented in the chapter 4 under 1 sun condition. For that, we extrapolated the value of the fill factor to 1 sun (see Figure 5.15), that gives a value of 19% for the fill factor (under 1 sun) after processing, listed in Table 5.2. Considering only the effective area of the InGaN nano PV device, the J_{sc} is almost 9 times larger than that of the J_{sc} measured for the semibulk $In_{0.08}Ga_{0.92}N$ structure. This could be attributed to the light trapping effect due to the rough p-GaN surface. As reported by Neufeld *et al.* [63] rough p-GaN surface results in an increase of the J_{sc}, due to the optical path length enhancement associated with increased scattering off of the rougher p-GaN surface. Another possibility could be the increase of the optical path length of the light inside the solar cell due to change in incidence angle by the InGaN nano pyramids. The V_{oc} is rather of the same order of magnitude and as mentioned earlier this rather low value could be attributed to the cracks and deep V-pits in the p-GaN layer. The difference in the fill factor is expected due to the high series resistance that comes from the scratch. This leads to a power conversion efficiency of 1.30% under a power density equivalent to 1 sun for InGaN nano PV device.

Table 5.2: Comparison of V_{oc}, J_{sc}, fill factor and efficiency of InGaN nano-structure to our semibulk InGaN approach (∗ The effective area of the device is taken into account)

Reference	Absorber (Thickness)	V_{oc} (V)	J_{sc} mA/cm^2	FF (%)	η (%)	Source
nano-structure* approach	$In_{0.09}Ga_{0.91}N$ (100 nm)	1.28	5.26	19	1.30	UV Light (1 sun)
semibulk approach	$In_{0.08}Ga_{0.92}N$ (144 nm)	1.04	0.57	64	0.39	AM 1.5G

Table 5.3 presents a comparison of the performances of our InGaN nano-structure PV device to the literature with InGaN nano-wires. The V_{oc} of our InGaN nano-structure PV device is

Table 5.3: Device performance reported for nano-structure PV cells (∗ The area of the InGaN nano PV device is corrected and only the effective area of the device is taken into account.

	Absorber	V_{oc} (V)	J_{sc} (mA/cm^2)	FF %	Efficiency (%	Source
Our nano* structure approach	$In_{0.09}Ga_{0.91}N$ (100 nm)	1.28	5.26	19	1.30	UV Light (1 sun)
Wierer *et al.* [120]	$In_{0.015}Ga_{0.985}N$	0.50	1	54 %	0.30	1 sun
Dong *et al.* [121]	$In_{0.27}Ga_{0.73}N$	1	0.39	56	0.19	1 sun

higher than the literature. The J_{sc} even with 9% indium concentration, is almost 5 or 10 times of what has been reported for nano wire InGaN PV devices with 10% and 27% indium concentration. This leads to a power conversion efficiency for our InGaN nano-structure based PV solar cells which is four times higher than the power conversion efficiency for nano InGaN structure PV cells. It is to be noticed that the 0.3% power conversion efficiency is the highest recorded in III-nitride nano wire solar cells by Wierer *et al.* [120]. However, the power conversion efficiency calculated for our InGaN nano PV device is based on rough estimations, therefore it's difficult to conclusively compare it to the literature and attribute the improvement to a single parameter.

5.5 Summary and Perspectives

The demonstration of the InGaN nano-structured device, to our knowledge is the first ever demonstration of a functional PV cell based on bulk InGaN nano-structures. Thick, high structural quality and defect-free InGaN nano-structure absorber layer is obtained with the nano selective growth approach. The PV devices results in a J_{sc} of 12 mA/cm^2 and a V_{oc} of 1.89 V under concentrated light. The key finding is that the bulk InGaN nano-structure is an elegant approach for the realization of high efficiency InGaN solar cells. These results are very encouraging as the technique may overcome current limitations in the growth of high quality thick InGaN nano-structures and may be important for the realization of InGaN-based high efficiency solar cells. For our future studies, thick high quality InGaN nano-structure with smooth p-GaN surface morphology have been grown as shown in Figure 5.21.

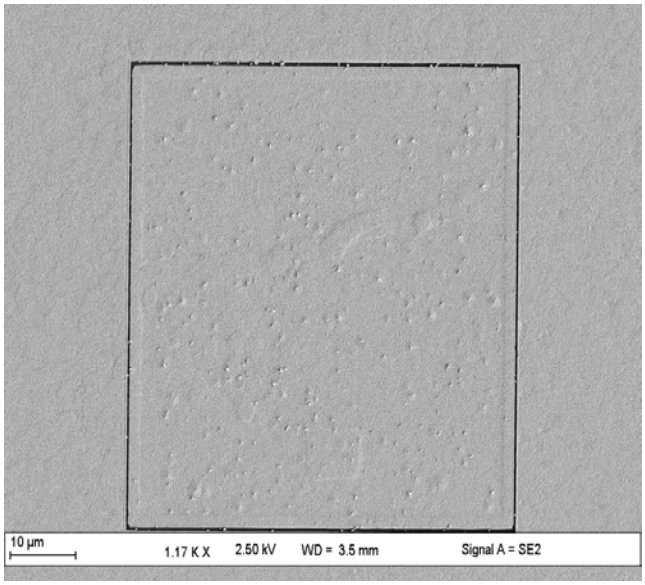

Figure 5.21: SEM images of the top surface of the InGaN nano PV structure for our future studies.

The p-GaN surface morphology has significantly improved compared to the InGaN nano PIN structures presented in this chapter. The device processing has been also improved by overcoming all the technologies issues observed in our previous InGaN nano-devices. With our new optimized device processing and growth conditions, these high quality thick InGaN PIN structures should result in significant improvement of the overall power conversion of InGaN solar cells.

The ability to incorporate more indium in the nano-structures depending on the geometry of the patterns and to grow selectively defect-free thick InGaN nano-structures via a simple patterning process offers a new route to develop monolithic InGaN-based high efficiency solar cells.

Chapter 6

Conclusion and Perspectives

6.1 Conclusions

The InGaN material system, with its bandgap from 0.7 eV to 3.4 eV spanning the entire visible spectrum, enables the design of multijunction solar cells of maximum efficiency. The high energy radiation resistance and high absorption coefficient (10^5 cm^{-1}) makes InGaN a potential candidate for high efficiency concentrated photovoltaic (PV) devices. The pre-requisite for the development of high efficiency InGaN solar cells is the growth of high crystalline quality thick InGaN epitaxial layers, which must be larger than 100 nm thick in order to absorb 90% of incident above- bandgap light. Despite its high optical absorption coefficient, the ability of InGaN to collect photogenerated carriers has been hindered by poor crys- talline quality. It is unsurprising that thick InGaN layers exhibit poor optical performance since the critical layer thickness for a fully strained high quality InGaN with high In content is only a few nanometers. In theory the unique properties of InGaN should translate into high efficiency, long lifetimes, and ultra thin solar cells. However, tuning the bandgap of InGaN epitaxial layer to lower energy with high indium incorporation has proven difficulties such as phase separation (compositional instability) due to the poor miscibility of InN and GaN and relaxation of the mismatch stress accommodated in the InGaN layers due to its growth on foreign substrates (with lattice and thermal expansion coefficient mismatch).

This thesis focused on investigating new approaches that could help to obtain high efficiency InGaN solar cells by overcoming the challenges mentioned above. Two novel approaches have been proposed (developed by our team) for the realization of high efficiency InGaN solar cells, and are compared to the classical bulk InGaN heterojunction solar cells. The first approach consists in the growth of a thick multi-layered InGaN/GaN absorber, called semibulk approach. The periodic insertion of the thin GaN interlayers should absorb the excess indium and relieve compressive strain. The InGaN layers need to be thin enough to remain fully strained and without phase separation. The second approach consists in the growth of InGaN nano-structures for the achievement of high indium content thick InGaN layers. It allows the elimination of the preexisting dislocations in the underlying template. It also allows strain relaxation of InGaN layers without any dislocations, leading to higher indium incorporation and reduced piezoelectric effect.

In the first part of the thesis, we studied, using $J - V$, SEM, HAADF-STEM, and EBIC characterization, the influence of the dislocations and V-pits on the overall conversion efficiency of bulk $In_{0.12}Ga_{0.88}N$ absorber based heterojunction solar cells. Using EBIC, we showed that the phenomenon of impurity gettering, which forms an impurity depleted zone around the threading dislocations and V-pits, significantly contributes to the enhancement of the extraction of the photo generated carriers in the InGaN absorber, resulting in a peak external quantum efficiency of 79% and a short circuit current density of 2.56 mA/cm^{-2} under an AM 1.5G solar spectrum,

i.e. a value twice the state of the art. Meanwhile, a high density of deep V-pits leads to large recombination, resulting in high leakage current, hence reducing the open circuit voltage. Since a low growth temperature for the p-GaN layer, leading to a high dislocation and pit density, is mandatory, a way to favor the formation of shallow against deep V-pits, should help to preserve and perhaps to improve InGaN based PV device performances. The key findings of the study are,

- As soon as the total pit density is decreased, a lowering of J_{sc} and an increase of V_{oc} are observed,
- To increase both J_{sc} and V_{oc} an increase of the shallow V-pit (size lower than 300 nm) density and a decrease of the deep V-pit (size larger than 300 nm) density are required,
- To decrease both J_{sc} and V_{oc} a decrease of the shallow V-pit (size lower than 300 nm) density and an increase of the Deep V-pit (size larger than 300 nm) density are required,
- An increase of the shallow V-pit density (size lower than 300 nm) leads to an increase of J_{sc},
- An increase of the Deep V-pit (size larger than 300 nm) density leads to a decrease of V_{oc}.

In the second part of the manuscript, we presented our first approach "Semibulk" as a potential candidate for replacement of the currently used absorber designs. The semibulk InGaN absorber based PV devices show significant improvement in the performance of the solar cells. The results obtained for the semibulk $In_{0.08}Ga_{0.92}N$-based PV cell show that the InGaN semibulk absorber approach is an effective method for achieving high efficiency InGaN PIN heterojunction solar cells. The semibulk absorber approach effectively helps to suppress the transition from two-dimensional to three-dimensional growth that occurs during the growth of thick epitaxial InGaN layers. The key finding is that solar cells based on semibulk absorber results in high power conversion efficiency in-spite of high density of structural defects in the p-GaN. The device has a power conversion efficiency of 0.39% under an AM 1.5G solar spectrum, almost three times higher than the current state of the art. Reducing absorption of light in metal contacts and using a back reflecting mirror will increase quantity of light to be absorbed by the active region, leading to further improvement of power conversion efficiency. The device has a maximum external quantum efficiency peak of 85% which is the highest external quantum efficiency peak reported so far for an InGaN PIN heterojunction solar cell. The J_{sc} measured under AM 1.5G is almost four times as high as previously reported values for 8% indium concentrations and thus confirms efficient light absorption and photocarriers collection in the semibulk absorber. The results obtained for semibulk $In_{0.12}Ga_{0.88}N$ solar cell agrees well with our proposed explanation that V-pits, particularly the shallow V-pits results in enhancement of the J_{sc} due to the formation fo impurity depleted zones around, whereas the deep V-pits results in a high leakage current, reducing the V_{oc} of the PV cell.

In order for InGaN materials to gain serious consideration for photovoltaics and compete with traditional single gap solar cell materials, we proposed another novel approach referred as the InGaN nano-structure PV cells. The growth of GaN and/or InGaN epitaxial layers on sapphire substrate suffers from a large mismatch of the lattice constants and the thermal expansion coefficients between the substrate and epitaxial structures causing large accumulation of strain and high dislocation densities generated in the epitaxial layers. These dislocations are believed to correlate to the carrier trap centers and the parasitic tunneling current, unavoidably leading to non-radiative recombination. A possible solution for preventing the strain-related limitations for the growth of thick InGaN epitaxial layer with high indium concentration and reduction of the threading dislocations is the nano-selective area growth (NSAG). This approach allows the elimination of the preexisting dislocations in the underlying template [157]. It also allows the strain relaxation of the InGaN material without any dislocations, leading to higher

indium incorporation [128, 158] and reduced piezoelectric effect. The PV devices for InGaN nano-structure approach show encouraging results. The nano-structure provide an opportunity to incorporate high indium concentration free from the intrinsic material defects. The ability to incorporate more indium depending on the geometry of the patterns and to grow selectively defect-free thick InGaN nano-structure via a simple patterning process offers a new route to develop monolithic InGaN-based high efficiency solar cells. The results obtained for InGaN nano-structure PV devices show significant improvement in the power conversion efficeincy compared to our semibulk apporach as well as bulk InGaN structures reported in the literature. The power conversion efficiency under 1 sun illumination is around 1.02% compared to the 0.30% of semibulk c. The J_{sc} of the InGaN nano PV device is around 5.26 mA/cm^2 which is alomost 9 times of the J_{sc} measured in semibulk $In_{0.12}Ga_{0.88}N$. The high series resistance significantly reduced the fill factor (20%) of the InGaN nano-PV cells, eventually leading to a low power conversion efficiency. Several critical challenges are involved in the device processing of the InGaN nano-structure PV cells due to their small size (60 $\times$ 60 μm^2). Optimization of the metal contacting and device processing will result in improvement of the InGaN PV cells based on nano-structure approach.

6.2 Perspectives

The trade-off between the degradation of the InGaN absorber during the growth of the subsequent top p-GaN layer and crystalline quality of the p-GaN epitaxial layer, remained a major challenge during our study, making difficult to utilize the full potential of our new approaches for high efficiency solar cells. Two possible options that could circumvent these issues, includes p-GaN growth using a different epitaxial growth technique like MBE and InGaN Schottky Solar Cells.

6.2.1 Growth of P-GaN via MBE

The growth temperature of the subsequent top p-GaN layer is very challenging in MOVPE espeically on top of InGaN absorber with $>$ 10% of indium concentration. The high growth temperature of the subsequent top p-GaN layer leads to unfavorable effects such as lattice relaxation and composition redistribution in the $In_xGa_{1-x}N$ absorber [60]. Decreasing the growth temperature of the p-GaN epitaxial layer leads to a rather low crystal quality of the p-GaN layer During the optimization study, we observed that p-GaN layer grown above 850°C, for indium incorporation above 10% in the absorber results in severe degradation of the InGaN active layer, leading to poor performance of the solar cell. This restriction of the growth temperature for the p-GaN epitaxial layer by MOCVD limited the efficiency of our semibulk absorber approach. The high quality growth of p-GaN epitaxial layer at lower temperature by MBE could circumvent the issues observed in MOCVD. Therefore, for the optimum use of semibulk approach for realization of high efficiency solar cells, it would be a good choice to grow the p-GaN layer via MBE. For this a semibulk $In_{0.14}Ga_{0.86}N$ PV structure grown on a 2" wafer, as shown in Figure 6.1 has been provided to our partner laboratory for the top p-GaN re-growth via MBE. The growth of high crystalline quality p-GaN layer without any InGaN degradation will definitely enhance the device performance leading to a high power conversion efficiency. This would also help in further increase of the indium incorporation in the InGaN epilayers.

6.2.2 InGaN Schottky Solar Cells

Schottky diodes have also been widely used for a wide variety of applications such as photodetectors, Schottky-clamped transistors, metal gate field-effect transistor, radio frequency atten-

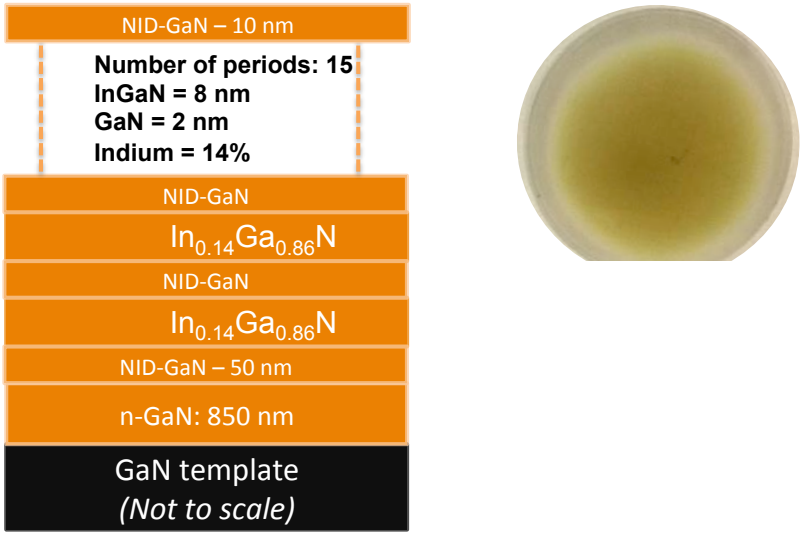

Figure 6.1: Semibulk $In_{0.14}Ga_{0.86}N$ PV structure grown for p-GaN re-gorwth via MBE.

uator, and rectifiers. InGaN Schottky solar cells configuration can be employed for the photo-generated carrier collection, without any impact of the p-GaN epitaxial layer. More specifically, thin metal (Ni/Au) bi-layers are placed in intimate contact with the InGaN to demonstrate the viability of InGaN Schottky barrier solar cells. Developing the high-quality and large-area InGaN Schottky contacts is a very meaningful work, but, at the same time, it is rather difficult for n-InGaN to obtain high-quality Schottky contacts due to a large amount of surface defects in InGaN layers. The main advantage of a Schottky barrier solar cell is the presence of the depletion region right next to the metal surface which reduces the surface recombination probability and thus, improves the spectral response for high energy photons. However, Schottky barrier solar cells have a few limitations. A Schottky barrier solar cell cannot produce high open circuit voltages because the maximum value is limited by the potential energy difference between the metal work function and semiconductor electron affinity. Whereas, for a p-n junction solar cell, the open circuit voltage can be roughly x% of the semiconductor band-gap. Secondly, in the case of highly doped semiconductors, thin barrier layers may result in tunneling of carriers which will reduce the photocurrent. Moreover, the material interface between the semiconductor and metal contains interface states which may trap charge and reduce the open circuit voltage. So far, there are only limited works on Schottky barriers of metal/n-InGaN [159–162], but the performances of Schottky contacts in these works are still very restricted due to the presence of a large number of defects in InGaN films.

The energy band diagram for a Schottky barrier (metal/n-semiconductor) solar cell is shown in Figure 6.2. The current density versus voltage characteristic of a Schottky barrier solar cell under illumination is similar to the PN junction equation, given by,

$$J = J_{sc} - J_0(e^{(qv/nK_BT} - 1) \tag{6.1}$$

where J_0, the saturation current density, is now given by:

$$J_0 = A^{**}.T^2.exp(-q\phi_B/K_BT) \tag{6.2}$$

where A^{**} is known as the Richardson constant and ϕ_B is the Schottky barrier height.

The structure of Ni/Au/InGaN/GaN Schottky solar cells is shown in Figure 6.3.

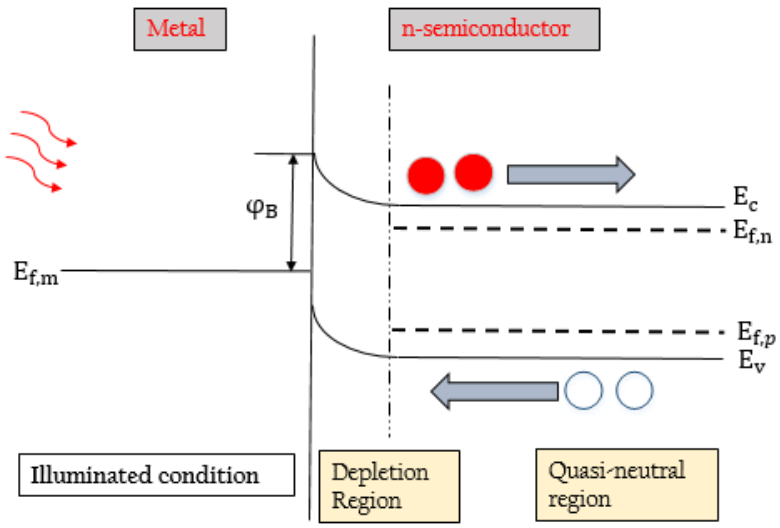

Figure 6.2: Energy band diagram of Schottky Barrier Solar Cell under illumination.

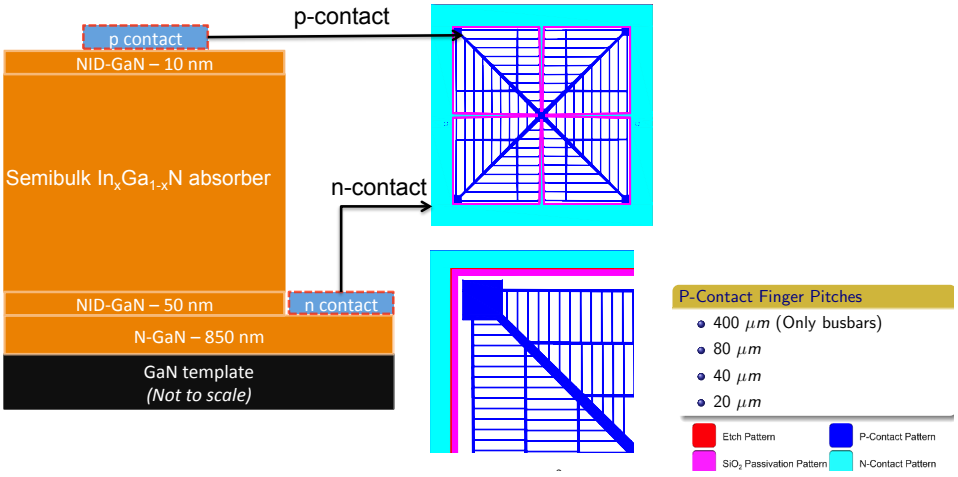

Figure 6.3: The structure of InGaN/GaN Schottky solar cell with p-contact n-contact grid type designs.

The device structure has a square-shaped mesa surrounded by another metal trace (Ti/Al/Ti/Au) that serves as the bottom-side electrode, forming an ohmic contact ohmic to n-type GaN. Different electrode geometries have been used for fabrication same GaN/InGaN layer structure that will also help in studying the effect of series resistance and light absorption loss within the metal contacts. For a detail study of InGaN Schottky solar cell, a number of PV structures are grown as listed in Table 6.1.

Table 6.1: List of bulk and Semibulk PV structures grown for $In_xGa_{1-x}N$ Schottky solar cells.

Referernce No.	Type	Indium	InGaN/GaN	No. of Periods	absorber thickness
T841-SB	Semibulk	8.5 %	24/2 nm	6	154 nm
T942-SB	Semibulk	8 %	24/2 nm	6	154 nm
T945-B	Bulk	10.5 %	-	-	130 nm

Referernce No.	Type	Indium	InGaN/GaN	No. of Periods	absorber thickness
T946-SB	Semibulk	16 %	24/2 nm	6	154 nm
T947-B	Bulk	18 %	-	-	130 nm
T949-SB	Semibulk	18 %	10/2 nm	15	178 nm
T950-SB	Semibulk	16 %	10/2 nm	15	178 nm
T951-SB	Semibulk	16 %	10/2 nm	15	178 nm
T952-B	Bulk	16 %	-	-	130 nm
T956-SB	Semibulk	12 %	8/3 nm	17	184 nm
T957-SB	Semibulk	14.3 %	8/1.5 nm	17	160 nm

The SEM images of the surface morphology of the PV structures grown for InGaN Schottky solar cells are shown in Figure 6.4. The initial demonstration of the metal contacting show that

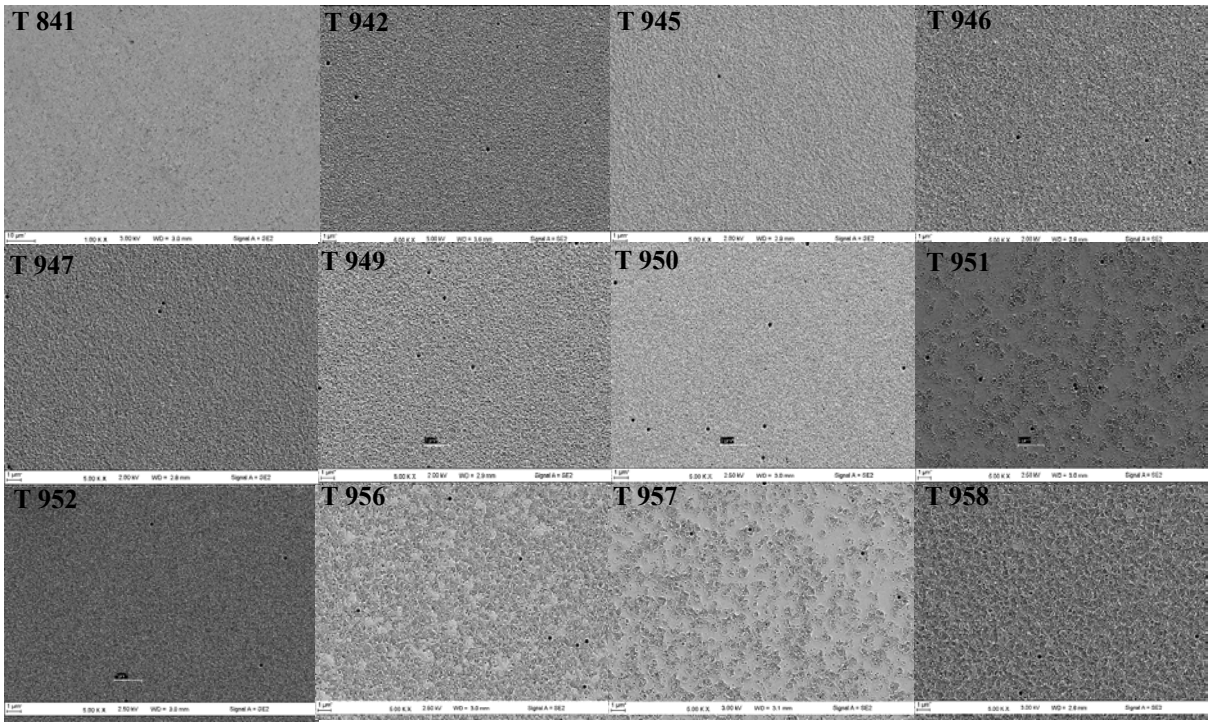

Figure 6.4: Surface morphology of different PV structures (listed in Table 6.1) grown for InGaN Schottky solar cells.

special attention is needed in obtaining high quality Schottky metal contacts. The selection of metals and surface treatment before lithography are crucial parameters that needs further optimization.

6.2.3 InGaN Nano-structure with >35% of Indium Composition

Photovoltaic devices with a bandgap greater than 2.0 eV are attractive because over half the available power in the solar spectrum is above the photon energy of 2.0 eV. To achieve this energy bandgap, high crystalline quality InGaN epitaxial layers with indium concentration above 35% are required, which can only be made possible using the novel InGaN nano-structure approach. Therefore an important future perspective of InGaN nano-structure solar cells is to incorporate high indium concentration *above 35%*. Though our team already obtained 33% of indium concentration in the InGaN epitaxial layer grown by nano-selective area growth on patterned AlN/Si (111) substrates as shown in Figure 6.5, but a further optimization study is needed in obtaining similar structures on sapphire substrates that could than be used for the realization of high efficiency InGaN solar cells.

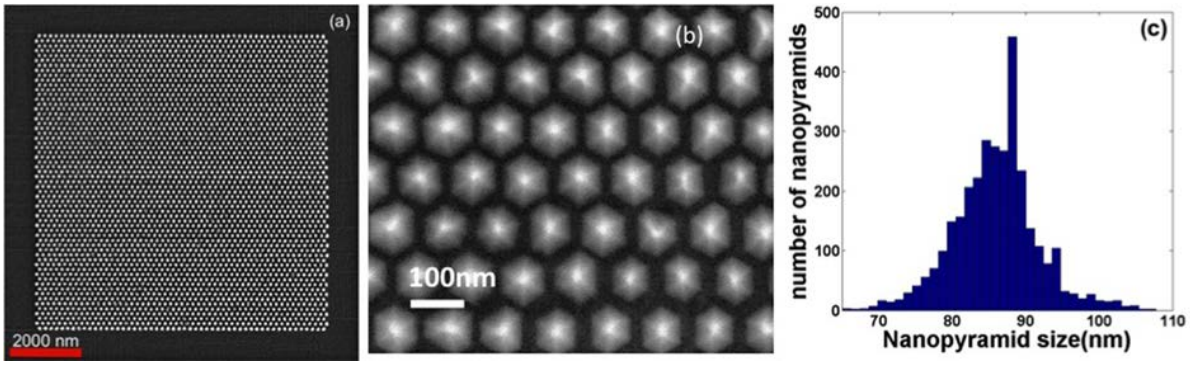

Figure 6.5: (a) SEM image of the InGaN nano-pyramids grown on the patterned AlN/Si template. The size (distance between the two opposite edges) of the patterned area is 10 $\times$ 10 μm^2, (b) Higher magnification SEM image of the InGaN nano-pyramids, (c) Size distribution histogram of InGaN nano-pyramids grown on AlN/Si (111).

Appendices

Appendix A

Introduction to III-Nitride Materials

The wide band gap III-Nitride are compounds of binary, ternary and quaternary (Ga,Al, In,B)-N alloys. They have been considered as promising system for opto-electronic devices. The III-nitrides family, AlN, GaN InN can crystalline in rocksalt, zinc-blende poly-types and Wurtzite. Epitaxial growth of rock-salt is not possible and is only possible under high pressures e.g. its 22.9GPa for AlN [163], 52.2 GPa for GaN [164] and 12.1 GPa for InN [165]. It has a space group of F $\bar{3}$m in the Hermann-Mauguin notation. The graphical representation of the ideal Zincblende is shown in Figure A.1. It has a cubic unit cell, containing four group III elements and four nitrogen elements. Its space group structure in the Hermann-mauguin notation is F $\bar{3}$3m.

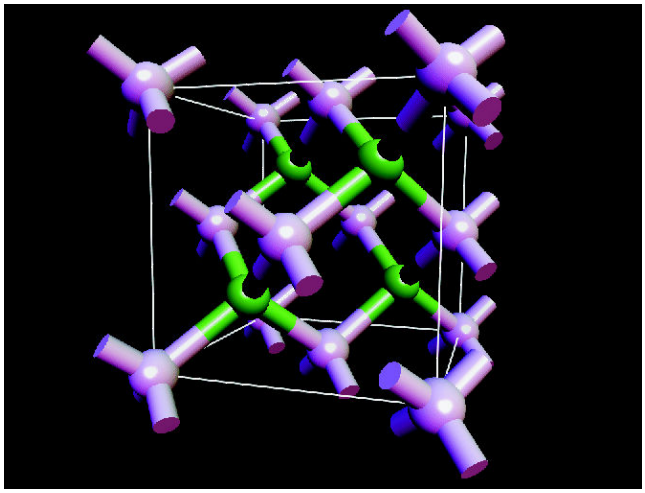

Figure A.1: 8-atom cubic cell of zinc blende GaN. Ga atoms are represented by large grey spheres, and N atoms by smaller green spheres [166].

Wurtzite is the most thermodynamically stable and commonly achieved phase in current high quality III-Nitride based optoelectronic devices grown usually by Metal Organic Vapor Phase Epitaxy (MOVPE). A graphical representation of the ideal wurtzite cell is shown in Figure A.2. It contains six atoms of each type. The space grouping for the wurtzite structure is $P6_3mc$ in the Hermann Mauguin notation. Wurtzite crystal is a member of the hexagonal crystal system and the structure is closely related to the structure of hexagonal diamond. The wurtzite and zincblende structures differ only in the bond angle of the second nearest neighbor. Three common types of crystal planes are usually used in a wurtzite system represented as (0001) c-, $(11\bar{2}0)$ a-, $(1\bar{1}00)$ m- planes with their respective directions as <0001>, $<11\bar{2}0>$ and $<1\bar{1}00>$ shown in Figure A.3. The c-plane is referred as **polar plane**. The asymmetry along the c-axis is the cause of this polarity. Crystal planes ($(11\bar{2}0)$a- and $(1\bar{1}00)$m-) parallel to the

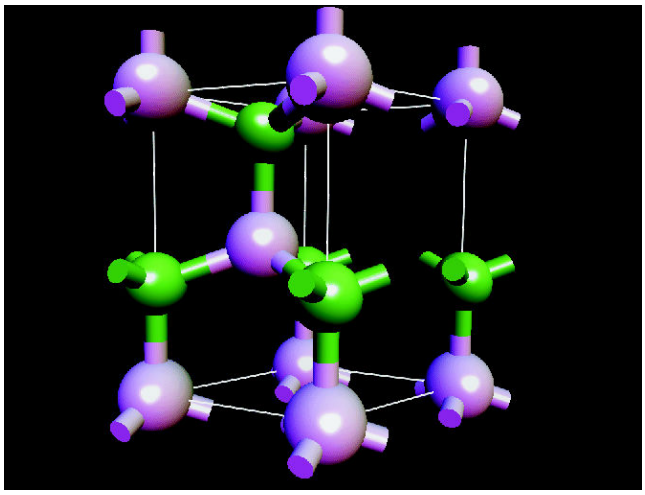

Figure A.2: 8-atom cubic cell of zinc blende GaN. Ga atoms are represented by large grey spheres, and N atoms by smaller green spheres [166].

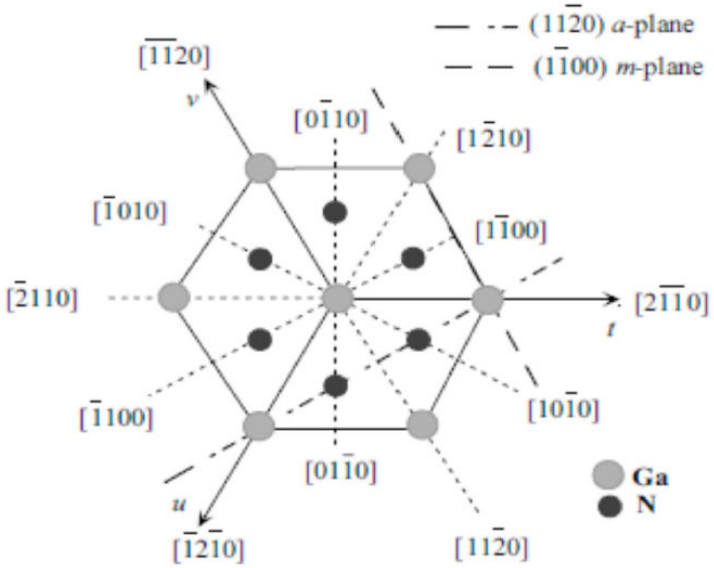

Figure A.3: Crystal planes used in a wurtzite system.

c-axis are referred as non-polar, because there are equal number of threefold coordinated Ga and N leading to charge neutrality. The planes making an angle other then 0°and 90°with c-axis are called semi-polar planes.

The lattice parameters and thermal properties for GaN, AlN and InN are given in Table A.1. The epitaxial growth of III-Nitride epilayers on bulk substrates results in the presence of in-plane strain. Depending on whether the lattice parameter of the epilayer is smaller or greater than the lattice parameter of the substrate. The two possible outcomes of the lattice parameters thus defines whether the strain is compressive or tensile. The critical thickness of the epilayer can thus be fully strained, partially or fully relaxed depending upon its thickness. The relaxation of the top epilayer to its own lattice parameters degrades the crystalline quality, thus creating defects known as dislocations. The mechanical deformations that may happen for the two possible outcomes of the lattice parameters i.e. in-strain plane or out-of-plane strain plane are shown in Figure A.4.

Table A.1: Lattice parameters and thermal properties of wurtzite GaN, InN and AlN [167] [168].

Material	Lattice parameters (A°)		Energy bandgap	Thermal expansion coefficient	Lattice mismatch with GaN
	a	c	at 300 K (eV)	($10^{-6}K^{-1}$)	(%)
GaN	3.19	5.19	3.42	5.6	0
InN	3.54	5.70	0.65	2.85-3.15(at 300 K)	+11
AlN	3.10	4.97	6.2	4.2	-2.7

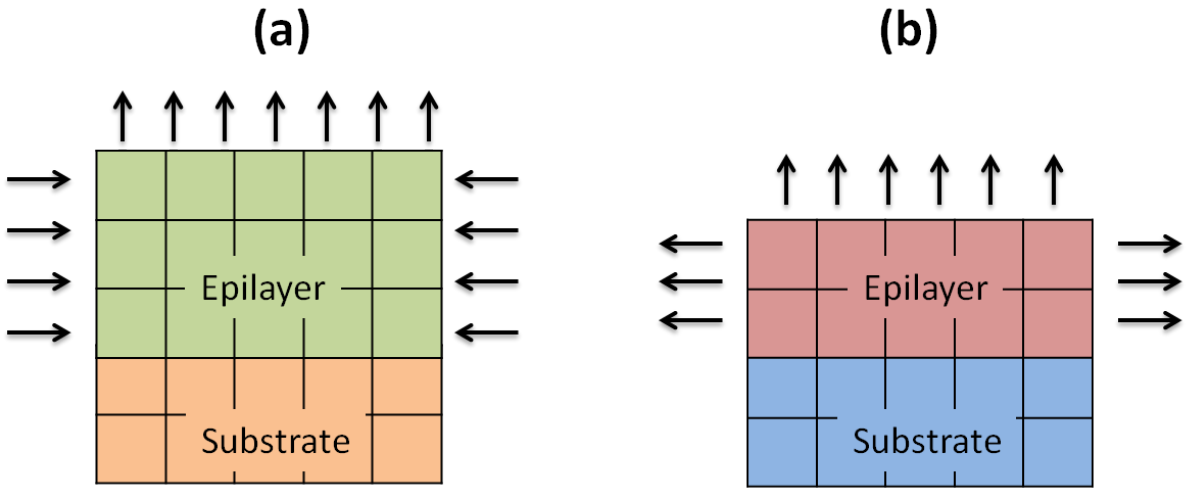

Figure A.4: Elastic deformations in the Nitride epitaxial layers (a) Compressive strain, (b) Tensile strain.

According to Vegard's law, the lattice parameters of nitride alloys vary linearly with compositions, given by the following relations [169];

$$\begin{aligned} a(A_xB_{1-x}N) &= x * a(AN) + (1-x) * a(BN) \\ c(A_xB_{1-x}N) &= x * c(AN) + (1-x) * c(BN) \end{aligned} \tag{A.1}$$

A.1 Spontaneous and Piezoelectric Polarization

Polarization is a crucial parameter for III-nitride semiconductor materials, that differs them from the other semiconductor materials. Depending on the requirements of the device, it can be useful as it is in the case of AlGaN/GaN high electron mobility transistors (HEMTs), but in-case of solar cells, it has been a challenging parameter in limiting the efficiency of the devices. III-nitride materials have two types of polarization, known as the Spontaneous polarization and the Piezoelectric polarization.

Spontaneous Polarization

The wurtzite group of III-nitrides lack an inversion plane perpendicular to the c-axis i.e. center of inversion symmetry. Therefore, the two [0001] and [000-1] directions are not equivalent. This leads nitride surfaces to have either group III element (Al, Ga, or In) polarity (referred to as Ga-polarity or Ga-face Figure A.5(a)) with a designation of (0 0 0 1) or (0 0 0 1)A plane or an N-polarity (referred as N-face Figure A.5(b)) with a designation of (0 0 0 $\bar{1}$) or (0 0 0 1)B plane. The different properties of materials grown along these two directions results in:

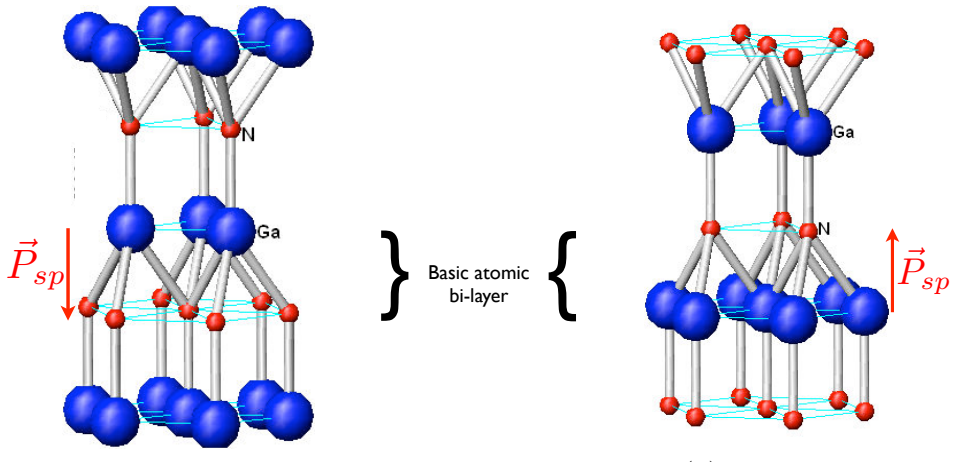

Figure A.5: Lattice orientations and corresponding spontaneous polarization vectors [170].

different surface morphology, dislocation density and chemical stability [171–173]. The growth of nitrides by Metal Beam Epitaxy (MBE) or MOVPE results in Ga-face on sapphire substrates. Thus the spontaneous polarization points along the [0 0 0 $\bar{1}$] direction, the opposite of the growth direction. The values for spontaneous polarization in GaN, AlN and InN calculated by Vurgaftman *et al.* [174] are $-0.034\ C/m^2$, $-0.090\ C/m^2$ and $-0.042\ C/m^2$, respectively. The spontaneous polarization in nitride ternary and quaternary alloys has a strong nonlinear dependence on alloy composition and micro-structure. The non-linearity can be modeled using the relation given below [175, 176];

$$P_{sp}(In_xGa_{1-x}N) = x \times P_{sp}(InN) + (1-x) \times P_{sp}(GaN) - b \times x \times (1-x) \tag{A.2}$$

where b is the bowing parameter and is given by;

$$b = 2P_{sp}(InN) + 2P_{sp}(GaN) - 4P_{sp}(In_xGa_{1-x}N) \tag{A.3}$$

Piezoelectric Polarization

The second type of polarization in III-nitrides is called the piezoelectric polarization. This effect is particularly observed in strained epitaxial layers. It arises due to the modification of atomic positions and the charge distribution in the supper-lattice with an external mechanical stress. It has been argued for InGaN materials [61], that piezoelectric polarization depends on crystal quality, and in particular on indium segregation [177]. Piezoelectric polarization along the c-axis is given by;

$$\vec{P_{pz}} = E.\vec{\epsilon}_{ij} \tag{A.4}$$

where e_{ij} are the piezoelectric coefficients of III-nitrides and ϵ_{ij} is the strain tensor. The piezoelectric polarization in hexagonal structures can be estimated using the relation;

$$\begin{bmatrix} 0 & 0 & 0 & 0 & e_{15} & 0 \\ 0 & 0 & 0 & e_{15} & 0 & 0 \\ e_{31} & e_{31} & e_{33} & 0 & e_{15} & 0 \end{bmatrix} \times \begin{bmatrix} \epsilon_{xx} \\ \epsilon_{yy} \\ \epsilon_{zz} \\ \epsilon_{yz} \\ \epsilon_{xz} \\ \epsilon_{xy} \end{bmatrix} \tag{A.5}$$

The value of piezoelectric polarization for III-nitride with the growth direction along c-axis is given by;

$$P_{pz} = 2\epsilon(e_{31} - \frac{C_{13}}{C_{33}}e_{33}) \tag{A.6}$$

The different Values of piezoelectric coefficients and elastic constants for GaN, InN and AlN are listed in Table A.2.

Table A.2: Values of piezoelectric and elastic constants of GaN, InN and AlN [178].

Parameters	GaN	AlN	InN
Eleastic constant, C_{13} (GPa)	103	92	108
Elastic constant, C_{33} (GPa)	405	224	373
Piezoelectric constant, e_{33} (C/m2)	-0.49	-0.57	-0.60
Piezoelectric constant, e_{33} (C/m2)	0.73	0.97	1.46
Spontaneous polar. coefficient (C/m2)	-0.034	-0.042	-0.09

Effect of the Net Polarization

The net polarization is a sum of spontaneous and piezoelectric polarization. The P_T may be negative or positive, depending on the orientation of the structure, whether its under tension or compression. The P_T is high in-case of crystal under tension, because, the two polarization, i.e. P_{sp} and P_{pz} are in the same direction. The sum of these two thereby increases the net polarization. However, if the given crystal is in compression, the two polarization P_{sp} and P_{pz} are in the opposite directions, therefore the net polarization is decreased. A schematic representation of the orientation of the polarization in InGaN/GaN is shown in Figure A.6. The total polarization is given by;

$$P_T = P_{sp} + P_{pz} \tag{A.7}$$

The net polarization is a crucial parameter in III-nitride devices, as it can significantly modify the band bending and transport properties. The magnitude of electric field induced by polarization in PIN InGaN solar cells can be as high as the electric field induced by the doping concentrations [170]. In the conventional PIN design, where the p-GaN cap layer is at the top of the structure, the two fields may even cancel each other out. An inverted PIN, or NIP, design that would use a n-GaN cap layer might be more suitable [61, 179].

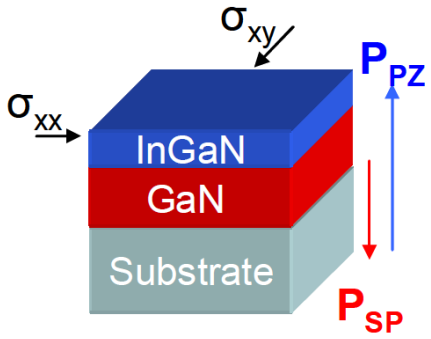

Figure A.6: Schematic for the piezoelectric polarization (crystal under compression) and the spontaneous polarization of the InGaN/GaN.

A.2 Electron Band-Structure Properties

The temperature dependence of the energy bandgap for the wurtzite III-nitride semiconductors in the Varshni form is given by,

$$E_g(T) = E_g(T=0) - \frac{\alpha T^2}{T+\beta} \tag{A.8}$$

where E_g is the gap at 0 K, α and β are Varshni thermal coefficients. The values of Varshnis constants together with values of band gaps for GaN and InN are given in Table A.3. The

Table A.3: Band structure parameters for wurzite nitride semiconductor materials [174]

	E_g at 0K (eV)	α (meV/K)	β (K)
GaN	3.51	0.909	830
InN	0.78	0.245	624

validity of this equation is within few meV for bulk nitride materials. Table A.4 list all the essential band structure parameters for wurtzite nitride parameters, that needs to be taken into account for a heteroepitaxial layer calculated with Vurgaftman et al [174]. The different parameters listed in Table A.4 are, a_1 and a_2 as the inter-band deformation potentials, D_1, D_2, D_3, D_4, D_5 and D_6 as the valence band deformation potentials, C_{11}, C_{12}, C_{13}, C_{33} and C_{44} as the elastic constants, A_1, A_2, A_3, A_4, A_5, A_6 and A_7 as the valence band parameters, d_{13}, d_{33} and d_{15} as the piezoelectric modules, Δ_{cr} as the crystal field splitting, Δ_{so} as the spin orbit splitting and P_{sp} as the spontaneous polarization.

The graph representing the evolution of band-gap energy with the basal-plane lattice parameter for III nitrides is presented in Figure A.7. The figure supports the claim of InGaN as a potential candidate for designing high efficiency solar cells, covering almost the entire solar spectrum, by simply adjusting the indium composition. The energy bandgap for InGaN on dependence with the indium composition for an un-strained ternary alloy can be calculated with simple Vegards law as following;

$$E_g(A_{1-z}B_z) = (1-x)E_g(A) + xE_g(B) - x(1-x)C \tag{A.9}$$

where C is known as the bowing parameter. The different values for bowing parameter for InGaN, AlGaN and AlInN are listed in Table A.5. The bowing parameter (C) is always positive and reflects a reduction of the alloy energy gaps.

Table A.4: Band structure parameters for wurzite nitride semiconductor materials [174]

Parameters	GaN	AlN	InN
E_g(eV)	3.510	6.25	0.78
α (meV/K)	0.909	1.799	0.78
β (K)	830	1462	624
a_1 (eV)	-4.9	-3.4	-3.5
a_2 (eV)	-11.3	-11.8	-3.5
D_1 (eV)	-3.7	-17.1	-3.7
D_2 (eV)	4.5	7.9	4.5
D_3 (eV)	8.2	8.8	8.2
D_4 (eV)	-4.1	-3.9	-4.1
D_5 (eV)	-4.0	-3.9	-4.1
D_6 (eV)	-5.5	-3.4	-5.5
C_{11} (GPa)	390	396	223
C_{12} (GPa)	145	137	115
C_{13} (GPa)	106	108	92
C_{33} (GPa)	398	373	224
C_{44} (GPa)	105	116	48
A_1 (GPa)	-7.21	-3.86	-8.21
A_2 (GPa)	-0.44	-0.25	-0.68
A_3 (GPa)	6.68	3.58	7.57
A_4 (GPa)	-3.46	-1.32	-5.23
A_5 (GPa)	-3.40	-1.47	-5.11
A_6 (GPa)	-4.90	-1.64	-5.96
A_7 (eV A)	0.00937	0	0
d_{13} (pm/V)	-1.6	-2.1	-3.5
d_{33} (pm/V)	3.1	5.4	7.6
d_{15} (pm/V)	3.1	3.6	5.5
Δ_{cr} (eV)	0.010	0.169	0.040
Δ_{so} (eV)	0.017	0.019	0.005
P_{sp} (C/m^2)	-0.034	-0.090	-0.042

Table A.5: Bowing parameters for III-nitride semiconductor alloys [25, 174, 180]

Variables	b (eV)
InGaN	1.43
AlGaN	0.7
AlInN	2.5

A.3 Absorption

The Energy bandgap for Wurtzite III-nitride compound semiconductors spreading over, from 0.7 eV (near infra-red) to 6.2 eV (ultraviolet) is not only the factor of its attraction for high

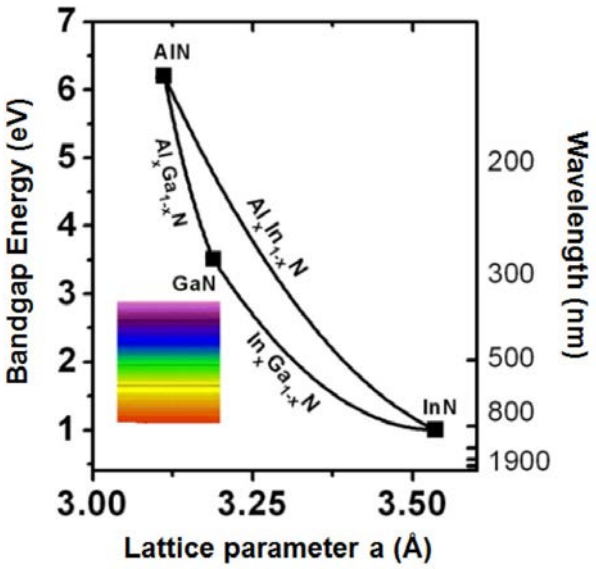

Figure A.7: III-nitrides lattice parameter vs. bandgap energy.

efficiency solar cells but another major parameter is the high absorption coefficient of the order of 1×10^5 cm^{-1} [42]. The high absorption coefficient makes it possible for InGaN to absorb incident light in few nano-meters as compared to silicon where a material in micron is required for the same light absorption. It makes InGaN a possible candidate for designing ultra-thin solar cells. A relation modeling the absorption by a semiconductor material is given as,

$$I_t(\lambda) = I_i(\lambda)e^{\alpha(\lambda)d} \tag{A.10}$$

where I_i is the incident light on to the semiconductor and I_t is the transmitted light, λ is the wavelength, α is the absorption coefficient and d is the thickness of the semiconductor material. The absorption coefficient is the property of the semiconductor material and is represented in the unit of cm^{-1}. Figure A.8 shows the experimental transmission and/or reflection of a pseudo GaN substrate. The transmission curve is located around 360 nm corresponds to the bandgap of GaN (3.42 eV).

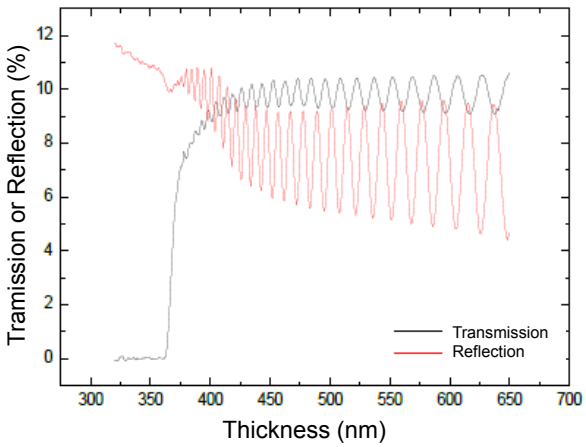

Figure A.8: Transmission and reflection curves for a pseudo GaN substrate (3.5 μm on sapphire substrate) [181]

A.4 Typical Defects - Threading Dislocations

In spite of the interesting thermal, optical and electrical performance of devices produced so far, GaN materials suffer from numerous threading dislocations and lattice mismatch due to their growth on foreign substrates. The growth on in-appropriate substrates leads to a substantial density of misfit and threading dislocations in the range of 10^6 cm^{-2} – 10^{12} cm^{-2}, contributing to the low mobility and high residual carrier density. Sapphire is the most widely, substrate choice for growing GaN layers and has the advantage of ease of surface cleaning, inter-facial adhesion, availability, chemical stability and thermal stability. It is also stable at high temperature ($\sim 1000°C$), which is normally required for GaN film grown by metalorganic chemical vapor deposition (MOCVD) method. Sapphire exhibits a higher thermal expansion coefficient relative to GaN. GaN films grown on sapphire substrate experiences compressive and tensional biaxial strain , that eventually ends up with formation for threading dislocations in the epilayer. These threading dislocations originate from the substrate/GaN interface and propagate into the epilayer as shown in Figure A.9. The large difference of lattice constant and thermal expansion

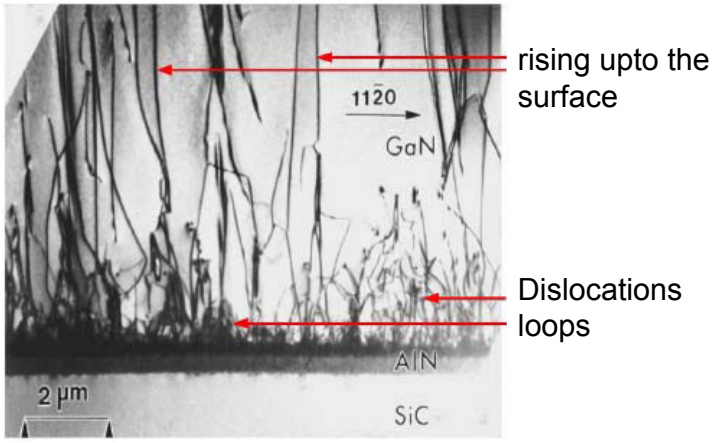

Figure A.9: TEM-cross section image of a GaN epitaxial layer grown on SiC substrate.

coefficient between the foreign substrate and GaN is considered to be the major factor attributing to the high density of defects. A dislocation is an extended defect (line defect) causing a displacement in a perfect crystal. It is defined by it's Burger vectors, b, representing the magnitude and direction of the lattice distortion. Figure A.10 shows the unit cell of GaN, which has a wurtzite structure. There are three types of dislocations in GaN materials, (i) Edge dislocations (ii) Screw dislocations and (iii) mixed dislocations.

The geometry of edge dislocations in GaN is shown in Figure A.10(b). The line direction of these dislocations is [0001] and the Burgers vectors are one of the three basal plane translations and their inverses, which include $\pm a_1 = \frac{1}{3}[2\bar{1}\bar{1}0]$,$\pm a_2 = \frac{1}{3}[\bar{1}2\bar{1}0]$, and $\pm a_3 = \frac{1}{3}[\bar{1}\bar{1}20]$, and are perpendicular to the dislocation line [182]. The edge dislocations are formed from coalescence of islands with twist mis-orientation about the [0001] axis. Figure A.11(a) shows the cross-sectional schematic of V-pits contributed by edge dislocations, with a polygonal shape, denoted by the symbol γ. The top view of the V-pits associated to edge dislocations is shown in Figure A.11(b). Edge dislocations represent a larger fraction of the total threading dislocations density in thicker films [182, 184]. Wu *et al.* [184] examined both 1 and 5 μm thick films grown under identical conditions and showed that the edge threading dislocations make up 40% of the total threading dislocations density in 1 mm thick MOCVD-grown films, while after 5 μm of growth, they make up 70% of all TDs.

The geometry of screw dislocations in GaN is shown in Figure A.10(c). The line direction and Burger vector for screw dislocations lie along the Both [0001] direction. Figure A.11(a)

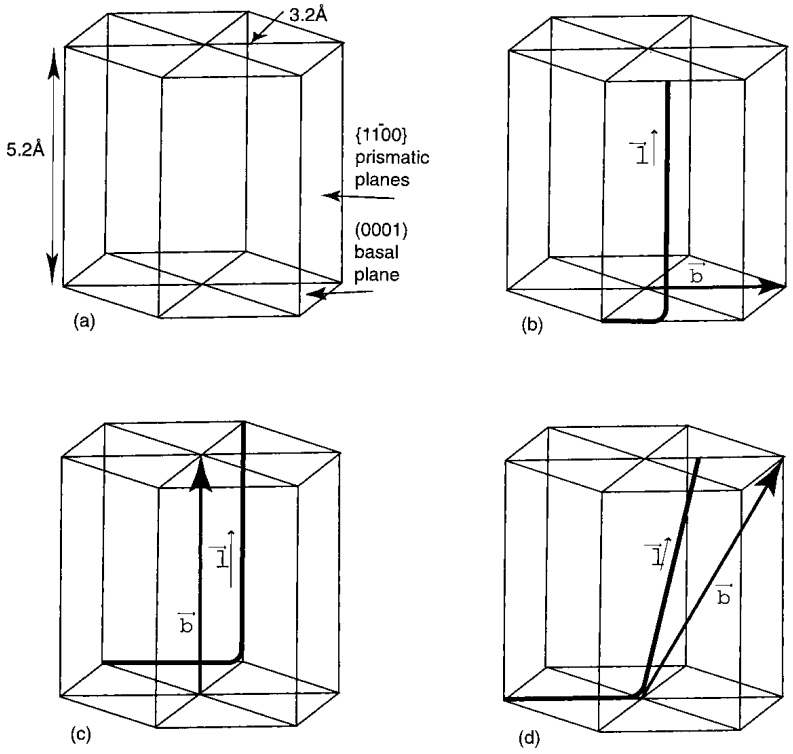

Figure A.10: GaN crystallography, a). The GaN unit cell has c = 1.62a, b). Edge dislocations in GaN with Burgers vectors of the type <11$\bar{2}$0> and a vertical line direction, c). Perfect screw dislocations with b =± [0001] and line direction [0001], d). Mixed character dislocations with Burgers vectors of the type <11$\bar{2}$1> and inclined line directions [182].

shows the cross-sectional schematic of V-pits contributed by screw dislocations, with a triangular shape, denoted by the symbol α. The top view of the V-pits associated to screw dislocations is shown in Figure A.11(c). Pure screw dislocations are the most uncommon type of threading dislocations in GaN films [182]. Wu *et al.* [184] reported that pure screw threading dislocations had a very small proportion much less than 1%) of the total threading dislocations density in MOCVD-grown GaN. Nanopipes, which are sometimes observed in GaN films grown on SiC and on sapphire, have been associated with open-core screw dislocations [185]. However, nanopipes appear not to have appreciable density in high-quality material, and often screw dislocations have closed cores [186].

The geometry of screw dislocations in GaN is shown in Figure A.10(d). Burgers vectors for mixed dislocations are b = $\frac{1}{3}$ <11$\bar{2}$3>. Figure A.11(a) shows the cross-sectional schematic of V-pits contributed by mixed dislocations, with a combination of triangular and trapezoidal shape, denoted by the symbol β. The top view of the V-pits associated to mixed dislocations is shown in Figure A.11(d). The reported fraction of mixed dislocations varies from 2% of the total density in the case of MBE- initiated growth to 68% in metalorganic vapor phase epitaxy-grown (MOVPE-grown) material [186]. Mixed dislocations are the only threading dislocations with an (energetically favored) inclined line direction relative to the film normal, they are the only threading dislocations moving laterally relative to other threading dislocations during growth [182].

The crystalline quality of GaN material has been highly improved by using different growth techniques, including hydride vapor phase epitaxy (HVPE), organic metallic vapor phase epitaxy (OMVPE) and molecular beam epitaxy (MBE). Selective area lateral overgrowth (ELOG) has

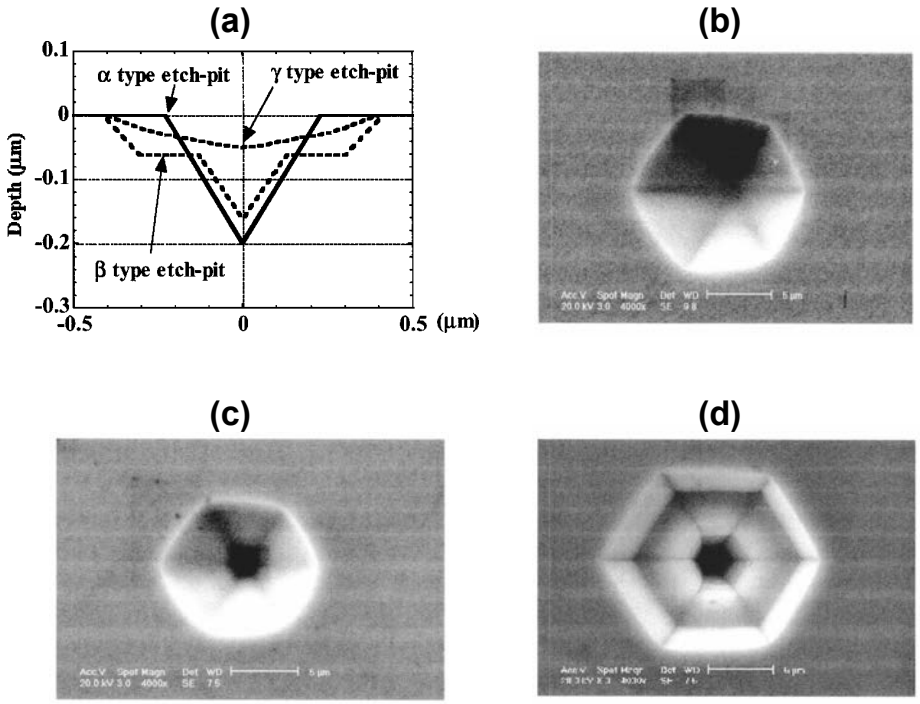

Figure A.11: (a) Schematic depth profiles of α, β, and γ type V-pits [183]. High-resolution SEM image of three different types of V-pits associated to (b) edge dislocations, (c) screw dislocations and (d) mixed dislocations [140].

shown very promising results reducing the threading dislocation down to around 10^6 cm^{-2} [187]. The best alternatives for growing high quality GaN now lie in the development of Al_2O_3, SiC, or AlN substrates [188]. Interest in AlN substrates has increased recently owing to the closer lattice match over Al_2O_3, matched stacking order, and high thermal conductivity [189]. The lattice-mismatch between various III-N materials and substrates is listed in Table A.6. Although,

Table A.6: Mismatch comparison for the III-N binary materials for [0001] directions at 300K [190].

Material substrate	GaN (%)	AlN (%)	InN (%)
GaN	0	2.3	10.6
AlN	2.4	0	12
InN	10.6	12	0
SiC	3.3	1	14
Al_2O_3	14.8	12.5	25.4
Si	16.9	18.7	7.6

the growth of GaN on Si has shown encouraging results with low dislocations, however several challenges including the poor wetting of Ga on SiC has limited the use of such techniques [191].

A.5 Major Breakthroughs in III-Nitride Opto - electronic Devices

Over the last decade, solid state lighting technologies have emerged rapidly and penetrated deeply into various segments of market such as automotive, medical applications, aviation lighting, indoor and outdoor lighting as well as lifestyle products. The global light emitting diode (LED) market volume in general lightening is currently around US 26 billion dollar and it is expected to grow much more than US$ 72 billion by 2020 [192]. This has been possible by the remarkable progress in III-Nitride materials (Refer to appendix A for properties of III-Nitride materials).

Driven by a vision of then-futuristic flat panel displays, the first demonstration of gallium nitride (GaN) deposition was achieved by Maruska and Tietjen at RCA Laboratories (New York, NY, USA) using hydride vapor-phase epitaxy on a sapphire substrate in 1969 [193,194]. Due to the lack of p-type semiconductor material, the first GaN based blue and violet Light Emitting Diodes (LEDs) were fabricated as metal-insulator-semiconductor (MIS), doped with Zn and Mg as a color center in 1971-1973 [195–197]. The output power for these LEDs was on the order of 1-5 μw, resulting in poor efficiency and brightness to be used in general lightning applications. Amano *et al.* [198] reported the first GaN based PN junction LED, after their successful growth of Mg-doped GaN using post-growth low-energy electron beam irradiation (LEEBI) treatment in 1989. They achieved p-GaN with hole concentration of $2 \times 10^{16} cm^{-3}$ and mobility $8 \times cm^2/Vs$, however it was not well explained of how they obtained p-GaN. Nakamura *et al.* [199] demonstrated GaN based PN junction LED with power, external quantum efficiency (EQE), peak emission wavelength, and forward voltage at 20 mA as 42 W, 0.18%, 430 nm, and 4 V respectively. The p-GaN obtained by Nakamura *et al.* [199] had hole concentration of $2 \times 10^{17} cm^{-3}$ and mobility 10 cm^2/Vs. They reported hydrogen passivation as the possible mechanism behind hole compensation in p-GaN. The achievement of p-type conductivity in GaN materials, made it possible to fabricate highly efficient LEDs with not only PN junction but also a p-GaN/i-InGaN/n-GaN (PIN) hetero-junction [200]. The LEDs demonstrated with a PN junction or PIN hetero-junction results in a way higher efficiency and brightness compared to previously used LEDs. The encouraging results led Nakamura *et al.* [201] to demonstrate bright blue, yellow and green LEDs based on single InGaN quantum well (QW) by adjusting the indium content in InGaN alloy. These results formed the base for the commercialization of the first generation of green and blue LEDs [192]. In 2014, for the invention of efficient blue light emitting diodes which has enabled bright and energy-saving white light sources, S. Nakamura, I. Akasaki and H. Amano were honored by the Nobel Prize. The enormous efforts by S. Nakamura, I. Akasaki and H. Amano enormous in fabrication of GaN based bright LEDs revised the concept of using GaAlAs and/or InGaP type semiconductor materials delivering poor efficiency and brightness.

Indium nitride (InN) is an important III-nitride semiconductor with many potential applications. The use of InN and its alloys with GaN and AlN makes it possible to extend the emission of nitride-based LEDs from ultraviolet to near infrared region. In the early 90's Indium Gallium Nitride (InGaN) was developed as a new material to be used in LEDs. Initially it was used in blue LEDs but is also capable of generating a wide range of green and blue colors including UV radiation. Blue LEDs are also used in conjunction with a phosphor to make white LEDs [202], as shown in the Figure A.12. InN has been grown by sputtering for a long time [204]. Nataranjan *et al.* [205] demonstrated the detail mechanism of reactive sputtering of indium, and growth of InN in mixed Ar-N_2 discharges. However, the film qualities were very poor and have universally high carrier concentration near 10^{20} cm^{-3} and constantly low electron mobility of less than 100 cm^2/Vs [203]. InN was not of much interest until the growth of a high quality single crystalline epitaxial InN film by the most popular growth technique, MOVPE, in 1989 by Matsuoka *et*

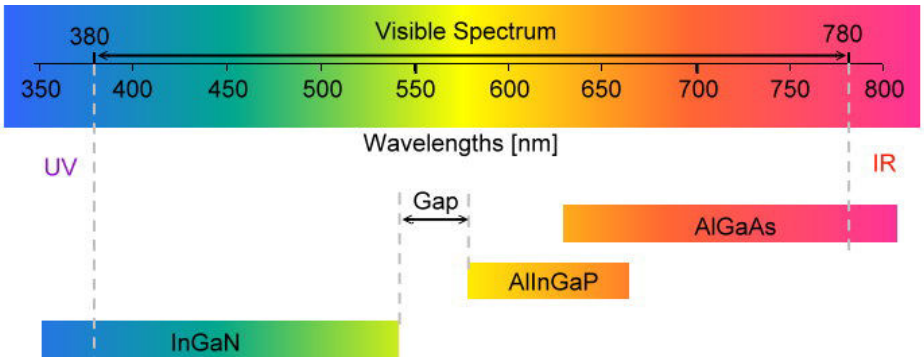

Figure A.12: InGaN spectrum coverage for LEDs in conjunction with AlInGaP and AlGaAs [203].

al. [206] and Wakahara *et al.* [207, 208]. As-grown InN is unintentionally n-type. The origin of high n-type conductivity was suggested as native defects such as Nitrogen vacancy, point defects and edge-type threading dislocations that generate sources of free electrons in InN [209].

Appendix B

Physics of solar cells

B.1 Solar Cells Operation

The basic goal of solar cells is to convert sun light into electricity. There are several key factors which are crucial in determining how the incident sunlight interacts with a solar cell, given as;

* The radiant power density from the sun
* The spectral content of interacting light
* The angle of the incident light
* The radiant energy from the sun at a particular surface

A schematic of a solar cell operation is shown in Figure B.1. The process of a solar cell

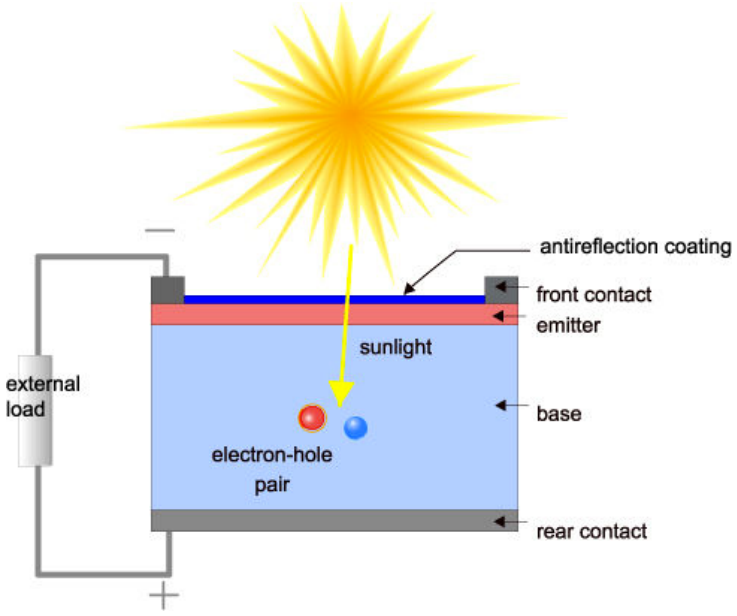

Figure B.1: Schematic of a solar cell operation (http://www.pveducation.org/pvcdrom/solar-cell-operation/solar-cell-structure).

operation can be categorized in multiple ways, but the key factors can be classified into three main categories, electron-hole pair generation, electron-hole pair separation and transport of the generated electron-hole pair. All the key factors involved in operation of a solar cell discussed in-depth in details later in the thesis, however a brief overview is presented in this section.

Light absorption and generation of electron-hole pair

The generation of charges occurs when the semiconducting material absorbs photons and excites electrons to higher energy states creating electron-hole pairs. Every photon has its own energy that depends on the wavelength of the incoming light and can be expressed through the Planck-Einstein relation:

$$E = \frac{hc}{\lambda} \tag{B.1}$$

where h is the planck's constant ($= 4.135 \times 10^{-}15$ eV.s), c is the speed of light ($= 3 \times 10^{8}$ m/s), and λ is the wavelength of the incident sunlight.

The electron-hole pair in a semiconductor material will be only generated provided that the incident photon has an energy greater than and/or equal to that of the energy bandgap of the semiconductor material (Figure B.2(a-b). Semiconductor materials with larger bandgap are

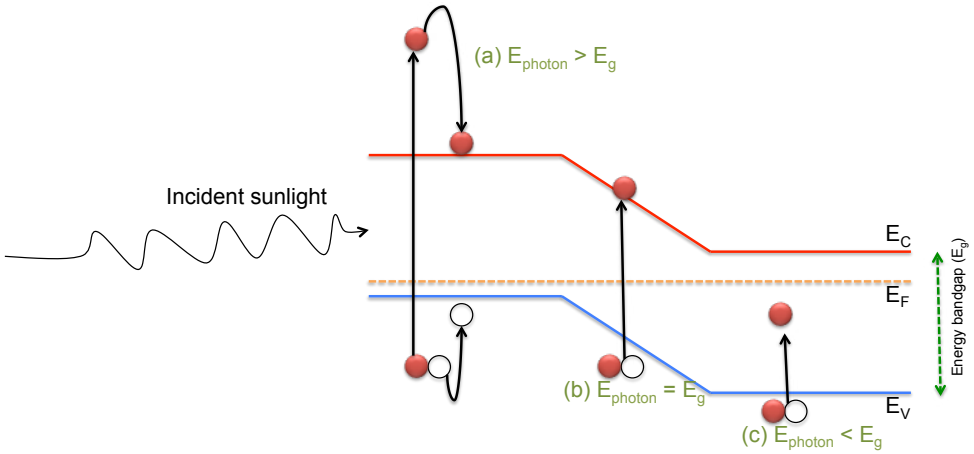

Figure B.2: Generation of electron-hole pair by incident light for the three different cases, (a). Incident photon has an energy greater than the energy bandgap, (b). incident photon has an energy equal to the energy bandgap, (c). incident photon has an energy lower than the energy bandgap.

useful in obtaining higher open circuit voltage (V_{oc}). However these semiconductor materials are than limited to absorb only high energy photons since photons below the bandgap are not absorbed which results in less photocurrent. Therefore materials with smaller bandgap are more useful due to the higher probability of absorbing more photons leading to high photocurrent but the excess energy of the excited electron above the bandgap is lost to thermalisation and the electron energy is reduced to that of the bandgap (Figure B.2(c)).

In an ideal situation, an incoming with an energy greater than and/or equal to the energy bandgap of the semiconductor material should generate an electron-hole pair (at least one pair), however there is also a possibility that the incident photon is reflected back or transmitted without being absorbed. These photons do not contribute to the generation of electron-hole pair. This mechanism reduces the rate of electron-hole pair generation, therefore needs a special attention during the choice of the solar cell design and/or thickness of the absorber layers. An efficient way of reducing the light reflection at the surface is to use textured surfaces while for minimizing the incomplete light absorption, the thickness of the absorber layer should be increased. Light absorption in a given semiconductor material is defined by its thickness and absorption coefficient, as described by the Beer-Lambert law [210].

$$I(x) = I(0)e^{-\alpha x} \tag{B.2}$$

where $I(0)$ is the intensity of the incident light, $I(x)$ is the intensity of the light transmitted

through the semiconductor material, α is the absorption coefficient of the semiconductor and x is the thickness of the semiconductor material.

The penetration of an incident light in a semiconductor material without being absorbed is defined by the absorption coefficient. It is inversely proportional to the wavelength of the light, resulting in full absorption of shorter wavelength (higher energy) photons at the top layer, while permitting the longer wavelengths (lower energy) photons penetrate deeper into the substance. For instance, for an InGaN layer with α=10^5 cm^{-1}, 95% of the incoming light will be absorbed in the first 300 nm [211].

Separation of the electron-hole pair

This is an essential part of the solar cells. The excited electron-hole pair needs to be separated before they recombine and give up their energy. The electron-hole pair recombination can either happen by a fundamental physical processes or due to the imperfect crystalline quality of the semiconductor material. For example, interaction of the excited carriers can result in exchange of energy. This results in the decay of one of the carriers across the energy bandgap and an increase in the kinetic energy of the other carrier, which later loses the excess energy through thermalisation. This process is a physical process called Auger recombination. Another form of recombination that occurs due to the presence of the impurities and/or defects in the crystalline structure of the semiconductor material is relaxation of the excited carriers into trap states. In solar cells, the non-radiative recombination via defects is a major challenge due to the presence of high density of defects in the epitaxial layers. The challenges involved in semiconductor materials, particularly InGaN materials will be discussed in detail in Chapter 2.

A PN junction is formed when two materials with different polarities (p-type and n-type) comes into contact. Due to the gradient difference, the electrons in the p-type diffuse into the n-type leaving positively charged ions behind, whereas the holes in the n-type diffuse into the p-type material leaving negatively charged ions behind, thus forming a barrier which neutral region called space charge or depletion region as shown in Figure B.3(a). A built-in electric

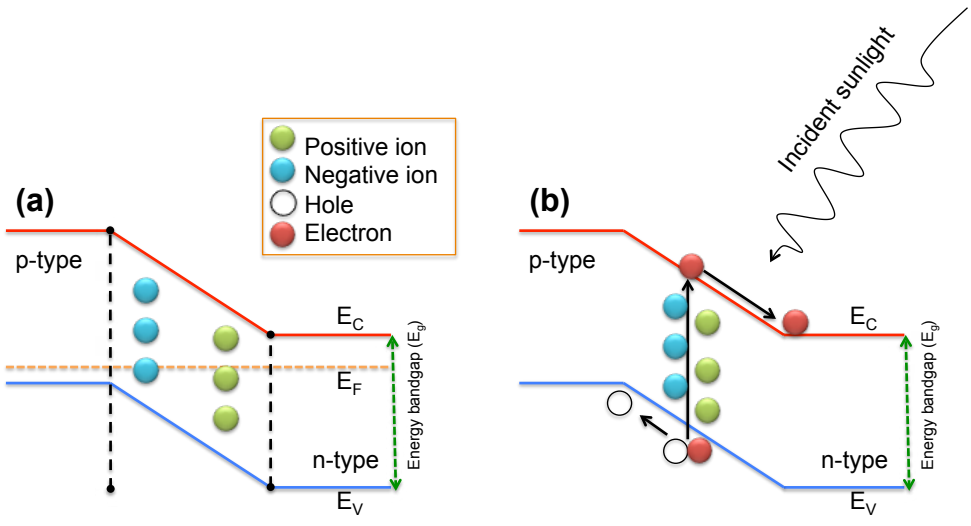

Figure B.3: A PN junction under, (a). Equilibrium, (b). Illumination.

generated within the depletion region opposes any further diffusion of the carriers across the semiconductor material. The strenth of the electric field within the depletion region highly depends on the doping concentrations and quality of the epitaxial layers. Under illumination, the electron-hole pair generated within the depletion region is drifted towards the electrods, with hole towards the p-type material and electrons towards the n-type material as shown in Figure B.3(b).

Transport mechanism of the generated electron-hole pair

Transport of the generated electron-hole pair is majorly dependent on the crystalline quality of the epitaxial layers. The electron-hole pair generated by the incident photon need to reach the junction before they recombine as discussed in previous section. The parameter that defines how far a a generated carried can go before it recombines is the *diffusion length*. The diffusion length of generated carrier depends on the trap density and degree of disorder in the semiconductor material. The average diffusion length for an electron in GaN is reported around 0.20μm [212]. The diffusion length is defined by;

$$L_c = \sqrt{D_c \tau_c} \tag{B.3}$$

where, τ_c is the minority carrier lifetime, D_c is the diffusion coefficient given by the equation D_c=kT/q μ_c.

B.2 Ideal Diode Behavior

The built-in voltage within the depletion region, forms a barrier thus gives the device a rectifying (diode) behavior. The net current density flowing through an ideal diode under dark conditions, J_{dark} is given by;

$$J_{dark}(V) = J_0 \left(e^{\frac{qV}{kT}} - 1 \right) \tag{B.4}$$

where J_0 is the dark saturation current density, V is applied voltage across the terminals of the diode, k is the Boltzmann constant, and T is the temperature. At 300K, the thermal voltage, kT/q is 25.85 mV.

The J_0 is an extremely important parameter which differentiates one diode from another. This basically represents the carrier recombination mechanism in the device. It will be further discussed later.

Figure B.4 shows the schematic for different processes of a PN junction under different condition i.e. no bias (at equilibrium), forward bias voltage and reverse bias voltage. According to the ideal diode equation the flow of current across a diode has an exponential dependence on the applied voltage, while at negative voltage yields a very small current.

The diffusion of carriers at the PN junction interface happens until they reach a threshold point called *equilibrium*. Despite the presence of the electric field, which creates an impediment to the diffusion of carriers across the electric field, some carriers still cross the junction by diffusion. These carriers eventually recombines after traveling, on average, its diffusion length. The current caused by the diffusion of carriers across the junction is called a diffusion current. Minority carriers that are thermally generated within a diffusion length from the junction have a good probability of reaching the junction where they are swept across to become majority carriers. In equilibrium these two currents .i.e. diffusion current and drift current, are equal and the net current flow across the diode is zero. The process of the drift and diffusion in PN junction under no bias voltage is demonstrated in Figure B.4(b).

When the diode is forward biased i.e. positive voltage at the p-type material and a negative voltage at the n-type material as shown in Figure B.4(c), an electric field results that is in opposition to the electric field created by the space charge region at the junction. This reduces the net electric field across the junction, that eventually destroys the depletion region. Reducing the electric field disturbs the equilibrium existing at the junction, reducing the barrier to the diffusion of carriers from one side of the junction to the other and increasing the diffusion current. The applied voltage increase the diffusion current, while the drift current remained unchanged, because it depends on the number of minority carriers thermally generated within a diffusion length of the depletion region, which doesn't increase as much as the diffusion current. The increase in the diffusion current means that the injection of the minority carrier has been increased at the diode's junction and therefore increases the recombination with the majority

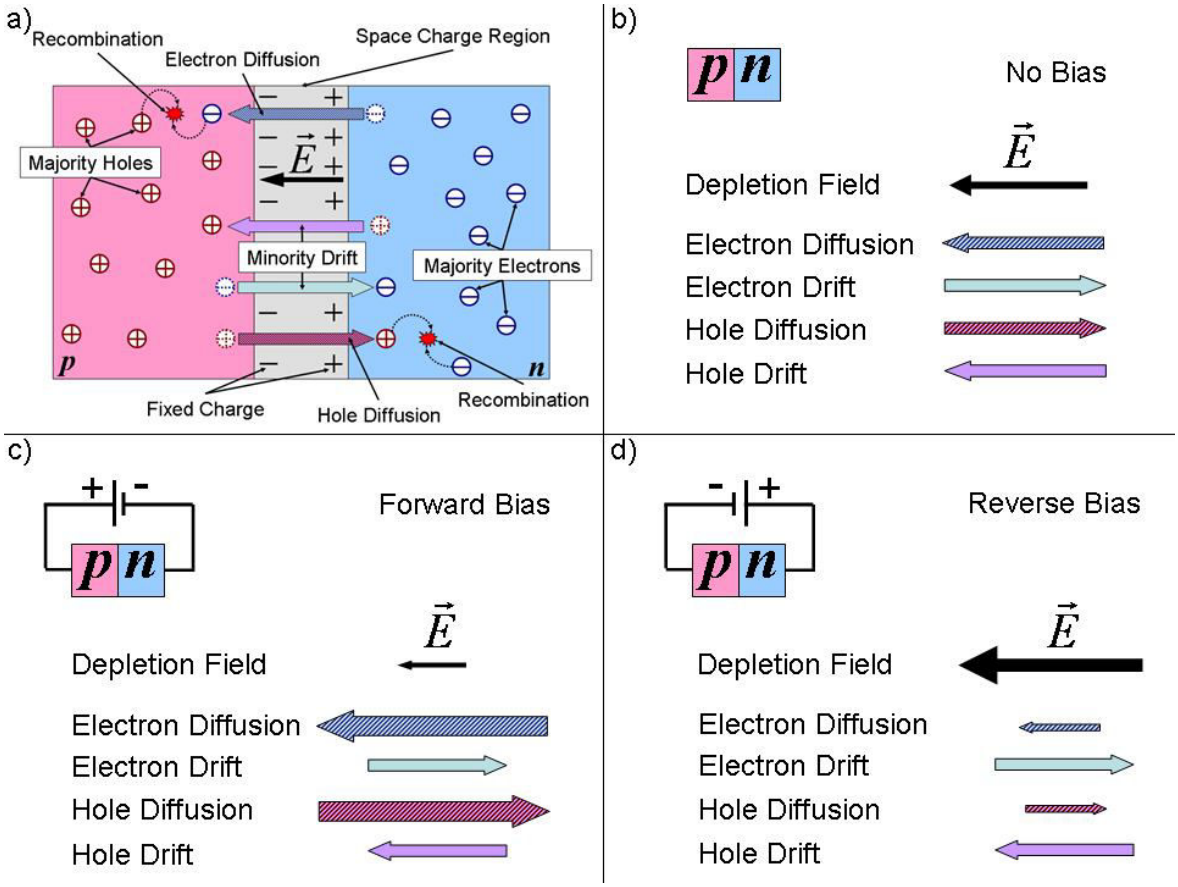

Figure B.4: (a). Majority carrier diffusion and minority carrier drift at a PN junction, (b). Drift and diffusion currents cancel out to zero with no bias applied to the junction, (c). The majority carrier diffusion is larger under forward bias due to the reduced junction barrier height, (d) There is very little majority carrier diffusion under reverse bias, leaving the drift current to be larger [213]

carriers supplied by the external source. The removal of minority carriers by recombination allows more majority carriers to diffuse across the junction to become minority carriers, sustaining the current. The diffusion current can then be thought of as a recombination current where a greater recombination results in a larger current across the junction. The measure of this recombination current is denoted by J_0 given in the ideal diode's equation 1.4. It highly depends on the crystalline quality of the semiconductor materials. For instance, in InGaN materials, the recombination current take place via tunneling of carriers through the defects states. The J_0 is a crucial parameter in defining the quality of the diode, particularly in solar cells it highly affects the open circuit voltage.

When the diode is reverse bias, i.e. negative voltage at the p-type material and a positive voltage at the n-type material as shown in Figure B.4(d), the applied electric field is in the same direction as the electric field within the depletion region. The higher electric field in the depletion region decreases the probability that carriers can diffuse from one side of the junction to the other, hence the diffusion current decreases.

Ideal solar cell

Figure B.5(a) shows the equivalent electrical circuit for an ideal solar cell, modeled as a current generator with a parallel load resistor. The current across the diode depends on the source of

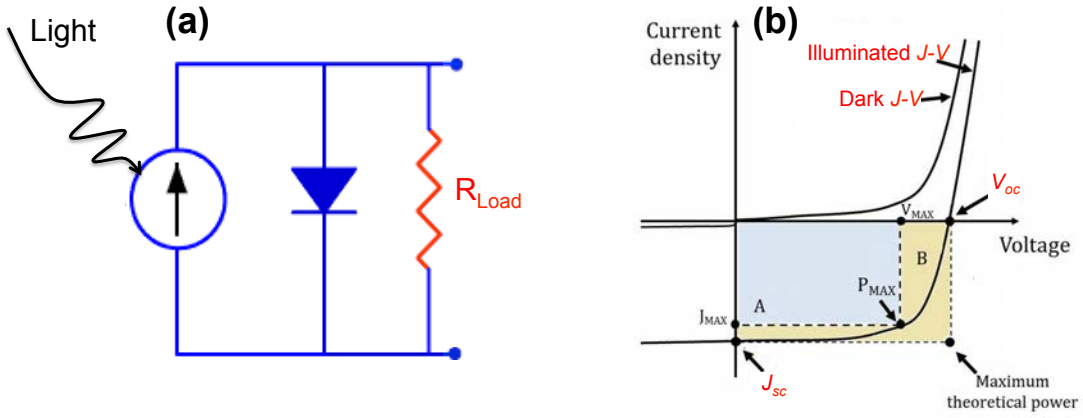

Figure B.5: (a). Equivalent electric circuit for an ideal solar cell. The load resistance (R_L) determines the amount of current across the diodes and the load, (b). Electrical characteristics of a solar cell under dark and illumination.

illumination. The load resistor determines the amount of current flowing through the diode. The electrical characteristics of the solar cell under dark and illuminated conditions are given in Figure B.5(b), with the corresponding key parameters of the solar cell. The key findings extracted from the $J-V$ characteristics of the solar under illumination are discussed in the next section.

Short circuit current density (J_{sc})

This is the maximum current through the solar cell given that the voltage across the solar cell is zero, as shown in Figure B.5(b). The J_{sc} is due to the generation and collection of light-generated carriers. The J_{sc} of a solar cell is dependent on the intensity of the incident light and crystalline quality of the epitaxial layer, particularly the absorber layer. Additionally, the diffusion length and the surface recombination significantly affect the J_{sc}. In a solar cell with perfectly passivated surface and uniform generation, the equation for the J_{sc} can be approximated as:

$$J_{sc} = qG(L_n + L_p) \tag{B.5}$$

where G is the generation rate of the electron-hole pairs, and L_n and L_p are the electron and hole diffusion lengths respectively.

Open circuit voltage (V_{oc}

This is the maximum voltage available from a solar cell given that the there is no current across the solar cell, as shown in Figure B.5(b). The V_{oc} for a solar cell can be calculated using the equation,

$$V_{oc} = \frac{nkT}{q} ln\left(\frac{J_{sc}}{J_0} + 1\right) \tag{B.6}$$

where n is the ideality factor of a diode, in-case of an ideal diode n=1, kT/q is the thermal voltage (25.85 mV at 300K), J_{sc} is the short-circuit current density and J_0 is the saturation current density.

The above equation shows that for an ideal diode (n=1) the V_{oc} strongly depends on the J_{sc} and J_0. The dependence of V_{oc} on J_{sc} is rarely observed due to the small variations in the J_{sc}, however the key effect is the J_0, since this may vary by orders of magnitude. The J_0 is basically the recombination current discussed in section 1.3.2. It can be calculated as;

$$J_0 = Aqn_i^2 \left(\frac{D_n}{L_n N_A} + \frac{D_p}{L_n N_d} \right) \tag{B.7}$$

where A is the cross-sectional area of the device, q is the electron electron charge, n_i is the intrinsic carrier concentration, D_n and D_p are the diffusion coefficients of electrons and holes respectively, L_n and L_p are the diffusion lengths of electrons and holes respectively, N_a and N_d are acceptor and donor concentrations respectively.

The V_{oc} of a solar cell can also be determined from the carrier concentration [214];

$$V_{oc} = \frac{kT}{q} ln \left(\frac{N_a + \Delta n}{n_i^2} \times \Delta n \right) \tag{B.8}$$

where kT/q is the thermal voltage (25.85 mV at 300K), N_A is the doping concentration, Δn is the excess carrier concentration and n_i is the intrinsic carrier concentration.

Fill Factor (FF)

The fill Factor (FF) determines the maximum power of the solar cell. The FF relates the actual maximum power obtained from the cell to the theoretical maximum power. It is the ratio of the area A (indicated with blue color) to the area B (colored with yellow), shown in Figure B.5(b), and is given by;

$$V_{oc} = \frac{V_{max} J_{max}}{V_{oc} J_{sc}} \tag{B.9}$$

Power conversion efficiency (PCE)

PCE is the most commonly used parameter in demonstrating the performance of the solar cell device under given source of illumination. It is defined as the ratio of energy output from the solar cell to input energy from the sun. The PCE of a solar cell is given as;

$$\eta = \frac{V_{oc} J_{sc} FF}{P_{in}} \tag{B.10}$$

where V_{oc} is the open circuit voltage, J_{sc} is the short circuit current density, FF is the fill factor and P_{in} is the power density of the illumination.

B.3 Non Ideal Behavior of Solar Cell

The real devices of solar cells comes with a lot of real world challenges. In real solar cell devices the power is dissipated through the resistance of the metal contacts and through current leakage around the sides of the devices. Such effects contributes to the presence of the parasitic resistances that highly degrades the performance of the solar cells. Figure B.6 shows the equivalent electric circuit of a non-ideal solar cell with its corresponding parasitic resistances i.e. the series resistance (R_s) and the shunt resistance (R_{sh}).

The key impact of these resistances is the reduction of the fill factor, however, excessively high values for R_s and low values for R_{sh} may also reduce the J_{sc} and V_{oc} respectively, as shown in Figure B.7. The series resistance is majorly contributed by the bulk material and the metal contacts. Whereas the R_{sh} arises from the leakage current via defects in the materials

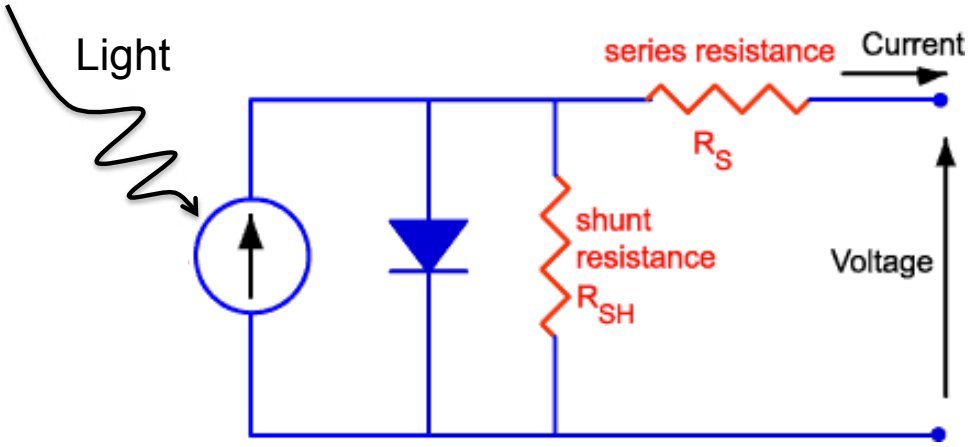

Figure B.6: Equivalent electric circuit for an non-ideal solar cell, with the parasitic series resistance (R_s and shunt resistance (R_{sh}).

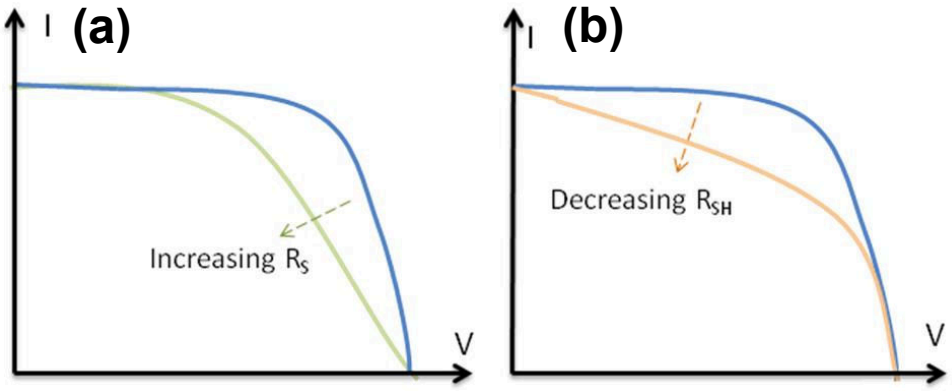

Figure B.7: Effect of (a). increasing the series resistance while keeping R_{sh}=∞, (b). decreasing the shunt resistance while keeping $R_s = 0$. In each case the outer $I - V$ has R_s=0 and R_{sh}=∞. In each case the effect of parasitic resistances is to reduce the FF

(pathways) and around the edges of the devices. The impact of both R_s and R_{sh} depends on the geometry of the device and crystalline quality of the material. For an efficiency solar cell, we want R_s to be as small as possible (ideally zero), and R_{sh} to be as large as possible (ideally infinity).

The equation for a solar cell in presence of only a series resistance is;

$$J = J_L - J_0 exp\left(\frac{q(V + JR_s)}{nkT}\right) \tag{B.11}$$

where J is the output current density of the solar cell, J_L is the current density generated by light, V is the voltage across the solar cell, kT/q is the thermal voltage (25.82 mV at 300K), n is the diode ideality factor and R_s is the series resistance.

The equation for a solar cell in presence of only a shunt resistance is;

$$J = J_L - J_0 exp\left(\frac{qV}{nkT}\right) - \frac{V}{R_{sh}} \tag{B.12}$$

where J is the output current density of the soar cell, J_L is the current density generated by light, V is the voltage across the solar cell, kT/q is the thermal voltage (25.82 mV at 300K), n is the diode ideality factor and R_{sh} is the shunt resistance.

The above equation are implicitly for solar cell with either R_s or R_{sh}, however, in a given device both of these resistance are present and therefore, the effect of both the resistance should be taken into account. When both the resistances are taken into account, the full diode equation becomes;

$$J = I_L - J_0 exp\left(\frac{q(V + JR_s)}{nkT}\right) - \frac{V + JR_s}{R_{sh}} \tag{B.13}$$

Appendix C

Growth of III-Nitride Materials

C.1 Growth by Metal-Organic Vapor Phase Epitaxy

III-Nitride based heterostructures are grown by different techniques, including the more advanced epitaxial methods such as molecular beam epitaxy (MBE) and metalorganic vapor-phase epitaxy (MOVPE). MBE is considered as the most precisely controlled epitaxial technique it terms of layer thickness and doping concentrations. Its also a useful technique in obtaining epitaxial layers with large homogeneity and less defects. The slow growth rate (about 0.2-0.5 μm/h) and difficulty to maintain ultra-high vacuum (about 10^{-10}–10^{-11} Torr) are the main disadvantages of this technique that limit its utilization for mass-production. Compared to MBE, MOVPE is the most commonly used epitaxial method of growing III-nitride based heterostructure devices, for instance, most of the light emitting diodes (LEDs) available in the market are grown by MOVPE. This is because of the fact that, MOVPE does not need a very high vacuum as well as the growth rate can reach (more than 2 μm/h). Though both the techniques are well developed for the growth of III-nitride materials, however regardless of the growth method, the growth of high quality InGaN epitaxial layers still remains one of the major challenges of this technology. All the InGaN based devices demonstrated in this thesis are grown by MOVPE at UMI-CNRS Georgia Tech, Lorraine.

The MOVPE technique is also known by a variety of names, including metaloragnic chemical vapor deposition (MOCVD), organometallic vapor phase epitaxy (OMVPE), and organometallic chemical-vapor deposition (OMCVD). Manasevit in 1968 demonstrated the very first growth of gallium arsenide (GaAs), gallium phosphide (GaP), gallium aluminum arsenide (GaAlAs), gallium nitride (GaN), and aluminum nitride (AlN) using MOVPE [215, 216]. In MOVPE, organometallic compounds of group III metals are transported in vapor phase to a reaction chamber, where they react with hydrides of group V elements in a chain of reactions that are generalized by:

$$R_3M_{(g)} + EH_{3(g)} \rightarrow ME_{(s)} + 3RH_{4(g)} \tag{C.1}$$

where, M and E represent the group III and group V elements respectively, R the organic compound (typically an alkyl) the group III element is attached to, and H elementary hydrogen.

The formation of GaN using trimethylgallium ($(CH_3)_3Ga$, TMGa) and ammonia (NH_3) is given by:

$$(CH_3)Ga_{(g)} + NH_{3(g)} \rightarrow Ga_{(s)} + 3CH_{4(g)} \tag{C.2}$$

The chemical reactions that happen inside the chamber during the growth of GaN are much more complicated. A detailed schematic of the one of the possible chemical processes during GaN growth is shown in Figure C.1, Similarly, the formation of InGaN using trimethylindium ($(CH_3)_3In$, TMIn), TMGa, and NH_3 is described by:

$$x(CH_3)3In_{(g)} + (1-x)(CH_3)_33Ga_{(g)} + NH_3 \rightarrow In_xGa_{1-x}N_{(s)} + 3CH_{4(g)} \tag{C.3}$$

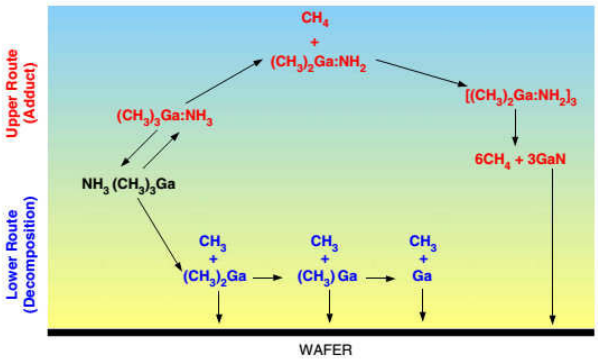

Figure C.1: A schematic of the chemical reactions inside the reactor chamber during GaN growth proposed by Parikh *et al.* [217]

In MOCVD, the metal organic precursors for III-Nitrides are trimethylgallium (TMGa) or Triethylgallium (TEGa), trimethylindium (TMIn). For doping of n-type GaN and p-type GaN, dopant elements Si and Mg are transported to the reactor through organometallics, *i.e.* Bis (cyclopentadienyl) magnesium (Cp_2Mg) and hydrides *i.e.* Silane (SiH_4).

All the samples processed and characterized in this thesis were grown by MOVPE reactor shown in Figure C.2. The study on growth of GaN and InGaN materials is outside the scope of

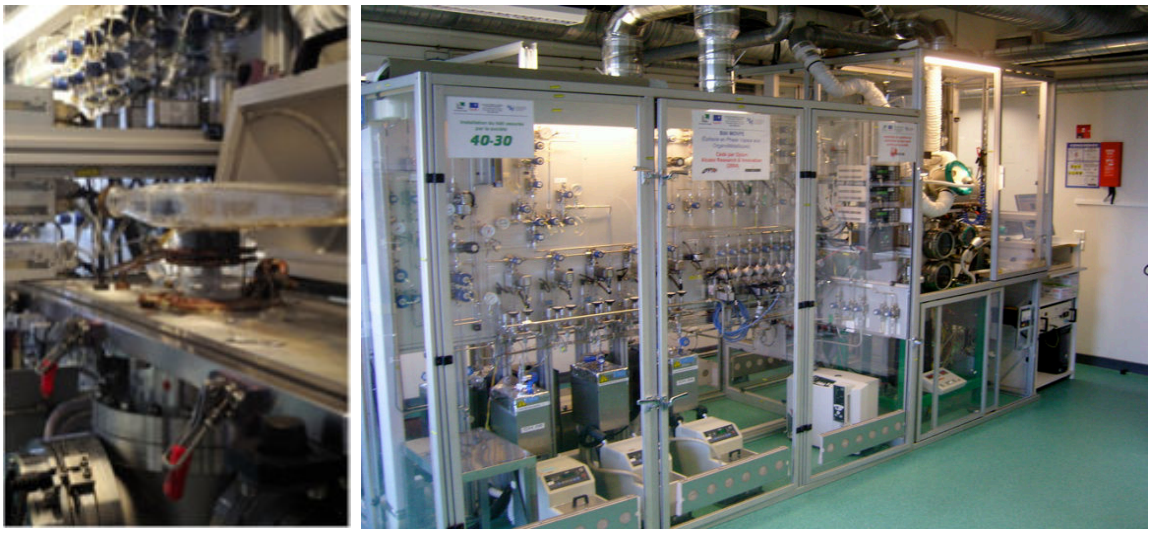

Figure C.2: The reaction chamber (left) and the gas panel of the MOVPE reactor (right) at UMI Georgia Tech Lorraine.

this thesis. Therefore, further details on growth and MOVPE setup can be found in Reference [170] and [218].

C.2 Nano Selective Area Growth

The density of threading dislocations in GaN is typically in the order of 10^7 - 10^9 cm^{-2}. With such a high density of threading dislocations, it is very challenging to high efficient and high performance devices. Therefore, the reduction of the threading dislocations is crucial for the improving the performance of InGaN based solar cells. Vennegues *et al.* was the first to reported the use of Si_xN_y as a micro-mask to reduce threading dislocation density in GaN structures [219].

The density of threading dislocations has been reduced upto 10^9 cm^{-2} by using Si_xN_y as a micromask [220]. Cheng *et al.* [221] has reported growth of GaN layers on silicon (111) substrate with a dislocation density of 10^9 cm^{-2} using a combination of AlGaN intermediate layers and a Si_xN_y interlayer. Selective area growth (SAG) of GaN on sapphire using MOVPE was first reported by Kato *et al.* [222]. Currently, MOVPE SAG is one of the main technology platforms for production of conventional monolithically integrated optoelectronic devices [223]. The SAG potentially provides an opportunity to allow spatially controlled growth through openings in a patterned substrate. The process of SAG begins with deposition of dielectric masks on the substrate by a photo-lithography process. The purpose of these dielectric masks is to introduce a "dead zone with no growth" on the substrate during the MOVPE process [223]. Therefore, the reactive precursors arriving from the gas phase to the wafer surface will not crystallize on the dielectric mask; they will, however, diffuse to the exposed region of the wafer, where the epitaxy process will take place.

Nano selective area growth (NSAG) is an extension of SAG to the level of the nano scale. The dielectric mask (in our case SiO_2) on the substrate contains nano openings (10-100 nm typically) where the nano-structures are selectively grown. Nano-structures due to tiny size of the epitaxial layer posses unique mechanical properties. In the conventional epitaxial growth, the epitaxial layer can only relax in the vertical direction (parallel to the growth direction) while the biaxial lattices are constrained to the substrate. Nanostructures, on the other hand, can relax in both the vertical and the lateral direction [223]. Figure C.3 shows the difference of stress relaxation between the conventional epitaxy growth and the NSAG. According to the theoretical study

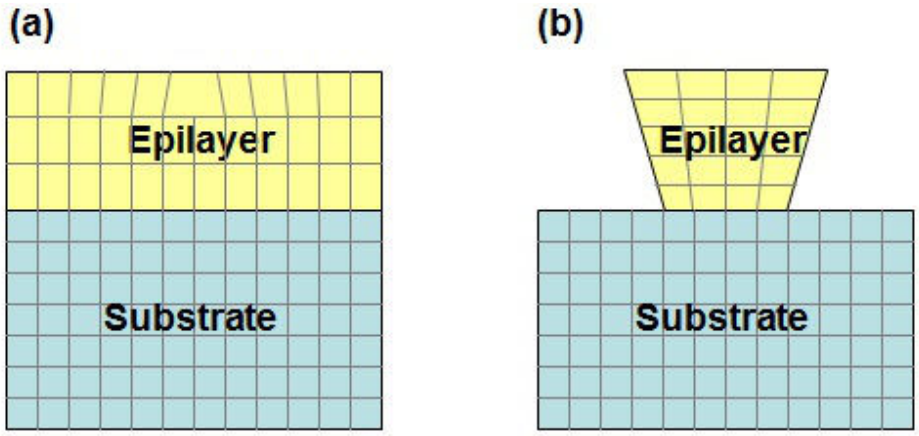

Figure C.3: The difference of stress relaxation between (a) the conventional growth and (b) nano selective area growth. The epilayer grown by the conventional epitaxial growth can only relax in the vertical direction while the epilayer grown by NSAG can relax in both vertical and lateral direction [223].

of stress relaxation in the nano-structure by Luryi *et al.* [224], the critical thickness strongly depends on the lateral dimension of the epitaxial layer for a given lattice mismatch. It is therefore possible to obtain dislocation free growth of lattice mismatched materials when the lateral dimension of the epilayer is smaller than a critical length. In conventional epitaxy, the total strain energy stored in the system increases linearly (blue line in Figure C.4) with the thickness of epitaxial growth until a dislocation is created. On the other hand, the total strain energy stored in the nano-structure does not increase linearly but saturates at after a certain height (red line in C.4) due to complete relaxation beyond that height. In theory, if the total energy at the saturation level is less than the amount of energy required to form a dislocation, a complete dislocation free epilayer can be grown regardless of the thickness [223].

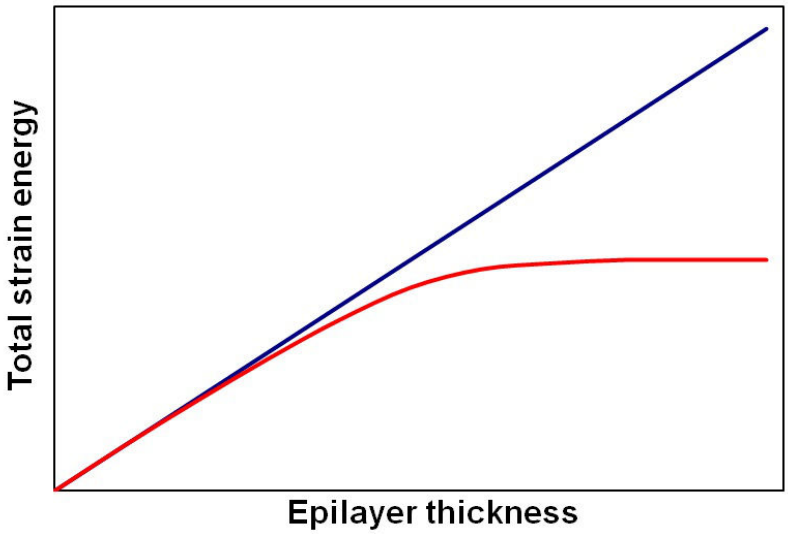

Figure C.4: Total strain energy stored in the system versus the thickness of the epilayer grown by (a) conventional growth and (b) nano selective area growth [223].

Appendix D

P-GaN Metal Contacting

D.1 Progress of Metallization Schemes to P-GaN

For the realization of all the applications including LEDs, laser diodes, UV photodetectors, photovoltaics, betavoltaic cells etc based on GaN materials, the achievement of ohmic contacts with low specific contact resistance (ρ_c) is of great technological importance. The large (6.5 eV) work function of p-GaN and the absence of any metal with a work function greater than 5.8 eV make it impossible to select a contact metal based on matching the work functions of the materials. The additional difficulty to deal with the impeding low resistance ohmic contacts on p-GaN come from the low carrier concentration of the Mg-doped p-GaN. The p-GaN is doped usually doped with Mg concentration upto 10^{20} cm^{-3}. However, such high concentration of impurities leads to growth disturbances, such as the creation of inclusions, stacking faults or inversion domains. Hence, as a consequence of high Mg- doping, the crystalline quality degrades [225]. In addition, the activation rate is extremely low, and only 0.1-1% of Mg atoms are activated. This is due to the requirement of high activation energy (170 meV) and the formation of Mg-H complexes, leading to a carrier concentration of around 1×10^{17} cm^{-3}. This poor Mg-activation limits the tunneling current needed for low resistance ohmic contacts.

The resistance of an ohmic contact on a specific semiconductor is determined by four major factors: (i) the fabrication of the GaN epilayer, (ii) the preparation method of the contact structure before contact deposition; the most important is the treatment of the semiconductor surface, (iii) the choice of the contact materials and their deposition, and (iv) the treatment of this contact by thermal annealing.

In the metal contact study of p-GaN, a wide variety of metallization schemes have been investigated as listed in Table D.1.

Table D.1: Metal contacts to p-GaN reported in literature. They are arranged in descending order of specific contact resistance (ρ_c), where NR = Not Reported.

Metal	thermal treatment (°C)	Ambient	Specific contact resistivity ($\Omega.cm^2$)	Reference
Ni/Au	500	Air	4×10^{-6}	[226]
Pd/Ag/Au/Ti/Au	800	Nitrogen	1.6×10^{-6}	[227]
Pd/Ru	600	NR	1×10^{-6}	[228]
Pt/Ru	600	NR	2.2×10^{-6}	[229]

Metal	thermal treatment (°C)	Ambient	Specific contact resistivity ($\Omega.cm^2$)	Reference
Pd/Ir/Au	400	NR	2×10^{-5}	[230]
Pt	As deposited	NR	2.0×10^{-5}	[231]
Ta/Ti	800	Vacuum	3×10^{-5}	[232]
Ta/Ti	800	Air	3×10^{-5}	[233]
Pt	NR	NR	3×10^{-5}	[234]
Ru/Ni	500	Oxygen	4.5×10^{-5}	[235]
Ti/Pt/Au	800	Nitrogen	4.2×10^{-5}	[236]
Ni/Pd/Au	550	Oxygen	1.0×10^{-4}	[237]
Pt/Ni/Au	350	NR	5.1×10^{-4}	[238]
Pd/Au	NR	NR	4.3×10^{-4}	[239]
Pd/Ni/Au	450	Nitrogen	5.03×10^{-4}	[240]
Ni/ITO	600	Air	8.6×10^{-4}	[241]
Pt	600	N_2/O_2	1×10^{-3}	[242]
W	700	Nitrogen	1×10^{-3}	[243]
Pt/Re/Au	600	Nitrogen	1.4×10^{-3}	[244]
Al/Pt	700	Nitrogen	2.1×10^{-3}	[245]
Ni/Pt/Au	500	NR	2.1×10^{-3}	[238]
Ni/AuZn	NR	NR	3.6×10^{-3}	[246]
Ni/AuZn	800	NR	8×10^{-3}	[246]
Ni/Pt/Au	500	Argon	2.1×10^{-2}	[238]
Cr/Ni/Au	700	Nitrogen	8.3×10^{-2}	[247]
Ni/Au	450	NR	1.7×10^{-2}	[248]
Ni/Ag	700	Nitrogen	3.5×10^{-1}	[249]
Ni/Ag	700	Nitrogen	1.7×10^{-1}	[250]

Metal	thermal treatment (°C)	Ambient	Specific contact resistivity ($\Omega.cm^2$)	Reference

Ishikawa et al. [251] reported that Ni with its high work function potentially provides a small Schottky barrier height to p-GaN. They stated that Ni can easily diffuse into the GaN surface, forming Ga-Ni phases which are instrumental to the ohmic contact formation to p-type GaN. Sheu *et al.* added the importance of Ga-Ni phases formed at p-GaN and Ni metal contacting after annealing [252]. Ni has been extensively used in the schemes of ohmic contacts to p-GaN: Pd(20nm)/Ni(30nm)/Au(200nm) [240], Ni(5nm)/Au(5nm) [226], Pt(20nm)/Ni(30nm)/Au(80nm) [231], Ni(10nm)/ITO(250nm) [253], Ni(20nm)/ Pt(30nm)/Au(80nm) [238], Ni(50nm)/Au(100nm) [254].

A significant breakthrough occurred when Ho *et al.* [235] carried out annealing of Ni/Au films in an oxygen-containing atmosphere. They reported a specific contact resistivity (ρ_c) of 1×10^{-4} $\Omega.cm^2$ by annealing in air at temperatures between 400° and 600°, and in some cases the reported resistivity was as low as 4×10^{-6} $\Omega.cm^2$ [226]. In contrast, annealing in an oxygen ambient, or annealing in pure nitrogen did not lead to improvement of the contact performance. Ho *et al.* [235] investigated the structure of the annealed contacts using transmission electron microscopy (TEM). They concluded that the contact structure undergoes significant transformation during annealing. They indicated that three types of the domains are created: crystalline NiO grains, crystalline Au grains and an amorphous compound of Ni-Ga-O with voids situated close to the GaN surface [255]. During their study, they observed that the decrease of the contact resistance is due mainly due to formation of NiO during the annealing process. The NiO itself was found to be a p-type conducting with a carrier concentration of about 2×10^{17} cm^{-3} as measured by the Hall measurements [226]. Jang *et al.* [256] also reported that the Ga atoms were dissolved in the Au contact layer and the oxygen atoms incorporated during annealing promoted the out diffusion of Ga atoms from the GaN layer, leaving Ga vacancies below the contact. This formation of Ga vacancies results in the enhancement of net hole concentration and reduction of the Fermi level position, which is the important part to reduce the contact resistivity.

Another model, proposed by Koide *et al.*, assumes that low contact resistance is due to the increase of the hole concentration in GaN subsurface layer, by removal of hydrogen atoms and de-passivation of Mg-acceptors [257]. During annealing, in-diffusion of Au atoms and dissolution of Ga atoms takes place, due to high solubility of gallium in gold. This out diffusion of Ga atoms results an increase in the acceptors-type Ga vacancies, thus lowering the resistivity of p-GaN and improving the contact performance [258]. Yan et al. [259] studied the the effect of Au amount to dissolve Ga atoms on ohmic characteristics. The TEM cross-sectional observation indicated that Ni did not diffuse to the GaN surface during annealing and the Ni transformed to NiO at the same time. They show [259] that the final micro-structure after annealing becomes Au/NiO/Au/p-GaN, where the Au layer agglomerated into the semi-continuous and NiO was considered a barrier to prevent the diffusion of Ga atoms. Therefore, the presence of Au plays a role to dissolve the Ga atoms from p-GaN, leaving Ga vacancies below the metal contact, thus increased the hole concentration of p-GaN.

D.2 P-GaN Surface Treatment

The surface and interface between the various layers of semiconductor device structures are fundamental components of solid state architecture. The surface stiochiometry of p-GaN prior to metallization can significantly influence the electrical properties of the metal/p-GaN interface.

Over the course of the development of semiconductor device technology, surface cleaning procedures have been devised to [260], (i) degrease and remove gross contamination, (ii) remove particulates and metal atom contamination, and (iii) remove surface oxides to provide surfaces as atomically clean as possible.

In practice, surface cleaning is as much of an art form as it is a science; understanding of the surface composition and structure often lags well behind the successful application of processing steps. Procedures are frequently derived empirically with little detailed investigation of the chemistry or physics involved. Often, the meaning of the word "clean" varies depending on the surface conditions required for success with different processing steps, though surface impurity concentrations may vary by orders of magnitude [260]. Given that the sensitivity of surface analytical techniques for detection of sub-mono-layer coverage is limited, there are inherent limits on the ability to show conclusively that a surface is truly atomically clean [261].

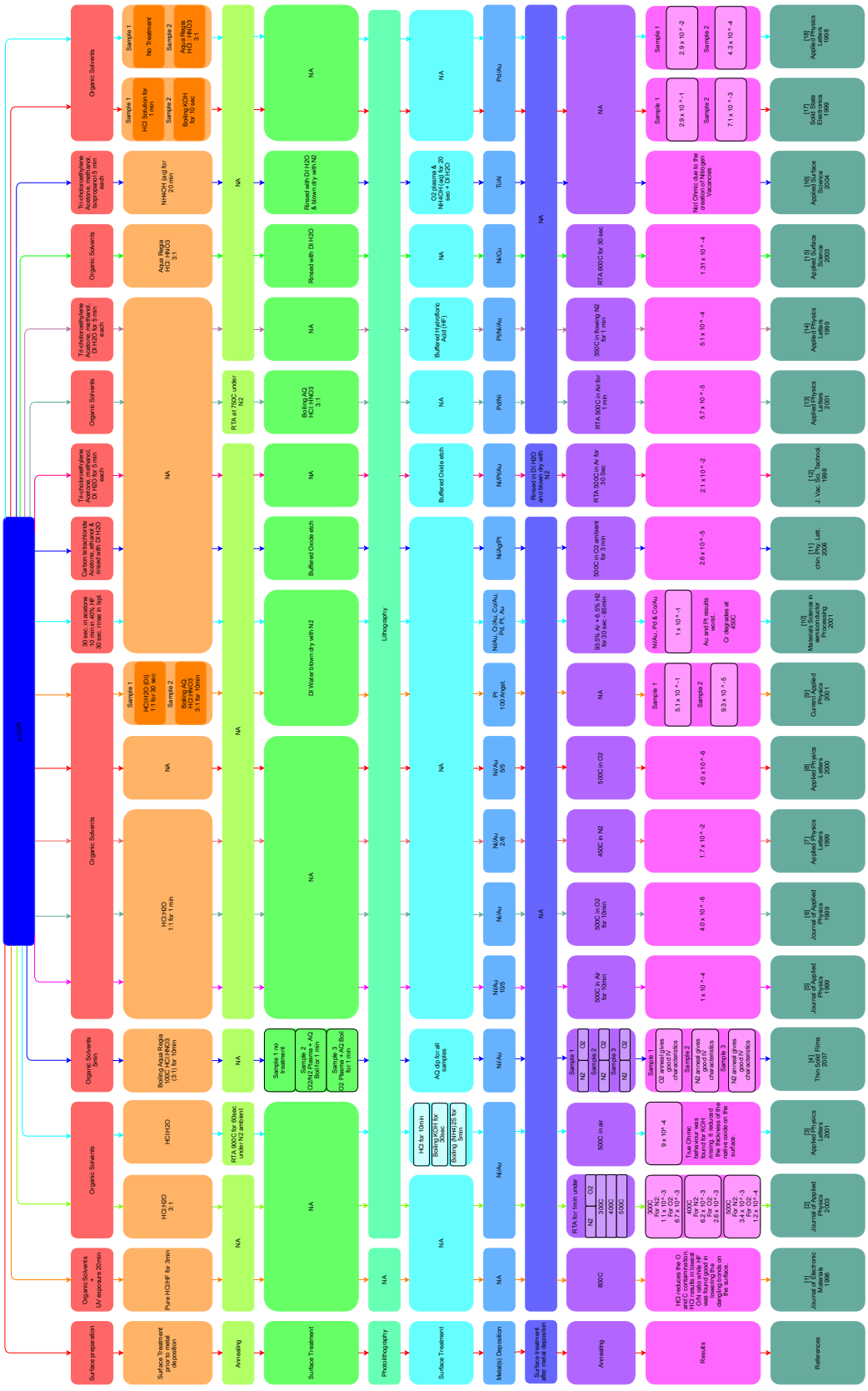

Figure D.1: Flow chart listing the different metal/p-GaN optimization studies.

D.3 Work Plan for the P-GaN Metal Contacting

The literature findings reported so far, describing the metal/p-GaN contacting can thus be summarized into a flow chart shown in Figure D.1. It shows that the optimization study of achieving low resistance ohmic contacts to p-GaN includes several significant parameters. For instance, the selection of the surface chemical treatment and/or metal selection and/or annealing temperature and ambient etc.

A detailed parametric study wok plan for optimization of metal contact to p-GaN carried out during this study, is given in Figure D.2. Since most of the findings for metal/-pGaN

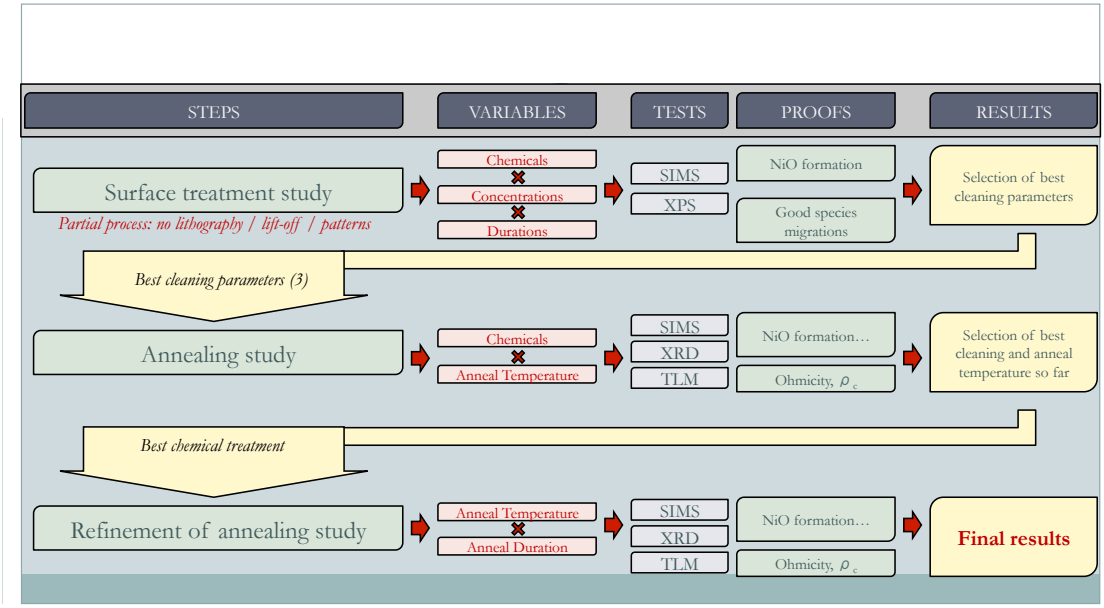

Figure D.2: Parametric study plan for the optimization of the metal/p-GaN contacts.

contacting provide the evidence that Ni is a potential candidate involved in formation of low resistance ohmic contacts to p-GaN. Therefore, Ni is used a major metal candidate along a bi-layer metallization scheme i.e. Ni/Au, Pd/Au and Ni/Ag.

As it is known the most important step in the lithographic process is the minimization of the defects, caused by particles either falling on the surface prior to epitaxy or during the steps of lithography. This is the reason why semiconductor processing is performed in ultra clean facilities, known as a clean-rooms, which uses sophisticated filtration such as filters employing laminar or turbulent air flow (Figure D.3) to remove airbone particulate. The cleanliness of a clean- room is measured by the size and number of dust particles in a given volume of air. The photo-detector fabrication was carried out in the Minalor Platform in the Institute Jean Lamour (IJL) clean room facility (Figure D.4) at Université de Lorraine.

D.4 Photolithography

The process of patterning the given material with a mask sensitive to the photons, electrons or ions is referred as lithography. During this study, optical lithography or photo-lithography is used. An optical lithography tool consists of an ultraviolet (UV) light source, a photo-mask, an optical system, and a wafer covered with a photosensitive layer, called photo-resist because of its ability to resist chemicals used in subsequent processing. The mask is flooded with UV light and the mask pattern is imaged onto the resist by the optical system. All these processing

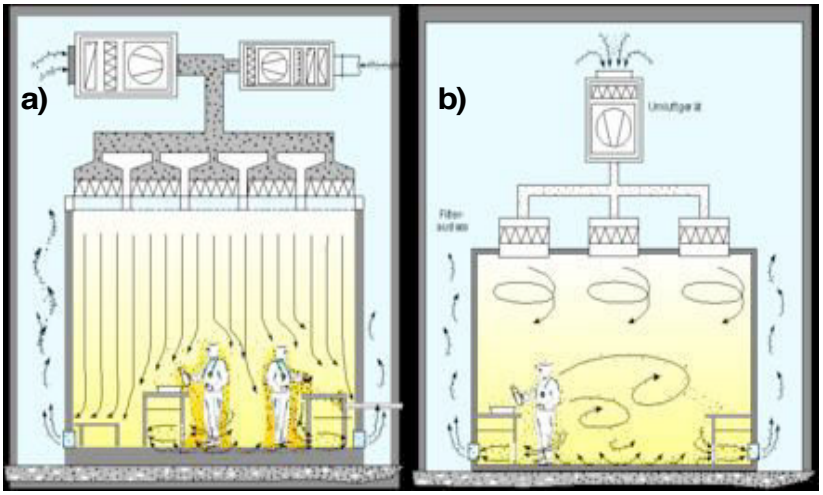

Figure D.3: (a) Laminar air flow system, directly filter downward air in a constant stream towards filters located on walls near the clean-room floor, (b) Turbulent air flow which uses both laminar air flow hoods and non-specific velocity filters to keep air in a clean-room in constant motion [188]

Figure D.4: Minalor clean-room facilities and equipment's used in our device processing and fabrication. To the right is the "salle rouge" for doing lithography and to the left is the sputtering and thermal evaporator for doing metal deposition.

steps, including the different type of surface chemical treatments, lithography and metallization schemes used during this thesis, are discussed in detail below.

D.5 Surface Treatments

The appropriate chemical etchants to clean the surface prior to the deposition of metal contact is the most important step. In p-GaN contacting schemes, a major part in the key achievement of obtaining the low resistance ohmic contacts comes from the surface treatments. The particular step for chemical treatment i.e. before lithography and/or after lithography (Figure D.5) remained a major challenge during this study for surface treatment. The organic solvents (acetone, isopropanol) are not included in the surface treatment process. Every sample before getting into the chemical treatment, before lithography and/or after lithography was cleaned in acetone for 5 minutes, followed by isopropanol for 5 minutes and rinsed in de-ionized (DI) water

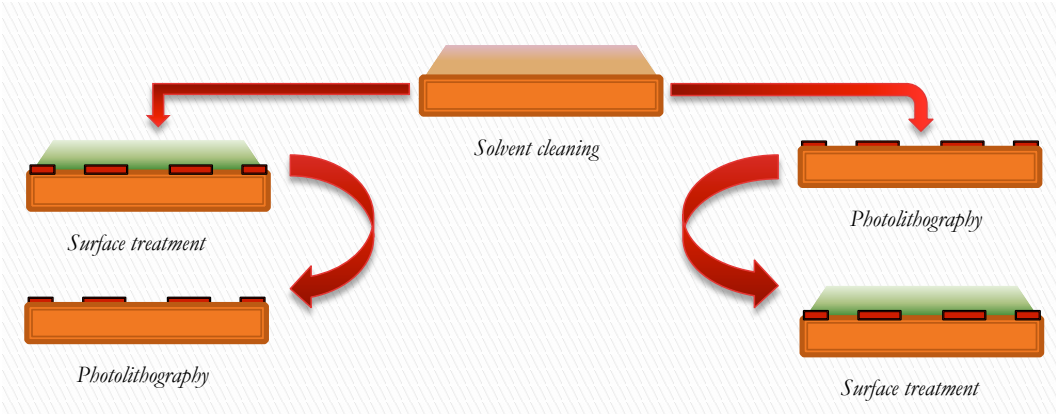

Figure D.5: Surface treatment processes used in this thesis.

for 1 minute.

Three main surface chemical treatment process were chosen for the optimization along with two steps i.e. before lithography and after lithography as shown in Figure D.6. Although

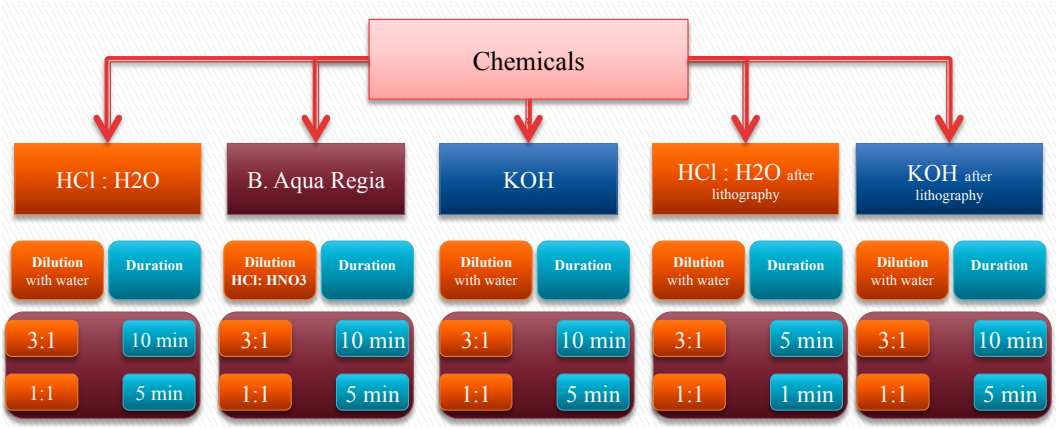

Figure D.6: The different chemicals, concentrations and duration used in this thesis for optimization of p-GaN metal contacting.

these chemical treatments are intended to remove the native oxide on p-GaN surface but it is reasonable to expect that the degree of their effectiveness in removing oxide may vary. Due to limitations of the clean-room, the boiling aqua regia and KOH were limited to a maximum temperature of 80°C.

The surface treatment of p-GaN after lithography was pretty challenging due to the risk of losing the mask patterning, as shown in Figure D.7. We tried HCl:H_2O and KOH with different concentration and duration (see Figure D.6), after lithography. The mask patterning were lost and/or damaged, therefore, the surface treatment after lithography was later on avoided for all the other samples.

The surface treatment before lithography was carried out with different chemicals, concentrations and duration as shown in Figure D.6. The samples were than rinsed with DI-water for one minute and finally blown dry with nitrogen flux.

D.6 Photoresist Parameters

The resist used in the photolithography process, referred as the photo-resist is a photosensitive material composed of three main components: a resin or base material, a photo-active compound

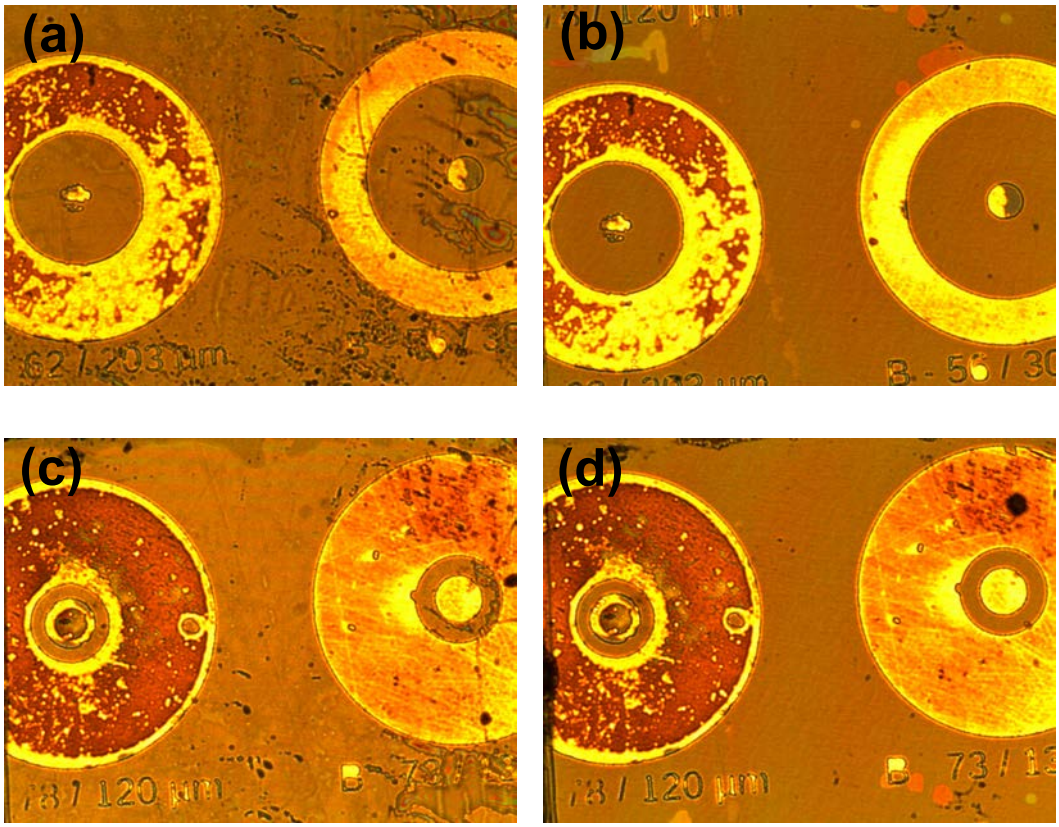

Figure D.7: (a)–(b). Surface treatment by HCl:H_2O before and after lithography respectively, (c)–(d). Surface treatment by KOH before and after lithography respectively.

and an organic solvent. The photoresist can be of two types: a positive and a negative photoresist depending on its chemistry which determines its property when exposed to light. Depending on the duration and light exposure, they can be more or less easily dissolved using a developing solution. The transfer of the mask image onto the wafer significantly depends on the duration of light exposure and developing time. The choice of photoresist i.e. positive or negative depends on the subsequent process. During the optimization study in this study, a positive photoresist was used.

The samples after been passed through the different chemical surface treatments, as discussed in the previous section, were fired dried using a hot plate at 115°C for 120 seconds. They were than attached to a spindle using a vacuum chuck, a small puddle of a lift-off resist film (LOR3A) in a yellow light clean-room environment, to avoid any white light (rich in ultraviolet) that can degrade the resist. The spindle is then spun rapidly; rotating the sample at seven thousand revolutions per minute for ninety seconds. The rotation of the spindle was optimized first for achieving the desired thickness of the photoresist film. After the photoresist was applied, the sample was placed onto a hot plate at 140°C for 10 minutes.This step known as the pre-bake or a soft-bake step, is performed to drive out the solvents present in the resist and to improve adhesion. After the deposition of the first resist layer the same procedure is used for the deposition of a second layer of the photoresist (S1813) as shown in Figure D.8 with a soft-bake step at 115°C during 120 seconds. Once this was done, the samples ready for the mask alignment and exposure. In FigureD.8(a), the positive photoresist (S1813) is exposed using a source of intense ultraviolet light during 8 seconds which alters its chemical bonding to make it more soluble where it has been exposed. After the exposure, they were ready for the etching. During this thesis, we used chemical etching also known as wet etching shown in Figure D.8(b), however there also exist a physical etching also called dry etching. The samples were immersed

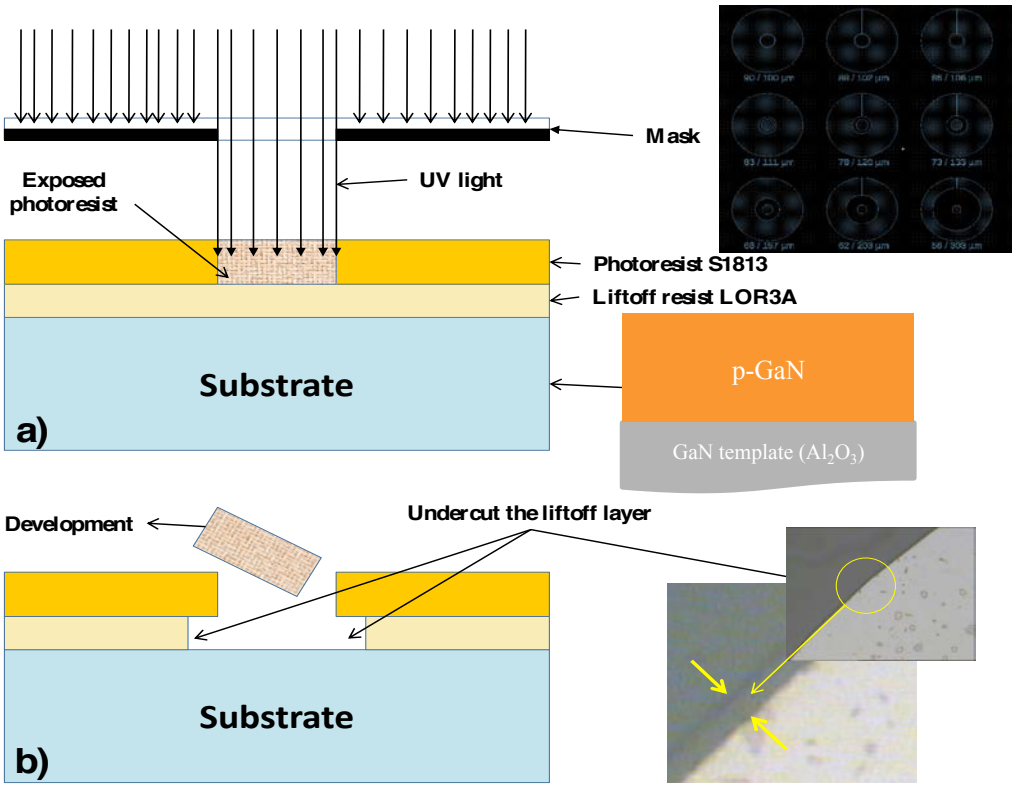

Figure D.8: Photolithography process sequence. When using positive resist, the exposed regions are dissolved in the developing solution, while the unexposed areas remain intact. (a) The positive photoresist is exposed using a source of intense ultraviolet light. (b) The wafer is removed from the alignment station and areas exposed are dissolved in a solution.

into a developer solution for 80 seconds followed by rinsing in DI-water. The exposed regions of the photoresist layer are dissolved in the developing solution, leaving the unexposed areas intact. The duration of exposure and immersing in the developer solution were quite challenging. Even a difference of few seconds could bring a big shift in the output results. Once this was done, the samples were ready for the metal deposition.

D.7 Metal Deposition

The vacuum deposition system shown in Figure D.9, consists of a vacuum chamber, maintained at a reduced pressure by a pumping system. It is generally a metal chamber, made of stainless steel. The deposition system contains a wafer holder, a shutter, a thickness range monitor, heaters, and an ion gauge to monitor the chamber pressure. It is important to maintain vacuum deposition system at low pressure, to ensure that the concentration of oxygen molecules is small enough to minimize the risk of oxidation reaction.

Since the thickness of the metals particularly the Ni layer thickness significantly affects the contact resistance, therefore the different layer thicknesses were first optimized. Poor adhesion of Ni was challenging, as bad adhesion of the Ni/p-GaN layer would undoubtedly lead to the separation of epitaxial films and the metal contact. This problem was solved by using thin (10 nm) Ni layer, however, we observed that the optimization of the subsequent Au or Ag layer remain unimportant in both improving the Ni adhesion and/or obtaining low resistance ohmic contacts. Finally, after trying different thicknesses for the Ni/Au and Ni/Ag metals, an optimized thickness of 10 nm/10 nm was found effective in obtaining the low resistance ohmic

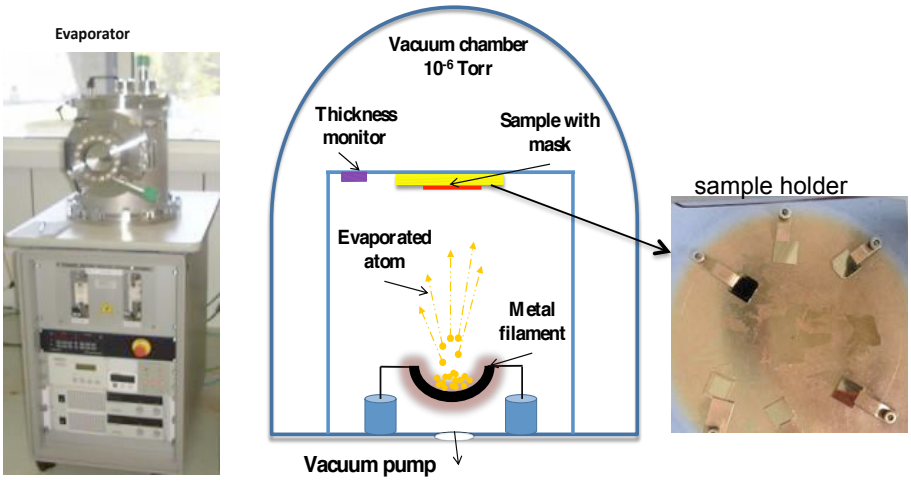

Figure D.9: Cross-section of a typical vacuum evaporation system which includes a vacuum chamber, a sample holder, a metal filament, and a thickness monitor. The samples are mounted onto the holder for metal deposition.

contacts. The deposition of metal contacts including the Ni/Au and Ni/Ag on p-GaN was accomplished through vacuum deposition, as shown in Figure D.10.

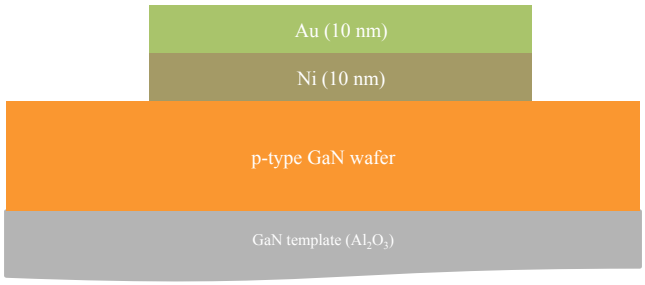

Figure D.10: A typical metallization scheme consisting of Ni(10nm)/Au(10nm).

D.8 Rapid Thermal Annealing

The thermal annealing optimization was performed with rapid thermal anneal (RTA). To achieve short time annealing time trade off is made in temperature and process uniformity, temperature measurement and control and wafer stress as well as throughput. One of the key challenges in rapid thermal processing is accurate measurement and control of the wafer temperature. Monitoring the ambient with a thermocouple has only recently become feasible, in that the high temperature ramp rates prevent the wafer from coming to thermal equilibrium with the process chamber. The reaction chamber inside the RTA equipment can be filled with gas, pumped down to vacuum or kept filled with air during the annealing. The processing gases vary according to the requirement of the process. Typical process gases are inert, e.g., Oxygen, Nitrogen or Air.

The RTA equipment named Jipelec JetFirst 200C furnace, used in this thesis is shown in Figure D.11. Heating in Jipelec JetFirst 200C RTP is done with 18 infra red lamps as shown in Figure D.11(b). The process temperature is measured using a pyrometer. Annealed sample is located on a susceptor and the pyrometer measure the temperature from the bottom of the susceptor. During the optimization study, we used nitrogen and oxygen as the input gases, with different annealing temperature and duration. Finally the optimum was found as 500°C for

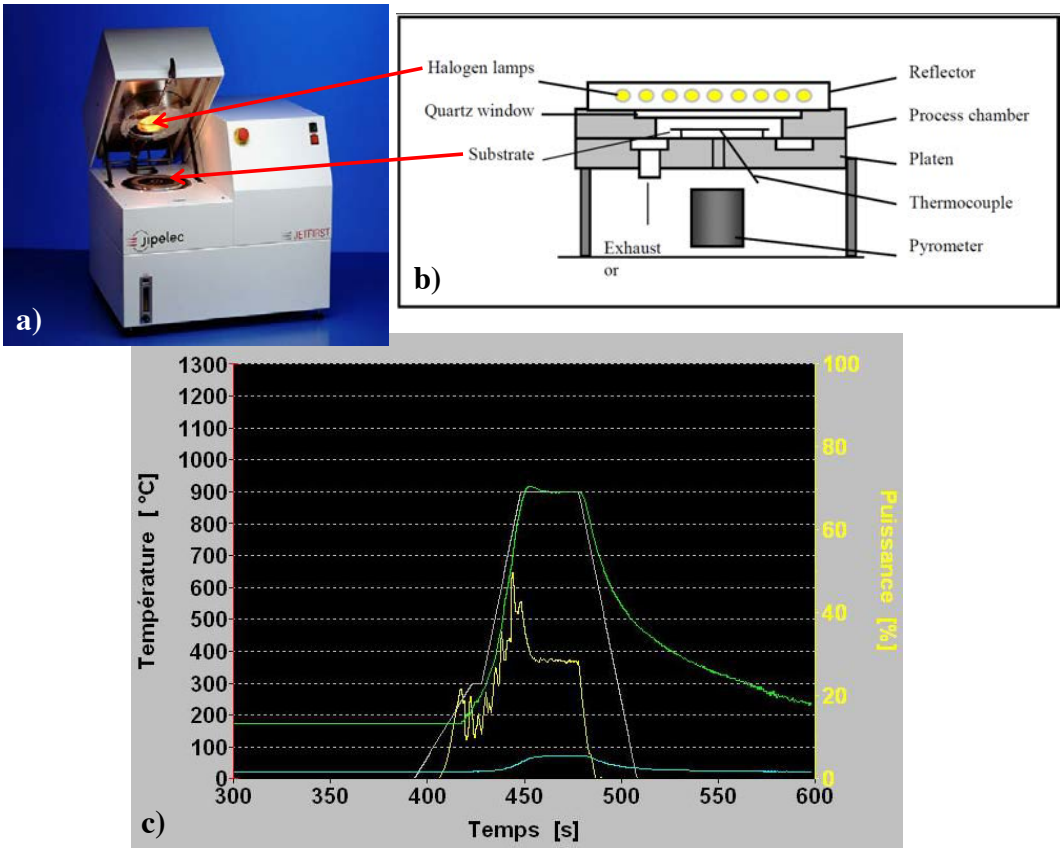

Figure D.11: General overview of the furnace (a), infrared halogen lamps heat up the substrate through a quartz window located on the topside of the process chamber (b)–(c). Temperature versus time profile, yellow line represent the power, green line represent the real-time temperature of the sample and the white line shows the rise, steady and fall time.

5 minutes, for both nitrogen and oxygen. The ramp up rate was set to 10°C/sec. After the ramp up the temperature was kept steady for 5 minutes, as shown in Figure D.11. The drop in temperature was kept around 10°C/sec.

One of the problems observed during annealing of the metal contacts was the over exposure to the high annealing temperature. For instance, Figure D.12 shows an example of the deteriorated metal contacts to p-GaN due to the over annealing temperature and/or duration. This problem was later on sorted out by reducing the temperature and duration.

Device Characterization

The electrical characterization performed for the metal/p-GaN devices are described in this section. It includes an overview of the basic principles of ohmic contact formation, followed by the introduction to the specific contact resistance (ρ_c), in reference to the circular transmission line models (CTLM). Finally the results obtained for the optimization of the metal/p-GaN contacts are described in this section.

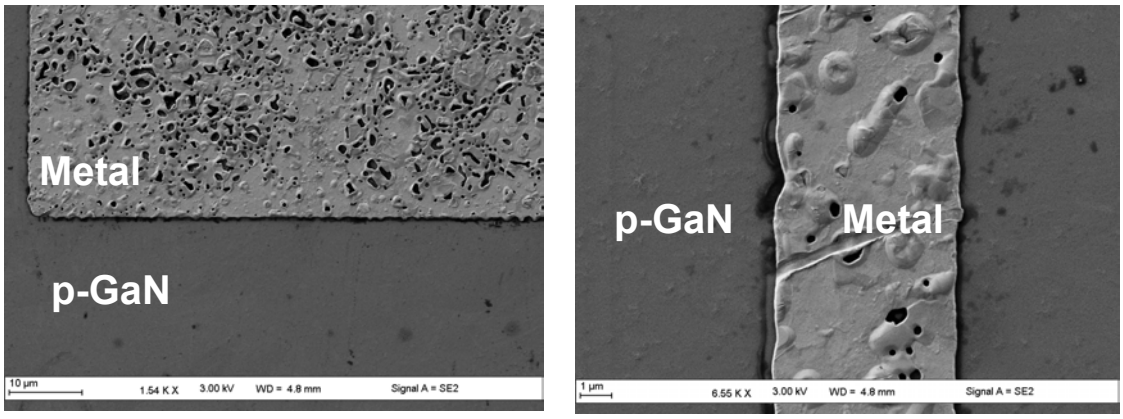

Figure D.12: Metal/p-GaN contacts after RTA under nitrogen at 800°C.

D.9 Ohmic Contacts

It is imperative that a semiconductor material can be connected to the outside world with no adverse change to its current-voltage characteristics and power losses. To accomplish the task, extremely low resistance ohmic contacts are needed at the semiconductor interface. The term "ohmic contact" is generally used to refer to contacts for which the current - voltage characteristics are determined by the resistivity of the semiconductor material or by the behavior of the device to which they belong, rather than by the characteristics of the contacts themselves. Ideally, an ohmic contact is a metal contact, when combined with the semiconductor, no barriers to the carrier flow are encountered in either the positive and negative direction. To obtain this condition, metal with a large work function and/or high doping concentration of the semiconductor are needed. However, in case of wide bandgap material such as p-GaN, its challenging not only in finding a metal with a large work function but also in obtaining high p-type doping concentration. The work-function of p-GaN is 7.5 eV while the highest work-function for a metal (Pt) is only 5.7 eV, making it quite challenging for the formation of low resistance ohmic contacts. In addition the poor p-type Mg doping makes it further challenging in achieving low resistance ohmic contacts at p-GaN interface. Until researchers are only able to activate upto 1% of the incorporated Mg.

D.9.1 Basic Principle of Ohmic Contact Formation

The formation of an ohmic contact in particular to p-GaN is more an art than a science. Since there are so many optimization parameters involved, therefore it is hard to define a particular recipe that would work for every body. The work function plays an important role in defining the type of contact formation at the p-GaN interface. In general when a metal and a semiconductor with different work function comes into contact, the Fermi levels are forced to align at the thermal equilibrium [262, 263]. The depiction of the energy band diagram between the metal and semiconductor depends on the type of the semiconductor. The energy band diagrams for the metal to p-type semiconductor interface is depicted in Figure D.13. The work function of metal (ϕ_m) is the energy gap between Fermi level of the metal and the vacuum level. Table D.2 lists the work function for the most commonly used metals for the ohmic contacts to p-GaN. The work function of semiconductor (ϕ_s) is the energy gap between Fermi level of semiconductor and the vacuum level. The electron affinity (χ) is defined by the energy gap between the conduction band and the vacuum level.

The work function of the metal ($q\phi_m$) and the semiconductor ($q\phi_s$) defines the type of the contact *i.e.* rectifying or ohmic contact. If the metal work function is greater than that

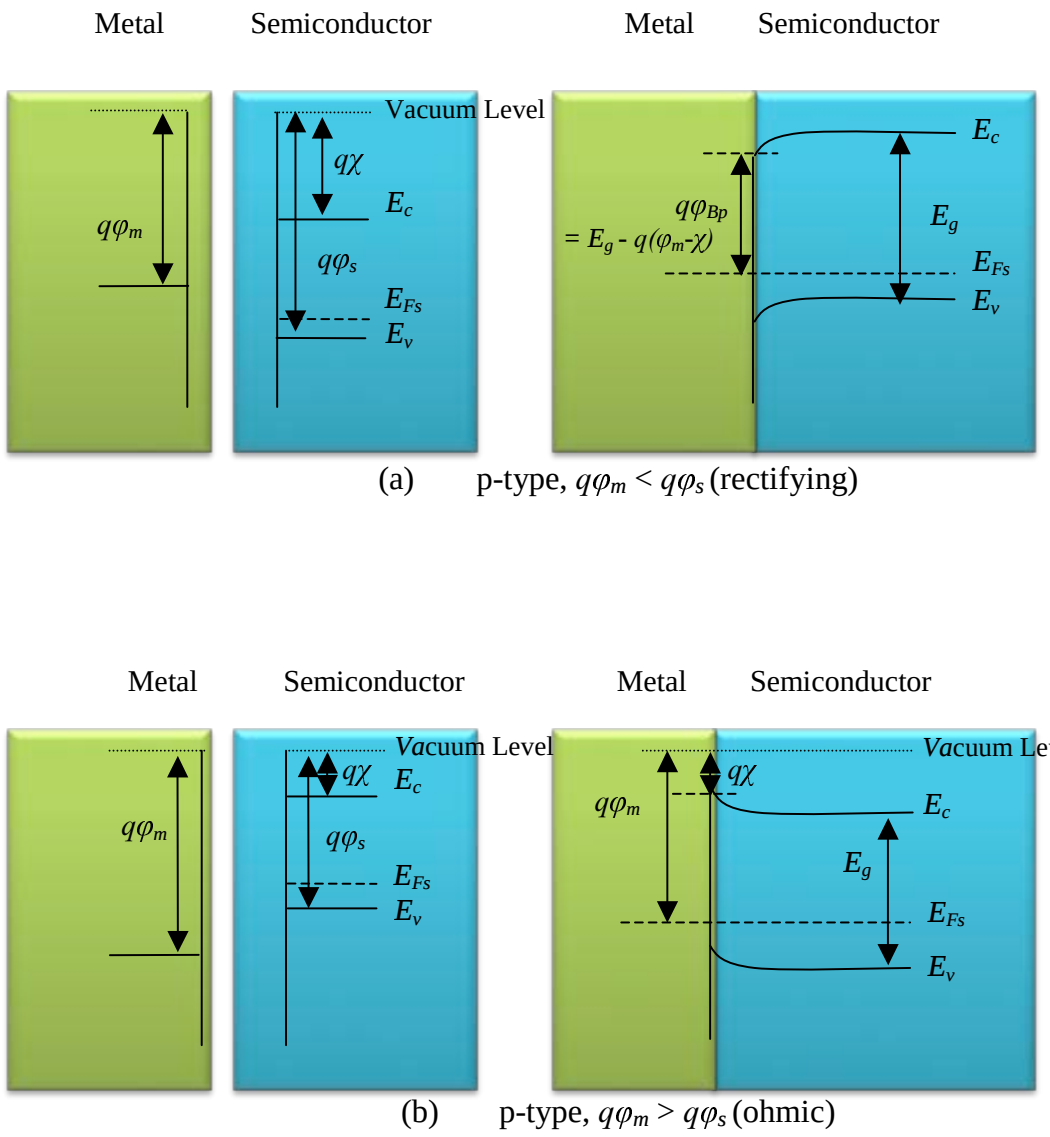

Figure D.13: The energy band diagram of metal to p-type semiconductor contacts.

of the semiconductor, the contact thus formed will be ohmic. According to the Schottky-Mott model, the metal contact formed between a metal and a semiconductor with $\phi_m < \phi_s$, is called a Schottky contact with a barrier known as the Schottky barrier [262]. The Schottky barrier height formed between a metal/p-GaN interface can be measured as shown in Figure D.13(a) [264].

$$q\phi_{Bp} = E_g - q(\phi_m - \chi) \tag{D.1}$$

where,

qϕ_{Bp} is the Schottky barrier height of p-type semiconductor,

E_g is the energy bandgap,

qϕ_m is the work function of the metal in contact,

qχ is the electron affinity of the semiconductor in contact.

Table D.2: The work function of some common metals.

Metal	Work function
Pt	5.36
Pd	5.12
Ni	5.03
Au	4.89
W	4.54
Ag	4.50
Cu	4.45
Mo	4.20
Ti	4.17
Al	4.08

D.9.2 Specific Contact Resistance

The contact resistance between a metal and a semiconductor is a metal and geometry dependent parameter as its magnitude is determined by the sheet resistance of the conducting semiconductor, the contact area, and etc. Consequently, contact resistance is not a useful parameter to characterize contacts.

The parameter that is independent of the measurement and geometry of the contact, providing the most systematic way to compare different metallization schemes with respect to the contact resistance is known as the specific contact resistance ρ_c. It is determined by the barrier height, the doping concentration and the temperature [265]. The specific contact resistance is due to the potential barrier at the metal-semiconductor interface and is defined as the resistance of a unit area of the thin interfacial layer between the bulk metal and semiconductor substrate, as given by [266],

$$\rho_c = \left(\frac{\partial x}{\partial V}\right)^{-1}_{V=0} [\Omega.cm^2] \tag{D.2}$$

where J is the current density through the interface, and V is the potential drop across the interface. The expression for the current density depends on the ruling current transport mechanism.

The ρ_c is basically the finite resistance observed by the current flowing through the metal/p-GaN interface, as shown in the schematic Figure D.4. The current transport mechanisms that are of interest in ohmic contacts are thermionic emission (TE), thermionic field emission (TFE) and field emission (FE) respectively.

The thermionic emission (TE) occurs, when the doping density is less than 10^{17} cm^{-3} [264]. Under the TE, the carriers have to be thermally excited over the barrier as shown in Figure D.15(a). In intermediate doping range, thermionic-field emission (TFE) dominates [267,268]. As shown in Figure D.15(b), the carriers are thermally excited to an energy level where the barrier is sufficiently narrow for the tunneling effect to take place. For a high doping density ($> 10^{20}$ cm^{-3}), the barrier is sufficiently narrow at the bottom of conduction band, as shown in Figure D.15(c). The Field Emission (FE) dominates in the high doping density, and the electrons can tunnel across to the barrier directly.

The universal expression for the current densities in the different current transport mecha-

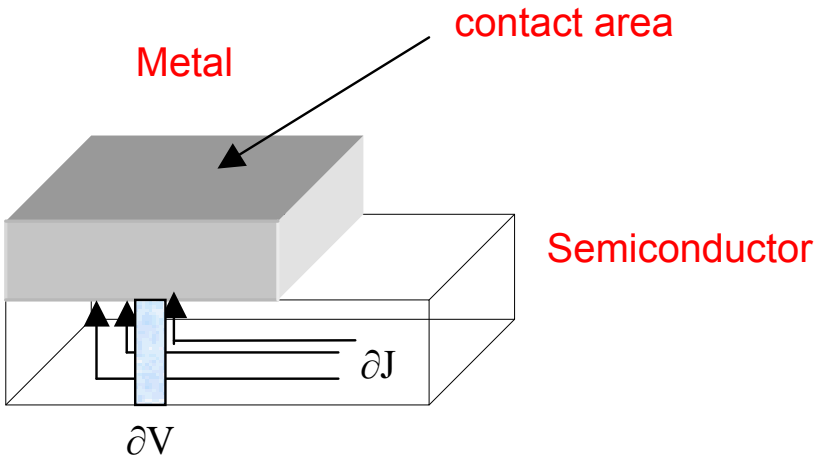

Figure D.14: The metal/p-GaN(semiconductor) contact for the specific contact resistance layout.

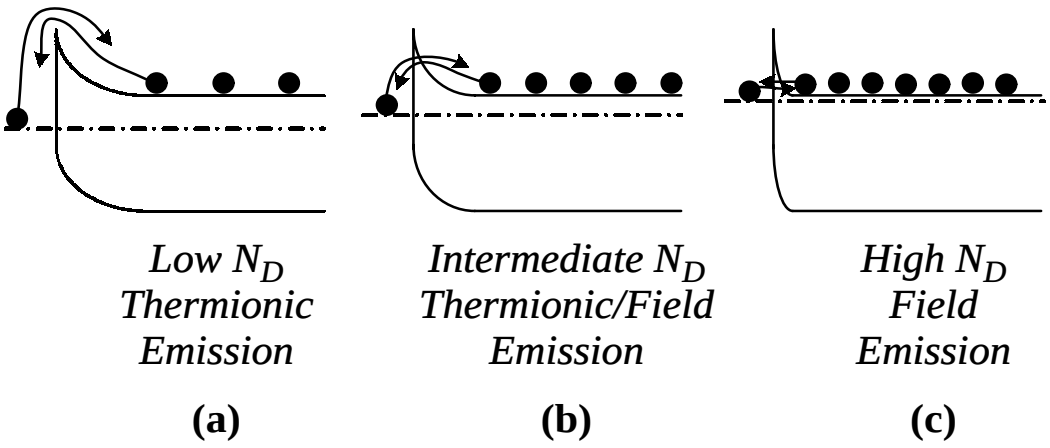

Figure D.15: The current transport mechanism of the carriers, (a) Thermionic Emission, (b) Thermionic/Field Emission, (c) Field Emission across the barrier.

nisms (TE, TFE, FE), with the use of the diode's ideality factor are given as [269],

$$J = J_s exp\frac{qV}{nk_BT}\left[1 - exp - \frac{qV}{K_BT}\right]\begin{cases} n = 1 & \text{(TE)} \\ 1 < n < 2 & \text{(TFE)} \\ n \geq 2 & \text{(FE)} \end{cases} \tag{D.3}$$

Using the definition of ρ_c and equations D.3 that give the expressions for the current densities in the case of TE, TFE and FE respectively, the expressions for the ρ_c in each of these cases can be determined by [265],

$$\rho_c \propto \exp(\frac{q\phi_{Bn}}{K_BT}) \qquad TE \tag{D.4}$$

$$\rho_c \propto \exp\frac{4\pi\sqrt{m^*\epsilon\epsilon_{r,s}}}{h}(\frac{\phi_{Bn}}{\sqrt{N_d}})tanh\left[\frac{qh}{4\pi K_BT}\sqrt{\frac{N_d}{m^*\epsilon\epsilon_{r,s}}}\right] \qquad TFE \tag{D.5}$$

$$\rho_c \propto \exp\left(\frac{4\pi\sqrt{m^*\epsilon\epsilon_{r,s}}}{h}\right)\frac{\phi_{Bn}}{\sqrt{N_d}} \qquad FE \qquad \text{(D.6)}$$

The value of ρ_c in a given metal-semiconductor system is determined by the combination of the following three parameters [265],

1. the potential barrier height ϕ_{Bn}
2. the doping concentration N_d (in our case, its a p-type semiconductor),
3. the temperature T.

The relative effect of the parameters like, barrier height, doping concentration and temperature in various current transport mechanisms can be from the exponential terms that contribute to ρ_c. As obvious from the equation D.4, the thermionic emission current transport mechanism is independent of the carrier concentration. However, in the case of the thermionic field emission (equation D.5) and field emission (equation D.6), the current transport mechanism across the barrier is dependent on the doping concentration.

Characterization: LTLM and CTLM

The transmission line model (TLM), proposed by Shockley *et al.* [270] is the most widely used model for accessing the quality of metal contacts as well as electrical properties of the devices, eventually resulting in obtaining the specific contact resistance. Murramann and Widmann [271], Reeves and Harbison [272] after couple of modifications, used this model with rectangular and concentric metal contacts to obtain the semiconductor sheet resistance R_{sh}, and the specific contact resistivity. The R_{sh} can be calculated from the specific contact resistance, given as [273] ;

$$R_{sh} = \frac{\rho_c}{t} \qquad \text{(D.7)}$$

where t is the thickness of the semiconductor layer used and R_{sh} has the dimensions of ohms, but it is universally given in the units "ohms per square" (Ω/sq).

Two basic transmission line models are currently used for estimation of the specific contact resistance i.e. LTLM and CTLM. The linear transmission line model (LTLM), as shown in Figure D.16, is the simplest and most widely used configuration of the transmission length mode. In LTLM, the linear array of ohmic metal contacts are placed with an increasing distances d_i

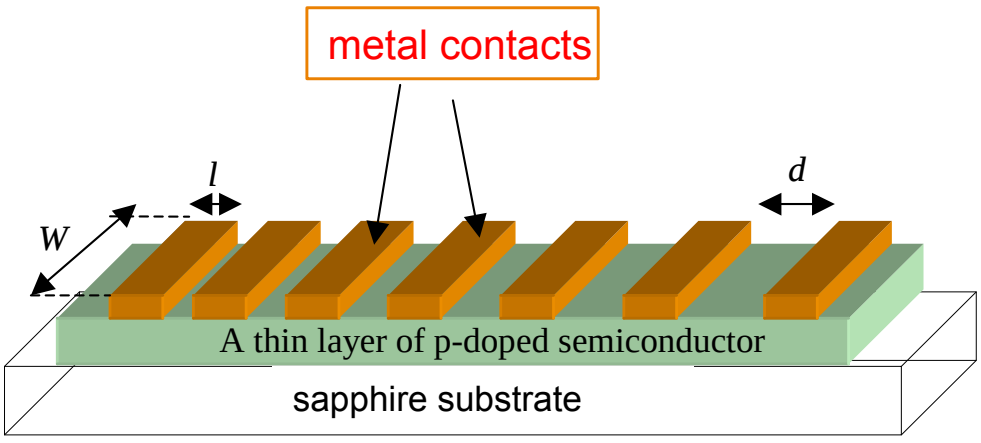

Figure D.16: Rectangular pattern where W is the width of the pads, l is the length of the pads and d is the distance between the metal contacts.

($d_1 < d_2 < ... < d_i$). A major challenge in the LTLM is the isolation of the metal contacts

in order to confine the current flow between the metal contacts only. The isolation is obtained during the photolithography techniques, by etching away areas of the electrically active semiconductor material down to the semi-insulating substrate. However, its also possible to avoid the complicated step of mesa formation in the LTLM metal contacting as it was done by one of our colleague for the solar blind ultra-violet photo-diodes [188].

The second transmission line model is the known as the circular transmission line model. The CTLM metal contacting eliminates the need of the mesa etching of the epitaxial layer for current restriction. In addition, it also eliminates the the errors that are introduced by the lateral current crowding and gap effect, which are always present in the LTLM structures. The CTLM proposed by Reeves *et al.* [272] has a test pattern consisting of a central disc contact and two concentric ring contacts to determine the specific contact resistance. Marlow *et al.* [266] used a CTLM configuration with an inner disc contact defined by removing the circular rings with varying diameter from the metal plate. The metal contacting scheme of Reeves [272], was finally refined by Rechid and Heime [274] in 1999, where they increased the number of concentric ring contacts, similar to the schematic shown in Figure D.17. Since Reeves used only three contacts (one disc

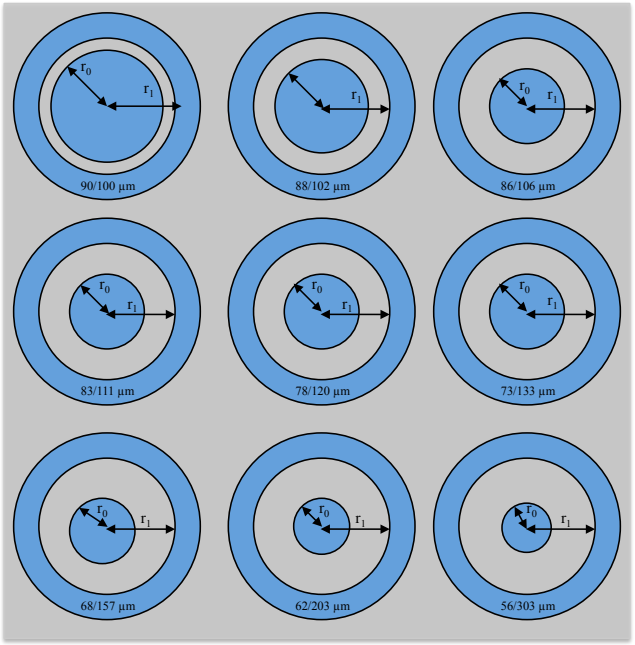

Figure D.17: Circular TLM pattern, where r_o is the radii of the inner circular contact; r_1 is the radii of the outer region; and d is the difference between r_o and r_1.

and two rings), he was not able to see the influence of the metallayer resistivity [274]. Due to the ease of processing and unavailability of the mesa formation in LTLM, we used the CTLM line model during the optimization of the metal contacting at p-GaN interface. Though, some of the p-GaN metal contacting was performed by our partner Laboratory at Institut délectronique de microélectronique et de nanotechnologie (IEMN), where they used the LTLM line model. Further details on both metal contacting schemes will be presented in the discussion section.

Derivation of the specific contact resistance

As mentioned earlier, the CTLM line model has an inner circle and an outer circle metal contacts. A constant output current (i_0) is measured via the inner circle contact for a given input voltage.

A voltage drop (ΔV) takes place between the two metal contacts, i.e. the inner circle and the outer circle, separated by a distance (d) as shown in Figure D.18, and is given by [275];

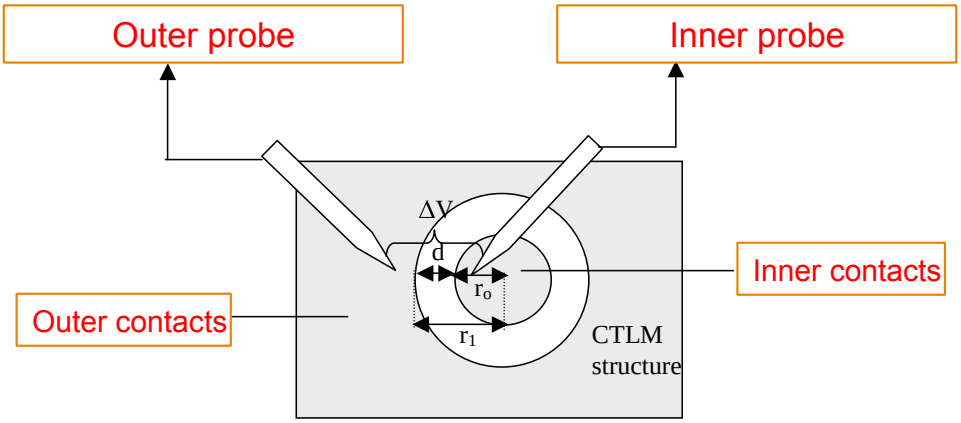

Figure D.18: Circular TLM pattern, deviation of specific contact resistance.

$$\Delta V = \frac{i_0 R_s}{2\pi}\left(ln\left(\frac{r_1}{r_0}\right) + \frac{L_T}{r_0}\frac{I_0(r_0/L_T)}{I_1(r_0/L_T)} + \frac{L_T}{r_1}\frac{K_0(r_1/L_T)}{K_1(R_1/L_T)}\right) \tag{D.8}$$

where, i_0 is the current flowing across the two metal contacts, separated by the distance d, R_s is the sheet resistance of the semiconductor, L_T is the transfer length, I_0, I_1, K_0 and K_1 are the modified bessel functions, r_0 and r_1 are the radii of the inner circular contact and the outer contact.

The transfer length is defined as;

$$L_T = \sqrt{\frac{\rho_c}{R_s}} \tag{D.9}$$

where, ρ_c is the specific contact resistivity, and R_s is the sheet resistance of the semiconductor material.

In cases where r_o and r_1 are greater than L_T by at least a factor of 4, both $\frac{I_0}{I_1}$ and $\frac{K_0}{K_1}$ approximate to unity [275]. Hence the equation D.8 becomes,

$$\Delta V = \frac{i_0 R_s}{2\pi}\left(ln\left(\frac{r_1}{r_1 - d}\right) + L_T\left(\frac{1}{r_1 + \frac{1}{r_1 - d}}\right)\right) \tag{D.10}$$

According to Ohms law, the resistance between the metal contacts is proportional to the voltage drop across them and inversely proportional to the current flowing across the metal contacts. Thus the total resistance (R_T) is given by;

$$R_T = \frac{\Delta_V}{i_0} \tag{D.11}$$

Using the Δ_V given in equation D.10, the equation D.11 becomes,

$$R_T = \frac{R_s}{2\pi r_1}\left(ln\left(\frac{r_1}{r_1 - d}\right) + L_T\left(\frac{1}{r_1 + \frac{1}{r_1 - d}}\right)\right) \tag{D.12}$$

Since $2\pi(r_1 - d) >> d$, so the equation D.12 becomes,

$$R_T = \frac{R_s}{2\pi r_1}\left(2L_T + d\right) \tag{D.13}$$

Considering the contact resistance, $R_T = 0$ at the probes, a plot of the R_T versus the distance (d) provides the $R_s/2\pi r_1$ as the slope and L_T as the intercept at the R_T, as demonstrated in

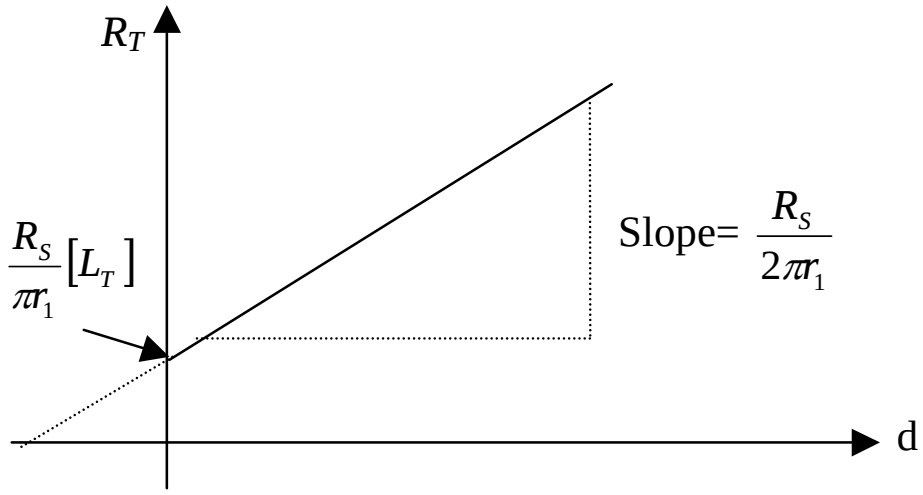

Figure D.19: Plot for the R_T versus d used to deduce the specific contact resistance in CTLM

the Figure D.19. In order to deduce the values of the transfer length, L_T, and sheet resistance, R_s, from the plot given in Figure D.19 is given as;

$$L_T = \frac{y - intercept}{Slope} \times 2 \tag{D.14}$$

$$R_s = Slope \times 2\pi r_1 \tag{D.15}$$

Once L_T, is determined, the specific contact resistance can be calculated using equation D.9;

$$\rho_c = L_T^2 \times R_s \tag{D.16}$$

Characterization

The Current dependence on Voltage ($I-V$) measurements for the p-GaN processed wafers were carried out using a Keithely Source Measure Unit 4200 Figure D.20.

D.10 Results and Discussion

Figure D.21 show the current-voltage characteristics for the p-GaN wafers before and after annealing. The as-deposited Ni/Au metal contacts (Figure D.21(a)(c)) show a rectifying behavior. Although the metal contacts were fabricated on different parts of the same wafer but the magnitude of current for the two devices was quite different. However, the order of current still remained the same and therefore, not much of the attention was given to the difference in current.

Figure D.21(b) and Figure D.21(d) show the $I-V$ characteristics of the p-GaN metal contacts after annealing in RTA under Oxygen (O_2) and Nitrogen (N_2) respectively. The rectifying behavior of the metal contacts is completely changed into non-rectifying behavior. However, the key finding is that the magnitude of the current for the metal contacts annealed under oxygen increased almost four times compared to the increase by twice in the magnitude of the current for the metal contacts annealed under nitrogen. A possible mechanism that could explain the

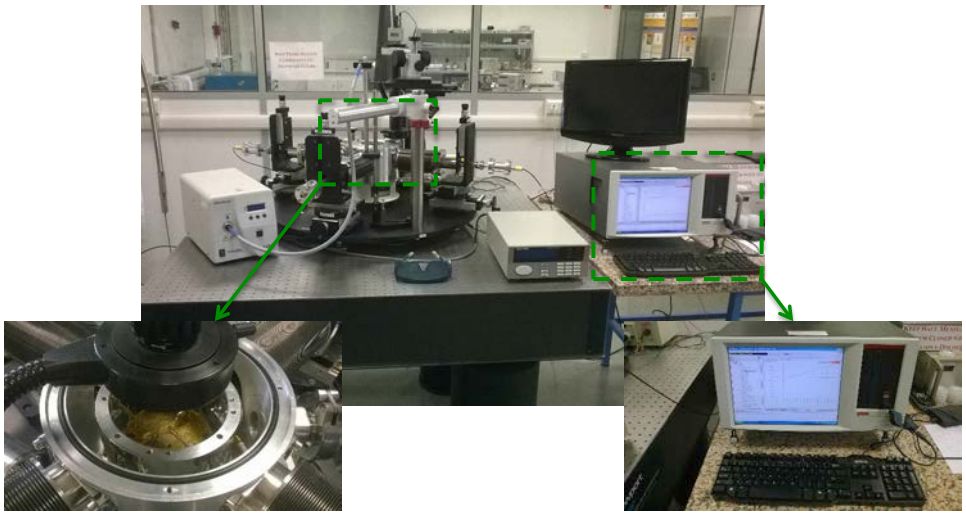

Figure D.20: The Keithly source measure unit 4200 used for the $I-V$ measurements.

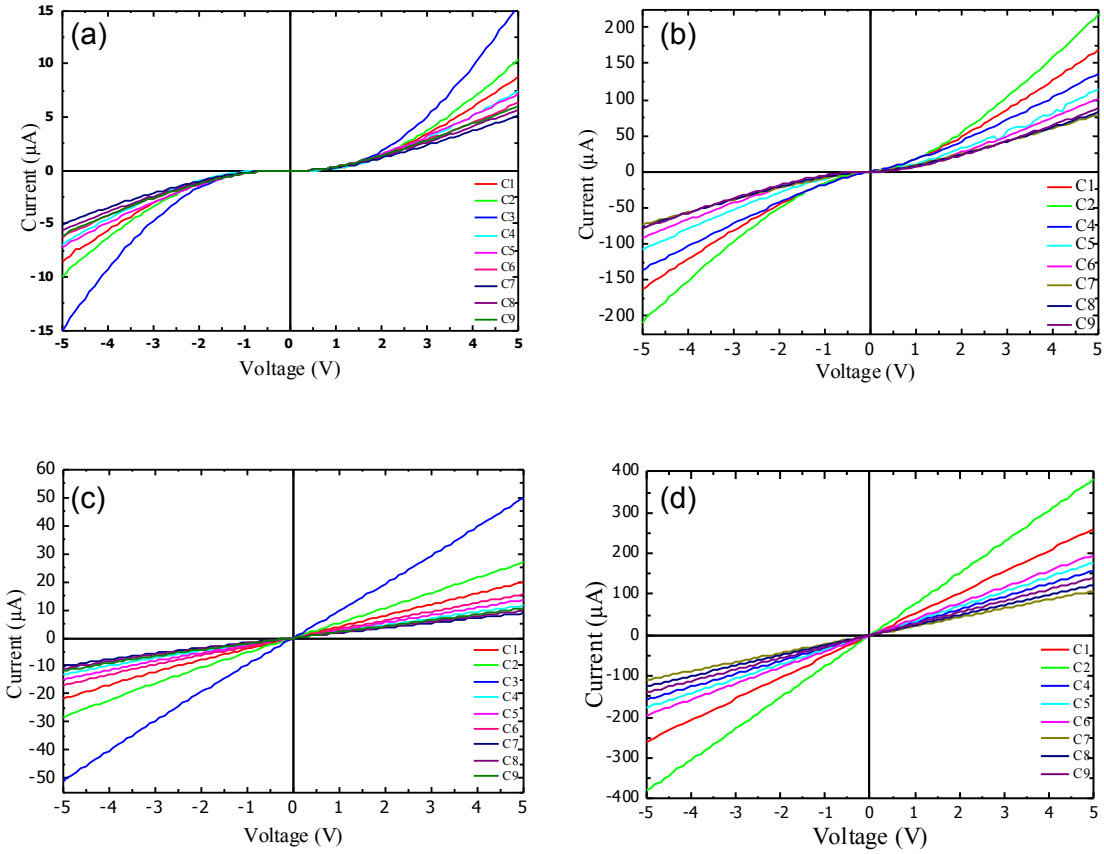

Figure D.21: Current-Voltage characteristics before and after annealing for 300 seconds in RTA under, (a)–(b) Oxygen, (c)–(d) Nitrogen.

change of electric behavior for the Ni/Au metal contacts from non-ohmic to ohmic after annealing is the formation of NiO. The different values calculated for the metal contacts annealed under oxygen and nitrogen are listed in Table D.3.

Table D.3: Results obtained for metal contacts annealed under oxygen and nitrogen.

Parameters	P^+-GaN (nm)	P^+-GaN (nm)	R_{sh} (KΩ)	L_t (μ m)	ρ_c (Ω. cm^2)
Oxygen	150	50	3.86×10^3	0.84	2.7×10^{-2}
Nitrogen	150	50	4.1×10^3	0.93	4.5×10^{-2}

A key point in obtaining low resistance ohmic contacts to p-GaN, by using Ni in a bi-layer metallization scheme is to take care of the out diffusion of Ni under annealing. The Ni layer should be thick enough to out diffuse to form the NiO, which is a p-type and plays a significant role in reducing the Schottky barrier at the surface. However, part of the Ni layer should also remain in contact with the GaN surface to form the favorable phases with GaN, such as Ga-Ni phases. The NiO film prepared by oxidation of a Ni film was determined as p-type conducting with carrier concentration of about 2×10^{17} cm^3 via Hall effect measurement [226]. There upon, an energy band model based on the Au/p-NiO/p-GaN heterostructure was proposed to explain the low-resistance ohmic characteristic [276]. Two energy barriers, which correspond to Au/p-NiO and p-NiO/p-GaN junctions, respectively, exist in the Au/p-NiO/p-GaN heterostructure. The barrier heights at Au/p-NiO and p-NiO/p-GaN junctions are estimated to be 0.3 and 0.185 eV, respectively [226].

These results suggest that there is an optimal microstructure of the oxidized Ni/Au obtained for annealing under oxygen compared to the nitrogen. Since the quality of the ohmic contacts highly depends on the formation of the NiO. Therefore it is speculated that the rate of out-diffusion of Ni atoms through the Au layer to form a crystalline NiO film on the surface is higher for annealing under oxygen compared to nitrogen. Meanwhile, the inter-diffusion between Ni and Au consequently let the formation of Au rich island, that enhances the absorption of Ga, resulting in formation of Ga vacancies [277]. The in-diffusion of Au atoms and dissolution of Ga atoms takes place during annealing, due to the high solubility of gallium in gold [258]. As a result, a high concentration of acceptor-type Ga vacancies are created, lowering the p-type resistivity and improving the metal contact performance.

The different values obtained for the specific contact resistivity on different wafer grown under conditions are listed in Table D.4.

Table D.4: Results for different p-GaN wafers grown under different conditions, annealed under Oxygen ambient.

Parameters	T1151	T1156	T1209	T1210	T1211	T1212
P^+-GaN(nm)	50	50	25	50	50	50
CP_2Mg (sccm)	300	300	300	300	300	250
P-GaN (nm)	150	150	150	75	155	155
CP_2Mg (sccm)	200	200	200	200	200	150
R_{sh} (KΩ)	185	185	185	315	252	185
L_t (μ m)	4.73	4.73	4.73	0.94	1.85	1.15
ρ_c (Ω. cm^2)	4.1×10^{-2}	4.1×10^{-2}	4.1×10^{-2}	2.8×10^{-3}	8.6×10^{-3}	2.8×10^{-3}

Appendix E

Characterization Techniques

E.1 Electron Beam Induced Current (EBIC)

The EBIC technique allows to measure the electric current induced by an electron beam in a material. These measures allow to determine a number of physical properties related to the phenomena of electronic transport in these materials such as the diffusion length, the life time of the carriers and the surface recombination velocity. It is also adapted for the qualitative characterization through video signal formation of the crystalline defects, namely, the dislocations and grain boundaries. It is necessary to note that the quantitative measures of the EBIC remain a difficult problem, and require a good knowledge of the electron- matter interaction. It is also a powerful tool for junction delineation and defects investigation.

The first observation of charge collection phenomena in the SEM was that of Everhart (1958). The historical contributions to the EBIC technique can be redrawn by evoking the works of States *et al.* (1963), Everhart (1964), Wittry *et al.* (1965), and more recently those of Bresse (1974,1977) on the quantitative analysis of the signal, Texier (1980) for his works on the grain boundaries, Tabet and Tarento (1989), as well as the papers of Kimerling and al (1977), Hanoka and Bell (1981) and Leamy (1982) [278]. In the modern day physics, this characterization technique is extremely useful in the characterization of semiconductor materials. A typical EBIC system includes the following,

- A scanning electron microscope which is the source of the electron beam.
- A low external noise current amplifier.
- Low noise signal cabling electrically connect the external power amplifier to the sample within the SEM chamber.
- A holder with electrical contact points to facilitate the required electrical connection to the sample.

E.1.1 Physics of the EBIC technique

The principle of the technique is based on the generation of the electron-hole pair using an injected electron beam. Under the presence of an electric field, these generated electrons and holes are influenced to follow a non-random motion and reach the contact, what induce a current which can be detected by an outside circuit. It can be best understood by analogy: in a solar cell, photons of light fall on the entire cell, thus delivering energy and creating electron hole pairs, and cause a current to flow. In EBIC, energetic electrons take the role of the photons, causing the EBIC current to flow. However, because the electron beam of an SEM or STEM is very small, it is scanned across the sample and variations in the induced EBIC are used to map

the electronic activity of the sample. A similarity of EBIC with cathodoluminescence also exist, however they differ in the principle of imaging because the EBIC is not based on an analysis of emitted particles by matter but on a measure of the current induced in the sample.

E.1.2 Different Geometries

Two types of electron beam excitation can be distinguished for an EBIC measurement,

1. A crossectional geometry where the electron beam is parallel to the depletion region or junction as shown in Figure E.1(a).

2. A planar geometry where the electron beam is perpendicular to the depletion region or junction as shown in Figure E.1(b).

There is also a third configuration proposed by Hackett's (1972) which consists on a beveled specimen geometry (see Figure E.1(c)) in a given way to vary the distance between the point of impact and the space charge region [278]. This geometry was effective to alleviate some of the uncertainty associated with the diffusion length determination due to surface recombination velocity, but it requires accurate fabrication of the beveled edge and careful surface preparation.

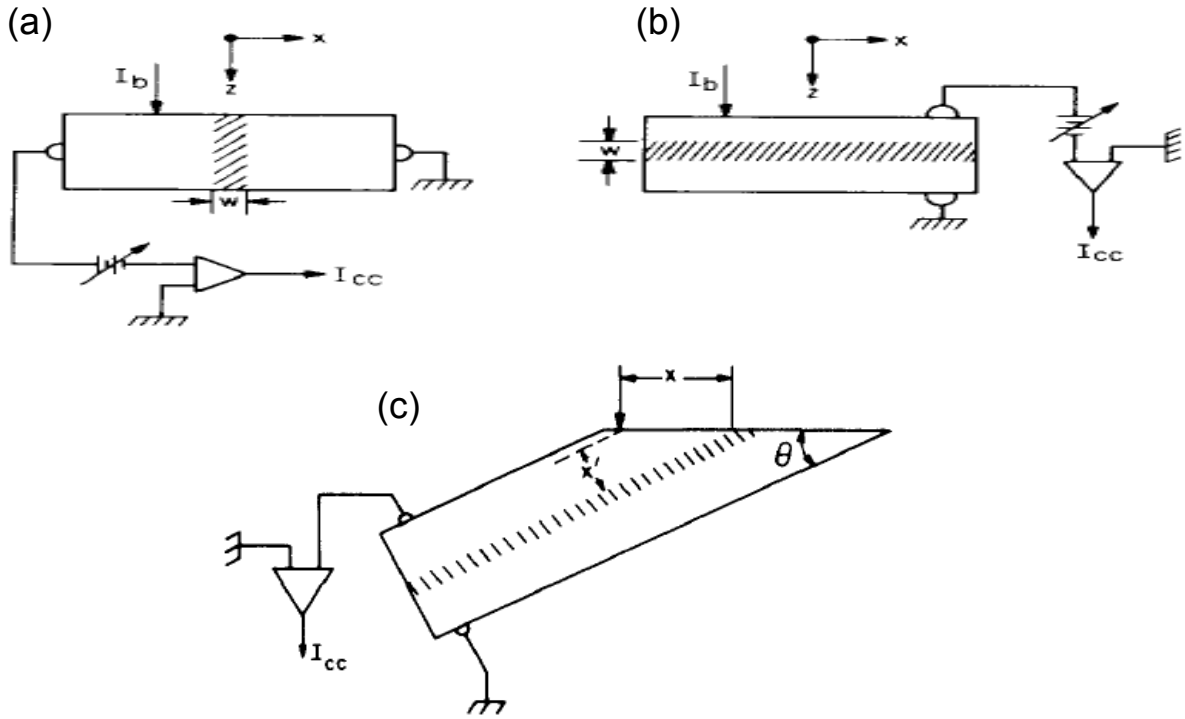

Figure E.1: Different EBIC geometries where the depletion region is denoted by cross hatching, (a) crossectional geometry, (b) Planar geometry and (c) beveled geometry [278].

In general, the e-beam induced current or EBIC current is given by;

$$I = k.x^{\alpha} exp(\frac{-x}{L}) \tag{E.1}$$

where L is the diffusion length, k is a constant, α depends on the surface recombination velocity where it varies from -1/2 for velocity equal to zero and -3/2 for infinite velocity.

In the case of the cross-sectional and planaer geometries, the effect of surface recombination velocity can be neglected so considering α=0. Hence the EBIC current is given by;

$$I = I_{max} exp(\frac{-x}{L}) \tag{E.2}$$

For the beveled specimen geometry, the EBIC current is given by [278];

$$I = I_{max} exp(\frac{-xsin(\theta)}{L}) \tag{E.3}$$

where I_{max} is the maximum current when the e-beam is at the center of the depletion region.

E.1.3 Applications

E.1.3.1 Qualitative EBIC

Imaging was the first application of the EBIC technique associated with scanning electron microscopy. Images are obtained by recording the induced current during a two- dimensional scan of a specimen in any of the geometries. It provides information on the location of p-n junctions (Figure E.2(a)), electrical activity of localized defects (dislocations and grain boundaries) and in-homogeneity in semiconductors. The EBIC current intensity increases with the minority carriers diffusion length, and the presence of a defect in the generation volume causes a degradation in this latter parameter due to recombination, thus the collected EBIC current decreases and hence these electrically active defects appears in the image as black spots on a white background as shown in Figure E.2(b).

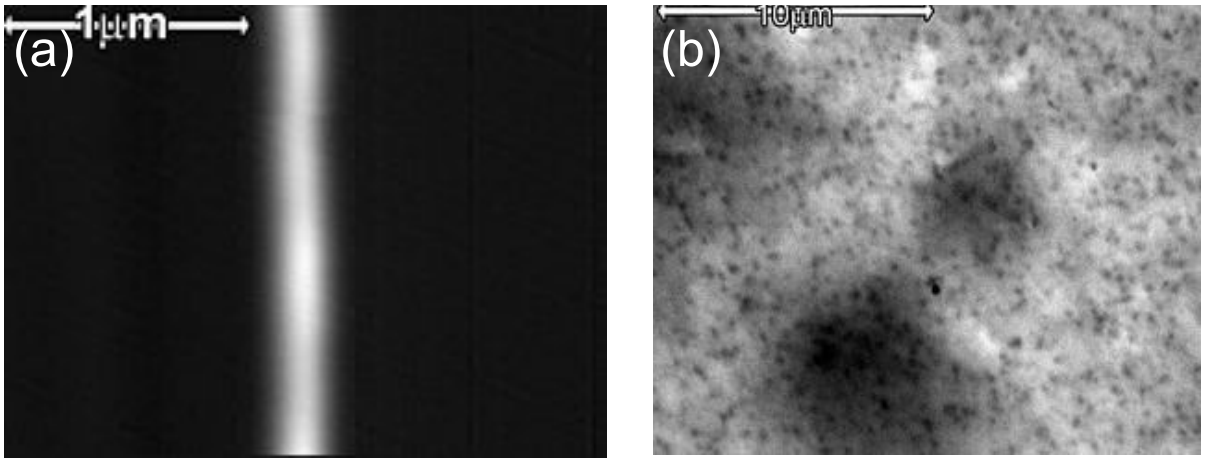

Figure E.2: Different EBIC geometries (a) Cross-sectional EBIC of a p-n junction and (b) Planar-view EBIC showing defects in a diode. Ref: https://wikipedia.org/wiki/Electron$_b eam - induced_c urrent$

E.1.3.2 Quantitative EBIC

EBIC is an attractive tool used for determination of the minority carrier diffusion length (L). Thus, using the equation (eq. E.2) a record of $L_n(I_{cc})$ produced by scanning the e-beam along a line perpendicular to the junction plane exhibits a linear rise of slope L to I_{max} which is obtained when x = 0, *i.e.* when the beam is centered upon the space charge region.

E.1.4 Smart EBIC System

SmartEBIC is a set of high specifications for the quantitative analysis and the acquisition of EBIC signals. This system uses a DigitalMicrograph interface for acquisition and image processing. SmartEBIC is a new product that brings the power, flexibility and ease and it is suitable for scanning electron microscopes (SEM). The EBIC setup shown in Figure E.3 includes the following components;

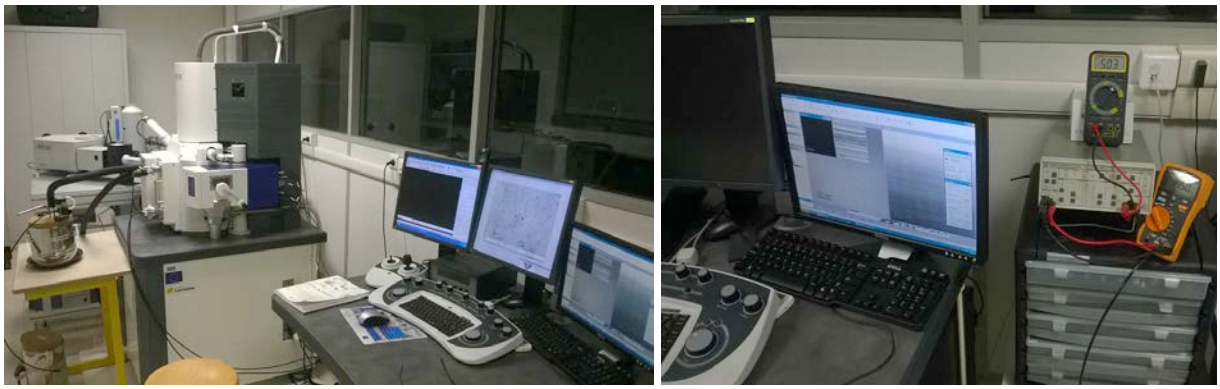

Figure E.3: EBIC setup used for the measurements in this thesis.

- Advanced sample holder shown in Figure E.4
- DigiScan unit including two analog inputs for sampling SEM and EBIC signal.
- Low noise battery powered (rechargeable) current amplifier with RS232 interface and cable.
- DigitalMicrograph and SmartEBIC software for automatic control of amplifier, electron beam and signal sampling.
- 4 BNC type, low noise and vacuum compatible feed-through. One feed through is dedicated to beam current measurements.
- Internal low noise signal cabling.

Figure E.4: Advanced EBIC sample holder with two probes.

E.2 Estimating the Number of Suns

Figure E.5 show a comparison of the power distribution spectrum for an AM 1.5G and UV lamp used during the $J-V$ measurements. The lamp has a total power of 320 mW, distributed at

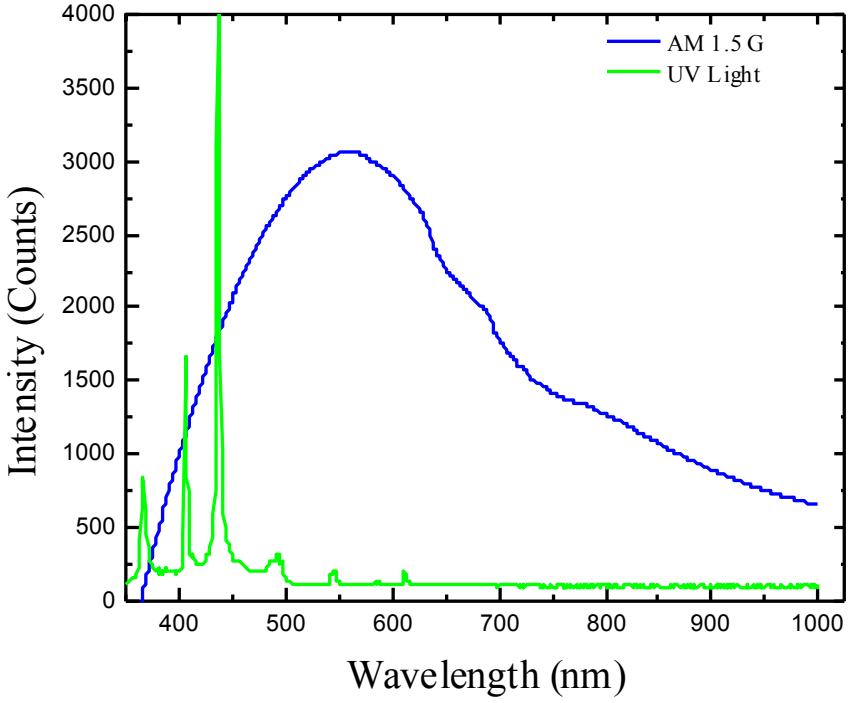

Figure E.5: Power distribution spectrum comparison of an AM 1.5G and UV light used during the $J-V$ measurements.

wavelengths of 390 nm, 410 nm and 440 nm (power distibution above 440 is negligible). The maximum power of UV lamp is at 440 nm, which is more than 50% of the total power. Since, in all of our $J-V$ measurements the power of the UV light above 430 nm is not useful because of 8%, 9% and 12% indium incorporation. Therefore, we can neglect the 50% of the UV power at 440 nm (see Figure E.5). The remaining power distribution at 390 nm and 410 nm is 170 mW. The total area of the UV light spot is 1.22 cm^2, making the power density of the UV lamp around 139 mW/cm^2. The power density of an AM 1.5G solar spectrum below 420 nm is around 10 mW/cm^2. This means that the power density of the UV lamp is around 14 suns.

Bibliography

[1] Antonio Marti and Gerardo L Araújo. Limiting efficiencies for photovoltaic energy conversion in multigap systems. *Solar Energy Materials and Solar Cells*, 43(2):203–222, 1996. pages vii, 7

[2] ISE Fraunhofer. New world record for solar cell efficiency at 46% french-german cooperation confirms competitive advantage of european photovoltaic industry, 2014. pages vii, 6

[3] L Hsu and W Walukiewicz. Modeling of ingan/si tandem solar cells. *Journal of Applied Physics*, 104(2):024507, 2008. pages vii

[4] Kirill A Bulashevich and Sergey Yu Karpov. Assessment of factors limiting conversion efficiency of single-junction iii-nitride solar cells. *physica status solidi (c)*, 11(3-4):640–643, 2014. pages vii, 8

[5] Intergovernmental Panel On Climate Change. Climate change 2007: The physical science basis. *Agenda*, 6(07):333, 2007. pages 1

[6] James Hansen, Larissa Nazarenko, Reto Ruedy, Makiko Sato, Josh Willis, Anthony Del Genio, Dorothy Koch, Andrew Lacis, Ken Lo, Surabi Menon, et al. Earth's energy imbalance: Confirmation and implications. *science*, 308(5727):1431–1435, 2005. pages 1

[7] Thomas R Karl and Kevin E Trenberth. Modern global climate change. *science*, 302(5651):1719–1723, 2003. pages 1

[8] Bruce Podobnik. *Global energy shifts*. The Energy and Resources Institute (TERI), 2006. pages 1

[9] AJ Nozik. Exciton multiplication and relaxation dynamics in quantum dots: applications to ultrahigh-efficiency solar photon conversion. *Inorganic chemistry*, 44(20):6893–6899, 2005. pages 1

[10] NATHAN S Lewis. Global energy perspective. *Caltech, The Lewis Group, http://www. its. caltech. edu/˜ mmrc/nsl/energy. html. USGS*, 2003. pages 1

[11] Solar Generation. 6: Solar photovoltaic electricity empowering the world. *European Photovoltaic Industry AssociationEPIA*, 2011. pages 2

[12] P Fath. Latest developments in crystalline silicon based photovoltaics manufacturing process technologies. *Centrotherm Solar AG*, 2011. pages 2

[13] Harry Wirth and Karin Schneider. Recent facts about photovoltaics in germany. *Report from Fraunhofer Institute for Solar Energy Systems, Germany*, 2013. pages 2

[14] Martin A Green. Third generation photovoltaics: advanced solar electricity generation. *Spriinger-Verlag, Berlin*, 2003. pages 4

[15] B Oliva-Chatelain and A Barron. An introduction to solar cell technology (https://cnx.org/contents/3qu3ovtd@1/an-introduction-to-solar-cell-). pages 5

[16] Kazuo Jimbo, Ryoichi Kimura, Tsuyoshi Kamimura, Satoru Yamada, Win Shwe Maw, Hideaki Araki, Koichiro Oishi, and Hironori Katagiri. Cu 2 znsns 4-type thin film solar cells using abundant materials. *Thin Solid Films*, 515(15):5997–5999, 2007. pages 5

[17] Hironori Katagiri, Kazuo Jimbo, Win Shwe Maw, Koichiro Oishi, Makoto Yamazaki, Hideaki Araki, and Akiko Takeuchi. Development of czts-based thin film solar cells. *Thin Solid Films*, 517(7):2455–2460, 2009. pages 5

[18] K Wang, O Gunawan, T Todorov, B Shin, SJ Chey, NA Bojarczuk, D Mitzi, and S Guha. Thermally evaporated cu2znsns4 solar cells. *Applied Physics Letters*, 97(14):3508, 2010. pages 5

[19] Marina S Leite, Robyn L Woo, Jeremy N Munday, William D Hong, Shoghig Mesropian, Daniel C Law, and Harry A Atwater. Towards an optimized all lattice-matched inalas/ingaasp/ingaas multijunction solar cell with efficiency> 50%. *Applied Physics Letters*, 102(3):033901, 2013. pages 7

[20] Omkar Kujadkumar Jani. *Development of wide-band gap InGaN solar cells for high-efficiency photovoltaics*. PhD thesis, Georgia Institute of Technology, 2008. pages 8, 11, 12

[21] Alauddin Bhuiyan, Kei Sugita, Akihiro Hashimoto, and Akiyasu Yamamoto. Ingan solar cells: present state of the art and important challenges. *Photovoltaics, IEEE Journal of*, 2(3):276–293, 2012. pages 7, 15

[22] http://www2.lbl.gov/Science-Articles/Archive/MSD-perfect-solar-cell 2.html. pages 8

[23] Li Liang, Zhao De-Gang, Jiang De-Sheng, Liu Zong-Shun, Chen Ping, Wu Liang-Liang, Le Ling-Cong, Wang Hui, and Yang Hui. The effects of a low-temperature gan interlayer on the performance of ingan/gan solar cells. *Chinese Physics Letters*, 30(2):028801, 2013. pages 8, 18, 21, 38, 55

[24] JJ Wierer, AJ Fischer, and DD Koleske. The impact of piezoelectric polarization and nonradiative recombination on the performance of (0001) face gan/ingan photovoltaic devices. *Applied Physics Letters*, 96(5):051107, 2010. pages 8

[25] J Wu, W Walukiewicz, KM Yu, JW Ager III, EE Haller, Hai Lu, and William J Schaff. Small band gap bowing in in1àxgaxn alloys. *Appl. Phys. Lett*, 80:4741–4743, 2002. pages 11, 12, 105

[26] Allen Barnett, Douglas Kirkpatrick, Christiana Honsberg, Duncan Moore, Mark Wanlass, Keith Emergy, Richard Schwartz, Dave Carlson, Stuart Bowden, Dan Aiken, et al. Milestones toward 50% efficient solar cell modules. Technical report, DTIC Document, 2007. pages 11

[27] Macho Anani, Hamza Abid, Zouaoui Chama, Christian Mathieu, A Sayede, and B Khelifa. Inxga 1- xn refractive index calculations. *Microelectronics Journal*, 38(2):262–266, 2007. pages 12

[28] M Hori, K Kano, T Yamaguchi, Y Saito, T Araki, Y Nanishi, N Teraguchi, and A Suzuki. Optical properties of inxga1xn with entire alloy composition on inn buffer layer grown by rf-mbe. *physica status solidi (b)*, 234(3):750–754, 2002. pages 12

[29] Christiana Honsberg, Omkar Jani, Alan Doolittle, Elaissa Trybus, G Namkoong, I Ferguson, D Nicol, and A Payne. Ingan–a new solar cell material. In *Proceedings of the 19th European Photovoltaic Science and Engineering Conference, Paris, France*, pages 15–20, 2004. pages 13

[30] A Matoussi, T Boufaden, S Guermazi, B Eljani, Y Mlik, and A Toureille. Minority carrier diffusion lengths and optical self-absorption coefficient in undoped gan. *physica status solidi (b)*, 240(1):160–168, 2003. pages 13

[31] ZZ Bandić, PM Bridger, EC Piquette, and TC McGill. Minority carrier diffusion length and lifetime in gan. *Applied physics letters*, 72(24):3166–3168, 1998. pages 13, 65

[32] Aditya Jain. Impact of electrical contacting scheme on performance of ingan/gan schottky solar cells. Master's thesis, Virginia Tech, 2014. pages 13

[33] Ig-Hyeon Kim, Hyeong-Soo Park, Yong-Jo Park, and Taeil Kim. Formation of v-shaped pits in ingan/gan multiquantum wells and bulk ingan films. *Applied physics letters*, 73(12):1634–1636, 1998. pages 13

[34] R People and JC Bean. Calculation of critical layer thickness versus lattice mismatch for gexsi1- x/si strained-layer heterostructures. *Applied Physics Letters*, 47(3):322–324, 1985. pages 13

[35] R People and JC Bean. Erratum: Calculation of critical layer thickness versus lattice mismatch for gexsi1- x/si strained-layer heterostructures [appl. phys. lett. 47, 322 (1985)]. *Applied Physics Letters*, 49(4):229–229, 1986. pages 13

[36] A Fischer, H Kühne, and H Richter. New approach in equilibrium theory for strained layer relaxation. *Physical review letters*, 73(20):2712, 1994. pages 13, 14

[37] JW Matthews and AE Blakeslee. Defects in epitaxial multilayers: I. misfit dislocations. *Journal of Crystal Growth*, 27:118–125, 1974. pages 13

[38] Gaëlle Orsal, Youssef El Gmili, Nicolas Fressengeas, Jérémy Streque, Ryad Djerboub, Tarik Moudakir, Suresh Sundaram, Abdallah Ougazzaden, and Jean-Paul Salvestrini. Bandgap energy bowing parameter of strained and relaxed ingan layers. *Optical Materials Express*, 4(5):1030–1041, 2014. pages 13, 14, 37, 53, 54

[39] Y El Gmili, G Orsal, K Pantzas, A Ahaitouf, T Moudakir, S Gautier, G Patriarche, D Troadec, JP Salvestrini, and A Ougazzaden. Characteristics of the surface microstructures in thick ingan layers on gan. *Optical Materials Express*, 3(8):1111–1118, 2013. pages 14

[40] I-hsiu Ho and GB Stringfellow. Solid phase immiscibility in gainn. *Applied Physics Letters*, 69(18):2701–2703, 1996. pages 15

[41] RA Oliver, SE Bennett, T Zhu, DJ Beesley, MJ Kappers, DW Saxey, A Cerezo, and CJ Humphreys. Microstructural origins of localization in ingan quantum wells. *Journal of Physics D: Applied Physics*, 43(35):354003, 2010. pages 15

[42] R Singh, D Doppalapudi, TD Moustakas, and LT Romano. Phase separation in ingan thick films and formation of ingan/gan double heterostructures in the entire alloy composition. *Applied Physics Letters*, 70(9):1089–1091, 1997. pages 15, 106

[43] Nadia A El-Masry, EL Piner, SX Liu, and SM Bedair. Phase separation in ingan grown by metalorganic chemical vapor deposition. *Applied physics letters*, 72(1):40–42, 1998. pages 15

[44] Yuichi Sato and Susumu Sato. Hydride vapor phase epitaxy of inxga1-xn thin films. *Japanese journal of applied physics*, 36(7R):4295, 1997. pages 15

[45] S Yu Karpov. Suppression of phase separation in ingan due to elastic strain. *MRS Internet Journal of Nitride Semiconductor Research*, 3:e16, 1998. pages 15

[46] KY Lai, GJ Lin, YL Lai, YF Chen, and JH He. Effect of indium fluctuation on the photovoltaic characteristics of ingan/gan multiple quantum well solar cells. *Applied Physics Letters*, 96(8):081103, 2010. pages 15, 22, 23, 25

[47] Anna Mukhtarova. *Puits quantiques de composés nitrures InGaN/GaN pour le photovaoltaique*. PhD thesis, Grenoble Alpes, 2015. pages 15

[48] Omkar Jani, Christiana Honsberg, Ali Asghar, David Nicol, Ian Ferguson, Alan Doolittle, and Sarah Kurtz. Characterization and analysis of ingan photovoltaic devices. In *Photovoltaic Specialists Conference, 2005. Conference Record of the Thirty-first IEEE*, pages 37–42. IEEE, 2005. pages 15

[49] Omkar Jani, Christiana Honsberg, Yong Huang, June O Song, Ian Ferguson, Gon Namkoong, Elaissa Trybus, Alan Doolittle, and Sarah Kurtz. Design, growth, fabrication and characterization of high-band gap ingan/gan solar cells. In *Photovoltaic Energy Conversion, Conference Record of the 2006 IEEE 4th World Conference on*, volume 1, pages 20–25. IEEE, 2006. pages 15

[50] Cuibai Yang, Xiaoliang Wang, Hongling Xiao, Junxue Ran, Cuimei Wang, Guoxin Hu, Xinhua Wang, Xiaobin Zhang, Jianping Li, and Jinmin Li. Photovoltaic effects in ingan structures with p–n junctions. *physica status solidi (a)*, 204(12):4288–4291, 2007. pages 15, 27, 29

[51] Omkar Jani, Ian Ferguson, Christiana Honsberg, and Sarah Kurtz. Design and characterization of gan/ ingan solar cells. *Applied Physics Letters*, 91(13):132117, 2007. pages 15, 16, 20

[52] Omkar Jani, Hongbo Yu, Elaissa Trybus, Balakrishnam Jampana, Ian Ferguson, Alan Doolittle, and Christiana Honsberg. Effect of phase separation on performance of iii-v nitride solar cells. In *22nd European Photovoltaic Solar Energy Conference*, pages 64–67, 2007. pages 15

[53] X Chen, KD Matthews, D Hao, WJ Schaff, and LF Eastman. Growth, fabrication, and characterization of ingan solar cells. *physica status solidi (a)*, 205(5):1103–1105, 2008. pages 15, 29

[54] Yong Huang, Andrew Melton, Balakrishnam Jampana, Muhammad Jamil, Jae-Hyun Ryou, Russell D Dupuis, and Ian T Ferguson. Growth and characterization of inxga1-xn alloys by metalorganic chemical vapor deposition for solar cell applications. *Journal of Photonics for Energy*, 2(1):028501–1, 2012. pages 16

[55] AG Melton, B Kucukgok, BZ Wang, N Dietz, N Lu, and IT Ferguson. Development of indium-rich ingan epilayers for integrated tandem solar cells. In *MRS Proceedings*, volume 1493, pages 175–180. Cambridge Univ Press, 2013. pages 16

[56] Xinhe Zheng, Ray-Hua Horng, Dong-Sing Wuu, Mu-Tao Chu, Wen-Yih Liao, Ming-Hsien Wu, Ray-Ming Lin, and Yuan-Chieh Lu. High-quality ingan/gan heterojunctions and their photovoltaic effects. *Applied Physics Letters*, 93(26):261108, 2008. pages 16, 17, 18, 20, 37

[57] Carl J Neufeld, Nikholas G Toledo, Samantha C Cruz, Michael Iza, Steven P DenBaars, and Umesh K Mishra. High quantum efficiency ingan/gan solar cells with 2.95 ev band gap. *Applied Physics Letters*, 93(14):3502, 2008. pages 17, 20

[58] Jae-Phil Shim, Seong-Ran Jeon, Yon-Kil Jeong, and Dong-Seon Lee. Improved efficiency by using transparent contact layers in ingan-based pin solar cells. *Electron Device Letters, IEEE*, 31(10):1140–1142, 2010. pages 17, 21

[59] Jae-Phil Shim, Minhyeok Choe, Seong-Ran Jeon, Dongju Seo, Takhee Lee, and Dong-Seon Lee. Ingan-based p–i–n solar cells with graphene electrodes. *Applied physics express*, 4(5):052302, 2011. pages 17

[60] Li Liang, Zhao De-Gang, Jiang De-Sheng, Liu Zong-Shun, Chen Ping, Wu Liang-Liang, Le Ling-Cong, Wang Hui, and Yang Hui. The effects of ingan layer thickness on the performance of ingan/gan pin solar cells. *Chinese Physics B*, 22(6):068802, 2013. pages 17, 18, 21, 37, 91

[61] ZQ Li, M Lestradet, YG Xiao, and S Li. Effects of polarization charge on the photovoltaic properties of ingan solar cells. *physica status solidi (a)*, 208(4):928–931, 2011. pages 18, 102, 103

[62] Mu-Tao Chu, Wen-Yih Liao, Ray-Hua Horng, Tsung-Yen Tsai, Tsai-Bau Wu, Shu-Ping Liu, Ming-Hsien Wu, and Ray-Ming Lin. Growth and characterization of p-ingan/i-ingan/n-gan double-heterojunction solar cells on patterned sapphire substrates. *Electron Device Letters, IEEE*, 32(7):922–924, 2011. pages 18

[63] Carl J Neufeld, Zhen Chen, Samantha C Cruz, Nikholas G Toledo, Steven P DenBaars, and Umesh K Mishra. Optimization of the p-gan window layer for ingan/gan solar cells. In *Photovoltaic Specialists Conference (PVSC), 2010 35th IEEE*, pages 002089–002092. IEEE, 2010. pages 18, 21, 38, 64, 65, 85

[64] XH Wu, CR Elsass, A Abare, M Mack, S Keller, PM Petroff, SP DenBaars, JS Speck, and SJ Rosner. Structural origin of v-defects and correlation with localized excitonic centers in ingan/gan multiple quantum wells. *Applied Physics Letters*, 72(6):692–694, 1998. pages 19

[65] Elison Matioli, Carl Neufeld, Michael Iza, Samantha C Cruz, Ali A Al-Heji, Xu Chen, Robert M Farrell, Stacia Keller, Steven DenBaars, Umesh Mishra, et al. High internal and external quantum efficiency ingan/gan solar cells. *Applied Physics Letters*, 98(2):021102, 2011. pages 19, 21, 38, 45, 63

[66] RM Farrell, AA Al-Heji, CJ Neufeld, X Chen, M Iza, SC Cruz, S Keller, S Nakamura, SP DenBaars, UK Mishra, et al. Effect of intentional p-gan surface roughening on the performance of ingan/gan solar cells. *Applied Physics Letters*, 103(24):241104, 2013. pages 19, 38

[67] Y Zhang, MJ Kappers, D Zhu, F Oehler, Feng Gao, and CJ Humphreys. The effect of dislocations on the efficiency of ingan/gan solar cells. *Solar Energy Materials and Solar Cells*, 117:279–284, 2013. pages 19, 20, 21

[68] SJ Rosner, EC Carr, MJ Ludowise, G Girolami, and HI Erikson. Correlation of cathodoluminescence inhomogeneity with microstructural defects in epitaxial gan grown by metalorganic chemical-vapor deposition. *Applied Physics Letters*, 70(4):420–422, 1997. pages 19

[69] D Cherns and CG Jiao. Electron holography studies of the charge on dislocations in gan. *Physical review letters*, 87(20):205504, 2001. pages 19

[70] Ming-Hsien Wu, Sheng-Po Chang, Shoou-Jinn Chang, Ray-Hua Horng, Wen-Yih Liao, and Ray-Ming Lin. Characteristics of gan/ingan double-heterostructure photovoltaic cells. *International Journal of Photoenergy*, 2012, 2012. pages 20, 21

[71] Ray-Hua Horng, Shih-Ting Lin, Yu-Li Tsai, Mu-Tao Chu, Wen-Yih Liao, Ming-Hsien Wu, Ray-Ming Lin, and Yuan-Chieh Lu. Improved conversion efficiency of gan/ingan thin-film solar cells. *Electron Device Letters, IEEE*, 30(7):724–726, 2009. pages 21

[72] Chia-Lung Tsai, Guan-Shan Liu, Gong-Cheng Fan, and Yu-Sheng Lee. Substrate-free large gap ingan solar cells with bottom reflector. *Solid-State Electronics*, 54(5):541–544, 2010. pages 21, 24

[73] JR Lang, CJ Neufeld, CA Hurni, SC Cruz, E Matioli, UK Mishra, and JS Speck. High external quantum efficiency and fill-factor ingan/gan heterojunction solar cells grown by nh3-based molecular beam epitaxy. *Applied Physics Letters*, 98, 2011. pages 21

[74] Xinhe Zheng, Longjuan Tang, Dongyan Zhang, Jianrong Dong, and Hui Yang. Effect of contact spreading layer on photovoltaic response of InGaN-based solar cells. *Physica Status Solidi (A)*, 208(1):199–201, 2011. pages 21

[75] R Dahal, B Pantha, J Li, JY Lin, and HX Jiang. Ingan/gan multiple quantum well solar cells with long operating wavelengths. *Applied Physics Letters*, 94(6):063505, 2009. pages 22, 25

[76] R Dahal, J Li, K Aryal, JY Lin, and HX Jiang. Ingan/gan multiple quantum well concentrator solar cells. *Appl. Phys. Lett*, 97(7):073115, 2010. pages 22, 25, 73

[77] Zhang Xiao-Bin, Wang Xiao-Liang, Xiao Hong-Ling, Yang Cui-Bai, Hou Qi-Feng, Yin Hai-Bo, Chen Hong, and Wang Zhan-Guo. Ingan/gan multiple quantum well solar cells with an enhanced open-circuit voltage. *Chinese Physics B*, 20(2):028402, 2011. pages 23

[78] JJ Wierer Jr, DD Koleske, and Stephen R Lee. Influence of barrier thickness on the performance of ingan/gan multiple quantum well solar cells. *Applied Physics Letters*, 100(11):111119, 2012. pages 23, 26

[79] Noriyuki Watanabe, Haruki Yokoyama, Naoteru Shigekawa, Ken-ichi Sugita, and Akio Yamamoto. Barrier thickness dependence of photovoltaic characteristics of ingan/gan multiple quantum well solar cells. *Japanese Journal of Applied Physics*, 51(10S):10ND10, 2012. pages 23, 24

[80] Carl J Neufeld, Samantha C Cruz, Robert M Farrell, Michael Iza, Stacia Keller, Shuji Nakamura, Steven P DenBaars, James S Speck, and Umesh K Mishra. Observation of positive thermal power coefficient in ingan/gan quantum well solar cells. *Applied Physics Letters*, 99(7):071104, 2011. pages 24, 26

[81] CH Ho, GJ Lin, PH Fu, CA Lin, PC Yang, I-Min Chan, KY Lai, and JH He. An efficient light-harvesting scheme using sio 2 nanorods for ingan multiple quantum well solar cells. *Solar Energy Materials and Solar Cells*, 103:194–198, 2012. pages 24

[82] Ming-Jer Jeng and Yu-Lin Lee. Increasing solar efficiency of ingan/gan multiple quantum well solar cells with a reflective aluminum layer or a flip-chip structure. *Journal of The Electrochemical Society*, 159(5):H525–H528, 2012. pages 24

[83] Dong-Ju Seo, Jae-Phil Shim, Sang-Bae Choi, Tae Hoon Seo, Eun-Kyung Suh, and Dong-Seon Lee. Efficiency improvement in ingan-based solar cells by indium tin oxide nano dots covered with ito films. *Optics express*, 20(106):A991–A996, 2012. pages 24

[84] NG Young, EE Perl, RM Farrell, M Iza, S Keller, JE Bowers, S Nakamura, SP DenBaars, and JS Speck. High-performance broadband optical coatings on ingan/gan solar cells for multijunction device integration. *Applied Physics Letters*, 104(16):163902, 2014. pages 24, 25

[85] Ming-Jer Jeng, Yu-Lin Lee, and Liann-Be Chang. Temperature dependences of inxga1- xn multiple quantum well solar cells. *Journal of Physics D: Applied Physics*, 42(10):105101, 2009. pages 25

[86] Chia-Lung Tsai, Guan-Shan Liu, Chien-Yu Wang, Ju-Ping Huang, and Jia-Qing Lin. The improved photoresponse of the substrate-free ingan solar cells with a bottom reflector. In *Photovoltaic Specialists Conference (PVSC), 2009 34th IEEE*, pages 002051–002054. IEEE, 2009. pages 25

[87] Ming-Jer Jeng, Te-Wen Su, Yu-Lin Lee, Yuan-Hsiao Chang, Liann-Be Chang, Ray-Ming Lin, Jhong-Hao Jiang, and Yuan-Chieh Lu. Effect of silicon doping on performance of 30-pair inxga1-xn/gan quantum well solar cells. *Japanese Journal of Applied Physics*, 49(5R):052302, 2010. pages 25

[88] Qingwen Deng, Xiaoliang Wang, Hongling Xiao, Cuimei Wang, Haibo Yin, Hong Chen, Qifeng Hou, Defeng Lin, Jinmin Li, Zhanguo Wang, et al. An investigation on inxga1-xn/gan multiple quantum well solar cells. *Journal of Physics D: Applied Physics*, 44(26):265103, 2011. pages 25

[89] Rober M Farrell, CJ Neufeld, SC Cruz, JR Lang, Michael Iza, Stacia Keller, S Nakamura, SP DenBaars, UK Mishra, and JS Speck. High quantum efficiency ingan/gan multiple quantum well solar cells with spectral response extending out to 520 nm. *Applied Physics Letters*, 98(20):201107, 2011. pages 26, 38, 73

[90] Ya-Ju Lee, Min-Hung Lee, Chun-Mao Cheng, and Chia-Hao Yang. Enhanced conversion efficiency of ingan multiple quantum well solar cells grown on a patterned sapphire substrate. *Applied Physics letters*, 98(26):263504, 2011. pages 26

[91] Bor Wen Liou. Design and fabrication of in x ga 1- x n/gan solar cells with a multiple-quantum-well structure on sicn/si (111) substrates. *Thin Solid Films*, 520(3):1084–1090, 2011. pages 26

[92] Carl J Neufeld, Samantha C Cruz, Robert M Farrell, Michael Iza, Jordan R Lang, Stacia Keller, Shuji Nakamura, Steven P DenBaars, James S Speck, and Umesh K Mishra. Effect of doping and polarization on carrier collection in ingan quantum well solar cells. *Applied Physics Letters*, 98(24):243507, 2011. pages 26

[93] Yan-Ling Hu, Robert M Farrell, Carl J Neufeld, Michael Iza, Samantha C Cruz, Nathan Pfaff, Dobri Simeonov, Stacia Keller, Shuji Nakamura, Steven P DenBaars, et al. Effect of quantum well cap layer thickness on the microstructure and performance of ingan/gan solar cells. *Applied Physics Letters*, 100(16):161101, 2012. pages 26

[94] Sang-Bae Choi, Jae-Phil Shim, Dong-Min Kim, Hoon-Il Jeong, Young-Dahl Jho, Young-Ho Song, and Dong-Seon Lee. Effect of indium composition on carrier escape in ingan/gan multiple quantum well solar cells. *Applied Physics Letters*, 103(3):033901, 2013. pages 26

[95] Bor Wen Liou. Temperature of in x ga 1- x n/gan solar cells with a multiple-quantum-well structure on sicn/si (111) substrates. *Solar Energy Materials and Solar Cells*, 114:141–146, 2013. pages 26

[96] NG Young, RM Farrell, YL Hu, Y Terao, M Iza, S Keller, SP DenBaars, S Nakamura, and JS Speck. High performance thin quantum barrier ingan/gan solar cells on sapphire and bulk (0001) gan substrates. *Applied Physics Letters*, 103(17):173903, 2013. pages 26

[97] L Redaelli, A Mukhtarova, S Valdueza-Felip, A Ajay, C Bougerol, C Himwas, J Faure-Vincent, C Durand, J Eymery, and E Monroy. Effect of the quantum well thickness on the performance of ingan photovoltaic cells. *Applied Physics Letters*, 105(13):131105, 2014. pages 26

[98] Jinn-Kong Sheu, Fu-Bang Chen, Shou-Hung Wu, Ming-Lun Lee, Po-Cheng Chen, and Yu-Hsiang Yeh. Vertical ingan-based green-band solar cells operating under high solar concentration up to 300 suns. *Optics express*, 22(105):A1222–A1228, 2014. pages 27

[99] Anna Mukhtarova, Sirona Valdueza-Felip, Luca Redaelli, Christophe Durand, Catherine Bougerol, Eva Monroy, and Joël Eymery. Dependence of the photovoltaic performance of pseudomorphic ingan/gan multiple-quantum-well solar cells on the active region thickness. *Applied Physics Letters*, 108(16):161907, 2016. pages 27

[100] P Misra, C Boney, N Medelci, D Starikov, A Freundlich, and A Bensaoula. Fabrication and characterization of 2.3 ev ingan photovoltaic devices. In *Photovoltaic Specialists Conference, 2008. PVSC'08. 33rd IEEE*, pages 1–5. IEEE, 2008. pages 27, 29

[101] A Yamamoto, K Sugita, M Horie, Y Ohmura, Md R Islam, and A Hashimoto. Mg-doping and n+-p junction formation in movpe-grown in x ga 1-x n (x 0.4). In *Photovoltaic Specialists Conference, 2008. PVSC'08. 33rd IEEE*, pages 1–3. IEEE, 2008. pages 27, 29

[102] Xiao-mei Cai, Sheng-wei Zeng, and Bao-ping Zhang. Fabrication and characterization of ingan pin homojunction solar cell. *Applied Physics Letters*, 95(17):3504, 2009. pages 27, 28, 29

[103] Balakrishnam R Jampana, Andrew G Melton, Muhammad Jamil, Nikolai N Faleev, Robert L Opila, Ian T Ferguson, and Christiana B Honsberg. Design and realization of wide-band-gap (2.67 ev) ingan pn junction solar cell. *Electron Device Letters, IEEE*, 31(1):32–34, 2010. pages 28, 29

[104] Sheng-wei Zeng, Xiao-mei Cai, and Bao-ping Zhang. Demonstration and study of photovoltaic performances of ingan pin homojunction solar cells. *Quantum Electronics, IEEE Journal of*, 46(5):783–787, 2010. pages 28, 29

[105] C Boney, I Hernandez, R Pillai, D Starikov, A Bensaoula, M Henini, M Syperek, J Misiewicz, and R Kudrawiec. Growth and characterization of ingan for photovoltaic devices. *physica status solidi (c)*, 8(7-8):2460–2462, 2011. pages 28, 29

[106] Xiaomei Cai, Yu Wang, Bihua Chen, Ming-Ming Liang, Wen-Jie Liu, Jiang-Yong Zhang, Xue-Qin Lv, Lei-Ying Ying, and Bao-Ping Zhang. Investigation of ingan pin homojunction and heterojunction solar cells. *IEEE Photonics Technology Letters*, 1(25):59–62, 2013. pages 28

[107] Han Cheng Lee, Yan Kuin Su, Wen kuei Chuang, Jia Ching Lin, Kuo Chin Huang, Yi Cheng Cheng, and Kuo Jen Chang. Discussion on electrical characteristics of i-in 0.13 ga 0.87 n pin photovoltaics by using a single/multi-antireflection layer. *Solar Energy Materials and Solar Cells*, 94(7):1259–1262, 2010. pages 29

[108] Liwen Sang, Meiyong Liao, Naoki Ikeda, Yasuo Koide, and Masatomo Sumiya. Enhanced performance of ingan solar cell by using a super-thin aln interlayer. *Applied Physics Letters*, 99(16):161109, 2011. pages 29

[109] Liwen Sang, Meiyong Liao, Yasuo Koide, and Masatomo Sumiya. Temperature and light intensity dependence of photocurrent transport mechanisms in ingan p–i–n homojunction solar cells. *Japanese Journal of Applied Physics*, 52(8S):08JF04, 2013. pages 30

[110] K Pantzas, G Patriarche, G Orsal, S Gautier, T Moudakir, M Abid, Vanessa Gorge, Zakaria Djebbour, PL Voss, and A Ougazzaden. Investigation of a relaxation mechanism specific to ingan for improved movpe growth of nitride solar cell materials. *physica status solidi (a)*, 209(1):25–28, 2012. pages 30

[111] K Pantzas, Y El Gmili, J Dickerson, S Gautier, L Largeau, O Mauguin, G Patriarche, S Suresh, T Moudakir, C Bishop, et al. Semibulk ingan: A novel approach for thick, single phase, epitaxial ingan layers grown by movpe. *Journal of Crystal Growth*, 370:57–62, 2013. pages 31

[112] Y El Gmili, G Orsal, K Pantzas, T Moudakir, S Sundaram, G Patriarche, J Hester, A Ahaitouf, JP Salvestrini, and A Ougazzaden. Multilayered ingan/gan structure vs. single ingan layer for solar cell applications: A comparative study. *Acta Materialia*, 61(17):6587–6596, 2013. pages 30, 31, 32

[113] DM Van Den Broeck, D Bharrat, Z Liu, Nadia A El-Masry, and SM Bedair. Growth and characterization of high-quality, relaxed in y ga1- y n templates for optoelectronic applications. *Journal of Electronic Materials*, 44(11):4161–4166, 2015. pages 32, 33

[114] Hon-Way Lin, Yu-Jung Lu, Hung-Ying Chen, Hong-Mao Lee, and Shangjr Gwo. Ingan/gan nanorod array white light-emitting diode. *Applied Physics Letters*, 97(7):073101, 2010. pages 32

[115] Fang Qian, Silvija Gradecak, Yat Li, Cheng-Yen Wen, and Charles M Lieber. Core/multishell nanowire heterostructures as multicolor, high-efficiency light-emitting diodes. *Nano letters*, 5(11):2287–2291, 2005. pages 32

[116] K Kishino, A Kikuchi, H Sekiguchi, and S Ishizawa. Ingan/gan nanocolumn leds emitting from blue to red. In *Integrated Optoelectronic Devices 2007*, pages 64730T–64730T. International Society for Optics and Photonics, 2007. pages 32

[117] Zang Keyan, Wang Yadong, and Chua Soo Jin. Low dimensional nanostructured ingan multi-quantum wells by selective area heteroepitaxy. *physica status solidi (c)*, 6(S2):S514–S518, 2009. pages 32, 33, 35

[118] Hajime Goto, Katsutoshi Nosaki, Katsuhiro Tomioka, Shinjiro Hara, Kenji Hiruma, Junichi Motohisa, and Takashi Fukui. Growth of core–shell inp nanowires for photovoltaic application by selective-area metal organic vapor phase epitaxy. *Applied Physics Express*, 2(3):035004, 2009. pages 32, 33, 34

[119] C Colombo, M Heiss, M Grätzel, and A Fontcuberta i Morral. Gallium arsenide pin radial structures for photovoltaic applications. *Applied Physics Letters*, 94(EPFL-ARTICLE-148563), 2009. pages 32, 34

[120] Jonathan J Wierer Jr, Qiming Li, Daniel D Koleske, Stephen R Lee, and George T Wang. Iii-nitride core–shell nanowire arrayed solar cells. *Nanotechnology*, 23(19):194007, 2012. pages 32, 33, 34, 86

[121] Yajie Dong, Bozhi Tian, Thomas J Kempa, and Charles M Lieber. Coaxial group iii-nitride nanowire photovoltaics. *Nano letters*, 9(5):2183–2187, 2009. pages 32, 34, 86

[122] YB Tang, ZH Chen, HS Song, CS Lee, HT Cong, HM Cheng, WJ Zhang, I Bello, and ST Lee. Vertically aligned p-type single-crystalline gan nanorod arrays on n-type si for heterojunction photovoltaic cells. *Nano letters*, 8(12):4191–4195, 2008. pages 32

[123] Bozhi Tian, Xiaolin Zheng, Thomas J Kempa, Ying Fang, Nanfang Yu, Guihua Yu, Jinlin Huang, and Charles M Lieber. Coaxial silicon nanowires as solar cells and nanoelectronic power sources. *Nature*, 449(7164):885–889, 2007. pages 33, 34

[124] X Kong, S Albert, A Bengoechea-Encabo, MA Sanchez-Garcia, E Calleja, and A Trampert. Lattice pulling effect and strain relaxation in axial (in, ga) n/gan nanowire heterostructures grown on gan-buffered si (111) substrate. *physica status solidi (a)*, 212(4):736–739, 2015. pages 34

[125] Yadong Wang, Keyan Zang, Soojin Chua, Melissa S Sander, Sudhiranjan Tripathy, and Clifton G Fonstad. High-density arrays of ingan nanorings, nanodots, and nanoarrows fabricated by a template-assisted approach. *The Journal of Physical Chemistry B*, 110(23):11081–11087, 2006. pages 34

[126] V Jindal, N Tripathi, M Tungare, O Paschos, P Haldar, and F Shahedipour-Sandvik. Selective area heteroepitaxy of low dimensional a-plane and c-plane ingan nanostructures using pulsed mocvd. *physica status solidi (c)*, 5(6):1709–1711, 2008. pages 34

[127] Jie Song, Benjamin Leung, Yu Zhang, and Jung Han. Growth, structural and optical properties of ternary ingan nanorods prepared by selective-area metalorganic chemical vapor deposition. *Nanotechnology*, 25(22):225602, 2014. pages 34

[128] Suresh Sundaram, Renaud Puybaret, Xin Li, Youssef El Gmili, Jeremy Streque, Konstantinos Panztas, Gaelle Orsal, Gilles Patriarche, Paul L Voss, Jean Paul Salvestrini, et al. High quality thick ingan nanostructures grown by nanoselective area growth for new generation photovoltaic devices. *physica status solidi (a)*, 212(4):740–744, 2015. pages 34, 91

[129] D Zubia, Saleem H Zaidi, SRJ Brueck, and SD Hersee. Nanoheteroepitaxial growth of gan on si by organometallic vapor phase epitaxy. *Applied Physics Letters*, 76(7):858–860, 2000. pages 34

[130] Doo-Hyeb Yoon, Kyu-Seok Lee, Ji-Beom Yoo, and Tae-Yeon Seong. Reduction of threading dislocations in ingan/gan double heterostructure through the introduction of low-temperature gan intermediate layer. *Japanese journal of applied physics*, 41(3R):1253, 2002. pages 38, 56

[131] Seunghwan Yeon, Taejoon Son, Dong Su Shin, Kyung-Young Jung, and Jinsub Park. Enhancement of device performances in gan-based light-emitting diodes using nano-sized surface pit. *Journal of nanoscience and nanotechnology*, 15(7):5211–5214, 2015. pages 38

[132] Hung-Wen Huang, CC Kao, JT Chu, HC Kuo, SC Wang, and CC Yu. Improvement of ingan-gan light-emitting diode performance with a nano-roughened p-gan surface. *Photonics Technology Letters, IEEE*, 17(5):983–985, 2005. pages 38

[133] Kayo Koike, Seogwoo Lee, Sung Ryong Cho, Jinsub Park, Hyojong Lee, Jun-Seok Ha, Soon-Ku Hong, Hyun-Yong Lee, Meoung-Whan Cho, and Takafumi Yao. Improvement of light extraction efficiency and reduction of leakage current in gan-based led via v-pit formation. *Photonics Technology Letters, IEEE*, 24(6):449–451, 2012. pages 38

[134] Nikhil Sharma, Paul Thomas, David Tricker, and Colin Humphreys. Chemical mapping and formation of v-defects in ingan multiple quantum wells. *Applied Physics Letters*, 77(9):1274–1276, 2000. pages 39

[135] Yong-Tae Moon, Dong-Joon Kim, Keun-Man Song, Chel-Jong Choi, Sang-Heon Han, Tae-Yeon Seong, and Seong-Ju Park. Effects of thermal and hydrogen treatment on indium segregation in ingan/gan multiple quantum wells. *Journal of Applied Physics*, 89(11):6514–6518, 2001. pages 39

[136] Shota Kitamura, Kazumasa Hiramatsu, and Nobuhiko Sawaki. Fabrication of gan hexagonal pyramids on dot-patterned gan/sapphire substrates via selective metalorganic vapor phase epitaxy. *Japanese journal of applied physics*, 34(9B):L1184, 1995. pages 39

[137] Sofiane Belahsene, Gilles Patriarche, David Troadec, Suresh Sundaram, Abdallah Ougazzaden, Anthony Martinez, and Abderrahim Ramdane. Microstructural and electrical investigation of Pd/Au ohmic contact on p-GaN. *Journal of Vacuum Science & Technology B*, 33(1):010603, 2015. pages 41

[138] AF Wright and Ulrike Grossner. The effect of doping and growth stoichiometry on the core structure of a threading edge dislocation in gan. *Applied physics letters*, 73(19):2751–2753, 1998. pages 43

[139] S Hegedus, D Ryan, K Dobson, B McCandless, and D Desai. Photoconductive cds: how does it affect cdte/cds solar cell performance? In *MRS Proceedings*, volume 763, pages B9–5. Cambridge Univ Press, 2003. pages 44

[140] S Maximenko, S Soloviev, D Cherednichenko, and T Sudarshan. Observation of dislocations in diffused 4h-sic pin diodes by electron-beam induced current. *Journal of applied physics*, 97(1):3533, 2005. pages 46, 47, 49, 109

[141] SI Maximenko, JA Freitas Jr, RL Myers-Ward, K-K Lew, BL VanMil, CR Eddy Jr, DK Gaskill, PG Muzykov, and TS Sudarshan. Effect of threading screw and edge dislocations on transport properties of 4h–sic homoepitaxial layers. *Journal of Applied Physics*, 108(1):013708, 2010. pages 46

[142] M Haugk, J Elsner, Th Frauenheim, TEM Staab, CD Latham, R Jones, HS Leipner, T Heine, G Seifert, and M Sternberg. Structures, energetics and electronic properties of complex iii-v semiconductor systems. *Physica Status Solidi B Basic Research*, 217(1):473–512, 2000. pages 47

[143] C Frigeri. Characterization of lec GaAs by electron beam induced current analysis. *Materials Science and Engineering: B*, 20(1):175–179, 1993. pages 47

[144] Frank S Ham. Stress-assisted precipitation on dislocations. *Journal of Applied Physics*, 30(6):915–926, 1959. pages 47

[145] S Maximenko, S Soloviev, D Cherednichenko, and T Sudarshan. Electron-beam-induced current observed for dislocations in diffused 4h-sic pn diodes. *Applied physics letters*, 84:1576, 2004. pages 47

[146] Muhammad Arif, Jean-Paul Salvestrini, Jérémy Streque, Matthew B Jordan, Youssef El Gmili, Suresh Sundaram, Xin Li, Gilles Patriarche, Paul L Voss, and Abdallah Ougazzaden. Role of v-pits in the performance improvement of ingan solar cells. *Applied Physics Letters*, 109(13):133507, 2016. pages 51

[147] Jeramy Dickerson, Konstantinos Pantzas, Tarik Moudakir, Abdallah Ougazzaden, and Paul L Voss. Modeling of polarization effects on n-GaN/i-InGaN/p-GaN solar cells with ultrathin GaN interlayers. *Optical and Quantum Electronics*, 45(7):681–686, 2013. pages 53

[148] FK Yam and Z Hassan. InGaN: An overview of the growth kinetics, physical properties and emission mechanisms. *Superlattices and Microstructures*, 43(1):1–23, 2008. pages 54

[149] V. Gorge, A. Migan-Dubois, Z. Djebbour, K. Pantzas, S. Gautier, T. Moudakir, S. Suresh, and A. Ougazzaden. Theoretical analysis of the influence of defect parameters on photovoltaic performances of composition graded InGaN solar cells. *Materials Science and Engineering: B*, 178(2):142–148, Feb 2013. pages 54

[150] GF Brown, JW Ager, W Walukiewicz, and J Wu. Finite element simulations of compositionally graded ingan solar cells. *Solar Energy Materials and Solar Cells*, 94(3):478–483, 2010. pages 55

[151] Di Zhu. The origin of the high diode-ideality factors in GaInN/GaN multiple quantum well light-emitting diodes. *Applied Physics Letters*, 94:081113, 2009. pages 64

[152] CL Reynolds Jr and A Patel. Tunneling entity in different injection regimes of InGaN light emitting diodes. *Journal of Applied Physics*, 103(8):086102, 2008. pages 65

[153] SW Lee, DC Oh, H Goto, JS Ha, HJ Lee, T Hanada, MW Cho, T Yao, SK Hong, HY Lee, et al. Origin of forward leakage current in GaN-based light-emitting devices. *Applied Physics Letters*, 89(13):132117, 2006. pages 65

[154] Chloe AM Fabien and W Alan Doolittle. Guidelines and limitations for the design of high-efficiency ingan single-junction solar cells. *Solar Energy Materials and Solar Cells*, 130:354–363, 2014. pages 70

[155] Muhammad Arif, Suresh Sundaram, Jérémy Streque, Youssef El Gmili, Renaud Puybaret, Sofiane Belahsene, Abderahim Ramdane, Anthony Martinez, Gilles Patriarche, Thomas Fix, Abdelilah Slaoui, Paul L Voss, Jean-Paul Salvestrini, and Abdallah Ougazzaden. Investigation of new approaches for InGaN growth with high indium content for cpv application. In *11TH International Conference on Concentration Photovoltaic System, CPV-11*, volume 1679, page 040001. AIP Publishing, 2015. pages 71

[156] Wolfgang Guter, Jan Schöne, Simon P Philipps, Marc Steiner, Gerald Siefer, Alexander Wekkeli, Elke Welser, Eduard Oliva, Andreas W Bett, and Frank Dimroth. Current-matched triple-junction solar cell reaching 41.1% conversion efficiency under concentrated sunlight. *Applied Physics Letters*, 94(22):223504, 2009. pages 81

[157] WH Goh, G Patriarche, PL Bonanno, S Gautier, T Moudakir, M Abid, G Orsal, AA Sirenko, Z-H Cai, A Martinez, et al. Structural and optical properties of nanodots, nanowires, and multi-quantum wells of iii-nitride grown by movpe nano-selective area growth. *Journal of Crystal Growth*, 315(1):160–163, 2011. pages 90

[158] Suresh Sundaram, Renaud Puybaret, Y El Gmili, X Li, PL Bonanno, K Pantzas, G Orsal, D Troadec, Z-H Cai, G Patriarche, et al. Nanoscale selective area growth of thick, dense, uniform, in-rich, ingan nanostructure arrays on gan/sapphire template. *Journal of Applied Physics*, 116(16):163105, 2014. pages 91

[159] Ja-Soon Jang, Donghwan Kim, and Tae-Yeon Seong. Schottky barrier characteristics of pt contacts to n-type ingan. *Journal of applied physics*, 99(7):073704, 2006. pages 92

[160] Yan-Kuin Su, Yu-Zung Chiou, Fuh-Shyang Juang, Shoou-Jin Chang, and Jinn-Kung Sheu. Gan and ingan metal-semiconductor-metal photodetectors with different schottky contact metals. *Japanese Journal of Applied Physics*, 40(4S):2996, 2001. pages 92

[161] DJ Chen, Y Huang, B Liu, ZL Xie, R Zhang, YD Zheng, Y Wei, and V Narayanamurti. High-quality schottky contacts to n-ingan alloys prepared for photovoltaic devices. *Journal of Applied Physics*, 105(6):063714, 2009. pages 92

[162] Kevin T Chern, Louis J Guido, Timothy A Ciarkowski, Noah P Allen, Oleg A Laboutin, Roger E Welser, and Victor C Elarde. Gainn/gan-ni/au transparent conducting oxide schottky barrier solar cells. In *Photovoltaic Specialist Conference (PVSC), 2014 IEEE 40th*, pages 1139–1142. IEEE, 2014. pages 92

[163] Qing Xia, Hui Xia, and Arthur L Ruoff. Pressure-induced rocksalt phase of aluminum nitride: A metastable structure at ambient condition. *Journal of applied physics*, 73(12):8198–8200, 1993. pages 99

[164] Piotr Perlin, Claude Jauberthie-Carillon, Jean Paul Itie, Alfonso San Miguel, Izabella Grzegory, and Alain Polian. Raman scattering and x-ray-absorption spectroscopy in gallium nitride under high pressure. *Physical Review B*, 45(1):83, 1992. pages 99

[165] Masaki Ueno, Minoru Yoshida, Akifumi Onodera, Osamu Shimomura, and Kenichi Takemura. Stability of the wurtzite-type structure under high pressure: Gan and inn. *Physical Review B*, 49(1):14, 1994. pages 99

[166] Michael Christopher Gibson. *Implementation and application of advanced density functionals*. PhD thesis, Durham University, 2006. pages 99, 100

[167] Hadis Morkoç. *Handbook of Nitride Semiconductors and Devices, Materials Properties, Physics and Growth*, volume 1. John Wiley & Sons, 2009. pages 101

[168] Stephen A Dyer. *Wiley survey of instrumentation and measurement*. John Wiley & Sons, 2004. pages 101

[169] Lars Vegard. Die konstitution der mischkristalle und die raumfüllung der atome. *Zeitschrift für Physik A Hadrons and Nuclei*, 5(1):17–26, 1921. pages 101

[170] Pantzas Konstantinos. *Elaboration par MOVPE et caractérisations des matériaux (B)InGaN pour les cellules solaires de 3émem génération*. PhD thesis, Université de Lorraine, 2013. pages 102, 103, 124

[171] XQ Shen, T Ide, SH Cho, M Shimizu, S Hara, and H Okumura. Stability of n-and ga-polarity gan surfaces during the growth interruption studied by reflection high-energy electron diffraction. *Applied Physics Letters*, 77(24):4013–4015, 2000. pages 102

[172] E Monroy, E Sarigiannidou, F Fossard, N Gogneau, E Bellet-Amalric, J-L Rouviere, S Monnoye, H Mank, and B Daudin. Growth kinetics of n-face polarity gan by plasma-assisted molecular-beam epitaxy. *Applied physics letters*, 84(18):3684–3686, 2004. pages 102

[173] F Tuomisto, K Saarinen, B Lucznik, I Grzegory, H Teisseyre, T Suski, S Porowski, PR Hageman, and J Likonen. Effect of growth polarity on vacancy defect and impurity incorporation in dislocation-free gan. *Applied Physics Letters*, 86(3):031915, 2005. pages 102

[174] I Vurgaftman and JR Meyer. Band parameters for nitrogen-containing semiconductors. *Journal of Applied Physics*, 94(6):3675–3696, 2003. pages 102, 104, 105

[175] Fabio Bernardini and Vincenzo Fiorentini. Nonlinear macroscopic polarization in iii-v nitride alloys. *Physical Review B*, 64(8):085207, 2001. pages 102

[176] O Ambacher, J Majewski, C Miskys, Al Link, M Hermann, M Eickhoff, M Stutzmann, F Bernardini, V Fiorentini, V Tilak, et al. Pyroelectric properties of al (in) gan/gan hetero-and quantum well structures. *Journal of physics: condensed matter*, 14(13):3399, 2002. pages 102

[177] Vincenzo Fiorentini, Fabio Bernardini, and Oliver Ambacher. Evidence for nonlinear macroscopic polarization in iii–v nitride alloy heterostructures. *Applied physics letters*, 80(7):1204–1206, 2002. pages 102

[178] Fabio Bernardini, Vincenzo Fiorentini, and David Vanderbilt. Spontaneous polarization and piezoelectric constants of iii-v nitrides. *Physical Review B*, 56(16):R10024, 1997. pages 103

[179] M Lestrade, ZQ Li, YG Xiao, and Z M Simon Li. Modeling of polarization effects in ingan pin solar cells. *Optical and quantum electronics*, 42(11):699–703, 2011. pages 103

[180] S Pereira, MR Correia, T Monteiro, E Pereira, E Alves, AD Sequeira, and N Franco. Compositional dependence of the strain-free optical band gap in inxga1-xn layers. *Applied physics letters*, 78(15):2137–2139, 2001. pages 105

[181] Vanessa Gorge. *Caractérisations de matériaux et tests de composants des cellules solaires à base des nitrures des éléments III-V*. PhD thesis, Université Paris Sud-Paris XI, 2012. pages 106

[182] SK Mathis, AE Romanov, LF Chen, GE Beltz, W Pompe, and JS Speck. Modeling of threading dislocation reduction in growing gan layers. *PHYSICA STATUS SOLIDI A APPLIED RESEARCH*, 179(1):125–146, 2000. pages 107, 108

[183] T Hino, S Tomiya, T Miyajima, K Yanashima, S Hashimoto, and M Ikeda. Characterization of threading dislocations in gan epitaxial layers. *Applied Physics Letters*, 76(23):3421–3423, 2000. pages 109

[184] XH Wu, LM Brown, D Kapolnek, S Keller, B Keller, SP DenBaars, and JS Speck. Defect structure of metal-organic chemical vapor deposition-grown epitaxial (0001) gan/al2o3. *Journal of applied physics*, 80(6):3228–3237, 1996. pages 107, 108

[185] W Qian, GS Rohrer, M Skowronski, K Doverspike, LB Rowland, and DK Gaskill. Open-core screw dislocations in gan epilayers observed by scanning force microscopy and high-resolution transmission electron microscopy. *Applied physics letters*, 67(16):2284–2286, 1995. pages 108

[186] Y Xin, SJ Pennycook, ND Browning, PD Nellist, S Sivananthan, F Omnes, B Beaumont, JP Faurie, and P Gibart. Direct observation of the core structures of threading dislocations in gan. *Applied physics letters*, 72(21):2680–2682, 1998. pages 108

[187] Shuji Nakamura, Masayuki Senoh, Shin-ichi Nagahama, Naruhito Iwasa, Takao Yamada, Toshio Matsushita, Hiroyuki Kiyoku, Yasunobu Sugimoto, Tokuya Kozaki, Hitoshi Umemoto, et al. Continuous-wave operation of ingan/gan/algan-based laser diodes grown on gan substrates. *Applied Physics Letters*, 72(16):2014–2016, 1998. pages 109

[188] Hussein Srour. *Conception, réalisation et caractérisation de photodétecteurs ultraviolets" Solar-blind" à base de nouveaux alliages BAlGaN*. PhD thesis, Université de Lorraine, 2012. pages 109, 133, 144

[189] Walter A Harrison. *Electronic structure and the properties of solids: the physics of the chemical bond*. Courier Corporation, 2012. pages 109

[190] Rüdiger Quay. *Gallium nitride electronics*, volume 96. Springer Science & Business Media, 2008. pages 109

[191] DD Koleske, RL Henry, ME Twigg, JC Culbertson, SC Binari, AE Wickenden, and M Fatemi. Influence of aln nucleation layer temperature on gan electronic properties grown on sic. *Applied physics letters*, 80(23):4372–4374, 2002. pages 109

[192] Ezgi DOGMUS. *Characterization and Fabrication of InGaN Solar Cells*. PhD thesis, Universite de Lille, 2015. pages 110

[193] Shigenari Nakamura and Michael R Krames. History of gallium–nitride-based light-emitting diodes for illumination. *Proceedings of the IEEE*, 101(10):2211–2220, 2013. pages 110

[194] H Pi Maruska and JJ Tietjen. The preparation and properties of vapor-deposited single-crystal-line gan. *Applied Physics Letters*, 15(10):327–329, 1969. pages 110

[195] HP Maruska, DA Stevenson, and JI Pankove. Violet luminescence of mg-doped gan. *Applied Physics Letters*, 22(6):303–305, 1973. pages 110

[196] M Ilegems and R Dingle. Luminescence of be-and mg-doped gan. *Journal of Applied Physics*, 44(9):4234–4235, 1973. pages 110

[197] JI Pankove, EA Miller, D Richman, and JE Berkeyheiser. Electroluminescence in gan. *Journal of Luminescence*, 4(1):63–66, 1971. pages 110

[198] Hiroshi Amano, Masahiro Kito, Kazumasa Hiramatsu, and Isamu Akasaki. P-type conduction in mg-doped gan treated with low-energy electron beam irradiation (leebi). *Japanese Journal of Applied Physics*, 28(12A):L2112, 1989. pages 110

[199] Shuji Nakamura, Takashi Mukai, and Masayuki Senoh. High-power gan pn junction blue-light-emitting diodes. *Japanese Journal of Applied Physics*, 30(12A):L1998, 1991. pages 110

[200] Shuji Nakamura, Masayuki Senoh, and Takashi Mukai. P-gan/n-ingan/n-gan double-heterostructure blue-light-emitting diodes. *Japanese Journal of Applied Physics*, 32(1A):L8, 1993. pages 110

[201] Shuji Nakamura, Masayuki Senoh, Naruhito Iwasa, Shin-ichi Nagahama, Takao Yamada, and Takashi Mukai. Superbright green ingan single-quantum-well-structure light-emitting diodes. *Japanese Journal of Applied Physics*, 34(10B):L1332, 1995. pages 110

[202] http://www.lighting.philips.com/pwc$_l i$/*main/connect/Lighting*$_U$*niversity/internet* − *courses/LEDs/ledlamps*2.*html.pages* 110

[203] Ashraful Ghani Bhuiyan, Akihiro Hashimoto, and Akio Yamamoto. Indium nitride (inn): A review on growth, characterization, and properties. *Journal of Applied Physics*, 94(5):2779–2808, 2003. pages 110, 111

[204] TL Tansley and CP Foley. Optical band gap of indium nitride. *Journal of Applied Physics*, 59(9):3241–3244, 1986. pages 110

[205] BR Natarajan, AH Eltoukhy, JE Greene, and TL Barr. Mechanisms of reactive sputtering of indium i: Growth of inn in mixed ar-n 2 discharges. *Thin Solid Films*, 69(2):201–216, 1980. pages 110

[206] Toshiaki Ikoma, H Watanabe, and Denshi Jōhō Tsūshin Gakkai. *Gallium Arsenide and Related Compounds 1989: Proceedings of the Sixteenth International Symposium on Gallium Arsenide and Related Compounds Held in Karuizawa, Japan, 25-29 September 1989*. Taylor & Francis, 1990. pages 111

[207] Akihiro Wakahara and Akira Yoshida. Heteroepitaxial growth of inn by microwave-excited metalorganic vapor phase epitaxy. *Applied Physics Letters*, 54(8):709–711, 1989. pages 111

[208] Akihiro Wakahara, Tohru Tsuchiya, and Akira Yoshida. Epitaxial growth of indium nitride. *Journal of crystal growth*, 99(1):385–389, 1990. pages 111

[209] Junqiao Wu. When group-iii nitrides go infrared: New properties and perspectives. *Journal of Applied Physics*, 106(1):011101, 2009. pages 111

[210] Jenny Nelson. *The physics of solar cells*, volume 1. World Scientific, 2003. pages 114

[211] Xiaoming Wen, Jeffrey A Davis, Lap Van Dao, Peter Hannaford, VA Coleman, HH Tan, C Jagadish, K Koike, S Sasa, M Inoue, et al. Temperature dependent photoluminescence in oxygen ion implanted and rapid thermally annealed zno/ znmgo multiple quantum wells. *Applied physics letters*, 90(22):221914, 2007. pages 115

[212] ZZ Bandić, PM Bridger, EC Piquette, and TC McGill. Electron diffusion length and lifetime in p-type gan. *Applied physics letters*, 73(22):3276–3278, 1998. pages 116

[213] Shawn Willis. *Advanced Optoelectronic Characterisation of Solar Cells*. PhD thesis, Oxford University, 2011. pages 117

[214] Ronald A Sinton and Andres Cuevas. Contactless determination of current–voltage characteristics and minority-carrier lifetimes in semiconductors from quasi-steady-state photoconductance data. *Applied Physics Letters*, 69(17):2510–2512, 1996. pages 119

[215] HM Manasevit and W It Simpson. The use of metal-organics in the preparation of semiconductor materials i. epitaxial gallium-v compounds. *Journal of the Electrochemical Society*, 116(12):1725–1732, 1969. pages 123

[216] HM Manasevit and KL Hess. The use of metalorganics in the preparation of semiconductor materials vii. gallium antimonide. *Journal of The Electrochemical Society*, 126(11):2031–2033, 1979. pages 123

[217] Rinku P Parikh and Raymond A Adomaitis. An overview of gallium nitride growth chemistry and its effect on reactor design: Application to a planetary radial-flow cvd system. *Journal of crystal growth*, 286(2):259–278, 2006. pages 124

[218] Simon Gautier. *Elaboration par MOVPE des nouveaux matériaux B (Ga, Al) N pour les applications dans l'ultra violet et l'électronique de puissance*. PhD thesis, Metz, 2007. pages 124

[219] P Vennegues, B Beaumont, S Haffouz, M Vaille, and P Gibart. Influence of in situ sapphire surface preparation and carrier gas on the growth mode of gan in movpe. *Journal of crystal growth*, 187(2):167–177, 1998. pages 124

[220] E Frayssinet, B Beaumont, JP Faurie, Pierre Gibart, Zs Makkai, B Pécz, P Lefebvre, and P Valvin. Micro epitaxial lateral overgrowth of gan/sapphire by metal organic vapour phase epitaxy. *MRS Internet Journal of Nitride Semiconductor Research*, 7:e8, 2002. pages 125

[221] Kai Cheng, Maarten Leys, Stefan Degroote, Marianne Germain, and Gustaaf Borghs. High quality gan grown on silicon (111) using a sixny interlayer by metal-organic vapor phase epitaxy. *Applied Physics Letters*, 92(19):2111, 2008. pages 125

[222] Yoshiki Kato, Shota Kitamura, Kazumasa Hiramatsu, and Nobuhiko Sawaki. Selective growth of wurtzite gan and alxga1- xn on gan/sapphire substrates by metalorganic vapor phase epitaxy. *Journal of crystal growth*, 144(3-4):133–140, 1994. pages 125

[223] Wui Hean Goh. *Selective area growth and characterization of GaN based nanostructures by metal organic vapor phase epitaxy*. PhD thesis, Georgia Institute of Technology, 2013. pages 125, 126

[224] Serge Luryi and Ephraim Suhir. New approach to the high quality epitaxial growth of lattice-mismatched materials. *Applied physics letters*, 49(3):140–142, 1986. pages 125

[225] Z Liliental-Weber, J Jasinski, M Benamara, I Grzegory, S Porowski, DJH Lampert, CJ Eiting, and RD Dupuis. Influence of dopants on defect formation in gan. *Lawrence Berkeley National Laboratory*, 2001. pages 127

[226] Li-Chien Chen, Jin-Kuo Ho, Charng-Shyang Jong, Chien C Chiu, Kwang-Kuo Shih, Fu-Rong Chen, Ji-Jung Kai, and Li Chang. Oxidized ni/pt and ni/au ohmic contacts to p-type gan. *Applied Physics Letters*, 76(25):3703–3705, 2000. pages 127, 129, 148

[227] V Adivarahan, A Lunev, M Asif Khan, J Yang, Grigory Simin, MS Shur, and R Gaska. Very-low-specific-resistance pd/ag/au/ti/au alloyed ohmic contact to p gan for high-current devices. *Applied Physics Letters*, 78(18):2781–2783, 2001. pages 127

[228] Ja-Soon Jang, Seong-Ju Park, Tae-Yeon Seong, et al. Low resistance and thermally stable pt/ru ohmic contacts to p-type gan. *PHYSICA STATUS SOLIDI A APPLIED RESEARCH*, 180(1):103–108, 2000. pages 127

[229] Ja-Soon Jang, Seong-Ju Park, and Tae-Yeon Seong. Metallization scheme for highly low-resistance, transparent, and thermally stable ohmic contacts to p-gan. *Applied Physics Letters*, 76(20):2898, 2000. pages 127

[230] JW Bae, T Hossain, I Adesida, KH Bogart, D Koleske, AA Allerman, and JH Jang. Low resistance ohmic contact to p-type gan using pd/ir/au multilayer scheme. *JOURNAL OF VACUUM SCIENCE AND TECHNOLOGY B MICROELECTRONICS AND NANOMETER STRUCTURES*, 23(3):1072, 2005. pages 128

[231] Ja-Soon Jang, In-Sik Chang, Han-Ki Kim, Tae-Yeon Seong, Seonghoon Lee, and Seong-Ju Park. Low-resistance pt/ni/au ohmic contacts to p-type gan. *Applied physics letters*, 74:70, 1999. pages 128, 129

[232] Masaaki Suzuki, T Arai, T Kawakami, S Kobayashi, S Fujita, Yasuo Koide, Y Taga, and Masanori Murakami. Formation and deterioration mechanisms of low-resistance tati ohmic contacts for p-gan. *Journal of applied physics*, 86(9):5079–5084, 1999. pages 128

[233] Masaaki Suzuki, T Kawakami, T Arai, S Kobayashi, Yasuo Koide, T Uemura, N Shibata, and Masanori Murakami. Low-resistance ta/ti ohmic contacts for p-type gan. *Applied physics letters*, 74:275, 1999. pages 128

[234] Ja-Soon Jang and Tae-Yeon Seong. Electronic transport mechanisms of nonalloyed pt ohmic contacts to p-gan. *Applied Physics Letters*, 76:2743, 2000. pages 128

[235] Ho Won Jang, W Urbanek, MC Yoo, and Jong-Lam Lee. Low-resistant and high-transparent ru/ni ohmic contact on p-type gan. *Applied physics letters*, 80:2937, 2002. pages 128, 129

[236] L Zhou, W Lanford, AT Ping, I Adesida, JW Yang, and A Khan. Low resistance ti/pt/au ohmic contacts to p-type gan. *Applied Physics Letters*, 76:3451, 2000. pages 128

[237] Chen-Fu Chu, CC Yu, YK Wang, JY Tsai, FI Lai, and SC Wang. Low-resistance ohmic contacts on p-type gan using ni/pd/au metallization. *Applied Physics Letters*, 77(21):3423–3425, 2000. pages 128

[238] Ja-Soon Jang, Kyung-Hyun Park, Hong-Kyu Jang, Hyo-Gun Kim, and Seong-Ju Park. Ohmic contacts to p-type gan using a ni/pt/au metallization scheme. *J. Vac. Sci. Technol. B*, 16(6):3105–3107, 1998. pages 128, 129

[239] Dae-Woo Kim, Jun Cheol Bae, Woo Jin Kim, Hong Koo Baik, Jae-Min Myoung, and Sung-Man Lee. The improvement of electrical properties of pd-based contact to p-gan by surface treatment. *Journal of electronic materials*, 30(3):183–187, 2001. pages 128

[240] EF Chor, D Zhang, H Gong, GL Chen, and TYF Liew. Electrical characterization and metallurgical analysis of pd-containing multilayer contacts on gan. *Journal of Applied Physics*, 90:1242–1249, 2001. pages 128, 129

[241] DB Ingerlya, Y Austin Chang, and Yong Chen. The electrical behavior of pt3in7 and niin contacts to p-gan. *Applied physics letters*, 74(17):2480–2482, 1999. pages 128

[242] T Arai, H Sueyoshi, Yasuo Koide, M Moriyama, and Masanori Murakami. Development of pt-based ohmic contact materials for p-type gan. *Journal of Applied Physics*, 89(5):2826–2831, 2001. pages 128

[243] XA Cao, SJ Pearton, SM Donovan, CR Abernathy, F Ren, JC Zolper, MW Cole, A Zeitouny, M Eizenberg, RJ Shul, et al. Thermal stability of wsi x and w ohmic contacts on gan. *Materials Science and Engineering: B*, 59(1):362–365, 1999. pages 128

[244] V Rajagopal Reddy, Sang-Ho Kim, June-O Song, and Tae-Yeon Seong. Electrical properties of thermally stable pt/re/au ohmic contacts to p-type gan. *Solid-State Electronics*, 48(9):1563–1568, 2004. pages 128

[245] Ho Gyoung Kim, Parijat Deb, and Timothy Sands. High-reflectivity al-pt nanostructured ohmic contact to p-gan. *Electron Devices, IEEE Transactions on*, 53(10):2448–2453, 2006. pages 128

[246] Doo-Hyeb Youn, Maosheng Hao, Yoshiki Naoi, Sourindra Mahanty, and Shiro Sakai. Comparison and investigation of ohmic characteristics in the ni/auzn and cr/auzn metal schemes. *Japanese journal of applied physics*, 37(9R):4667, 1998. pages 128

[247] Taek Kim, Myung C Yoo, and Taeil Kim. Cr/ni/au ohmic contacts to the moderately doped p-and n-gan. In *MRS Proceedings*, volume 449, page 1061. Cambridge Univ Press, 1996. pages 128

[248] JK Sheu, Yan-Kuin Su, Gou-Chung Chi, PL Koh, MJ Jou, CM Chang, CC Liu, and WC Hung. High-transparency ni/au ohmic contact to p-type gan. *Applied physics letters*, 74(16):2340–2342, 1999. pages 128

[249] Z Hassan, YC Lee, FK Yam, ZJ Yap, N Zainal, H Abu Hassan, and K Ibrahim. Thermal stability of ni/ag contacts on p-type gan. *physica status solidi (c)*, 1(10):2528–2532, 2004. pages 128

[250] LS Chuah, Z Hassan, and H Abu Hassan. Ohmic contacts properties of ni/ag metallization scheme on p-type gan. *Journal of Non-Crystalline Solids*, 356(3):181–185, 2010. pages 128

[251] Hidenori Ishikawa, Setsuko Kobayashi, Y Koide, S Yamasaki, S Nagai, J Umezaki, M Koike, and Masanori Murakami. Effects of surface treatments and metal work functions on electrical properties at p-gan/metal interfaces. *Journal of applied physics*, 81(3):1315–1322, 1997. pages 129

[252] JK Sheu, YK Su, GC Chi, WC Chen, CY Chen, CN Huang, JM Hong, YC Yu, CW Wang, and EK Lin. The effect of thermal annealing on the ni/au contact of p-type gan. *Journal of applied physics*, 83:3172–3175, 1998. pages 129

[253] Ray-Hua Horng, Dong-Sing Wuu, Yi-Chung Lien, and Wen-How Lan. Low-resistance and high-transparency ni/indium tin oxide ohmic contacts to p-type gan. *Applied Physics Letters*, 79(18):2925–2927, 2001. pages 129

[254] JT Trexler, SJ Pearton, PH Holloway, MG Mier, KR Evans, and RF Karlicek. Comparison of ni/au, pd/au, and cr/au metallizations for ohmic contacts to p-gan. In *MRS Proceedings*, volume 449, page 1091. Cambridge Univ Press, 1996. pages 129

[255] Li-Chien Chen, Fu-Rong Chen, Ji-Jung Kai, Li Chang, Jin-Kuo Ho, Charng-Shyang Jong, Chien C Chiu, Chao-Nien Huang, Chin-Yuen Chen, and Kwang-Kuo Shih. Microstructural investigation of oxidized ni/au ohmic contact to p-type gan. *Journal of applied physics*, 86(7):3826–3832, 1999. pages 129

[256] Ho Won Jang, Soo Young Kim, and Jong-Lam Leea. Mechanism for ohmic contact formation of oxidized niõau on p-type gan. *Journal of applied physics*, 94(3), 2003. pages 129

[257] T Maeda, Yasuo Koide, and Masanori Murakami. Effects of nio on electrical properties of niau-based ohmic contacts for p-type gan. *Applied Physics Letters*, 75:4145, 1999. pages 129

[258] Yasuo Koide, T Maeda, T Kawakami, S Fujita, T Uemura, N Shibata, and Masanori Murakami. Effects of annealing in an oxygen ambient on electrical properties of ohmic contacts to p-type gan. *Journal of electronic materials*, 28(3):341–346, 1999. pages 129, 148

[259] Jiin-Long Yang and Jen-Sue Chen. Effect of ga dissolution in au of ni–au system on ohmic contact formation to p-type gan. *Journal of alloys and compounds*, 419(1):312–318, 2006. pages 129

[260] LL Smith, SW King, RJ Nemanich, and RF Davis. Cleaning of gan surfaces. *Journal of electronic materials*, 25(5):805–810, 1996. pages 130

[261] S Ingrey. Iii–v surface processing. *Journal of Vacuum Science & Technology A*, 10(4):829–836, 1992. pages 130

[262] Metal-Semiconductor Contacts. Eh rhoderick and rh williams. *Clarendon, Oxford*, pages 1–70, 1988. pages 139, 140

[263] Hadis Morkoc. *Nitride semiconductors and devices*, volume 32. Springer Science & Business Media, 2013. pages 139

[264] Simon Min Sze. *Semiconductor devices: physics and technology*. John Wiley & Sons, 2008. pages 140, 141

[265] Simon S Cohen and Gennady Sh Gildenblat. *Metal–Semiconductor Contacts and Devices: VLSI Electronics Microstructure Science*, volume 13. Academic Press, 2014. pages 141, 142, 143

[266] Gregory S Marlow and Mukunda B Das. The effects of contact size and non-zero metal resistance on the determination of specific contact resistance. *Solid-State Electronics*, 25(2):91–94, 1982. pages 141, 144

[267] FA Padovani and R Stratton. Field and thermionic-field emission in schottky barriers. *Solid-State Electronics*, 9(7):695–707, 1966. pages 141

[268] CR Crowell and VL Rideout. Normalized thermionic-field (tf) emission in metal-semiconductor (schottky) barriers. *Solid-State Electronics*, 12(2):89–105, 1969. pages 141

[269] Heinz K Henisch. *Semiconductor contacts: an approach to ideas and models*. Number 70. Oxford University Press, USA, 1984. pages 142

[270] W Shockley. Rep al–tdr–64–207. *Air Force Avionics Laboratory, Wright Patterson AFB, OH*, 1964. pages 143

[271] HH Berger. Models for contacts to planar devices. *Solid-State Electronics*, 15(2):145–158, 1972. pages 143

[272] GK Reeves and HB Harrison. Obtaining the specific contact resistance from transmission line model measurements. *Electron Device Letters, IEEE*, 3(5):111–113, 1982. pages 143, 144

[273] Ralph E Williams. *Modern GaAs processing methods*. Artech House Publishers, 1990. pages 143

[274] J Rechid and K Heime. Concentric ring contacts used for the determination of contact resistances. *Solid-State Electronics*, 44(3):451–455, 2000. pages 144

[275] John Bernard Crofton. Ohmic contacts to compound semiconductors. 1992. pages 144, 145

[276] Jin-Kuo Ho, Charng-Shyang Jong, Chien C Chiu, Chao-Nien Huang, Kwang-Kuo Shih, Li-Chien Chen, Fu-Rong Chen, and Ji-Jung Kai. Low-resistance ohmic contacts to p-type gan achieved by the oxidation of ni/au films. *Journal of Applied Physics*, 86(8):4491–4497, 1999. pages 148

[277] Jong-Lam Lee, Marc Weber, Jong Kyu Kim, Jae Won Lee, Yong Jo Park, Taeil Kim, and Kelvin Lynn. Ohmic contact formation mechanism of nonalloyed pd contacts to p-type gan observed by positron annihilation spectroscopy. *Applied physics letters*, 74(16):2289–2291, 1999. pages 148

[278] HJ Leamy. Charge collection scanning electron microscopy. *Journal of Applied Physics*, 53(6):R51–R80, 1982. pages 151, 152, 153

Communications

Journals

Muhammad Arif, Walid Elhuni, Jérémy Streque, Suresh Sundaram, Sofiane Belahsene, Youssef El Gmili, Matthew B. Jordan, Xin Li, Gilles Patriarche, Abdelillah Slaoui, Anne Migan, Abderahim Ramdane, Zakaria Djebbour, Paul L. Voss, Jean Paul Salvestrini, and Abdallah Ougazzaden, "Improving InGaN heterojunction solar cells efficiency using a semibulk absorber", *Submitted to Solar Energy Materials and Solar Cells*, 159, 405–411 (2016)

Muhammad Arif, Jean Paul Salvestrini, Jérémy Streque, Matthew B. Jordan, Youssef El Gmili, Suresh Sundaram, Xin Li, Gilles Patriarche, Paul L. Voss and Abdallah Ougazzaden, "Role of V-pits in the performance improvement of InGaN solar cells", *Applied Physics Letters*, 109, 133507 (2016)

Charles E. Munson IV, **Muhammad Arif**, Jérémy Streque, Sofiane Belahsene, Anthony Martinez, Abderahim Ramdane, Youssef El Gmili, Jean Paul Salvestrini, Paul L. Voss, and Abdallah Ougazzaden, "Model of Ni-63 battery with realistic PIN structure", *Jounral of Applied Physics* 118, 105101 (2015)

Proceedings

Muhammad Arif, Suresh Sundaram, Jérémy Streque, Youssef El Gmili, Renaud Puybaret, Sofiane Belahsene, Abderahim Ramdane, Anthony Martinez, Gilles Patriarche, Thomas Fix, Abdelillah Slaoui, Paul L. Voss, Jean Paul Salvestrini, and Abdallah Ougazzaden, "Investigation of New Approaches for InGaN Growth with High Indium Content for CPV Application", *CPV-11* AIP Conference Proceedings 1679, 040001 (2015)

Oral Presentations

Muhammad Arif, Suresh Sundaram, Jérémy Streque, Youssef El Gmili, Renaud Puybaret, Anthony Martinez, Gilles Patriarche, Paul L. Voss, Jean Paul Salvestrini, and Abdallah Ougazzaden, "Investigation of New Approaches for InGaN Growth with High Indium Content for CPV Application", *11^{th} International Conference on Concentrated Photovoltaics (CPV-11)* Aix-les Bains, France (2015)

Muhammad Arif, Suresh Sundaram, Jérémy Streque, Youssef El Gmili, Renaud Puyabaret, Xin Li, Peter Bonanno, Konstantino Pantzas, Gilles Patriarche, Abderrahim Ramdane, Anthony

Martinez, Sofiane Belahsene, Paul L. Voss, Jean Paul Salvestrini and Abdallah Ougazzaden, "Towards the improvement of InGaN solar cells", Tunisia (2015)

Muhammad Arif, Suresh Sundaram, Gaelle Orsal, Youssef El Gmili, Jérémy Streque, Ali Ahaitouf, Paul Voss, Abdallah Ougazzaden, Jean-Paul Salvestrini, "InGaN nano and micro structures for efficient photovoltaics and smart lightning applications", China-France workshop on Advanced Materials, Wuhan China 9-12 November, (2014)

Suresh Sundaram, **Muhammad Arif**, Gaelle Orsal, Youssef El Gmili, Jérémy Streque, Ali Ahaitouf, Tarik Moudakir, Konstantino Pantzas, Gilles Patriarche, Paul L. Voss, Abdallah Ougazzaden and Jean Paul Salvestrini, "High indium content InGaN layers for efficient photolvoltaics", *Vers l'amélioration des rendements de conversion dans la filère des cellules InGaN/GaN*, Journées Nationale de photovoltaïque, Dourban (2014)

Suresh Sundaram, Gaelle Orsal, **Muhammad Arif**, Youssef El Gmili, Jérémy Streque, Ali Ahaitouf, Tarik Moudakir, Konstantino Pantzas, Gilles Patriarche, Paul L. Voss, Abdallah Ougazzaden and Jean Paul Salvestrini, "High indium content InGaN layers for efficient photolvoltaics", *12^{th} International Conference on condensed matter and Statistical Physics*, Errachida, Morocco (2013)

Posters

Muhammad Arif, Jérémy Streque, Suresh Sundaram, Ali Ahaitouf, Abdallah Ougazzaden and Jean Paul Salvestrini, "GaN based materials and devices, Fabrication and characterization: Applications to InGaN PIN structures", EMMA - Energie Mécanique et Matériaux, Nancy (2014)

Muhammad Arif, Jérémy Streque, Youssef El Gmili, Suresh Sundaram, Ali Ahaitouf, Matthew b. Jordan, Paul L. Voss, Abdallah Ougazzaden and Jean Paul Salvestrini, "InGaN based high efficiency concentrated photovoltaic", 1^{st} workshop de la cellule Energie du CNRS, CNRS campus Gerard-Megie (2014)

Résumé

Ce travail s′inscrit dans le cadre du développement de nouvelles applications des matériaux III-Nitrure en général, et de l'alliage InGaN en particulier, pour la réalisation de cellules solaire à base de multi-jonction. Les nombreux avantages du matériaux InGaN, à savoir son coefficient d'absorption élevé (10^5 cm^{-1}), sa résistance thermique élevée, et sa tolérance aux radiations ainsi que sa bande interdite couvrant presque tout le spectre solaire (0.64 - 3.4eV), en font un sérieux candidat pour les dispositifs photovoltaïques. Ainsi une cellule solaire à quadruple jonctions permettrait l'obtention d'une efficacité au-delà de 50%.

Cependant, les enjeux technologiques tels que la séparation de phase, le manque de substrat approprié donnant lieu à de forte densité de dislocations, et la difficulté de réalisation du dopage de type-p, sont considérés comme des obstacles pour atteindre les performances attendues. L'objectif de ce travail est d'étudier deux nouvelles approches qui peuvent résoudre les problèmes cités précédemment pour la réalisation de cellules solaires de haute efficacité à base d'InGaN.

La première approche est dite approche "semibulk". Elle consiste à élaborer une structure multicouches InGaN/GaN épaisse avec une optimisation de l'épaisseur de chaque couche (InGaN et GaN), de façon que les couches de GaN soient suffisamment épaisses pour être efficaces, et assez mince pour permettre le transport des porteurs de charges par effet tunnel. Les couches InGaN quant à elles, doivent être assez épaisses et nombreuses afin d'absorber efficacement le rayonnement lumineux et suffisamment minces pour éviter la relaxation et l'apparition de dislocations.

La deuxième approche consiste en la croissance de nanostructures InGaN qui autorise une incorporation d'indium élevée avec un matériau complètement relaxé et sans dislocation. La complète relaxation du matériau permet en outre de s'affranchir de l'effet piézoélectrique qui conduit à une chute du rendement.

Nous avons pu démontrer que les cellules photovoltaïques à base d'$In_{0.08}Ga_{0.92}N$ réalisées suivant l'approche "semibulk" présentent un pic de rendement quantique de 85%, ainsi qu'une efficacité de conversion en conditions AM 1.5G, presque trois fois plus élevée que l'état de l'art. Les premiers résultats obtenus sur les cellules photovoltaïques à base de nanostructures d'$In_{0.08}Ga_{0.62}N$ sont très encourageants.

Abstract

The InGaN material system, with high absorption coefficient (10^5 cm^{-1}) and a bandgap from 0.64 eV to 3.4 eV spanning the entire visual spectrum, make the development of all-InGaN multijunction solar cells with overall conversion efficiency larger than 50% theoretically possible. However, to reach this goal high-quality and thick InGaN layers with high indium concentration are required, which is not a trivial task. Studies of InGaN-based junctions with an indium mole fraction exceeding 0.3 are rare due to issues such as strong phase separation and relaxation of the layer due to lattice mismatch with the substrate which lead to InGaN layers with large dislocation density and indium-clustering. These material problems, significantly limit the performance of InGaN-based photovoltaic cells, and whatever the indium content, performance still remains far from the theoretical ones. The objective of this study is to investigate new approaches that may overcome the issues of phase separation and high dislocation density in InGaN materials with high indium concentration, for the realization of high efficiency InGaN based solar cells.

Two novel approaches are proposed that may overcome the basic challenges involved in the InGaN heterojunction solar cells. The first approach consists in the growth of a thick multi-layered InGaN/GaN absorber, called Semibulk. These GaN interlayers need to be thick enough to be effective and thin enough to allow carrier transport through tunneling. The InGaN layers need to be thick and numerous enough to absorb efficiently the incoming light beam, and thin enough to remain fully strained and without phase separation. The second approach consists in the growth of InGaN nano-structures to achieve high quality thick InGaN epitaxial layers with high indium concentration. It allows the elimination of the preexisting dislocations in the underlying template. It also allows strain relaxation of InGaN layers without any dislocations, leading to higher indium incorporation and reduced piezoelectric effect.

The electro-optical characterization of semibulk $In_{0.08}Ga_{0.92}N$ PV devices show a maximum external quantum efficiency (EQE) of 85%, which is the maximum EQE peak reported so far for an InGaN PIN heterojunction solar cell. The voltage dependence of the current density, under AM 1.5G solar spectrum for the semibulk $In_{0.08}Ga_{0.92}N$ solar cells results in values of J_{sc}, V_{oc}, fill factor (FF) and power conversion efficiency (PCE) as 0.57 mA/cm^2, 1.04 V, 65% and 0.39% respectively. A comparison of the results to the literature show that the J_{sc} is four to five times of what has been reported for a bulk $In_{0.08}Ga_{0.92}N$ PV structure. This value of J_{sc} lead to a PCE for the semibulk $In_{0.08}Ga_{0.92}N$-based PV cell which is at least three times higher than the PCE for the bulk $In_{0.08}Ga_{0.92}N$ structure under AM 0 solar spectrum. For our second approach, high crystalline structural quality for InGaN nano-structures with 35% of indium concentration has been obtained. The electro-optical characterization for $In_{0.09}Ga_{0.91}N$ nano-structure PV cells shows a significant enhancement in the performance of the devices. The PV devices result in a J_{sc} and V_{oc} of 12 mA/cm^2 and 1.89 V under concentrated light respectively.